MIT
SEA
GRANT
PROGRAM

MATHEMATICAL MODELING
OF NEAR COASTAL CIRCULATION

by
John D. Wang
and
Jerome J. Connor

Massachusetts Institute of Technology

Cambridge, Massachusetts 02139

MATHEMATICAL MODELING

OF

NEAR COASTAL CIRCULATION

by

John D. Wang

and

Jerome J. Connor

ABSTRACT

MATHEMATICAL MODELING OF NEAR COASTAL CIRCULATION

by

JOHN D. WANG

and

JEROME J. CONNOR

Hydrodynamic circulation in coastal waters is formulated in terms
of mathematical models. A systematic discussion of the derivation of a
set of governing equations, expressing conservation of mass and momentum
is presented. A simplification is introduced by integrating all varia-
bles and equations over the total water depth. The derivation of the
vertically integrated formulation for one and two layered situations is
discussed along with the underlying assumptions and closure problems.
The treatment of boundaries and boundary conditions is given particular
attention. By analogy to the mechanics of a particle it is postulated
that the admissible boundary conditions must either be in terms of
forces or discharges.

The solution of the formulated problem is achieved by using numeri-
cal techniques. For the spatial discretization the finite element method
is chosen because of its larger flexibility in grid layout and better
treatment of boundary conditions. A detailed discussion is given of the
transformation of the original equations to the mathematically better
based weak form on which the finite element method is applied. All steps
of this procedure are systematically motivated and it is therefore readily
extended to other kinds of problems. The weak form is not dependent on
the existence of a variational statement; but it is derived in a manner
somewhat similar to the method of weighted residuals. The transformed
finite element equations consist of a system of ordinary non-linear
differential equations in time. The structure of the linear homogeneous
part of these equations is shown to have a very attractive symmetric or
skewsymmetric form independent of element type and grid configuration.

Several different time integration schemes are considered and the
special structure of the finite element equations is used to determine
their stability properties. The split time technique which uses the
variables, discharges and depths, at alternating time steps is thus
theoretically found unconditionally stable for the pure initial value
problem. In practice, with prescribed boundary conditions and forcing,
the scheme is apparently only conditionally stable. It is, however,
the more efficient of the different methods examined, requiring least
storage and computational effort. Its accuracy is probably also ade-
quate for most problems. In cases where high accuracy is desired the
fourth order Runge-Kutta method is suggested, although this requires
six to eight times as much work as the split time scheme for the same

2

integration interval. There is need for more basic research in this area of time integrations of finite element equations.

The one layer model is verified against several known analytical solutions of long wave problems and is subsequently applied to determine the typical patterns of Massachusetts Bay, Narragansett Bay and the New Jersey coast. Verification against real field data of currents is very difficult, primarily because information about the correct boundary conditions usually does not exist; but also because reliable current measurements for the coastal environment are extremely difficult to obtain.

The two layer model is still in large part a conceptual model, since many of the processes, such as interfacial shear and mixing, cannot yet be quantified with any confidence. However, as a first estimate of current patterns for layered flow the model is very useful. The formulation and numerical solution techniques follow closely those already discussed for the one layer model. Again, comparisons with known analytical solutions are carried out. Verification against a laboratory experiment and an application to a rectangular approximation of Massachusetts Bay show the importance of being able to use a layered description. The model is very sensitive to the prescribed boundary conditions which further enhances the need for a field monitoring program coincident with its application.

The one layer circulation model has successfully been combined with a compatible dispersion model to describe the spreading of conservative or nonconservative suspended or dissolved matter.

ACKNOWLEDGEMENTS

4

CONTENTS

6

LIST OF SYMBOLS

a	amplitude
$a(-, -)$	inner product, equation (4.6)
a_i	element constants $i = 1, 2, 3$
b_i	element constants $i = 1, 2, 3$
c	wave velocity
c_3	scalar
dx, dy, dz	infinitesimal cube dimensions
e	mass addition rate per volume
e_3	scalar
f	coriolis parameter $= 2\omega_{earth} \cdot \sin\phi$
f_o	data
f_{DW}	Darcy-Weisbach friction coefficient
g	gravitational acceleration
g_3, g_4, g_5	scalars
h	bottom position
h_w	wind influenced depth
i	$\sqrt{-1}$
$<i>x, <i>y$	density gradients
k_s	relative roughness
ℓ	length
ℓ_{ijk}	permutation tensor $i, j, k = 1, 2, 3$
$\underline{m}_x, \underline{m}_y$	specific momentum addition rates per volume
m_x, m_y	specific momentum addition rates per horizontal area
m_3	scalar > 0
n	Mannings n
n_i	normal vector
p	pressure
p^b	bottom pressure
p^s	surface pressure
q_i	rate of volume addition in layer i
q_n, q_s	specific discharges per unit width in normal and tangential directions
q_x, q_y	specific discharges per unit width in x and y directions

7

q_{xo}, q_{yo}	initial values of q_x, q_y
q_r	rate of volume addition in one layer model
t	time
t_o	initial time
u	ensemble averaged x velocity
$\bar{u}$	vertical average of u
$\hat{u}$	trial function
u'	velocity fluctuation in x-direction
$\bar{u}'$	vertical average of u'
u'''	$u' - \bar{u}'$
u'_i	velocity fluctuations $i = 1, 2$
u^{As}	optimal trial function
u_i^{in}	initial velocity vector
v	emsemble averaged y velocity
$\bar{v}$	vertical average of v
v'	velocity fluctuation in y-direction
$\bar{v}'$	vertical average of v'
v'''	$v' - \bar{v}'$
v_{ent}	entrainment velocity
w	vertical velocity
x, y, z	cartesian coordinates, z vertically upwards
x_o, y_o	fixed position in plane
x_i	$= x, y, z$ $i = 1, 2, 3$
x_1, y_1	local cartesian coordinates
A	area
A_i	element constants $i = 1, 2, 3$
C	Chezy coefficient, also element constant
C_1	interface friction coefficient
C_f	bottom friction coefficient
C_D	wind drag coefficient
C, C_3	coefficient matrices
D_x, D_y	dispersion coefficients
E, E_x, E_y, E_{xx}, E_{xy}, E_{yy}, E_{ij}	horizontal eddy diffusion coefficients

8

E_1, E_2	principal values of E_{ij}
E_z	vertical eddy diffusion coefficient
$\underset{\sim}{E}$, $\underset{\sim}{E}_{xx}$, $\underset{\sim}{E}_{yx}$, $\underset{\sim}{E}_{yy}$, $\underset{\sim}{E}_3$	coefficient matrices
$\mathbb{F}_\Delta$	densimetric Froude number
FD	finite difference
FDM	finite difference method
FE	finite element
FEM	finite element method
F_{nn}, F_{ns}	see equations (3.4.7), (3.4.8)
F_p	specific pressure force measure
F_{xx}, F_{yx}, F_{yy}	internal specific force measures
$\underset{\sim}{F}$	nodal values of data
$\underset{\sim}{G}_1$, $\underset{\sim}{G}_3$, $\underset{\sim}{G}_x^i$, $\underset{\sim}{G}_y^i$, $\underset{\sim}{G}_x$, $\underset{\sim}{G}_y$	coefficient matrices
H	total depth
H_o	initial depth
$\underset{\sim}{H}$	vector of depth unknowns
J_o, J	Bessel functions
K	total number of layers
K_x, K_y	horizontal dispersion coefficients
L	differential operator, also channel length
L_1, L_2	segment lengths (L_2 also a function space $= W_2^o$)
$\underset{\sim}{M}$, $\underset{\sim}{M}_b$, $\underset{\sim}{M}_1$, $\underset{\sim}{M}_3$, $\underset{\sim}{M}_h^i$, $\underset{\sim}{M}^i$	coefficient matrices
$\underset{\sim}{M}_x$, $\underset{\sim}{M}_y$	nodal values of momentum addition rates
NBAND	bandwidth
NMEL	number of elements
NMNP	number of nodes
O( )	order of
$\underset{\sim}{P}_x$, $\underset{\sim}{P}_y$, $\underset{\sim}{P}_H$, $\underset{\sim}{P}_Q$, $\underset{\sim}{P}_3$	force vectors
Q	vector of discharge unknowns
R	residual

9

Ri	Richardson number
IR	Reynolds number
S	salinity
S_q	discharge boundary
S_F	force boundary
T	period of oscillation
T, T_s	transformation matrices
TE	truncation error
U	instantaneous local velocity in x-direction
U_{10}	wind velocity at 10 m above surface
V	instantaneous local velocity in y-direction
W_2^0, W_2^1, W_2^2	function spaces
WR	weighted residual
$\underset{\sim}{X}$	vector of unknowns
Y_0, Y_1	Neuman functions
$\underset{\sim}{Y}$	vector
$\underset{\sim}{Z}$	vector
α	bottom slope
α_{nx}, α_{ny}	direction cosines
ζ	$= x + ct$
η	surface displacement
θ	angle, see figure 5-6
θ_1	angle, see figure 5-4
κ	vertical dispersion coefficient, also transformed variable
λ	complex amplification factor
ν	kinematic viscosity
ξ	$= x - ct$
ξ_i	element coordinates $i = 1, 2, 3$
ρ	density
ρ_0	average density
τ_x^b, τ_y^b	bottom shear stresses
τ_x^i, τ_y^i	interface shear stresses

τ_x^s, τ_y^s	surface shear stresses
τ_{xx}, τ_{xy}, τ_{xz}, τ_{yy}, τ_{yz}, τ_{zz}	internal stresses (deviatoric)
ϕ	latitude (N)
$\underline{\phi}$	localized function vector
ω_{earth}	phase velocity of earth rotation
ω, ω_f, ω_F	phase velocities
ω_x, ω_y	x and y components of earth rotation vector
ΔH	test function
Δq_x, Δq_y	test functions
Δs	grid size
Δt	time increment
Δt_{cr}	Courant – Freidricks – Lewy critical time step
$\Delta \rho$	density variation
θ	interior boundary angle
Ω	interior domain
$\overline{\Omega}$	perimeter of Ω
[ ]	references
‖ ‖	norm
| |	absolute magnitude
< >	expected value

Subscripts:

1	layer 1
2	layer 2
k	layer k
n, n-1, n-1/2, n+1/2, n+1	time levels
, (comma)	partial differentiation with respect to following variables
x	x component or direction
y	y component or direction
~	matrix quantity

Superscripts:

b	bottom

e, e_i	element quantity	$i = 1$, NMEL
i, $i+1$	iteration step	
s	surface	
T	transpose of matrix	
ν	molecular viscosity term	
$\hat{}$	trial function	
$\bar{}$ (bar)	of matrix: complex conjugate	
$\cdot$ (dot)	time derivative	
$*$	prescribed variable	
$\blacktriangle$	scale	

LIST OF FIGURES

15

LIST OF TABLES

BLANK

CHAPTER 1

INTRODUCTION

Construction and operation of facilities interacting with coastal waters can change the natural physical, chemical, and biological processes. As a first step towards understanding how and why these changes occur, methods of analyzing the circulation patterns are needed. Estimates of how the water mass moves and where dissolved or suspended matter is transported are basic requirements for answering questions pertaining to many of those processes. They are essential for managing this natural resource in a technologically sound manner.

Based on the vertically integrated shallow water flow formulation, a finite element numerical model for the description/prediction of circulation patterns and surface elevation changes is developed in following chapters.

Two of the major natural causes of motion are the wind and the astronomical tides, which are easily observable. Less conspicuous and more difficult to account for is the forcing mechanism due to density differences within the medium. Density variations are consequences of heat exchange processes or dissolution of chemical compounds such as salt.

The effect of wind is explicitly included in the formulation, and the tide, which is considered as a long wave, is accounted for by the prescribed boundary conditions. Lateral density variations are possible, but their distribution must be specified. An explicit determination would require solving the conservation of energy and salt bal-

18

ance equations simultaneously with the momentum and continuity equations, which adds another degree of complexity to the problem.

The model lends itself also to studying flow generated by natural or man made streamflows and can be used for initial investigations of far field circulation induced by a once through cooling water system.

In a recent report [70], an assessment of the state of the art in estuarine modeling is presented. The vertically averaged equations presented by Pritchard in [70] are quite similar to the equations employed here, though the choice of variables is different. Also, we employ the finite element method to obtain numerical solutions. A review of previous mathematical modeling efforts is presented in Chapter 2.

The tractability of physical modeling is also discussed in [70]. These models are generally expensive, time consuming undertakings. Frequently, physical dimensions necessitate distortion in the model, making exact dynamic similitude impossible. Although physical models are very useful when properly verified, their predictive capabilities are sometimes questionable, especially when physical changes in geometry occur.

The vertically integrated formulation (shallow water) was derived around 1960. It is an attempt at simplifying a very complex problem by eliminating dependence on the vertical coordinate. The term "shallow water" is used to denote a water mass in which there is little variation of the variables over the depth. Since their introduction, the equations have been utilized to investigate circula-

tion problems. However, further simplifications and approximations are often introduced, unfortunately sometimes inconsistently. Similarly, little work has been done to establish the necessary and sufficient boundary conditions for a well-posed problem. Since both physical and numerical models can handle only a bounded domain, the problems must be formulated as mixed initial-boundary value problems. Just recently has there been any concern about existence and uniqueness of solutions to problems thus formulated, and these issues are still unresolved for shallow water circulation. In Chapters 3 and 4, the derivation of the vertically integrated flow equations is reviewed. The underlying assumptions, basis for constitutive equations, and boundary conditions are discussed in detail.

The numerical models have traditionally employed the finite difference method to solve the governing differential equations. In essence, this method satisfies the governing equations by replacing derivatives by difference approximations. For a problem in two spatial dimensions this implies a discretization with a constant size, square grid mesh. Although grids of other shapes are possible, they are usually too inefficient to use. In recent years, a more powerful method, the finite element technique, has emerged. In this method, the function satisfying the governing equations and boundary conditions is approximated by piecewise polynomials. Very flexible grid discretization is an essential virtue of this method. Its other merits and problems are discussed in Chapters 5 and 6.

Verification of the model is important. It assures that the formulation is consistent, the solution procedure is correct, and

also that the assumptions made are in fact reasonable. Model results must be compared with known solutions or actual field data. Verification against real data is the most difficult task. Synoptic data of sea surface level and especially currents are essential for proper verification, and specification of boundary conditions. Unfortunately, a sound and reliable current meter has not yet been perfected. The known propeller or rotor type meters take samples averaged over rather long time intervals (~5 sec) and are therefore influenced by oscillatory wave currents [78]. With the development of the more sophisticated electromagnetic meters with much faster response time and sturdier construction, these problems will hopefully be overcome soon. Some comparisons of actual data from Massachusetts Bay with model results are presented in Chapter 8.

As mentioned earlier, boundary conditions have been treated rather superficially with the result that sufficient data in most cases do not exist to prescribe these conditions accurately. By doing sensitivity studies (Chapter 8) we have found that model results are strongly dependent on the specified boundary conditions. There is therefore a need to establish systematic field monitoring programs providing synoptic real time data for coastal waters. The models can be used advantageously to identify the best places to install gauges and otherwise support the field programs.

In addition to the natural wind and tidal dominated flow situations, a growing interest is directed towards the circulation induced by large industrial or power generating facilities. There are many technical and mathematical problems associated with modeling such

cases. Questions of whether mass is conserved or how to apply the loads have received little attention. In Chapter 8, each of the different loading situations has been considered and solution strategies are outlined.

The one layer vertically integrated model is not applicable when the density varies significantly over the depth causing the flow to be stratified. One cannot neglect the z dependence and a truly three-dimensional formulation is required. Buoyancy effects are important and a complete solution must, in addition to solving the three-dimensional equations of motion, carry out an energy and salt balance to determine the local density. A model of this type is still very much a "dream". The existing soft-and hardware may be sufficient to carry out the solution so it is not a computational problem, although this in itself is formidable. The overwhelming obstacle lies in the formulation. There is at present no coherent way of handling surface and internal waves, real time wind and pressure distributions, turbulent momentum exchange or boundary conditions. With the increased accuracy that is desired, all these factors must be known better; but they cannot be quantified accurately yet. Our belief is, that a reliable predictive three-dimensional model is still a long way off in the future. In fact, there may be more promise in resorting to stochastic rather than deterministic modeling since both flow field and loadings display a random character.

A few attempts at creating a framework for three-dimensional descriptive models have been done as mentioned in Chapter 9. There is however no discussion of the important factors we noted above, or how

such models possibly could be calibrated and verified.

When the density structure shows a layering of the water mass, a compromise between three-dimensional or one-layer vertically averaged models seems reasonable. Figure 1-1 shows a typical vertical density profile for Massachusetts Bay in summer time. This special layered stratification is entirely due to heat exchange processes and is characteristic for many coastal areas. The warmer lighter surface layer (epilimnion) is separated from the colder, heavier bottom layer (hypolimnion) by a thin transition zone around the thermocline (metalimnion). Mixing between epi- and hypolimnion is radically reduced because of the density differences and as a first approximation it may be assumed that top and bottom layers (neglecting the thin metalimnion) only are coupled through the pressure distribution. In this case, a two-layered model will reflect the real physical world better than a simple vertically averaged one layer model and hopefully it will give as accurate results as a three-dimensional model for much less work.

In Chapter 9, the status in layered models is briefly reviewed and Chapter 10 describes the development of a two-layered, vertically averaged, transient, descriptive, mathematical model.
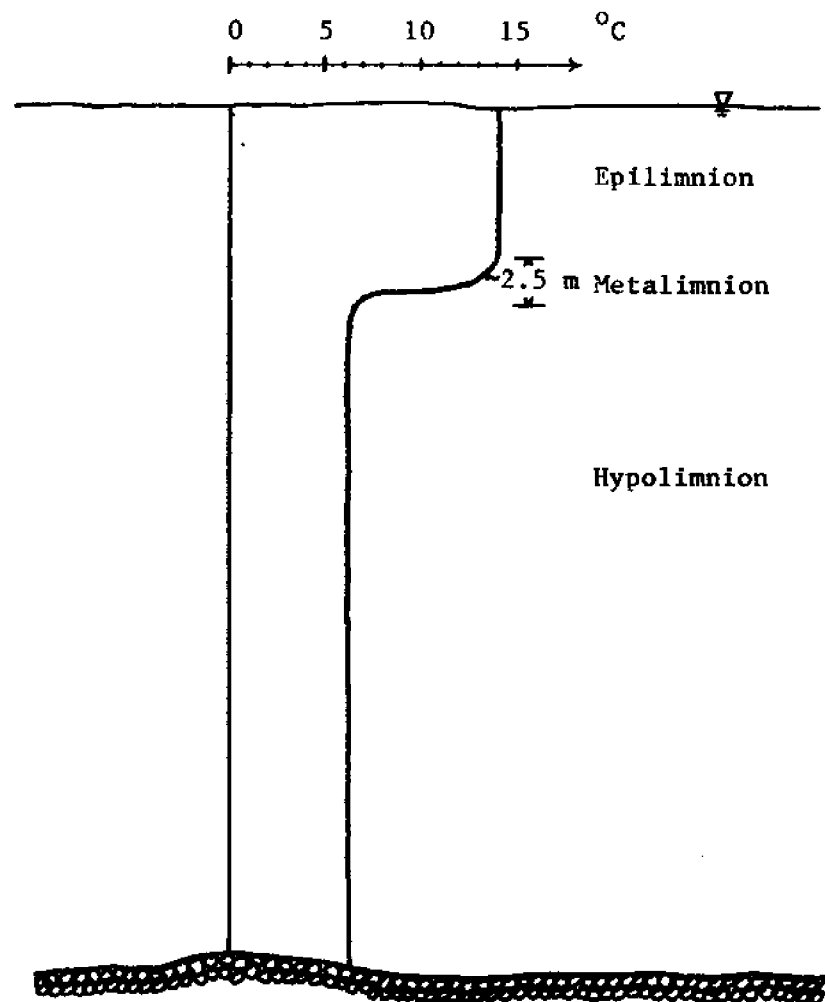
Figure 1-1. Typical summer temperature profile in Massachusetts Bay. Density profile has similar shape, since the salinity structure is fairly homogeneous.

CHAPTER 2

REVIEW OF PREVIOUS EFFORTS

The more significant one layer circulation models developed to date
are briefly reviewed. Both their formulation and solution strategy are
subjected to critical analyses. The objective is to demonstrate the
advantages and disadvantages of and to gain some insight into the var-
ious approaches that one may take. In a subsequent chapter a similar
overview of multilayered and three-dimensional models is presented.

To aid in the following discussion we list here the vertically
averaged equations from Pritchard [70]:

$$(2.1) \quad \frac{\partial \bar{u}}{\partial t} + \bar{u} \frac{\partial \bar{u}}{\partial x} + \bar{v} \frac{\partial \bar{u}}{\partial y} = -g\left(\frac{\partial \eta}{\partial x} + \langle i \rangle_x\right) - \frac{1}{\rho_0} \frac{\partial p^s}{\partial x} + f\bar{v} + \frac{1}{H\rho_0}(\tau_x^s - \tau_x^b)$$

$$(2.2) \quad \frac{\partial \bar{v}}{\partial t} + \bar{u} \frac{\partial \bar{v}}{\partial x} + \bar{v} \frac{\partial \bar{v}}{\partial y} = -g\left(\frac{\partial \eta}{\partial y} + \langle i \rangle_y\right) - \frac{1}{\rho_0} \frac{\partial p^s}{\partial y} - f\bar{u} + \frac{1}{H\rho_0}(\tau_y^s - \tau_x^b)$$

$$(2.3) \quad \frac{\partial \eta}{\partial t} + \frac{\partial (H\bar{u})}{\partial x} + \frac{\partial (H\bar{v})}{\partial y} = 0$$

Figure 3.2 shows the coordinate system; $\bar{u}$, $\bar{v}$ are the vertically aver-
aged velocities, η is the surface elevation, H is total depth, f is the
coriolis parameter , ρ_0 is an average density, p^s, τ^s and τ^b are sur-
face pressure, surface shear and bottom shear; $\langle i \rangle_x$ and $\langle i \rangle_y$ are the
pressure gradients due to variations in the density. The main differ-
ence between this set and the system of equations that we derive in
the next chapter is in the choice of dependent variables. The verti-
cally averaged equations (2.1) to (2.3) are all nonlinear and boundary
conditions must be prescribed on the velocities. In the vertically
integrated formulation that we employ, the conservation of mass equation

is linear and boundary conditions are specified on the discharges. For streamflow boundaries the natural condition is to prescribe the discharge and prescribing the velocity can lead to inconsistencies, because the surface must be left free to move. The bulk of previous work however, has used the vertically average approach, so for discussion purposes equations (2.1) - (2.3) are most suitable. For completeness it is finally noted that Pritchard chose to leave out the controversial eddy viscous terms in (2.1) and (2.2).

Circulation models were initiated in the field of mathematical weather prediction. Some of the earlier efforts in hydrodynamics are the works of Hansen [27] and Welander [76].

Although both were looking at shallow water circulation and employed vertically averaged equations, two widely different approaches have evolved from their work.

Hansen [27] outlined the vertically averaged formulation almost as we know it today. In fact recent models exactly copy his work [35]. He did not include variations in surface atmospheric pressure or density; but did include a horizontal virtual viscosity term with constant eddy viscosity coefficient in the momentum equations. The velocity components were assumed of the form

(2.4) $u = \bar{u}(1 + u'')$

(2.5) $v = \bar{v}(1 + v'')$

where u, v are the ensemble averaged velocity components as functions of (x, y, z, t); $\bar{u}$, $\bar{v}$ are the vertical average values of u, v and $\overline{uu''}$, $\overline{vv''}$ are the deviations over depth of u, v from $\bar{u}$, $\bar{v}$. The relationships (2.4) and (2.5) were used to express the contributions from the

convective accelerations to the virtual viscosity terms. These equations have the disadvantage that if $\bar{u}$ or $\bar{v}$ is zero the corresponding vertical deviation must be zero also which is not necessarily true in nature. Finally the viscosity coefficients due to turbulence and vertical shear were assumed identical which is without physical basis.

The formulated problem was solved by the finite difference method, FDM, using the variables η, $\bar{u}$ and $\bar{v}$ on a staggered grid in space and time. This particular scheme shown in figure 2-1 with later modifications has proven itself very successful in solving tidal flow-problems.

In a recent book by Roache [61] an introduction to the FDM is given for fluid dynamics problems and the importance of satisfying the conservation laws in the large is reviewed. The requirements of stability and consistency are also discussed. A more rigorous treatment of these concepts is given in [60].

One advantage of the staggered grid is that it allows the use of central differences in space and time, which is desirable for accuracy and numerical stability while keeping the number of variables low and partly uncoupled. Figure 2-1 shows there are problems with representing the physical boundaries properly and special treatment is necessary to avoid errors and instability. This aspect was not discussed in [27] and has remained a major problem in later modeling efforts. The usual procedures require assumptions of surface slope or direction of velocity in addition to prescribing the surface elevation or the velocity.

In his original report [38] Leendertse using the same equations as Hansen but without eddy viscosity terms very briefly discusses the problems encountered at the boundaries. However he devoted the main part of
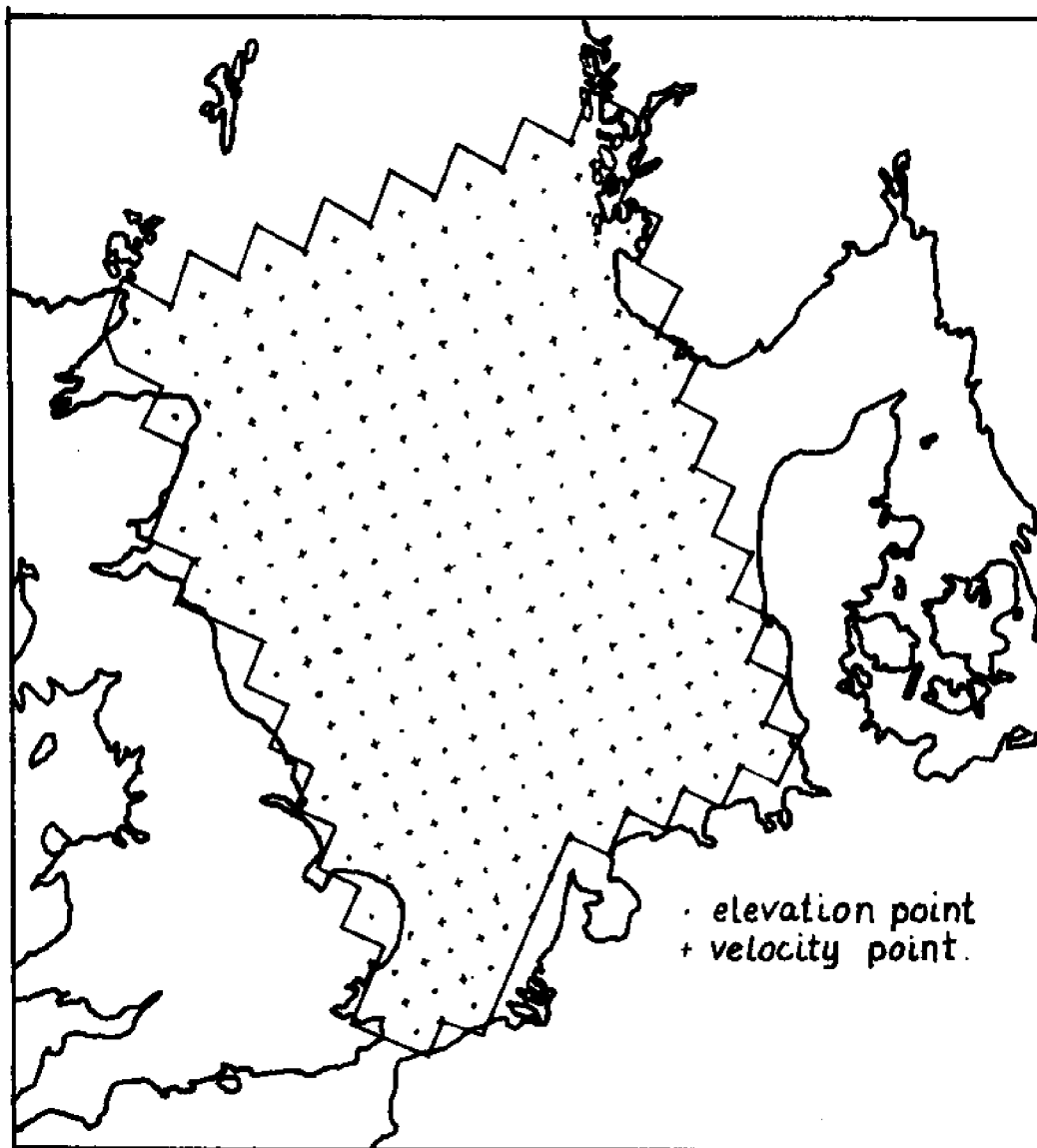
Figure 2-1. Discretization of the North Sea, by Hansen [27].

his efforts to the numerical stability and accuracy aspects, showing the importance of using centered differences. The treatment of the nonlinear terms as usual causes severe problems. Time centered differences cannot be used for the convective terms in the equations of motion if a tridiagonal coefficient matrix must be preserved. Similarly only the linearized equations are solved along the boundaries because the use of values extrapolated from the interior as would be required leads to instabilities. The nonlinear terms in the continuity equations are handled by an iteration procedure. The grid employed must basically consist of a lattice of squares with the configuration shown in figure 2-2.

\# Water level, ocean boundary — u velocity

\+ Water level   I v velocity

° Depth
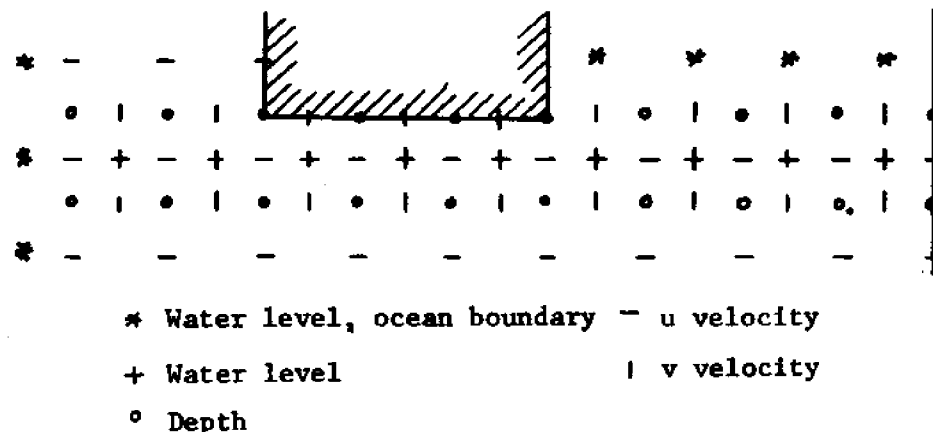
Figure 2-2. Space staggered grid employed by Leendertse and others.

Although computationally very attractive this layout, which also staggers the velocity components (compare with figure 2-1) still

suffers from difficulties with representing an arbitrary boundary properly. It has been argued that the staggering of variables makes it harder to comprehend the results, however, the problem can easily be solved by numerical interpolation, though accuracy of course is unchanged. Several applications are shown and the FORTRAN program is listed in the report. Other investigators frequently use this model or the same scheme; a few examples from the literature are found in [60, 75].

Heaps [28] looked at wind surges in the North Sea using the linearized and integrated dynamical equations in spherical coordinates. His numerical scheme uses a third type of staggered grid in space with velocities at the same points as shown in figure 2-3. Care was taken to center the differences in space and an explicit time integration scheme was used. Consistent treatment of boundary conditions require considering 22 different types of grid-point configurations. Since the linearized equations are used the "influence" method or simple superposition principles can be used. It is however, not certain that non-linear terms can be neglected, especially ignoring second order effects of the surface elevation change seems too crude for storm surge predictions. For shallower areas a linear relationship for bottom friction with constant coefficient would probably not reflect the physical reality very well either.

Reid and Bodine [59] also developed a storm surge model based on the vertically integrated equations without the convective acceleration terms. The space staggered grid of Leendertse was used for the finite difference solution with an explicit time integration method.

30
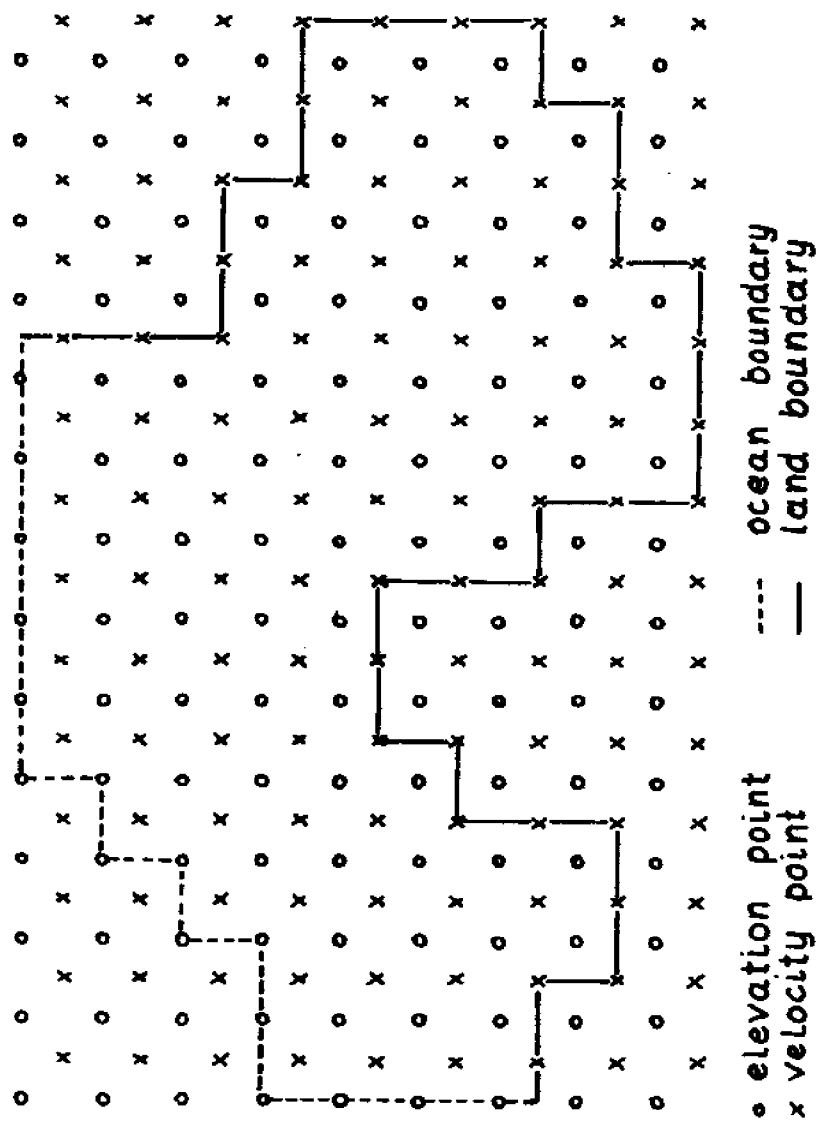
Figure 2-3. Grid employed by Heaps [28].

- elevation point
x velocity point

---- ocean boundary
—— land boundary

31

The flooding of flatlands was incorporated and a radiation type open ocean boundary condition was introduced of the form

(2.6) $$q_n = c\eta$$

where q_n is the discharge per unit width normal to the boundary, c is a coefficient and η is the surface displacement. The objective was to impose less restriction on the system and to avoid the reflection which normally occurs when the flow or surface elevation is fixed. The condition (2.6) is however equivalent to an elastic spring support for a solid and is physically unreasonable for a fluid, since q_n would have to change sign with η, whereas a dependence on the gradient of η would be more realistic, although not correct as coriolis, bottom and surface stresses also play a role.

Abbott et. al. [1] developed their models along the same lines as Leendertse with the space and time staggered grid. However a special implicit time integration method is used which has better conservation properties and thus seems to be more stable. A special feature that allows the model user to change the grid size, but not orientation, has also been developed. The model package includes graphical display capabilities, but the program listings are not available to the public.

Sobey [66] reports on a comparison study of the performance of the models discussed in [1, 28, 38, 59]. To make the investigation viable the governing equations were linearized and coriolis and frictional terms are neglected. Thus the formulation reduce to the simple linear long wave equations

(2.7) $$\frac{\partial \bar{u}}{\partial t} + g\frac{\partial \eta}{\partial x} = 0$$

32

(2.8)
$$\frac{\partial \bar{v}}{\partial t} + g\frac{\partial \eta}{\partial y} = 0$$

(2.9)
$$\frac{\partial \eta}{\partial t} + h\left(\frac{\partial \bar{u}}{\partial x} + \frac{\partial \bar{v}}{\partial y}\right) = 0$$

The existence and treatment of boundary conditions are totally ignored. Fourier series solutions for both the above set of differential equations and each of the 4 listed finite difference analogues were found. The wave frequency and amplitude characteristics were computed using the concept of the propagation factor [38] to describe the ratio of the numerical and analytical solutions. The results show that the simple explicit scheme of Reid and Bodine performed best as long as it remained stable. Their scheme shows less modulation of wave amplitude and phase than the others, however, its application is more restricted by numerical stability.

However, the performance of the implicit models [1] and [38] was also satisfactory and considering that larger time steps can be used these models seem more attractive.

For the great lakes Simons [64] implemented a finite difference model based on the vertically integrated equations with eddy viscosity using two space and time staggered grids simultaneously to avoid problems with the convective terms. Several variations on treatment of bottom friction and convective terms were tried. Since high resolution is desired and the time integration scheme is explicit considerable computation time is necessary.

Dronkers [18] reviews the harmonic method for tidal prediction. This technique relies on time series analysis to derive harmonic functions of known astronomical periods from data. Prediction is only

33

possible when the geometry remains the same and only yields the tidal components. For the coasts of the U.S. such predictions are made available through the tide tables.

An outline of the method of characteristics applied to the one-dimensional shallow water equation is given by Liggett and Woolhiser [43]. The advantage of this approach is that the original system of partial differential equations can be written as ordinary differential equations on the characteristics.

However, these are in general curved and time dependent thus making a solution more difficult to interpret. Although the same methodology can be extended to two-dimensional flow there seem to be no incentive for such work as the curvature of the characteristics makes it a difficult book-keeping and interpolation process to obtain a useful solution. Compared with well established finite difference methods, there does not seem to be any advantage in pursuing the method of characteristics for two-dimensional flow.

The approach initiated by Welander [76] based on the earlier work of Ekman is specifically designed for wind driven currents. The method is noteworthy because the dependence on the vertical x-coordinate is determined analytically. Because one of the assumptions is that the surface is fixed it is often called the "rigid lid" method and is primarily used to predict wind circulation in lakes [24, 41, 42]. The other main assumptions are that horizontal momentum diffusion, non-linear terms and density stratification are neglected. The vertical eddy viscosity is constant throughout, and all velocities vanish on the bottom (no-slip). The solution proceeds by expressing the z dependence as an

infinite fourier cosine series [41, 76]. Next the vertically integrated

equations are solved by introducing a stream function which identical-

ly satisfies the approximate continuity equation. The pressure is

eliminated from the momentum equations and one partial differential

equation in the stream function results. This equation with the proper

boundary conditions is solved using finite differences and the vertical-

ly averaged quantities can be derived. From these the velocity distri-

bution over depth and vertical velocity can be found. By cross differ-

entiating the momentum equations and adding, it is possible to obtain

a poisson type equation for the pressure from which the surface dis-

placement is inferred. Aside from the already mentioned assumptions

which are somewhat restrictive there are difficulties in establishing

boundary conditions, especially for the pressure. Also the stream

function solution has to be accurate enough so that the velocities can

be obtained by numerical differentiation. This can be very costly for

larger problems.

Discrete elements

In the last few years, a method with properties of both finite

difference and element techniques has evolved. Instead of starting

with the differential equations for the infinitesimal element all bal-

ances are performed directly on the computational element. Such a

discrete element can have an arbitrary shape. However, prisms with

square, rectangular or triangular cross sections are usually used.

The variation of variables in an element is characterized by discrete

nodal values. These nodes are usually located at the center of element

sides and at the centroid, and only vertical variations are considered

on an element side. Correctly formulated the conservation principles are satisfied and in theory an arbitrary grid can be used. In order to insure convergence the discrete equations must approximate the differential equations as the elements are made smaller. To show this by taking the limit of the discrete equations as the control volume goes to zero is often difficult for odd shaped elements. Some examples of applications of this method are found in [19, 63]. One disadvantage of this method is that a local grid refinement at x_0, y_0 basically require all elements along $y = x_0$ and $x = y_0$ to have same Δx and Δy as sketched on figure 2-4. It is however quite possible that an interpolation technique or trapezoidally shaped elements could be developed to circumvent this problem. The use of such schemes has so far not been documented in the literature.

Finally, the history and development of the finite element method, FEM, is briefly reviewed. As an engineering tool, it is relatively new and was first used in 1956 to analyse complex aeronautical structures. Until late 1960ies it was mainly applied to problems in solid and structural mechanics. Zienkiewicz has collected a number of such applications along with some more recent fluid flow problems [81]. A survey of the finite element method in continuum mechanics with a discussion of the Galerkin expression for a Newtonian fluid is given by Connor [11].

For a long time the success of the FEM relied upon whether a variational statement of the problem existed. This approach is for example followed by Chan et al [6] to solve some free surface ideal fluid flow problems. The functional was solved for by using the Galerkin method
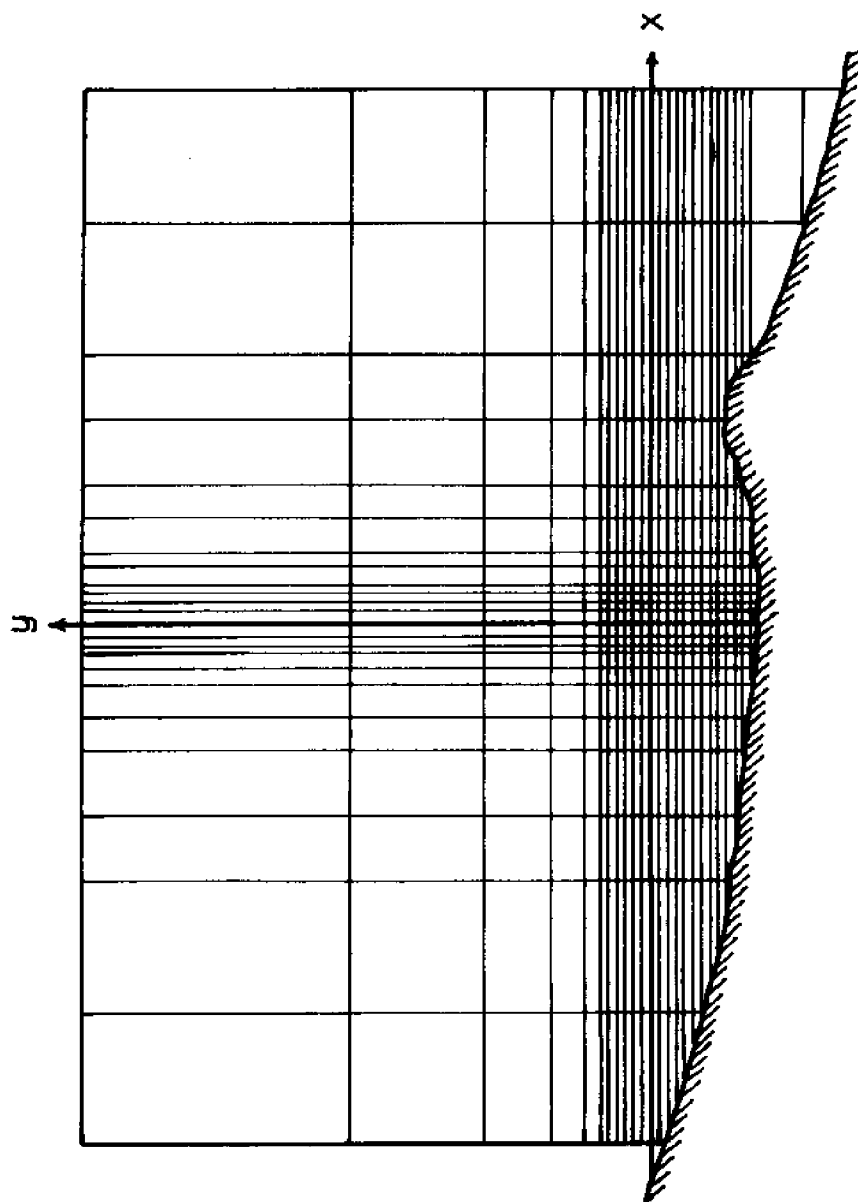
Figure 2-4. Application of discrete elements by Eraslan [19].

which may be interpreted as a piece-wise Rayleigh-Ritz technique. In the paper by Finlayson and Scriven [20] it was shown how Galerkin's method could be derived from the method of weighted residuals and thus the need for a variational principle was circumvented. Their approach is to define the residual as

(2.10) $R = L\hat{u} - f_o$

for the differential equation

(2.11) $Lu = f_o$

where 1 is a differential operator; u is the exact solution, $\hat{u}$ is an approximate solution and f is the data or inhomogeneous term.

Applying a weighting function w to the residual and summing over the entire domain Ω leads to

(2.12) $WR = \int_\Omega Rwd\omega = \int_\Omega (L\hat{u} - f)wd\omega$

Requiring the summed weighted residual, WR, to vanish yields the integral equation on which a finite element solution is based.

Some confusion exists with regard to the terminology of the Galerkin statement. Grotkop [26] thus interprets it as an orthogonalization of the residual to the weighting function. The difference in wording is unimportant and as we show in chapter 4 it is also unnecessary if a few essentials of functional calculus are introduced. Although there is general agreement that the weighting and expansion functions should have the same form (Galerkin principle), obtaining a well-posed formulation for a problem has been somewhat a matter of "feeling" and experience of the solver. This obviously deterred many less experienced people from applying it. However, a straight forward and rigorous mathematical procedure has been developed which enables one to transform

38

any problem from its differential form to an integral form (called the weak form) which is well suited for the FEM. This procedure is explained and demonstrated in chapter 4.

Shallow water circulation has attracted only a few finite element modelers. Gallagher et al. [22] analyzed steady wind driven circulation for shallow lakes using the rigid lid equations. Full advantage of the freedom of varying the grid was not taken in the examples given, however, the possibility of using existing general purpose finite element programs was emphasized.

Taylor and Davis [69] solved the vertically averaged equations for constant density and neglecting eddy viscosity terms. The plane was discretized with cubic isoparametric elements and for the time integration, a fourth order predictor-corrector method, the trapezoidal rule, and finite elements in time were compared. Grotkop [26] treated the same problem using the linear finite element in space and time. This particular scheme is easily shown to be less accurate than the trapezoidal rule although requiring the same computational effort. Applying the linear finite element in time to the equations

$$(2.13) \qquad M\dot{X} = F$$

where the tilde denotes a matrix quantity, leads to the recurrence relationship [69]:

$$(2.14) \qquad MX_{n+1} = MX_n + \Delta t\{\tfrac{1}{3}F_n + \tfrac{2}{3}F_{n+1}\}$$

whereas the trapezoidal rule is written

$$(2.15) \qquad MX_{n+1} = MX_n + \tfrac{1}{2}\Delta t\{F_n + F_{n+1}\}$$

The latter is centered around time $n + \tfrac{1}{2}$ and is therefore more

attractive than the skewed form (2.14). In [69] a cubic expansion in
time was also tested, and based on trial runs for a wave propagating in
a channel it was found that the trapezoidal rule is more efficient. Al-
though both the predictor corrector and the cubic finite element give
more accurate results with the same number of computational elements,
the increased amount of work discourages their use for larger problems.
Even the trapezoidal rule is quite cumbersome to use since the result-
ing matrices are unsymmetric.

The most comprehensive report to date on finite element models
for fluid flow is prepared by Norton et al. [49]. Both vertically aver-
aged and two dimensional flow in the vertical plane are considered. The
latter formulation allows for variable width in a cross section and
corresponds to the laterally integrated equations. Although the trape-
zoidal rule (linear acceleration) is suggested for time integration
all applications are for steady state cases. To handle the nonlinear
terms a Newton-Raphson iteration method is used. Compared to succes-
sive approximation methods this scheme has better convergence proper-
ties; but each iteration requires a considerable amount of computation
and is therefore less attractive for time varying problems. The
Galerkin principle is employed to transform the problem into a form
suitable for applying the finite element methods. The approximation
of curved land boundaries with triangular elements causes conceptual
difficulties when velocity slip is allowed. At the necessary break
points of the model boundary the free tangential velocity component
gives rise to flow across the adjoining segments. Thus it is claimed
that mass cannot be conserved unless both velocity components are

prescribed zero at such break points of the model land boundary. Norton et al. hence advocate that as few break points as possible be introduced and that both velocity components must vanish at these points. A significant decrease in the flexibility of the finite element grid follows and an obvious consequence of this strategy is that large gradients will persist in the vicinity of break points, which makes it necessary to use a fairly fine grid there. This however easily leads to highly distorted elements as displayed in the grids shown in [49], i.e. very long and narrow triangles which are intrinsically less accurate are employed. The apparent conflict reported above is rather ingeniously resolved by proper definition of a normal direction at the break points as we show in chapter 5 thus allowing for a tangential flow component and eliminating the need to reduce the number of breakpoints.

To conclude this overview we suggest that certain objectives can be identified as necessary for developing a general purpose vertically integrated circulation model for shallow water. These objectives are to present the most complete set of governing equations at the present time, using the more natural vertically integrated (instead of averaged) quantities as variables and to take a closer look at the turbulent and dispersive momentum transfers.

The latest developments in numerical approximation techniques furthermore indicate that the finite element method is the most sophisticated numerical tool available. The possibility of using arbitrary grid schematizations and the better handling of boundaries make this technique particularly attractive for our purpose. We

41

shall use the finite element method to solve the general problem of
coastal circulation as it will be formulated and also finally discuss
time integration schemes and other problems associated with obtaining
a solution for a real situation.

3.1 FORMULATION

Beginning with the basic principles of conservation of mass and of force equilibrium,(Newton's second law), a formal mathematical model is developed for transient vertically integrated flow in the plane. The approach is somewhat similar to the works by Hansen [27], Reid and Bodine [59], Leendertse [38], Norton et. al. [49] and Pritchard [70]. We attempt to include all important steps of the development and to account for assumptions and their basis as much as possible. Where numerical parameters are needed in the constitutive equations, numbers or relationships based on experience are indicated. The model is thus intended to be truly predictive with the singular reservation that boundary conditions must be prescribed. The necessary boundary conditions for a well posed problem is also discussed.

3.2 THREE-DIMENSIONAL FLOW.

The mathematical formulation of the conservation of mass and momentum principles for three-dimensional flow has previously been derived in an eulerian framework using a cartesian x-y-z coordinate system, (see f.ex. [15]). The operation consists of balancing mass fluxes or forces for a small cube dx-dy-dz, (see Figure 3-1), and then taking the theoretical limit as the volume of the cube approaches zero. The result is

$$(3.2.1) \qquad \rho_{,t} + (\rho u)_{,x} + (\rho v)_{,y} + (\rho w)_{,z} = e$$

which states that the local rate of change of mass per volume, added to the net flux out, is equal to the rate of adding mass per volume, e. If there are no internal sources (henceforth we shall define a sink as a negative source and therefore only need to talk about sources), e is zero. ρ is the density; u,v,w are the velocity components in x,y,z directions and partial differentiation is written as a subscript comma followed by the independent variable. Equation (3.2.1) expresses a fundamental principle for any continuous one phase fluid.

The equilibrium of forces acting on the control volume is written for the x- and y-directions:

$$(3.2.2) \qquad (\rho u)_{,t} + (\rho u^2)_{,x} + (\rho uv)_{,y} + (\rho uw)_{,z} - \rho f v =$$
$$-p_{,x} + \tau_{xx,x} + \tau_{yx,y} + \tau_{zx,z} + \rho m_x$$

$$(3.2.3) \qquad (\rho v)_{,t} + (\rho uv)_{,x} + (\rho v^2)_{,y} + (\rho vw)_{,z} + \rho f u =$$
$$-p_{,y} + \tau_{xy,x} + \tau_{yy,y} + \tau_{zy,z} + \rho m_y$$

A rotating right handed coordinate system fixed on the earth with the z-axis vertical upwards is chosen. The equations (3.2.1) - (3.2.3) apply to the expected values of velocities and pressures which are considered to be stochastic processes. The τ's are therefore due to molecular viscosity and turbulent momentum transfer [15, 62]:

$$(3.2.4) \qquad \tau_{ij} = \overset{\nu}{\tau_{ij}} - \rho < u'_i u'_j > \qquad i,j = 1,2,3$$

where < > signifies expected value of the argument, $\overset{\nu}{\tau_{ij}}$ is the viscous stress and u'_i is the turbulent velocity fluctuation in the i

44

direction. For convenience, here and in the following, frequent use of tensor notation will be made, the 1,2,3 directions being equivalent to x,y,z. The left hand sides of (3.2.2)and (3.2.3) represent the inertial forces on a unit volume and the right hand sides are the surface forces acting on the same volume plus internal sources of momentum m_x, m_y. In arriving at (3.2.2) and (3.2.3) is has been assumed that the vertical velocity w is small so that only $\rho f u$ and $\rho f v$ are retained from the fictitious coriolis force. f is the coriolis parameter $= 2\,\omega_{earth}$. sin ϕ , where ω_{earth} is the phase velocity of the earth's rotation and ϕ is the latitude (N) of the location.
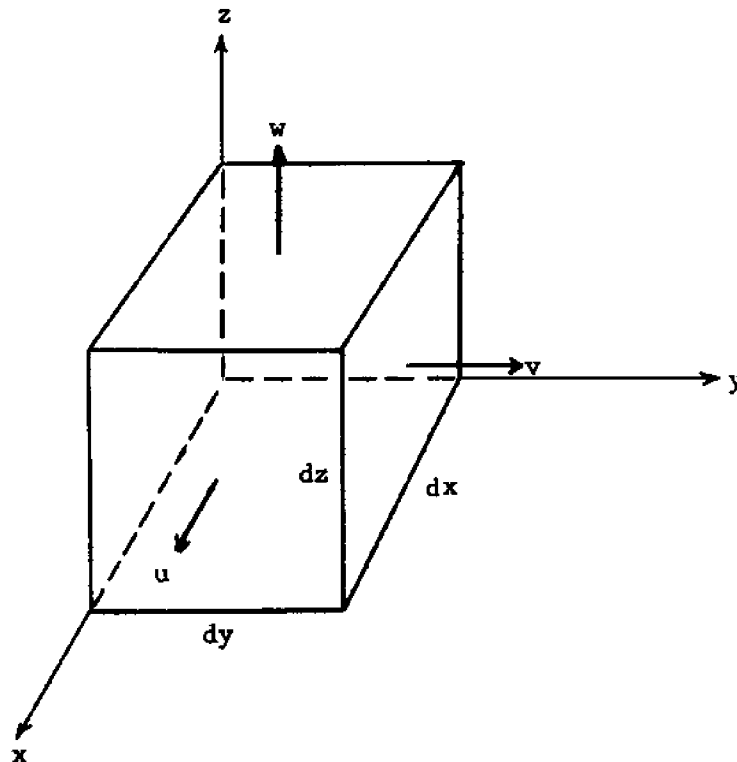
Figure 3-1. Infinitesimal control volume.

45

The isotropic normal stress in fluids is usually compressive and therefore denoted p for pressure (positive). The deviatoric stresses τ_{ij}, i,j = 1,2,3 are defined as usual, the first index denoting the normal direction of the face on which the stress acts and the second, the positive direction of the stress.

An order of magnitude comparison of the inertial terms in (3.2.2) and (3.2.3) is illustrative. Let $\hat{t}$, $\hat{\ell}$, $\hat{h}$, $\hat{u}$ and $\hat{w}$ be representative time, horizontal and vertical length and velocity scales. Scaling (3.2.2) then yields

$$\frac{\hat{u}}{\hat{t}} \sim \frac{\hat{u}^2}{\hat{\ell}} \sim \frac{\hat{u}\hat{w}}{\hat{h}} \sim \hat{f}\,\hat{u} \sim \hat{f}\,\hat{w}$$

where $\hat{f}\,\hat{w}$ is the so far ignored component of the coriolis force and $\hat{f} = f$ is equal to approximately $10^{-4}\sec^{-1}$ at 40° latitude. In order to drop $\hat{f}\,\hat{w}$ and keep the remaining terms we must have

$$\hat{u} \gg \hat{w} \;;\; \frac{\hat{u}}{\hat{\ell}} \simeq \frac{\hat{w}}{\hat{h}} \Rightarrow \hat{\ell} \gg \hat{h} \;;\; \hat{t} \simeq \frac{\hat{\ell}}{\hat{u}} \;;\; \frac{\hat{u}}{\hat{\ell}} \simeq \hat{f}$$

For a typical coastal area $\hat{u} = 0(0.5\text{m/sec})$, $\hat{w} = 0(0.05\text{m/sec})$ $\hat{\ell} = 0(10^3\text{m})$, $\hat{h} \simeq 0(100\text{m})$ giving a corresponding time scale $\hat{t} = 0(2.10^3\sec) = 0(0.6\text{ hr})$, indeed in agreement with the above scaling relations.

Vertical equilibrium requires

(3.2.5) $(\rho w)_{,t} + (\rho u w)_{,x} + (\rho v w)_{,y} + (\rho w^2)_{,z} + 2\rho\omega_x v - 2\rho\omega_y u =$

$- p_{,z} - \rho g + \tau_{xz,x} + \tau_{yz,y} + \tau_{zz,z}$

where ω_x and ω_y are the x and y components of the earth's rotation.

Scaling of this equation leaves only the pressure, gravity and normal stress terms as significant. Again τ_{zz} is related to molecular viscosity and the vertical velocity fluctuations, hence it can be neglected in comparison with ρg and we finally obtain the hydrostatic pressure condition.

$$(3.2.6) \qquad P_{,z} = -\rho g$$

Along the boundaries, special conditions apply. Thus the fact that the free surface is a material interface is expressed as the kinematical condition

$$(3.2.7) \qquad \frac{D}{Dt}(\eta - z)\bigg|_{z=\eta} = \left[\frac{\partial \eta}{\partial t} + u\frac{\partial \eta}{\partial x} + v\frac{\partial \eta}{\partial y} - w\right]_{z=\eta} = 0$$

where evaporation and rainfall are neglected. $\eta = \eta(x,y,t)$ is the surface elevation, Figure 3-2, and $\frac{D}{Dt}$ is the total or particle derivative. At the bottom $z = -h(x,y)$, which is assumed fixed and impermeable, the similar condition is

$$(3.2.8) \qquad \frac{D}{Dt}(z+h)\bigg|_{z=-h} = \left[u\frac{\partial h}{\partial x} + v\frac{\partial h}{\partial y} + w\right]_{z=-h} = 0$$

For lateral boundaries, which are assumed vertical, (see Figure 3-3) the flow must be continuous, implying

$$(3.2.9) \qquad u_i n_i \bigg|_-^+ = 0 \qquad\qquad i = 1,2$$

$$(3.2.10) \qquad \ell_{ijk} u_i n_j \bigg|_-^+ = 0 \qquad\qquad i,j,k = 1,2,3$$

where ℓ_{ijk} is the permutation tensor, $\ell_{123} = \ell_{312} = \ell_{231} = 1$ $\ell_{132} = \ell_{213} = \ell_{321} = -1$ and all other elements are zero.

47
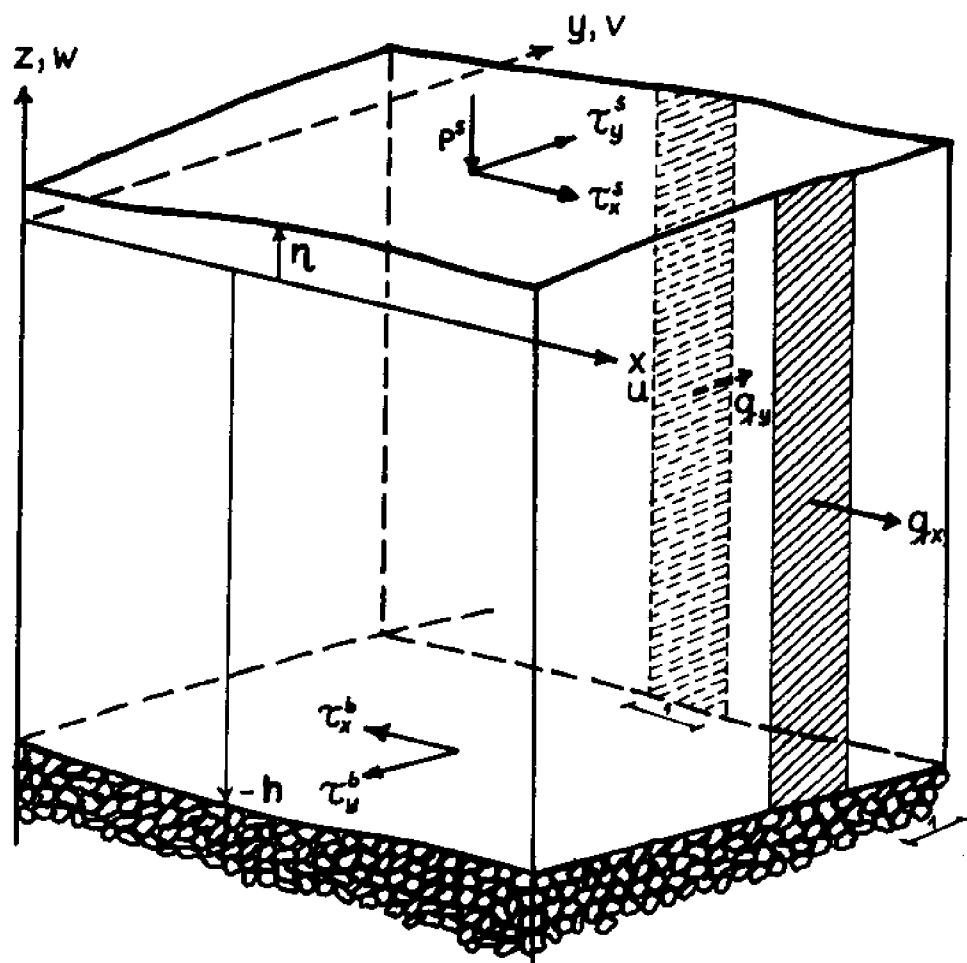
Figure. 3-2. Definition sketch.

48
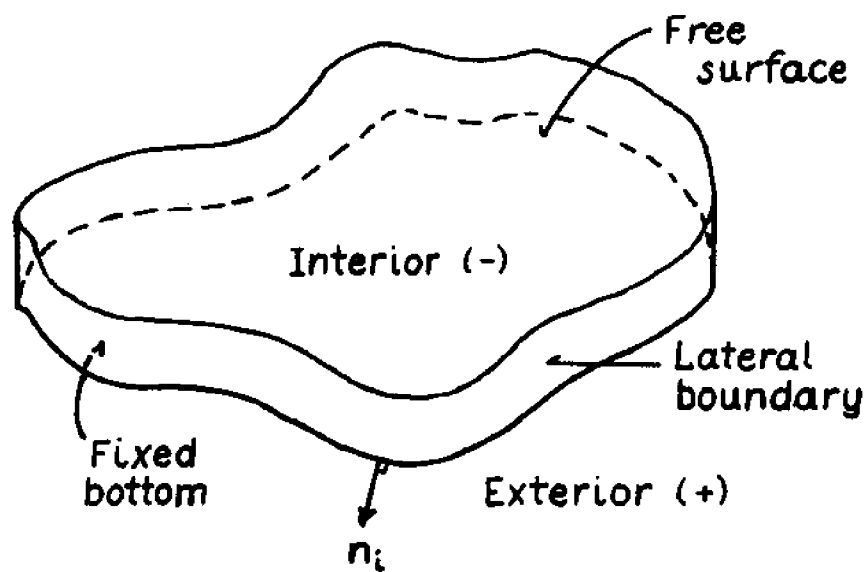
Figure 3-3. Domain terminology.
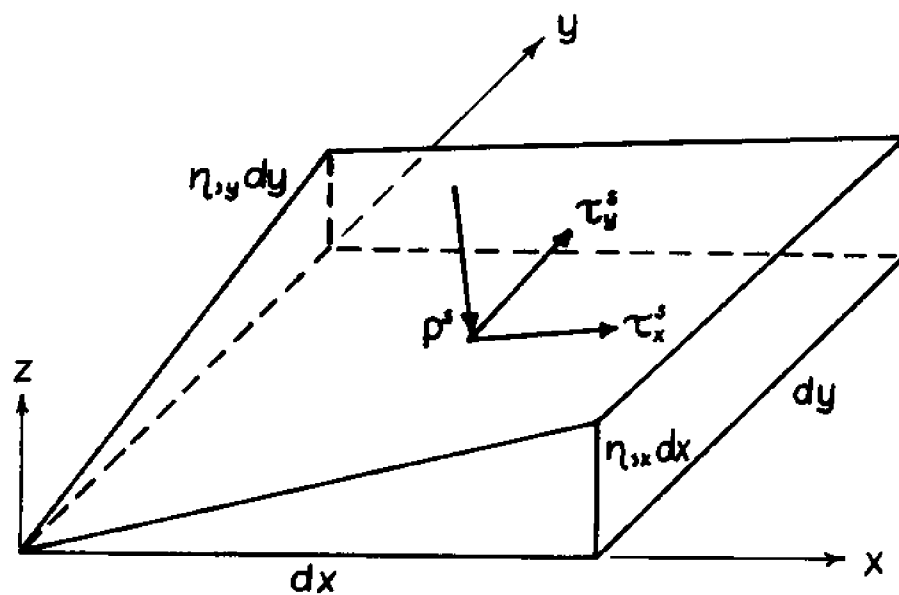
Figure 3-4. Surface force notation.

n_1 is a unit vector perpendicular to the boundary directed out of the area of interest. + and − are points just outside and inside of the boundary. Equations (3.2.9), (3.2.10) express that normal and tangential velocities just outside and inside the boundary must be equal.

Dynamic equilibrium must also be satisfied on the boundaries, see Figure 3-4. Projecting the forces for a surface element on x, y and z-directions result in

$$(3.2.11) \qquad (\tau_x^s + p^s\, \eta_{,x}) = \left[p\eta_{,x} - \tau_{xx}\, \eta_{,x} - \tau_{yx}\, \eta_{,y} - \tau_{zx} \right]_{z=\eta}$$

$$(3.2.12) \qquad (\tau_y^s + p^s\, \eta_{,y}) = \left[p\eta_{,y} - \tau_{xy}\, \eta_{,x} - \tau_{yy}\, \eta_{,y} - \tau_{zy} \right]_{z=\eta}$$

$$(3.2.13) \qquad -p^s + \tau_x^s\, \eta_{,x} + \tau_y^s\, \eta_{,y} = \left[-p - \tau_{xz}\, \eta_{,x} - \tau_{yz}\, \eta_{,y} + \tau_{zz} \right]_{z=\eta}$$

and similarly for the bottom $(z = -h(x,y))$.

$$(3.2.14) \qquad \tau_x^b - p^b\, h_{,x} = \left[-(p - \tau_{xx})\, h_{,x} + \tau_{yx}\, h_{,y} + \tau_{zx} \right]_{z=-h}$$

$$(3.2.15) \qquad \tau_y^b - p^b\, h_{,y} = \left[-\tau_{xy}\, h_{,x} - (p - \tau_{yy})\, h_{,y} + \tau_{zy} \right]_{z = -h}$$

$$(3.2.16) \qquad -p^b - \tau_x^s\, h_{,x} - \tau_y^s\, h_{,y} = \left[-p + \tau_{xz}\, h_{,x} + \tau_{yz}\, h_{,y} + \tau_{zz} \right]_{z=-h}$$

On lateral boundaries, continuity of the stresses is again required.

$$(3.2.17) \qquad [\text{normal stress}]_-^+ = 0$$

$$(3.2.18) \qquad [\text{tangential stress}]_-^+ = 0$$

In case the fluid is considered inviscid (3.2.10) and (3.2.18)

50

must be relaxed and only (3.2.9) and (3.2.17) enforced. Finally, for

a well defined problem, the initial flow field u_i^{in} must be known:

$$(3.2.19) \qquad u_i^{in} = u_{o_i} \qquad i = 1,2,3 \qquad x,y,z \ \varepsilon \ \Omega \quad t = 0$$

For an arbitrary geometry, the problem as formulated is not

easily solved. Numerical solutions are stymied by excessive computer re-

quirements and lack of information on the proper boundary conditions.

In coastal areas that are well mixed through the water column, a signifi-

cant simplification is achieved by eliminating the explicit dependence on

the vertical coordinate. This process is described in the following

section.

3.3 VERTICAL INTEGRATION

In shallow water bodies, the flow variation through the depth

is often less significant. In such cases, vertically integrated equations

and variables may adequately describe the situation. This approach yields

estimates for the transport through any cross section, however, detailed

information on the velocity structure is lost. In the following, the

water density is assumed constant in the z direction, i.e. $\rho = \rho(x,y,t)$.

This and the assumption of relatively small vertical velocities and accel-

erations are normally implied by the definition shallow.

The development of a boundary layer from an applied wind

stress on the surface is dependent on the magnitude of the vertical tur-

bulent momentum transfer. Several investigations have found the vertical

eddy viscosity falling in the range $E \sim 1 - 200 \ cm^2/sec$. If the time

scale of 1 hour is retained, a notion of the meaning of the expression

shallow in connection with wind driven circulation is obtained from the expression

$$(3.3.1) \qquad h_w = \sqrt{E \cdot t} \sim 1 - 10 \ m$$

The use of vertically integrated quantities to predict dispersion of a tracer in this situation is clearly less satisfactory because of the highly non-uniform velocity profile, although the total transport still may be well predicted. In two and multi-layered models, some improvement on this point can be expected. For tidal flow, the driving force which is the hydrodynamic pressure, acts over the entire depth, and vertically integrated values are expected to be representative for the local velocities also, except close to the bottom. Finally, neutrally buoyant stream flows entering or leaving the area are well suited for an integrated treatment since those flows generally are well mixed. Again, in-or outflows with a density difference are better simulated in multilayer models.

The governing equations are integrated over the total depth to eliminate the z-dependence. Beginning with Equation (3.2.1), we formally write

$$(3.3.2) \qquad \int_{-h}^{\eta} \rho_{,t} \ dz + \int_{-h}^{\eta} \rho(u)_{,x} \ dz + \int_{-h}^{\eta} (\rho v)_{,y} \ dz + \int_{-h}^{\eta} (\rho w)_{,z} dz = \int_{-h}^{\eta} e \, dz$$

Making use of Leibnitz's rule [29] we may change the order of integration and differentiation to obtain

$$(3.3.3) \qquad \frac{\partial}{\partial t} \int_{-h}^{\eta} \rho \, dz - \rho \frac{\partial \eta}{\partial t} + \frac{\partial}{\partial x} \int_{-h}^{\eta} \rho u \, dz - \rho u \Big|_{\eta} \frac{\partial \eta}{\partial x} + \rho u \Big|_{-h} \frac{\partial (-h)}{\partial x}$$

$$+ \frac{\partial}{\partial y} \int_{-h}^{\eta} \rho v \, dz - \rho v \Big|_{\eta} \frac{\partial \eta}{\partial y} + \rho v \Big|_{-h} \frac{\partial (-h)}{\partial y} + \rho w \Big|_{\eta} - \rho w \Big|_{-h} = \rho q_I$$

52

Finally applying the kinematic conditions on the surface and bottom results in

$$(3.3.4) \qquad (\rho H)_{,t} + (\rho q_x)_{,x} + (\rho q_y)_{,y} = \rho q_I$$

where we have introduced the integrated variables, total depth:

$$(3.3.5) \qquad H = \int_{-h}^{\eta} dz = h + \eta$$

discharges in x- and y-directions per unit width:

$$(3.3.6) \qquad q_x \equiv \int_{-h}^{\eta} u \, dz$$

$$(3.3.7) \qquad q_y \equiv \int_{-h}^{\eta} v \, dz$$

If we let q_I represent the net rate of volume addition per unit horizontal area, this result (3.3.4) is generally valid for any type of flow, including situations with permeable bottom and evaporation or precipitation at the free surface. The primary objective for including q_I is however to make possible modeling of internal sources such as the discharge from a diffuser pipe.

The integration of the momentum equations, (3.2.2) – (3.2.3) proceeds analogously:

$$(3.3.8) \quad \int_{-h}^{\eta} (\rho u)_{,t}\, dz + \int_{-h}^{\eta} \{ (\rho u^2)_{,x} + (\rho uv)_{,y} \}\, dz + \int_{-h}^{\eta} (\rho uw)_{,z}\, dz$$

$$- \int_{-h}^{\eta} \rho fv\, dz + \int_{-h}^{\eta} p_{,x}\, dz - \int_{-h}^{\eta} (\tau_{xx,x} + \tau_{yx,y})\, dz - \int_{-h}^{\eta} \tau_{zx,z}\, dz$$

$$- \int_{-h}^{\eta} \rho m_x\, dz \; = $$

$$\frac{\partial}{\partial t} \int_{-h}^{\eta} (\rho u)\, dz - (\rho u)\Big|_{z=\eta} \frac{\partial \eta}{\partial t} + \frac{\partial}{\partial x} \int_{-h}^{\eta} (\rho u^2)\, dz - (\rho u^2)\Big|_{\eta} \frac{\partial \eta}{\partial x}$$

$$+ (\rho u^2)\Big|_{-h} \frac{\partial(-h)}{\partial x} + \frac{\partial}{\partial y} \int_{-h}^{\eta} (\rho uv)\, dz - (\rho uv)\Big|_{\eta} \frac{\partial \eta}{\partial y} + (\rho uv)\Big|_{-h} \frac{\partial(-h)}{\partial y}$$

$$+ (\rho uw)\Big|_{\eta} - (\rho uw)\Big|_{-h} - \rho f q_y + \frac{\partial}{\partial x} \int_{-h}^{\eta} p\, dz - p\Big|_{\eta} \frac{\partial \eta}{\partial x}$$

$$+ p\Big|_{-h} \frac{\partial(-h)}{\partial x} - \frac{\partial}{\partial x} \int_{-h}^{\eta} \tau_{xx}\, dz + \tau_{xx}\Big|_{\eta} \frac{\partial \eta}{\partial x} - \tau_{xx}\Big|_{-h} \frac{\partial(-h)}{\partial x}$$

$$- \frac{\partial}{\partial y} \int_{-h}^{\eta} \tau_{yx}\, dz + \tau_{yx}\Big|_{\eta} \frac{\partial \eta}{\partial y} - \tau_{yx}\Big|_{-h} \frac{\partial(-h)}{\partial y} - (\tau_{zx})\Big|_{\eta} + (\tau_{zx})\Big|_{-h}$$

$$- \rho \bar{m}_x \; = $$

$$\frac{\partial}{\partial t} (\rho q_x) + \frac{\partial}{\partial x} \int_{-h}^{\eta} (\rho u^2)\, dz + \frac{\partial}{\partial y} \int_{-h}^{\eta} (\rho uv)\, dz - \rho f q_y + \frac{\partial}{\partial x} \int_{-h}^{\eta} p\, dz$$

$$- \frac{\partial}{\partial x} \rho F'_{xx} - \frac{\partial}{\partial y} \rho F'_{yx} - \tau_x^s + \tau_x^b - \rho \bar{m}_x - p^s \frac{\partial H}{\partial x} - p^b \frac{\partial h}{\partial x} = 0$$

in which we have defined

54

$$(3.3.9) \qquad \rho F_{xx}' \equiv \int_{-h}^{\eta} \tau_{xx} \, dz$$

$$(3.3.10) \qquad \rho F_{yx}' \equiv \int_{-h}^{\eta} \tau_{yx} \, dz$$

$$(3.3.11) \qquad \bar{m}_x \equiv \int_{-h}^{\eta} m_x \, dz$$

For computational reasons it is more convenient to work with the pressure in excess of hydrostatic pressure corresponding to the water level at datum and rest.

The density may be written as a mean value plus a deviation

$$(3.3.12) \qquad \rho(x,y,t) = \rho_o + \Delta\rho(x,y,t)$$

and assuming the instantaneous local deviation is small compared to the mean

$$(3.3.13) \qquad \Delta\rho \ll \rho_o$$

Boussinesque's approximation [57] is introduced whereby the density in all terms is replaced by the constant mean density ρ_o. This is a reasonable simplification provided the real density is used in the pressure term which now takes the form

$$(3.3.14) \qquad \rho_o F_p = \int_{-h}^{\eta} p \, dz - \frac{1}{2} \rho_o \, g \, h^2$$

$$\simeq \rho_o g \, h \eta + \frac{1}{2} \rho_o \, g \, \eta^2 + \frac{1}{2} \Delta\rho \, g \, H^2 + p^s H$$

With these definitions and approximations, the final form of the equilibrium equation (3.3.8) becomes

55

$$(3.3.15) \quad \frac{\partial}{\partial t}(q_x) + \frac{\partial}{\partial x}\int_{-h}^{\eta} u^2 dz + \frac{\partial}{\partial y}\int_{-h}^{\eta} uv\ dz - fq_y + \frac{\partial}{\partial x}(F_p - F'_{xx})$$

$$- \frac{\partial}{\partial y} F'_{yx} + \frac{\tau_x^s - \tau_x^b}{\rho_0} - \bar{m}_x - \frac{p^s}{\rho_0}\frac{\partial H}{\partial x} - g\eta\frac{\partial h}{\partial x} - \frac{\Delta\rho}{\rho_0} gH\frac{\partial h}{\partial x} = 0$$

By complete analogy, the force balance in y-direction gives

$$(3.3.16) \quad \frac{\partial}{\partial t}(q_y) + \frac{\partial}{\partial x}\int_{-h}^{\eta} uv\ dz + \frac{\partial}{\partial y}\int_{-h}^{\eta} v^2 dz + fq_x$$

$$- \frac{\partial}{\partial x} F'_{xy} + \frac{\partial}{\partial y}(F_p - F'_{yy}) + \frac{\tau_y^s - \tau_y^b}{\rho_0} - \bar{m}_y - \frac{p^s}{\rho_0}\frac{\partial H}{\partial x}$$

$$- \frac{\Delta\rho}{\rho_0} g H \frac{\partial h}{\partial y} - g\eta\frac{\partial h}{\partial x} = 0$$

with the corresponding definitions:

$$(3.3.17) \quad \rho F'_{xy} \equiv \rho F'_{yx} \equiv \int_{-h}^{\eta} \tau_{yx}\ dz$$

$$(3.3.18) \quad \rho F'_{yy} \equiv \int_{-h}^{\eta} \tau_{yy}\ dz$$

$$(3.3.19) \quad \bar{m}_y \equiv \int_{-h}^{\eta} m_y\ dz$$

The number of unknowns still exceeds the number of equations for our problem. To overcome this hurdle, the currently most successfully used empirical relations for bottom and surface friction are reviewed in order to establish a set of constitutive equations. Previous modeling has shown that a quadratic, (in mean velocity), bottom friction law in all cases adequately represents the damping due to the shear at the bottom. Several similar empirical expressions, Manning, Chezy, and Darcy-Weisbach equa-

56

tions [15], were originally derived from measurements of steady flow in channels or pipes; but have been modified for two-dimensional unsteady circulation. The quoted relationships are the most widely used and relates shear stress to discharge per unit width as follows:

$$(3.3.20) \qquad \tau_x^b = C_f \, \rho (q_x^2 + q_y^2)^{1/2} \, \frac{q_x}{H^2}$$

$$(3.3.21) \qquad \tau_y^b = C_f \, \rho (q_x^2 + q_y^2)^{1/2} \, \frac{q_y}{H^2}$$

where

$$(3.3.22) \qquad C_f = \begin{cases} \dfrac{1}{8} \, f_{DW} & \text{Darcy-Weisbach} \\[2mm] \dfrac{g}{C^2} & \text{Chezy} \\[2mm] \dfrac{n^2}{H^{1/3}} \, g & \text{Manning} \end{cases}$$

Values of Manning's n are only known for fully developed rough turbulent flow, which fortunately is the normal case in coastal areas, as the Reynolds number $R = \dfrac{u \cdot H}{\nu} = \dfrac{1 \cdot 10}{10^{-6}} = 10^7$ and the relative roughness $\dfrac{k_s}{H} \simeq 0.01 - 0.1$. For fixed roughness, the friction factor C_f is therefore inversely proportional to $H^{1/3}$. Normal values of n range 0.025 - 0.040. The values of C_f for some n and depth values are given in Table 3-1.

In other flow regimes, the use of a Moody diagram to find f_{DW} is the best approach. Choosing as an example $C_f = 0.005$ and a velocity of 1 m/sec gives a shear stress of 5 N/m² which is considered as a large bottom friction.

57

Bottom roughness k_s [m]	n [sec·m$^{-1/3}$]	H [m] 1	2	5	10	20	30	40	50	100
Stones 0.07	0.025	0.0061	0.0049	0.0036	0.0028	0.0023	0.0020	0.0018	0.0017	0.0013
Small rocks 0.20	0.030	0.0088	0.0070	0.0052	0.0041	0.0033	0.0028	0.0026	0.0024	0.0019
Dunes 0.50	0.035	–	0.0095	0.0070	0.0056	0.0044	0.0039	0.0035	0.0033	0.0026
1.10	0.040	–	–	0.0092	0.0073	0.0058	0.0051	0.0046	0.0043	0.0034

TABLE 3-1: Values of C_f

The wind stress on the surface is more complicated to handle because the water surface is deformable so that waves form, and also the length scale of the turbulent wind field is so large that the wind stress is highly variable in time and space [17, 25].

Several investigators have derived expressions for the average wind stress from measurements in the field [5, 16, 28, 74, 77, 79]. If the shear stress is related to the wind speed as follows,

$$(3.3.23) \qquad \tau^s = \rho_{air} \, C_D \, U_{10}^2$$

where ρ_{air} is the air density, (~1.2 kg/m^3) and U_{10} is the wind speed at 10 m above the surface, then the wind drag coefficient C_D has been found to vary from approximately 0.001 and up according to the following relations:

$$(3.3.24) \quad C_D = \begin{cases} 1.25/U_{10}^{1/5} \cdot 10^{-3} & U_{10} \leq 1 \text{ m/sec} \\[2ex] 0.5 \cdot U_{10}^{1/2} \cdot 10^{-3} & 1 < U_{10} \leq 15 \text{ m/sec} \quad \text{Ref.}[79] \\[2ex] 2.6 \cdot 10^{-3} & U_{10} \geq 15 \text{ m/sec.} \end{cases}$$

$$(3.3.25) \quad C_D = \begin{cases} 1.0 \cdot 10^{-3} & U_{10} \leq 5.6 \text{ m/sec} \quad \text{Ref.}[74] \\[2ex] 1.0 + 1.9(1 - \dfrac{5.6}{U_{10}})^2 \cdot 10^{-3} & U_{10} > 5.6 \text{ m/sec.} \end{cases}$$

$$(3.3.26) \quad C_D = 0.00228 + (1.0 - 7.0/U_{10})^2 \; 0.00263$$

$$20 \leq U_{10} \leq 40 \text{ m/sec}$$

$$\text{Ref.}[77]$$

$$(3.3.27) \quad C_D = \begin{cases} 0.577 \cdot 10^{-3} & U_{10} \leq 4.9 \text{ m/sec} \quad \text{Ref.}[28] \\[2ex] (-0.125 + 0.1427 \, U_{10}) \cdot 10^{-3} & 4.9 \leq U_{10} \leq 19.2 \text{ m/sec.} \\[2ex] 2.62 & 19.2 < U_{10} \text{ m/sec} \end{cases}$$

The values given in the referenced papers are plotted in Figure 3-5. The data in [5, 74, 77] were for ponds or lakes, and [16,28,79] used measurements on the open ocean. There is a significant scatter of the data and hence of the curves used to fit the data points. Wu's relationships based on ocean data seem to give the best overall fit. Unfortunately, there are two discontinuities in the suggested relation for C_D,(3.3.24) which physically does not seem reasonable although some justification is attempted [79]. Considering the spread of the curves with a factor of 2 difference between results,it is tempting to fit one straight line
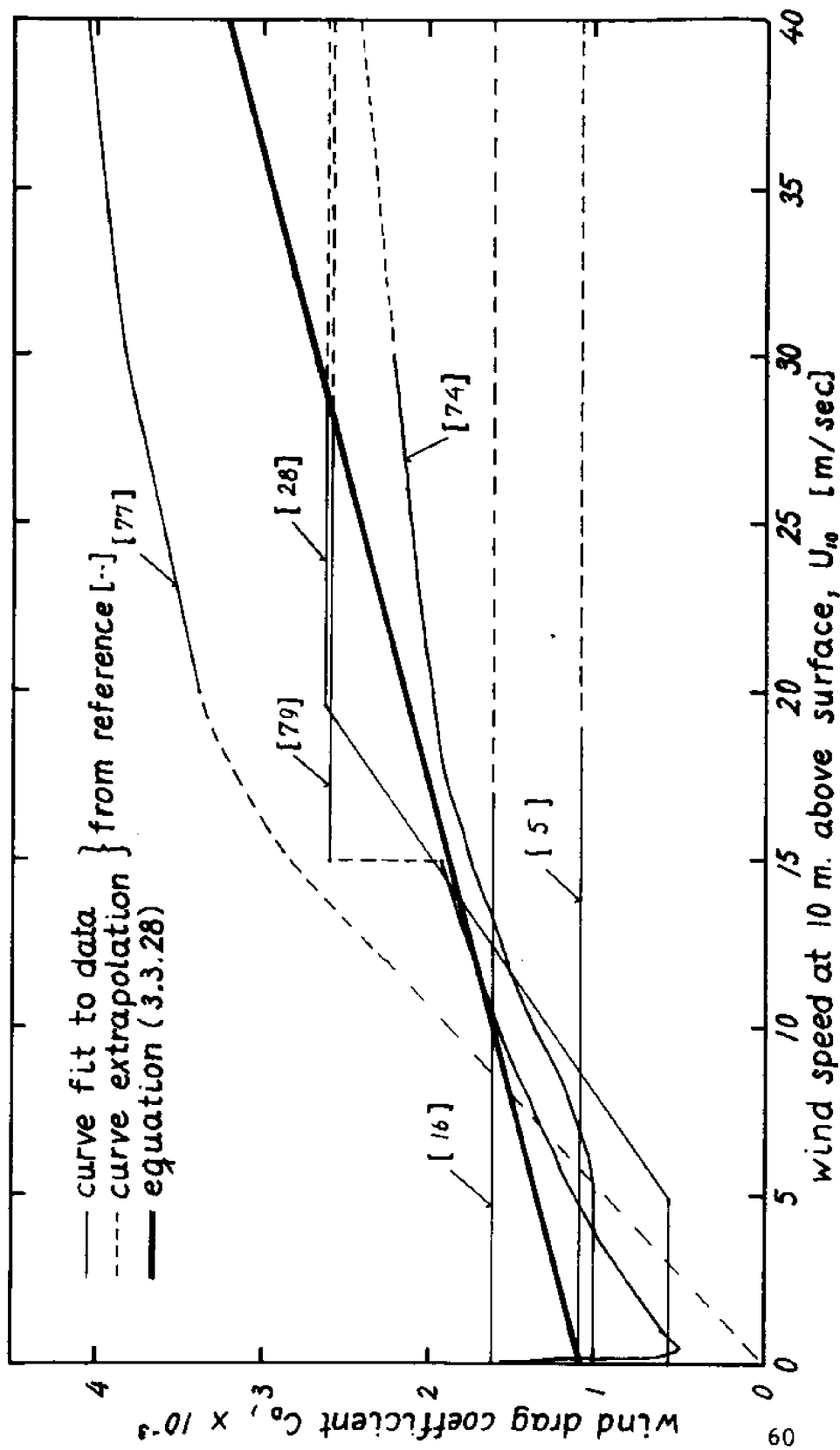
Figure 3-5. Wind drag coefficient, C_D, vs. wind speed, U_{10}.

curve fit to data }
curve extrapolation } from reference [--] [77]
equation (3.3.28)

[28]

[74]

[79]

[5]

[16]

wind speed at 10 m. above surface, U_{10} [m/sec]

wind drag coefficient C_D, $\times 10^{-3}$

relation as shown, with the equation

$$(3.3.28) \qquad C_D = \{1.1 + 0.0536 \cdot U_{10}\} \cdot 10^{-3} \qquad U_{10} \text{ in } [m/sec]$$

For $U_{10} = 10$ m/sec, the drag coefficient is $1.64 \cdot 10^{-3}$ and the predicted shear stress $\tau^S = 0.2$ N/m^2 which is somewhat larger than the ~ 0.1 N/m^2 normally measured in Massachusetts Bay for similar winds.[†] For wind speeds ranging from 0 - 30 m/sec, we can conclude, the present state of the art only allows us to predict the applied wind stress to within a factor of 2. However, considering the complexity of this problem, such an error seems tolerable.

Finally, the origin and significance of the internal stress terms τ_{xx}, $\tau_{xy} = \tau_{yx}$, τ_{yy} are investigated. To close the formulation we also try to express these terms as functions of the integrated flow variables by means of an eddy viscosity coefficient matrix. The approach, in many ways similar to the closure of turbulent flow problems [62], is admittedly based on a physically very loose foundation; but does yield an attractive structure reflecting many of the expected real effects, viz dissipation, and diffusion of momentum. The vertically integrated approach is only valid when the internal stresses are relatively small, so an exact representation of these terms is assumed to be of minor importance. All this trouble is directly caused by averaging the convective acceleration terms. However, the real root of the problem is the use of eulerian rather than lagrangian description (in the latter, the observer follows a particle and

[†] In the range 0 - 10 m/sec, Equation (3.3.28) agrees well with some new results by Parker and Pearce [55].

the convective terms do not appear). We have to live with the eulerian viewpoint in which the observer is fixed in space and propose taking a closer look at the implication of ensemble averaging and vertically integrating an instantaneous velocity product. Without loss of generality we may write the instantaneous local velocity components U, V as

$$(3.3.29) \qquad U \equiv u + u' \equiv (\bar{u} + \bar{u}') + (u'' + u''')$$

$$(3.3.30) \qquad V \equiv v + v' \equiv (\bar{v} + \bar{v}') + (v'' + v''')$$

where u, v are ensemble averages (assuming the flow field is basically random); u', v' are random fluctuations whose ensemble means per definition are zero; $\bar{u}, \bar{v}$ are the vertical average values of u, v; $\bar{u}', \bar{v}'$ are vertical average values of u', v'; u'', v'' are vertical deviations of u, v from $\bar{u}, \bar{v}$; and finally, u''', v''' are vertical deviations of u', v' from $\bar{u}', \bar{v}'$. The significance of each of the various components is shown in Fig. 3-6.

The product $U \cdot V$ is now written out in terms of its components

$$(3.3.31) \qquad U \cdot V = (\bar{u} + \bar{u}' + u'' + u''')(\bar{v} + \bar{v}' + v'' + v''')$$

$$= \bar{u}\,\bar{v} + \bar{u}\,\bar{v}' + \bar{u}\,v'' + \bar{u}\,v''' + \bar{u}'\,\bar{v} + \bar{u}'\,\bar{v}' + \bar{u}'\,v'' + \bar{u}'v'''$$

$$+ u''\,\bar{v} + u''\,\bar{v}' + u''\,v'' + u''\,v''' + u'''\,\bar{v} + u'''\,\bar{v}' + u'''v'''$$

and we want to perform an ensemble averaging and vertical integration of this product. Noting that the order in which these are done is arbitrary we first take the ensemble average with the result

$$(3.3.32) \qquad \langle UV \rangle_{ensemble} = \bar{u}\bar{v} + \bar{u}v'' + \bar{u}'\bar{v}' + \bar{u}'v''' + u''\bar{v} + u''v''$$

$$+ u'''\bar{v}' + u'''v'''$$
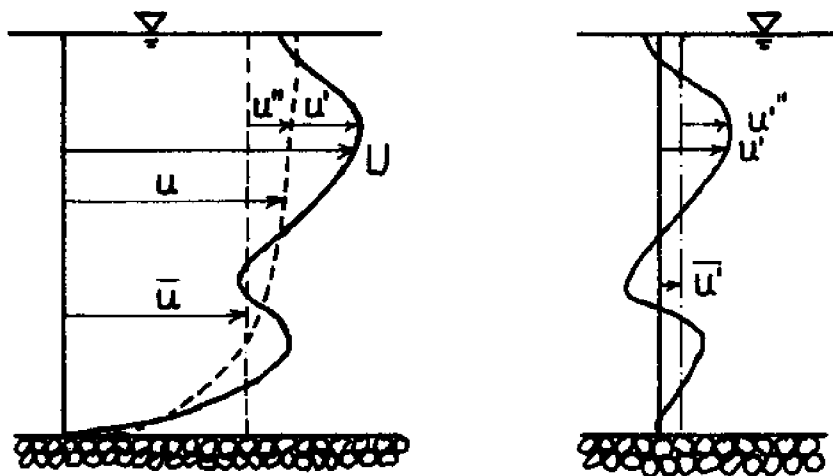
Figure 3-6. Sketch of velocity components.
U = instantaneous local value.
u = ensemble average local value.
$\bar{u}$ = ensemble average, vertical average.
u' = turbulent fluctuation
u''= vertical deviation of u from $\bar{u}$.
$\bar{u'}$ = vertical average of u' .
u'''= vertical deviation of u' from $\bar{u'}$.

since all terms containing only one turbulent fluctuation (') average out to zero. Similarly, an average over depth is carried out.

(3.3.33) $\overline{<UV>}_{ensemble} = \overline{\bar{u}\bar{v}} + \overline{\bar{u}'\bar{v}'} + \overline{\bar{u}''\bar{v}''} + \overline{\bar{u}'''\bar{v}'''}$

where overbar means vertical average according to

(3.3.34) $\bar{x} = \frac{1}{h+\eta} \int_{-h}^{\eta} x \, dz$

Again, all terms containing only one vertical deviation (") average to zero. We can now write the total contribution from the convective terms[†]

(3.3.35) $\int_{-h}^{\eta} <UV>_{ensemble} \, dz = \frac{q_x q_y}{H} + \int_{-h}^{\eta} (<u'v' + u'''v'''>_{ensemble} + u''v'') \, dz$

The first term in the integral on the right is the usual turbulent Reynolds stress and the two remaining terms are momentum transfers due to the vertical velocity distribution. The integral on the right has so far not been related to the mean flow in a consistent and satisfactory way. Consequently it is often neglected completely. The structure of the terms is similar to the molecular momentum transfer process. But while the latter is a homogeneous isotropic process characterized by the molecular viscosity, this is not the case with turbulent motion and vertical velocity shear. Prandtl used mixing length theory to derive a virtual viscosity for turbulent boundary layer flow [62]. In order to get a closed formulation we postulate a similar functional relationship without

---

† Note that this contribution as in (3.3.15) - (3.3.16) is not strictly correct, because we started out with the ensemble averaged equations.

invoking any mixing length theories.

$$(3.3.36) \qquad F_{x_i x_j} = \int_{-h}^{\eta} \{ \tau^{\nu}_{x_i x_j} / \rho_o - <(u_i' u_j') + (u_i''' u_j''')>_{ensemble}$$

$$- u_i'' u_j'' \} \ dz$$

$$= E_{ij} \ (\frac{\partial q_i}{\partial x_i} + \frac{\partial q_i}{\partial x_j}) \qquad i,j = 1,2 \quad \text{no summing over } i,j$$

E_{ij} is a symmetric "eddy viscosity" coefficient matrix that depends on the mean flow, depth, applied surface stresses and flow history. What values actually should be used must be determined from experience or by trial since the explicit dependence on the mentioned parameters is unknown. In the literature $1 - 10^{+5} m^2/sec$ have been quoted for the principal values of E_{ij}. In model applications to Massachusetts Bay, the use of values up to $10^4 \ m^2/sec$ has apparently not changed the results significantly. In spite of the nebulous circumstances we feel that the inclusion of $F_{x_i x_j}$ has several attractive properties. It allows for internal friction and thereby energy dissipation, provided E_{ij} is positive; it does represent actual physical processes(although not accurately) and it is particularly suitable for damping short wave noise generated by numerical methods.

As an attempt to bring some consistency into the anisotropic case the direction of the local mean current is chosen as the major principal axis of E_{ij} with the minor principal axis perpendicular thereto. This means that in a local coordinate system with the x-axis in the direction of the current, E_{ij} is diagonal:

65

$$(3.3.37) \qquad E_{ij} = \begin{bmatrix} E_1 & 0 \\ 0 & E_2 \end{bmatrix}$$

The corresponding E_{ij} in the global coordinate system is then found by simple rotation. If θ is the angle from global to local x-axes, (see Figure 3-7) the rotation is written

$$(3.3.38) \qquad E_{ij} = \underset{\sim}{T}^T \begin{bmatrix} E_1 & 0 \\ 0 & E_2 \end{bmatrix} \underset{\sim}{T}$$

where $\underset{\sim}{T}$ is the transformation matrix

$$(3.3.39) \qquad \underset{\sim}{T} = \begin{bmatrix} \cos\theta & \sin\theta \\ -\sin\theta & \cos\theta \end{bmatrix}$$

and superscript T means transpose. In [54] and [75], the ratio of E_1 to E_2 was found to be in the range 10 - 60 for a tidal coast and a lake. Locally negative values of eddy viscosity have been measured indicating energy being fed to the mean flow by turbulent eddies; however, this happens only under very special conditions. For large areas, the overall effect of the internal stresses is to dissipate energy. [14, 67] give a more detailed discussion of this topic with some examples.

We are finally in a situation where we can present a formulation in closed form. For convenience, all the pertinent equations are given below.

Conservation of mass
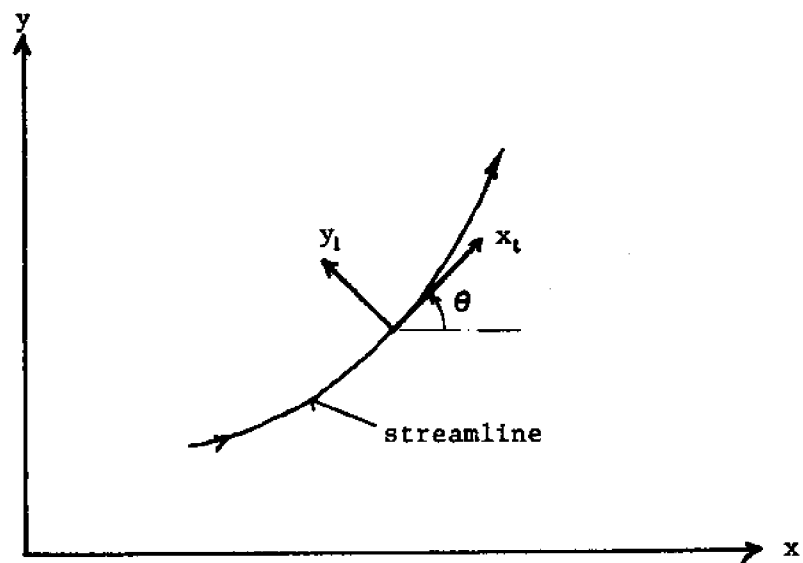
Figure 3-7. Global and local coordinate-system.

$$(3.3.40) \quad H_{,t} + q_{x,x} + q_{y,y} = q_I$$

x and y equilibrium

$$(3.3.41) \quad q_{x,t} + (\bar{u}q_x)_{,x} + (\bar{u}q_y)_{,y} - fq_y + (F_p - F_{xx})_{,x}$$

$$- F_{yx,y} + \frac{1}{\rho_0}(\tau_x^s - \tau_x^b) - \bar{m}_x - \frac{1}{\rho_0}(p^s H_{,x} + \Delta\rho g H h_{,x}) - g\eta h_{,x} = 0$$

$$(3.3.42) \quad q_{y,t} + (\bar{v}q_x)_{,x} + (\bar{v}q_y)_{,y} + fq_x - F_{xy,x} + (F_p - F_{yy})_{,y}$$

$$+ \frac{1}{\rho_0}(\tau_y^s - \tau_y^b) - \bar{m}_y - \frac{1}{\rho_0}(p^s H_{,y} + \Delta\rho g H h_{,y}) - g\eta h_{,y} = 0$$

with the constitutive relations.

$$(3.3.14) \quad F_p = g h \eta + \frac{1}{2} g \eta^2 + \frac{1}{2} \frac{\Delta\rho}{\rho_0} g H^2 + \frac{p^s}{\rho_0} H$$

$$(3.3.36) \quad F_{x_i x_j} = E_{ij} \left(\frac{\partial q_i}{\partial x_i} + \frac{\partial q_i}{\partial x_j} \right) \quad i,j = 1,2 \quad \text{no summing over } i,j$$

The bottom and surface shear stresses are given by (3.3.20)-(3.3.21) and (3.3.23) with (3.3.28).

3.4 Boundary Conditions

Defining the correct types of boundary conditions is one of the more critical parts of the formulation process. What prescribed values must be given, and where? The consequence of not specifying enough is normally the existence of non-unique solutions whereas too much may lead to the non-existence of any solution. These issues are often overlooked because the problems are formulated and solved by people who usually do not have

the necessary mathematical background (and time) to worry about the existence and uniqueness of solutions. Still, solutions have been obtained and verified with great success, which probably is due to luck and the fact that generally well behaved physical problems are solved.

In recent years, considerable efforts have been made by mathematicians to prove existence and uniqueness of fluid flow problems, notably solutions of Navier-Stokes equations [34]. Unfortunately, such proofs do not exist yet for our problem and are not likely to be made in the near future. We shall therefore take the "engineering" approach and assume an automatic proof if a reasonable solution is found. To that end, we have to be reasonably certain that the prescribed boundary conditions are proper.

Trying to get a better feeling for what boundary conditions are necessary, we note that the present flow problem is governed by one 2-component vector equation which is the equivalent of Newton's 2nd law:

$$(3.4.1) \qquad \text{Force} = \text{mass x acceleration}$$
$$\Downarrow$$
$$F_i = m(x_i)_{,tt}$$

The law of conservation of mass (3.3.4) is thus a constraint to be distinguished from an equilibrium equation.

It is well-known that for a single particle, a solution to (3.4.1) exists and is unique if an initial condition and either the force F_i or the displacement x_i is prescribed. The intuitive generalization to our flow problem is then to specify an initial condition and the force or the discharge which plays the role of displacement in a fluid [4]

69

at the boundaries. The initial situation is expressed as

$$(3.4.2) \qquad (q_x, q_y) = (q_{xo}(x,y), q_{yo}(x,y)) \text{ for all } (x,y) \text{ in } \Omega \text{ and } t = 0$$

Ω is the entire interior domain and the initial time is taken as zero.
Also the initial mass must be known, thus
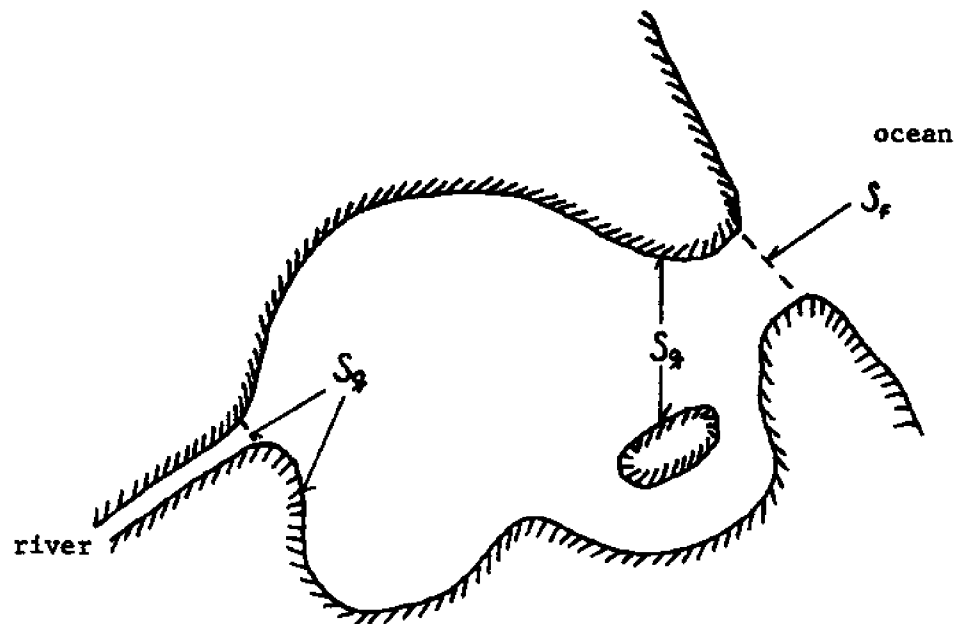
Figure 3-8: Discharge and Force Boundaries

$$(3.4.3) \qquad H = H_o(x,y) \text{ for all } (x,y) \qquad t = 0$$

On the boundaries there are two alternatives as previously mentioned.
Referring to Figure 3-8, we distinguish between discharge boundaries
S_q and force boundaries S_F. On S_q we write

$$(3.4.4) \qquad q_n = \alpha_{nx} q_x + \alpha_{ny} q_y = q_n^*$$

$$(3.4.5) \qquad q_s = -\alpha_{ny} q_x + \alpha_{nx} q_y = q_s^*$$

for the normal and tangential discharges, where the direction cosines are

$$(3.4.6) \qquad \alpha_{nx} = \cos (n,x) ; \quad \alpha_{ny} = \cos (n,y)$$

and the superscript * signifies a prescribed value.

On the remaining part of the boundary, S_F, the external force, must be given, thus

$$(3.4.7) \qquad F_{nn} = -F_p + \alpha_{nx}^2 F_{xx} + \alpha_{ny}^2 F_{yy} + 2\alpha_{nx} \alpha_{ny} F_{xy} = F_{nn}^*$$

$$(3.4.8) \qquad F_{ns} = (\alpha_{nx}^2 - \alpha_{ny}^2) F_{xy} + \alpha_{nx} \alpha_{ny} (F_{yy} - F_{xx}) = F_{ns}^*$$

must hold for the normal and tangential specific force measures. (Specific force measure is equal to a force per unit width and density).

In the idealized case of an inviscid fluid (3.4.4) and (3.4.7) must still hold, however F_{ns}^* must be zero since no shear can be developed and (3.4.5) can hence not be imposed either.

The continuity equation (3.3.4) is used to find the position of the free surface. It is a mass balance equation and does therefore not require any boundary conditions.

CHAPTER 4

THE WEAK FORM

The solution to the problem outlined in the previous chapter is in general too complicated to be obtained by analytical means. The only alternative is then to employ a numerical technique. In the finite element method, the true solution of the governing equations, constraints and boundary conditions is approximated by a function composed of piecewise polynomials. The rigorous mathematical procedure for developing the integral formulation on which the finite element method, FEM, is based, is discussed in this chapter. Actual applications of the FEM are described in the next chapter.

Prior to the use of approximative methods it is essential to establish means of determining how close a computed solution is to the exact answer. For finite difference methods this has lead to the important concept of consistency, i.e. the difference approximation should approach the differential equations asymptotically as the discretization is made finer. Since the finite element method generates an approximation to the exact solution of a given set of equations rather than to the equations themselves, a completely different approach is needed. As an example we consider the equation

$$(4.1) \qquad u(x) = 0 \qquad x \in [a;b]$$

and the three trial solutions shown in Figure 4-1.

A common approach would require (4.1) to be satisfied point by point in $[a;b]$. With this requirement, only u_1 is acceptable. The

error measure for u_2 or u_3 consistent with point by point comparison is given by the maximum deviation

(4.2)
$$\text{error} = ||u|| = \max_{x \in [a;b]} \{ |u| \}$$

Alternatively, a less severe approach uses an average error as measure. A simple average error is defined

(4.3)
$$||u|| = \int_a^b |u| \, dx$$
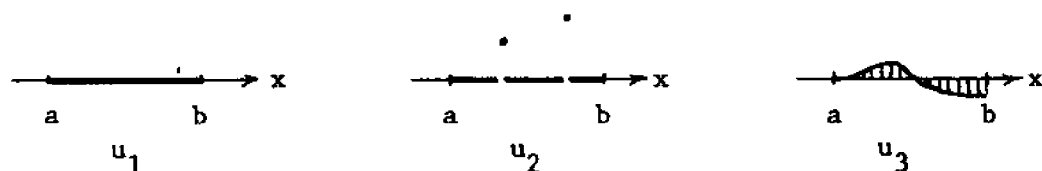
Figure 4-1. Different types of trial functions.

According to (4.3) both u_1 and u_2 would have zero error, whereas the error for u_3 is equal to the shaded area.

Finally, the variance or Euclidean norm is considered. It is defined as

(4.4)
$$||u|| = \left\{ \int_a^b (u(x))^2 dx \right\}^{1/2}$$

and does in fact belong to the class of positive norms which may be written

(4.5)
$$|| u ||_p = \left\{ \int_a^b (u(x))^p \, dx \right\}^{1/p} \qquad p = 1,2,3\ldots$$

The variance (4.4) is easily recognized as the $p = 2$

73

norm. Again u_1 and u_2 cannot be distinguished from the true solution or each other for any $2 \leq p < \infty$, whereas u_3 will have some error. The 1 norm $(p = 1)$ is equivalent to the geometrical mean and is normally too liberal for our purposes. Only with the max norm, (4.2), which is identical with the ∞ norm, $(p = \infty)$, can u_2 be distinguished from u_1, and u_2 is said to deviate in a set of points of measure zero. So far we have listed some commonly used metrics. These can, however, all be interpreted with an inner product representation.

$$(4.6) \qquad a(u,v) = \int_a^b u \cdot v \, dx$$

where u belongs to the space of trial functions and v is a test or weighting function. The norms given by (4.2) - (4.5) correspond to choosing v equal to a delta function, the sign of u, the function u itself and u^{p-1}. The test function is restricted only to the space of functions for which the inner product is finite.

The admissible function spaces for u and v are furthermore derived from (4.6). Consider for example the equation

$$(4.7) \qquad Lu = \frac{\partial^2}{\partial x^2} u = f_0(x) \qquad x\epsilon \, [a;b]$$

with the boundary conditions

$$(4.8) \qquad u = 0 \quad \text{for} \quad x = a$$

$$(4.9) \qquad u_{,x} = 0 \quad \text{for} \quad x = b$$

L is in general a differential operator, but for this example

$$(4.10) \qquad L \equiv \frac{\partial^2}{\partial x^2}$$

For the trial function $\hat{u}$, the following error measure is derived

$$(4.11) \qquad a(L\hat{u} - f, v) = \int_a^b (\hat{u}_{,xx} - f) \cdot v \, dx - [\hat{u}_{,x} \cdot v]_{x=b}$$

The trial function $\hat{u}$ must satisfy condition (4.8), which is called an essential condition. Equation (4.9) is a natural condition that will be automatically satisfied. However, since we do not require $\hat{u}$ to satisfy (4.9), we have added the possible error in (4.11). A more detailed discussion of natural boundary conditions is contained in [63]. Requiring the error given by Equation (4.11) to be zero yields an integrodifferential formulation on which all finite element work is based:

$$(4.12) \qquad \int_a^b (\hat{u}_{,xx} - f) \, v \, dx - [\hat{u}_{,x} \cdot v]_{x=b} = 0$$

Having seen how the error metric naturally leads to an equation for the trial solution, we now turn to the question of what restrictions must be imposed on the function spaces for $\hat{u}$, f, and v. To simplify the problem, we will not distinguish between solutions that only differ in a set of points of measure zero, thus we shall exclude v from containing delta functions. For most practical cases involving a continuum, this simplification is of no consequence. However, for discrete problems it is crucial, and these are therefore also excluded in our subsequent considerations.

The minimum requirements simply assure that the integral in (4.12) is defined and finite. Thus, each of the functions $\hat{u}_{,xx}$, f, and v must belong to the class of square integrable functions:

75

(4.13) $\qquad w(\omega) \in W_2^0(\Omega) \implies w(\omega) \in \{w(\omega) \mid \int_\Omega w^2(\omega)\, d\omega < \infty\}$

W_2^0 is a Hilbert (or Sobolev) space [46] and is also denoted by L_2. For our purposes it is equal to the space of piecewise continuous functions. The equivalent requirement to $\hat{u}$ is that it belongs to W_2^2 which has the property

(4.14) $\qquad w(\omega) \in W_2^2(\Omega) \implies w(\omega) \in \{w(\omega) \mid \int_\Omega (w^2(\omega) + w_{,\omega}^2(\omega) + w_{,\omega\omega}^2(\omega))\, d\omega < \infty\}$

The major advance from this point comes from realizing that several equivalent forms can be derived from (4.12). The objectives are to relax the functional requirements in order to facilitate the construction of admissible trial functions, but also to assure that the solution exists and is unique. It is obvious that any $\hat{u}$ satisfying (4.7) – (4.9) also satisfies (4.12). It remains yet to be shown that the opposite holds. This is achieved by proving existence and uniqueness of solutions to (4.12) or its equivalent forms. These other forms are derived by partial integration of the integrand in Equation (4.12). Integrating once yields

(4.15) $\qquad \int_a^b (\hat{u}_{,x} v_{,x} - fv)\, dx - [\hat{u}_{,x} \cdot v]_{x=a} = 0$

Equation (4.15) shows why (4.9) is called a natural condition and does not have to be satisfied explicitly. Since $\hat{u}_{,x}$ is not necessarily zero at $x = a$ we must require v to vanish where $\hat{u}$ is prescribed. However, there is no loss of generality as the error is eliminated by requiring $\hat{u} = u$ at $x = a$. More important is the change in functional

76

requirements to both $\hat{u}$ and v, that now must belong to W_2^1 with the property:

$$(4.16) \qquad w(\omega) \in W_2^1(\Omega) \implies w(\omega) \in \{w(\omega) \mid \int_\Omega (w^2(\omega) + w_{,\omega}^2(\omega))\, d\omega < \infty\}$$

The relationship between the three spaces mentioned so far is
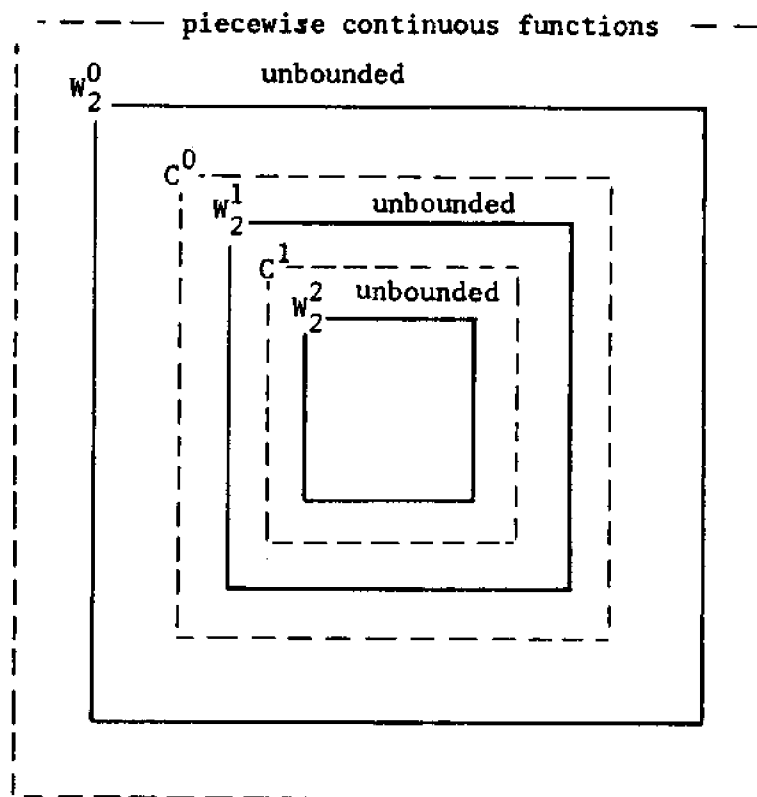
Figure 4-2. Relationship between function classes.

$$(4.17) \qquad W_2^2 \subset W_2^1 \subset W_2^0 \equiv L_2$$

which schematically is shown in Figure 4-2.

For our purposes we need not distinguish between W_2^1 and C^0

77

the continuous functions, or W_2^2 and C^1, the functions with continuous

first derivatives as long as these remain bounded. Clearly we have

achieved an extension of the space from which $\hat{u}$ is chosen when using

(4.15) rather than (4.12). As a general rule, this makes it easier to

find a solution – possibility of existence is improved – however, unique-

ness is harder to prove because the solution space is larger. First we

note that an extension of the class of functions from which $\hat{u}$ may be

chosen only occurs when the highest derivative of L is integrated by

parts. Secondly we postulate that the practically more optimal form is

achieved when $\hat{u}$ and v can be chosen from the same function space.

This applies to even (2m)order (self-adjoint) differential equations.

For differential equations of odd order (2m-1), there are two preferred

formulations $\{\hat{u} \in W_2^m , v \in W_2^{m-1}\}$ or $\{\hat{u} \in W_2^{m-1}, v \in W_2^m \}$. For equations

of order 2m, the optimal form is obtained by integrating by parts m

times, thus $\{\hat{u} \in W_2^m , v \in W_2^m \}$. These equations are called the weak

formulation [34, 68] and constitute a "balance" between existence

and uniqueness. More important, $\hat{u}$ and v are chosen from the same

function space W_2^m , facilitating the application of the finite element

method. The weak form is optimal from a computational point of view

because W_2^m is the most extensive class of functions from which both

$\hat{u}$ and v can be chosen. We note that the weak form is equal to

Galerkins principle and variational statements when these exist. To

distinguish between problems for which solutions of the weak form have

been proven to be unique these are called generalized solutions and

the weak form is called the generalized form [34,68]. We also point

out that homogeneous boundary conditions on $\dfrac{\partial^k \hat{u}}{\partial x^k}$ are natural for

$k \geq m$ and essential for $k < m$.

The simple example we have just discussed illustrates how the introduction of a general error measure logically leads to an integral transformation of the original governing differential equation. We indicated the reasoning behind choosing the weak form and how to derive it systematically when several equivalent integral formulations exist. We also advanced the hypothesis that the weak form is optimal, at least from a computational point of view, because it allows $\hat{u}$ and v to be chosen from the largest common class of functions. Finally, the weak form is balanced with regard to existence and uniqueness of solutions, and it is identical to the first variation of the functional when a variational principle exists.

The procedure outlined above is subsequently applied to derive a weak formulation of the vertically integrated circulation equations. First it is noted that an existence theorem of solutions to the three-dimensional transient Navier-Stokes equations so far has evaded the mathematicians, although Ladyzhenskaya [34] was able to show unique solvability given existence, when the velocities are prescribed everywhere on the boundary. Her approach has been extended by Aranha [3] to mixed problems with either pressure or velocity prescribed as boundary condition. Unfortunately, a rigorous proof of either existence or uniqueness of solutions to the vertically integrated formulation does not exist at present. A heuristic proof of these properties is given in the next chapter for the finite element approximate solutions. This is still a step away from showing existence and uniqueness of solutions to the original formulation and theoretically we must

79

therefore verify all solutions carefully.

First the continuity equation (3.3.40) is transformed:

$$(4.18) \qquad \int_{\Omega} \{H_{,t} + q_{x,x} + q_{y,y} - q_I\} \, \Delta H \, dA = 0$$

where Ω is the interior of the domain of interest, $\Delta H \in L_2$ is an arbitrary test function, and the special notation is used to point out the resemblance with an admissible variation. According to Equation (4.18) we must require $H, q_I, \Delta H \in L_2$ and $q_x, q_y \in W_2^1$. One might consider integrating the $q_{x,x}$ and $q_{y,y}$ terms by parts to relax the continuity requirements; but as we shall see, the dynamic equations make it impossible to achieve this improvement.

The momentum equations (3.3.41) – (3.3.42) with the boundary conditions (3.4.4) – (3.4.5) and (3.4.7) – (3.4.8) are rewritten

$$
\begin{aligned}
(4.19) \qquad & \int_{\Omega} \{q_{x,t} + (\bar{u}q_x)_{,x} + (\bar{u}q_y)_{,y} - fq_y + (F_p - F_{xx})_{,x} - F_{yx,y} \\
& + \frac{1}{\rho_0}(\tau_x^s - \tau_x^b) - \bar{m}_x - \frac{1}{\rho_0}(p^s H_{,x} + \Delta\rho g H \, h_{,x}) - g\eta h_{,x}\} \Delta q_x \, dA \\
& + \int_{S_F} \{\alpha_{nx}(F_{xx} - F_p) + \alpha_{ny} F_{yx} - F_{nx}^*\} \, \Delta q_x \, ds \\
& + \int_{S_q} \{\alpha_{nx} q_n - \alpha_{ny} q_S - q_x^*\} \, \Delta q_x \, ds = 0
\end{aligned}
$$

$$(4.20) \quad \int_{A} \{q_{y,t} + (\bar{v}q_x)_{,x} + (\bar{v}q_y)_{,y} + fq_x - F_{xy,x} + (F_p - F_{yy})_{,y}$$

$$+ \frac{1}{\rho_0}(\tau_y^s - \tau_y^b) - \bar{m}_y - \frac{1}{\rho_0}(p^s H_{,y} + \Delta\rho gHh_{,y}) - g^h h_{,y}\}\Delta q_y \ dA$$

$$+ \int_{S_F} \{\alpha_{nx} F_{xy} + \alpha_{ny}(F_{yy} - F_p) - F_{ny}^*\}\Delta q_y \ ds$$

$$+ \int_{S_q} \{\alpha_{ny} q_n + \alpha_{nx} q_s - q_y^*\} \Delta q_y \ ds = 0$$

In the integrals over the prescribed force boundary S_F and specified flow boundary S_q we have for convenience used the expressions for the x and y components of force and flow (Figure 4-3):

$$(4.21) \quad F_{nx} = \alpha_{nx}(F_{xx} - F_p) + \alpha_{ny} F_{yx}$$

$$(4.22) \quad F_{ny} = \alpha_{nx} F_{xy} + \alpha_{ny}(F_{yy} - F_p)$$

and

$$(4.23) \quad q_x = \alpha_{nx} q_n - \alpha_{ny} q_s$$

$$(4.24) \quad q_y = \alpha_{nx} q_s + \alpha_{ny} q_n$$

The existence of derivatives of the internal stresses means that when (3.3.36) is substituted, second derivatives of the discharges q_x, q_y appear. This again requires q_x, q_y to at least have continuous first derivatives and therefore belong to W_2^2. The test functions $\Delta q_x, \Delta q_y$ however still only have to belong to L_2. We would thus in our search for a solution have to restrict ourselves to trial func-

tions belonging to W_2^2 and test functions belonging to L_2. According to previous arguments, this "unbalanced" situation is undesirable. It is difficult to find admissible trial functions and it is also harder to prove existence of a solution. However, if a solution is found, it is easier to determine whether it is unique because the trial functions belong to a more restricted class of functions.

It is possible to obtain a better balanced form by integrating the terms containing the highest derivatives by parts. From (4.19) we
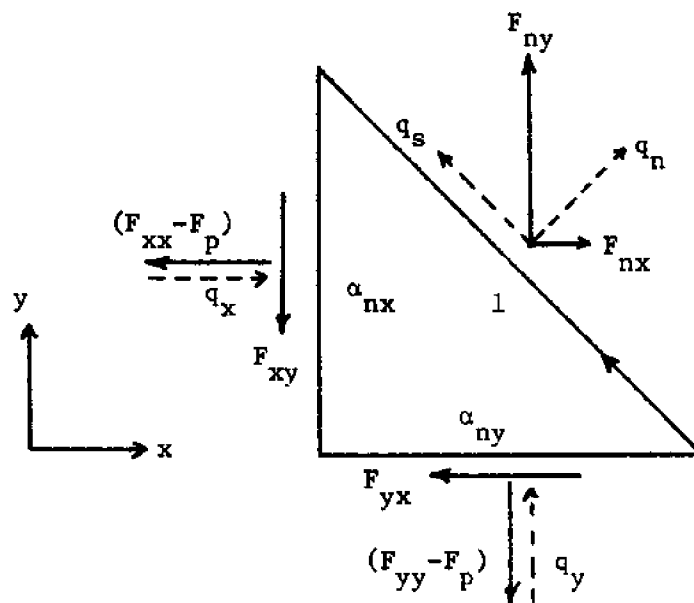
Figure 4-3. Boundary forces and discharges.

have

$$(4.25) \quad \int_\Omega \{ (F_p - F_{xx})_{,x} - F_{yx,y} \} \Delta q_x dA = \int_{\overline{\Omega}} \{ \alpha_{nx} (F_p - F_{xx}) \Delta q_x - \alpha_{ny} F_{yx} \Delta q_x \} ds$$

$$- \int_\Omega \{ (F_p - F_{xx}) \Delta q_{x,x} - F_{yx} \Delta q_{x,y} \} dA$$

where $\overline{\Omega}$ is the perimeter of Ω. Similarly for (4.20).

82

$$(4.26) \quad \int_\Omega \{- F_{xy,x} + (F_p - F_{yy})_{,y}\} \Delta q_y \, dA =$$

$$\int_{\bar\Omega} \{-\alpha_{nx} F_{xy} + \alpha_{ny}(F_p - F_{yy})\} \Delta q_y \, ds$$

$$-\int_\Omega \{- F_{xy} \Delta q_{y,x} + (F_p - F_{yy}) \Delta q_{y,y} \, dA$$

Substituting these results into (4.19) and (4.20) we finally obtain:

$$(4.27) \quad \int_\Omega [\{q_{x,t} + (\bar u q_x)_{,x} + (\bar u q_y)_{,y} - f q_y + \frac{1}{\rho_0}(\tau_x^s - \tau_x^b) - \bar m_x$$

$$- \frac{1}{\rho_0}(p^s H_{,x} + \Delta\rho g H h_{,x}) - g \eta h_{,x}\} \Delta q_x - \{(F_p - F_{xx})\Delta q_{x,x}$$

$$- F_{yx} \Delta q_{x,y}\}] \, dA$$

$$- \int_{\bar\Omega - S_F} \{\alpha_{nx}(F_{xx} - F_p) + \alpha_{ny} F_{yx}\} \Delta q_x \, ds - \int_{S_F} F_{nx}^* \Delta q_x \, ds$$

$$+ \int_{S_q} \{\alpha_{nx} q_n - \alpha_{ny} q_s - q_x^*\} \Delta q_x \, ds = 0$$

$$(4.28) \quad \int_\Omega [\{q_{y,t} + (\bar v q_x)_{,x} + (\bar v q_y)_{,y} + f q_x + \frac{1}{\rho_0}(\tau_y^s - \tau_y^b) - \bar m_y$$

$$- \frac{1}{\rho_0}(p^s H_{,y} + \Delta\rho g H h_{,y}) - g \eta h_{,y}\} \Delta q_y - \{-F_{xy}\Delta q_{y,x}$$

$$+ (F_p - F_{yy}) \Delta q_{y,y}\}] \, dA$$

$$- \int_{\bar\Omega - S_F} \{\alpha_{nx} F_{xy} + \alpha_{ny}(F_{yy} - F_p)\} \Delta q_y \, ds - \int_{S_F} F_{ny}^* \Delta q_y \, ds$$

$$+ \int_{S_q} \{\alpha_{ny} q_n + \alpha_{nx} q_s - q_y^*\} \Delta q_y \, ds = 0$$

Equations (4.18), (4.27) and (4.28) are called the weak form. As previously mentioned, when solutions of the weak form have been shown to be unique it is called the generalized form, and the solutions to the classical differential equations are contained as a subset in its solution space. Unfortunately, we are at present not able to establish uniqueness of solutions to our system of equations. Our primary objective is to find a solution, and relying on the fact that we are solving a well defined physical problem we shall assume it to be unique. However, we will have to evaluate such solutions to make certain they are reasonable and preferably real data verification should be done.

Before concluding this chapter with a closer look at the land boundary conditions, we must introduce one further approximation. So far the actual forces F_{nn} and F_{ns} on a forced boundary have never been measured and it is probably not possible to do in most cases. The reason is, that in order to determine F_{xx}, F_{xy}, F_{yy}, fairly accurate current measurements are required simultaneously along the boundary (synoptic data). This in itself is a tremendous data acquisition and handling problem; but even worse, reliable current meters for the ocean environment do simply not exist at present. Wiegel and Johnson give an introduction to current meters, measurements and their problems in their paper [78]. If current information was available at the boundary, it would anyway be easier and more direct to use those as prescribed conditions rather than trying to derive the internal stresses.

By now it is clear that we cannot expect to get the information we need, however, the surface elevation, its change and thus the

pressure force is usually known or can be obtained with reasonable ease. We shall therefore in view of the above and in order to get a solution assume that F_{ij} is zero along prescribed force boundaries.

At this point, a very pertinent question should have evolved, and that is, why do the F_{ij} enter in the boundary conditions when the mean convective terms do not? Originally they all came from the same convective inertial acceleration terms. The answer is that in an ensemble averaged, vertically integrated formulation the inertial acceleration consists of the local and the mean convective accelerations, whereas the momentum transfer due to turbulence and vertical velocity shear are internal stresses.

This section is summarized with the equations (note $\bar{\Omega} - S_F = S_q$) for conservation of mass and dynamic equilibrium:

(4.18)
$$\int_\Omega \{H_{,t} + q_{x,x} + q_{y,y} - q_I\} \, \Delta H dA = 0$$

(4.29)
$$\int_\Omega [\{q_{x,t} + (\bar{u}q_x)_{,x} + (\bar{u}q_y)_{,y} - fq_y + \frac{1}{\rho_0}(\tau_x^s - \tau_x^b) - \bar{m}_x$$
$$- \frac{1}{\rho_0}(p^s H_{,x} + \Delta\rho g H h_{,x}) - g n h_{,x}\} \Delta q_x - \{(F_p - F_{xx}) \Delta q_{x,x}$$
$$- F_{yx} \Delta q_{x,y}\}] \, dA - \int_{S_q} \{\alpha_{nx}(F_{xx} - F_p) + \alpha_{ny} F_{yx}\} \Delta q_x \, ds$$
$$+ \int_{S_F} \alpha_{nx} F_p^* \Delta q_x \, ds + \int_{S_q} \{\alpha_{nx} q_n - \alpha_{ny} q_s - q_x^*\} \Delta q_x \, ds = 0$$

$$(4.30) \quad \int_\Omega [\{ q_{y,t} + (\bar{v}q_x)_{,x} + (\bar{v}q_y)_{,y} + f q_x + \frac{1}{\rho_0} (\tau^s_x - \tau^b_x) - \bar{m}_y$$

$$- \frac{1}{\rho_0} (p^s H_{,y} + \Delta\rho gHh_{,y}) - g \cdot h_{,y} {}^1\Delta q_y - \{-F_{xy} \Delta q_{y,x}$$

$$+ (F_p - F_{yy}) \Delta q_{y,y} \}] \, dA - \int_{S_q} \{\alpha_{nx} F_{xy} + \alpha_{ny} (F_{yy} - F_p)\} \Delta q_y \, ds$$

$$+ \int_{S_F} \alpha_{ny} F_p^* \Delta q_y \, ds + \int_{S_q} \{\alpha_{ny} q_n + \alpha_{nx} q_s - q_y^*\} \Delta q_y \, ds = 0$$

Variables with superscript $*$ are prescribed. The surface wind pressure fields and the bottom elevation are assumed known. The trial functions H, q_x, q_y and the test functions Δq_x, Δq_y must all be of class W_2^1, i.e. they must be continuous in $\Omega + \bar{\Omega}$ and only ΔH can belong to L_2. We could have chosen to integrate the terms $p^s H_{,x} \Delta q_x$ and $p^s H_{,y} \Delta q_y$ by parts also, thereby relaxing the requirements to H from W_2^1 to L_2. We decide not to because we would have to work with surface pressure gradients rather than the pressures themselves. The possibility of choosing H and ΔH from L_2 is really not any help anyway, since q_x, q_y must come from W_2^1.

Finally we investigate the line integrals over S_q in more detail. Two cases are considered:

<u>Case 1: Eddy Viscosity Terms Included, $\|E_{ij}\| > 0$, both q_n and q_s prescribed.</u>

In this situation the specified discharges are easily transformed into conditions on q_x, q_y and as was seen in the example, this leads to a requirement of the vanishing of the test functions.

Thus for this case, the integrals over S_q can simply be neglected.

Case 2:   Eddy Viscosity Ignored $E_{ij} = 0$, q_n Prescribed

The boundary integrals reduce to

(4.31) $\int_{S_q} - \alpha_{nx} F_p \Delta q_x \, ds + \int_{S_q} \alpha_{nx}(q_n - q_n^*)\Delta q_x \, ds = 0$

(4.32) $\int_{S_q} - \alpha_{ny} F_p \Delta q_y \, ds + \int_{S_q} \alpha_{ny} (q_n - q_n^*) \Delta q_y \, ds = 0$

Adding (4.31) to (4.32) yields:

(4.33) $\int_{S_q} \{- F_p + (q_n - q_n^*)\}\{\alpha_{nx}\Delta q_x + \alpha_{ny} \Delta q_y\} \, ds$

$= \int_{S_q} \{- F_p + (q_n - q_n^*)\} \{\Delta q_n\} \, ds = 0$

(4.34) $\Delta q_n = \alpha_{nx} \Delta q_x + \alpha_{ny} \Delta q_y$

Since prescribing q_n means that Δq_n must be an admissible variation that is $\Delta q_n \equiv 0$ on S_q, the equation is automatically satisfied. Again the contributions from S_q can apparently be neglected. The reservation expressed by the word apparently is intentional because in actual applications the situation can be quite different, and this is largely due to the fact that we are dealing with a vector (velocity) rather than a scalar quantity. Since the actual treatment is dependent on the discretization, we delay further discussions until the finite element method is described.

CHAPTER 5

FINITE ELEMENT METHOD

Briefly stated, the finite element method FEM, provides a systematic way of generating approximate solutions to a given problem. Its great impact on the field of numerical methods is greatly due to the partitioning of the domain and the use of simple polynomial expansions in each subdomain. Thus, in two spatial dimensions, the total area is divided into subregions and in each of these a function is approximated by a simple polynomial in the coordinates x, y, called a trial function. For a more general discussion, the following references are useful [10, 11, 80, 68]. In the latter it is shown that provided the functional requirements to the trial functions are satisfied, convergence of the solution is assured as the subregions are made infinitesimal. The advantages of this method are that any (reasonable) function can be approximated, each subregion called an element has its own polynomial expansion independent of all other elements, and therefore the treatment of the entire domain is systematically handled by summing the contributions from each element.

In Chapters 3-4, the type of element used did not have to be considered, which - as mentioned earlier - is one of the great advantages of this method since the properties derived from the weak form are general. To proceed, we must now make some assumptions about the type of elements to be used. According to the weak form (4.18), (4.29) and (4.30), both test and trial functions must be continuous and belong to W_2^1. The linear triangular element is the simplest satisfying

this criterion. As our primary objective is to obtain a solution to our problem rather than trying to optimize the solution method per se, we choose to work with this simplest alternative and not consider higher order elements. The main incentive for using higher order elements lies in the improved accuracy for the same number of unknowns, which is an area perhaps worth investigating further.

The strategy is to develop the functional relationship for a typical element and then sum up the contributions from all elements to obtain the system equations. Following Connor [11], this element is based on a linear expansion for the variables.

$$(5.1) \qquad q_x = \xi_1 Q_{x1}^e + \xi_2 Q_{x2}^e + \xi_3 Q_{x3}^e = \phi Q_x^e$$

$$(5.2) \qquad q_y = \xi_1 Q_{y1}^e + \xi_2 Q_{y2}^e + \xi_3 Q_{y3}^e = \phi Q_y^e$$

$$(5.3) \qquad H = \xi_1 H_1^e + \xi_2 H_2^e + \xi_3 H_3^e = \phi H^e$$

where the superscript e designates element nodal values of the variables which are fixed in space; the tilde denotes a matrix; ξ_1, ξ_2, ξ_3 are normalized element coordinates (Figure 5-1), and

$$(5.4) \qquad \phi = [\xi_1 \ \xi_2 \ \xi_3]$$

The square bracket is used to denote a row vector or matrix. The transformation from x,y to ξ_1, ξ_2 is easily shown to be

$$(5.5) \qquad \xi_i = \frac{1}{2A} (2A_i + b_i x + a_i y)$$

89

where

(5.6) $\qquad a_i = x_k - x_j$

(5.7) $\qquad b_i = y_j - y_k$

(5.8) $\qquad 2A_i = x_j y_k - x_k y_j$

(5.9) $\qquad A = \frac{1}{2} (b_1 a_2 - b_{2a_1})$

(i,j,k) is an even permutation of $(1,2,3)$ and refers to the element nodes numbered counterclockwise.

Derivatives are conveniently found by chain differentiation, e.g.

(5.10) $\qquad \dfrac{\partial}{\partial x} q_x = \dfrac{\partial}{\partial \xi_i} q_x \cdot \dfrac{\partial \xi_i}{\partial x} = \sum_{i=1}^{3} \dfrac{b_i}{2A} Q^e_{x_i}$.

Similarly, integrals are found in the transformed $\xi_1 - \xi_2$ space, e.g.:

(5.11) $\qquad \displaystyle\int_A q_y \, dA = 2A \int_0^1 \int_0^{1-\xi_1} q_y \, d\xi_2 \, d\xi_1$

$\qquad\qquad = \dfrac{A}{3} (Q^e_{y_1} + Q^e_{y_2} + Q^e_{y_3})$

The general integration formula is

(5.12) $\qquad \displaystyle\int_A \xi_1^i \xi_2^j \xi_3^k \, dA = \dfrac{i! \, j! \, k!}{(i + j + k + 2)!} \cdot 2A$

These relationships for the linear triangular element actually only serve as an illustration, because we can proceed without making an explicit assumption of the type of element used, as long as the shape functions satisfy the functional requirements of the problem. This is another major advantage of the FEM, and the reason that it lends itself so well to higher order (more accurate) approximations.
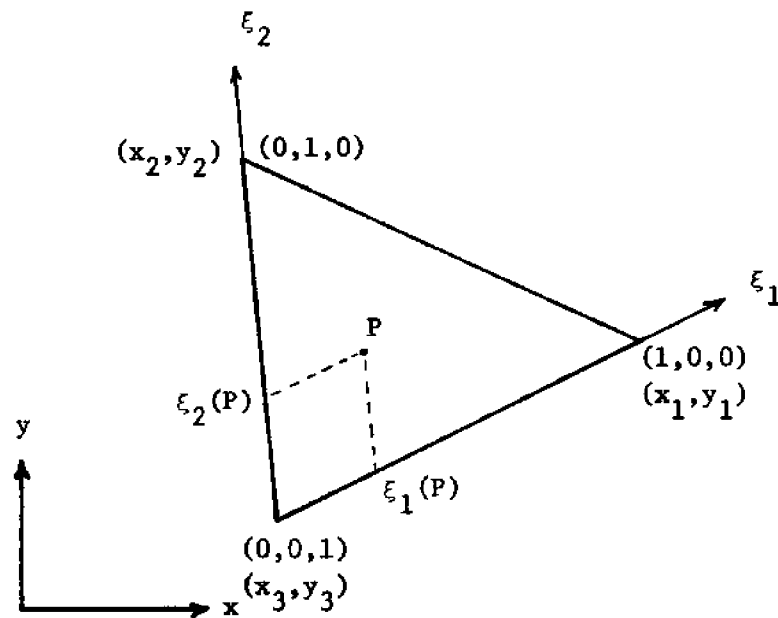
Figure 5-1. Normalized element coordinates,

Consider any arbitrary element for which it may be assumed that a variable is expressed in terms of shape functions ϕ and nodal variables $\underset{\sim}{U}$.

$$(5.13) \qquad u = \phi \, \underset{\sim}{U}^e = \underset{\sim}{\phi}(x,y) \cdot \underset{\sim}{U}^e(t)$$

where $\underset{\sim}{\phi}$ is a row vector relating element geometry similar to (5.4), and $\underset{\sim}{U}^e$ is a column vector of the element nodal values of u.

The finite element analogue of the weak equation (4.18) for one element is found by substituting the equivalents of (5.13) for each of the variables, resulting in (superscript T means transpose):

$$(5.14) \qquad (\Delta H^e)^T \int_A \underset{\sim}{\phi}^T \left(\underset{\sim}{\phi} H^e_{,t} + \underset{\sim}{\phi}_{,x} \underset{\sim}{Q}^e_x + \underset{\sim}{\phi}_{,y} \underset{\sim}{Q}^e_y - \underset{\sim}{\phi} \underset{\sim}{Q}^e_I \right) dA = 0$$

To obtain the integral over the entire domain Ω we simply sum the contributions from each element. However, rather than using (5.14), we choose to work with a slightly different form which is derived from (4.18) multiplied by g.h. This causes no loss of generality since h is a known positive smooth function; but it makes the FE equations particularly attractive as we show shortly.

Multiplying (4.18) by gh yields

$$(5.15) \qquad \int_\Omega \{ gh\ H_{,t} + gh\ q_{x,x} + gh\ q_{y,y} - gh\ q_I \}\ \Delta H\ dA = 0$$

It is obvious that (5.15) is obtained from (4.18) by a redefinition of ΔH:

$$(5.16) \qquad \Delta H = gh\ \Delta H$$

Applying the finite element method to (5.15) gives (again for one element):

$$(5.17) \qquad (\Delta H^e)^T \int_A \underset{\sim}{\phi}^T \left\{ g(\underset{\sim}{\phi}h)\ \underset{\sim}{\phi} H^e_{,t} + g\ (\underset{\sim}{\phi}h)\ \underset{\sim}{\phi}_{,x} \underset{\sim}{Q}^e_x + g(\underset{\sim}{\phi}h)\ \underset{\sim}{\phi}_{,y} \underset{\sim}{Q}^e_y \right.$$

$$\left. - g(\underset{\sim}{\phi}h)\ \underset{\sim}{\phi} \underset{\sim}{Q}^e_I \right\} dA = 0$$

where $\underset{\sim}{h}$ are the nodal values of the depth h.

To obtain the integral over the entire domain Ω we simply sum the contributions from each element:

$$(5.18) \quad \int_\Omega \{gh \cdot H_{,t} + gh\, q_{x,x} + gh\, q_{y,y} - ghq_I\}\, \Delta H\, dA$$

$$= \sum_{i=1}^{NMEL} (\Delta H^{ei})^T \int_{A_i} \phi^T \{g(\phi h)\, \phi H^e_{,t} + g(\phi h)\, \phi_{,x}\, Q^e_x$$

$$+ g(\phi h)\, \phi_{,y}\, Q^e_y - g(\phi h)\, \phi Q^e_I\}\, dA = 0$$

NMEL is the total number of elements. Only ϕ is a function of space (x,y) and the relationship is known for a given element type. The integrals are hence easily evaluated once the grid layout is determined. We introduce some symbols to simplify the writing:

$$(5.19) \quad M^i_h = \int_{A_i} g\phi^T \phi h\, \phi\, dA$$

$$= \frac{gA_i}{60} \begin{bmatrix} 6h_1+ 2h_2+ 2h_3 & 2h_1+ 2h_2+ h_3 & 2h_1+ h_2+ 2h_3 \\ 2h_1+ 2h_2+ h_3 & 2h_1+ 6h_2+ 2h_3 & h_1 + 2h_2+ 2h_3 \\ 2h_1+ h_2+ 2h_3 & h_1 + 2h_2+ 2h_3 & 2h_1+ 2h_2+ 6h_3 \end{bmatrix}$$

$$(5.20) \quad M^i = \int_{A_i} \phi^T \phi\, dA = \frac{A_i}{12} \begin{bmatrix} 2 & 1 & 1 \\ 1 & 2 & 1 \\ 1 & 1 & 2 \end{bmatrix}$$

$$(5.21) \quad G^i_x = \int_{A_i} g\, \phi^T (\phi\, h)\, \phi_{,x}\, dA = \frac{gM^i}{2A_i} \begin{bmatrix} h_1 a_1 & h_1 a_2 & h_1 a_3 \\ h_2 a_1 & h_2 a_2 & h_2 a_3 \\ h_3 a_1 & h_3 a_2 & h_3 a_3 \end{bmatrix}$$

93

$$(5.22) \qquad G_y^i = \int_{A_i} g\, \phi^T (\phi h)\, \phi_{,y}\, dA = \frac{g M^i}{2 A_i} \begin{bmatrix} h_1 b_1 & h_1 b_2 & h_1 b_3 \\ h_2 b_1 & h_2 b_2 & h_2 b_3 \\ h_3 b_1 & h_3 b_2 & h_3 b_3 \end{bmatrix}$$

For illustration, the results for the linear triangle are also shown. Due to the simple integration and differentiation rules for this element, (5.12) and (5.10), the integrals are easily evaluated analytically. For more complicated elements and trial functions, numerical integration is more attractive. We emphasize, though, that both M_h^i and M^i per definition are symmetric.

Equation (5.18) is now written.

$$(5.23) \qquad \sum_{i=1}^{NMEL} (\Delta H^{e_i})^T \{ M_h^i H_{,t}^{e_i} + G_x^i Q_x^{e_i} + G_y^i Q_y^{e_i} - M_h^i Q_I^{e_i} \}\, dA = 0$$

Formally carrying out the summation we obtain the system equation

$$(5.24) \qquad (\Delta H)^T \{ M_h H_{,t} + G_x Q_x + G_y Q_y - M_h Q_I \} = 0$$

Since the elements of ΔH determine the test function, which is an arbitrary function, the terms within the braces must vanish. This results in NMNP equations, where NMNP is the number of node points:

$$(5.25) \qquad M_h H_{,t} + G_x Q_x + G_y Q_y - M_h Q_I = 0$$

Next we prove an important property of M_h. For the sake of argument, let

$$(5.26) \qquad \Delta H = H$$

i.e. we choose the test function identical to the trial function.
Then the first term in (5.25) is:

$$(5.27) \quad \underset{\sim}{H}^T \underset{\sim h}{M} \underset{\sim}{H}_{,t} = \frac{1}{2} (\underset{\sim}{H}_{,t}^T \underset{\sim h}{M} \underset{\sim}{H} + \underset{\sim}{H}^T \underset{\sim h}{M} \underset{\sim}{H}_{,t}) = \frac{1}{2} \frac{\partial}{\partial t} (\underset{\sim}{H}^T \underset{\sim h}{M} \underset{\sim}{H})$$

$$= \frac{1}{2} \frac{\partial}{\partial t} \int_\Omega h \cdot H^2 \, dA$$

Thus we have

$$(5.28) \quad \underset{\sim}{H}^T \underset{\sim h}{M} \underset{\sim}{H} = \int_\Omega h \, H^2 \, dA \geq 0$$

For finite depth, $h > 0$ everywhere in Ω, the equality can only hold if $H \in \{ H \mid \int_\Omega H^2 \, dA = 0 \}$ which would imply that $\underset{\sim}{H}$ is a zero matrix. It follows that $\underset{\sim h}{M}$ is symmetric positive real and therefore also non-singular, i.e. the determinant of $\underset{\sim h}{M}$ is non-zero.

Other variables expressable according to (5.13) are the surface elevation η, surface pressure p^s, density difference $\Delta\rho$, surface stress τ^s and momentum source $\bar{m}$. Bottom friction coefficient C_f and eddy viscosities E_{ij} are assumed as element properties since this gives the more precise description

In Figure 5-2, a and b, this is demonstrated by showing the domain of influence for a prescribed nodal or elemental value respectively. The assemblage of the equivalent system equations for the equilibrium equations (4.29) and (4.30) is completely similar. The intermediate steps are therefore left to appendix A and the result is directly quoted here:

$$(5.29) \quad \underset{\sim}{M} \underset{\sim}{Q}_{x,t} - \underset{\sim x}{G}^T \underset{\sim}{\eta} + \underset{\sim xx}{E} \underset{\sim x}{Q} + \underset{\sim yx}{E} \underset{\sim y}{Q} - f \underset{\sim}{M} \underset{\sim}{Q}_y = \underset{\sim x}{P}$$

(5.30)
$$M \underset{\sim}{Q}_{y,t} - G_{\sim y}^T \underset{\sim}{\eta} + E_{xy} \underset{\sim}{Q}_x + E_{yy} \underset{\sim}{Q}_y + f \underset{\sim}{M} \underset{\sim}{Q}_x = \underset{\sim}{P}_y$$

where $\underset{\sim}{E}_{xx}$, $\underset{\sim}{E}_{xy} = E_{\sim yx}^T$, and $\underset{\sim}{E}_{yy}$, are assembled from

(5.31)
$$\underset{\sim}{E}_{ij}^k = \int_{A_k} \{ E_{\sim ij}^k \phi_{,i}^T \phi_{,j} + \delta_{i1} \delta_{j1} E_{21}^k \phi_{,2}^T \phi_{,2}$$

$$+ \delta_{i2} \delta_{j2} E_{12}^k \phi_{,1}^T \phi_{,1} \} \, dA$$

where δ_{ij} is the Kronecker δ, and $\underset{\sim}{M}$ is assembled from (5.20).
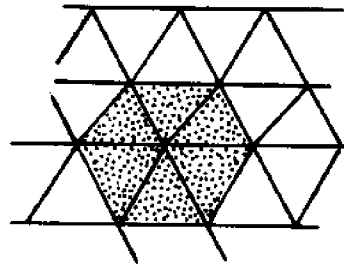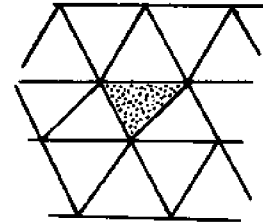
a Prescribed nodal value   b Prescribed element value

Figure 5-2. Domains of influence.

The terms in (5.29) and (5.30) represent the contributions of iner-
tial acceleration, linear part of specific pressure force measure,
eddy viscosity (2 terms) and coriolis acceleration. The remaining
terms are lumped in $\underset{\sim}{P}_x$ and $\underset{\sim}{P}_y$. Since prescribed discharge condi-
tions (see (3.44) and (4.33)) imply a coupling of q_x and q_y, we
find it more convenient to define a new nodal variable

96

(5.32)
$$\underset{\sim}{Q} = [\underbrace{Q_x \ Q_y}_{\text{node 1}} \ \underbrace{Q_x \ Q_y}_{\text{node 2}} \ \cdot \ \cdot \ \cdot \ \cdot \ \cdot \ \underbrace{Q_x \ Q_y}_{\text{node NMNP}} \ ]$$

Equations (5.25), (5.29) and (5.30) are then simply written

(5.33)
$$\underset{\sim}{M}_1 \ \underset{\sim}{H}_{,t} + \underset{\sim}{G}_1 \ \underset{\sim}{Q} = \underset{\sim}{P}_H$$

(5.34)
$$\underset{\sim}{M}_2 \ \underset{\sim}{Q}_t - \underset{\sim}{G}_1^T \underset{\sim}{\eta} + \underset{\sim}{E} \ \underset{\sim}{Q} + \underset{\sim}{C} \ \underset{\sim}{Q} = \underset{\sim}{P}_Q$$

where we define

(5.35)
$$\underset{\sim}{P}_H \equiv \underset{\sim}{M}_h \ \underset{\sim}{Q}_I$$

(5.36)
$$\underset{\sim}{M}_1 \equiv \underset{\sim}{M}_h$$

$\underset{\sim}{M}_2$, $\underset{\sim}{G}_1$, $\underset{\sim}{E}$, $\underset{\sim}{C}$ and $\underset{\sim}{P}_Q$ are simply the results of merging the element matrices according to (5.32). The structure of the finite element equations for the circulation problem is fully displayed by noting

(5.37)
$$\underset{\sim}{\eta}_{,t} \equiv \underset{\sim}{H}_{,t}$$

Substituting (5.37) into (5.33) finally yields

(5.38)
$$\underset{\sim}{M}_1 \ \underset{\sim}{\eta}_{,t} + \underset{\sim}{G} \ \underset{\sim}{Q} = \underset{\sim}{P}_H$$

It is now apparent why we chose to use (5.15) rather than (4.18). We have achieved complete symmetry or skew-symmetry in the total system coefficient matrices. This is most clearly demonstrated by showing the partitioned form of (5.34) and (5.30).

97

$$(5.39) \quad \begin{matrix} \text{NMNP} \\ 2\text{x NMNP} \end{matrix} \left\{ \underbrace{\left[\begin{array}{c|c} \underset{\sim}{M}_1 & \underset{\sim}{0} \\ \hline \underset{\sim}{0} & \underset{\sim}{M}_2 \end{array} \right]}_{\text{NMNP} \quad 2\text{x NMNP}} \left[\begin{array}{c} \dot{\underset{\sim}{n}} \\ \hline \dot{\underset{\sim}{Q}} \end{array} \right] + \underbrace{\left[\begin{array}{c|c} \underset{\sim}{0} & G \\ \hline G^T & E + \underset{\sim}{C} \end{array} \right]}_{\text{NMNP} \quad 2\text{x NMNP}} \left[\begin{array}{c} \underset{\sim}{n} \\ \hline \underset{\sim}{Q} \end{array} \right] \right\} = \left[\begin{array}{c} \underset{\sim}{P}_H \\ \hline \underset{\sim}{P}_Q \end{array} \right]$$

Recalling that both $\underset{\sim}{M}_1$ and $\underset{\sim}{M}_2$ are symmetric positive real, it is easily shown that the first coefficient matrix in (5.39) is also symmetric positive and non-singular. This in fact is, at least heuristically, sufficient and necessary proof that a solution to the finite element equations exist and is unique. The proof follows immediately from the theorems of linear algebra concerning systems of inhomogeneous equations with a non-zero Cramer determinant, see for example [48].

The second coefficient matrix in (5.39) is a sum of a purely symmetric non-negative (positive semi-definite real) matrix $\underset{\sim}{E}$ and two totally skew-symmetric matrices $(G -- G^T \text{ and } \underset{\sim}{C})$:

$$(5.40) \quad \left[\begin{array}{c|c} \underset{\sim}{0} & \underset{\sim}{G} \\ \hline -G^T & E + \underset{\sim}{C} \end{array} \right] = \left[\begin{array}{c|c} \underset{\sim}{0} & \underset{\sim}{0} \\ \hline \underset{\sim}{0} & E \end{array} \right] + \left[\begin{array}{c|c} \underset{\sim}{0} & G \\ \hline -G^T & \underset{\sim}{0} \end{array} \right] + \left[\begin{array}{c|c} \underset{\sim}{0} & \underset{\sim}{0} \\ \hline \underset{\sim}{0} & \underset{\sim}{C} \end{array} \right]$$

$\underset{\sim}{P}_H$ and $\underset{\sim}{P}_Q$ are arbitrary vectors containing the load and non-linear contributions. It is emphasized that the structure of the equations (5.34) and (5.38) or (5.39) is independent of choice of element type or grid configuration.

By applying the FEM we have transformed the integral equations to a system of non-linear ordinary differential equations in time. Before solution methods for such systems are discussed in the

next chapter we look at how boundary conditions are treated and the errors associated with the FEM.

First the problem of defining the normal at region boundaries has to be resolved. Figure 5-3 shows a physical boundary segment and the hypothetical finite element boundary. With straight element sides, "breaks" necessarily occur in the model boundary when a curved coastline is approximated,and a nodal normal direction cannot be defined to agree with both normals of adjoining segments. Consequently, when the tangential discharge is left free it gives rise to flow across the adjoining segments as sketched on Figure 5-3. This in itself is not necessarily a bad effect, in fact, it is perhaps a better simulation of the real flow, however, there is a question of whether mass is conserved. Considering this as the key issue we use the criteria of conservation of mass to define the nodal normal. Using the definitionson Figure 5-4 which shows both a convex and a concave break, we find θ_1 by balancing the flow through segment 1 of length L_1 with flow through segment 2 of length L_2. To obtain a general relationship we define a positive direction of traverse of the segments such that the area under consideration is to the left and the normal to the right. For a contour enclosing the domain this will be a counterclockwise sense. The interior angle is denoted θ and the angle from n to L is θ_1. Simple geometry then yields

$$(5.41) \quad \frac{1}{2} q_s \cdot L_1 \cdot \sin(\pi/2 - \theta_1) = \frac{1}{2} q_s L_2 \sin(\pi/2 - \theta + \theta_1)$$

which is equivalent to
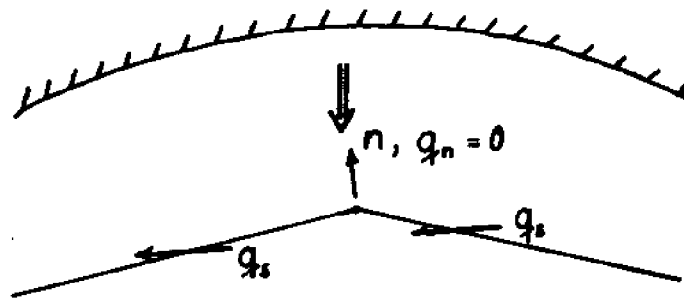
Figure 5-3. Curved boundary with FE approximation.
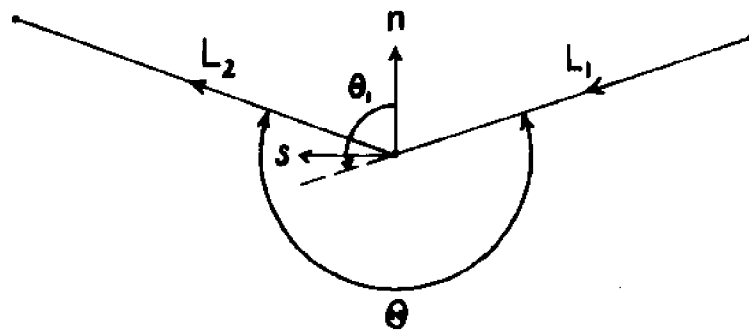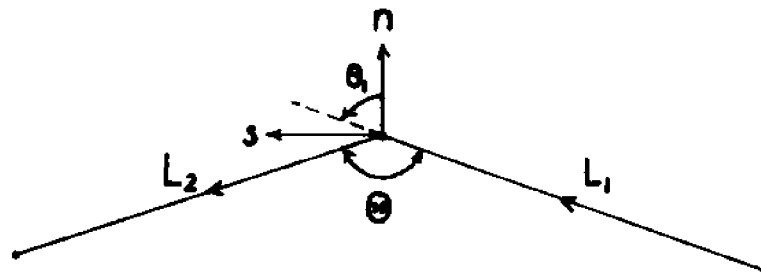
Figure 5-4. Definition sketches for boundary normals. Convex and concave corners.

(5.42) $\qquad L_1 \cos \theta_1 = L_2 \cos (\Theta - \theta_1)$

Solving for θ_1, we first expand the right hand side

(5.43) $\qquad L_1 \cos \theta_1 = L_2 \cos \Theta \cos \theta_1 + L_2 \sin \Theta \sin \theta_1$

and then rearrange to obtain the final answer

(5.44) $\qquad \cot \theta_1 = \dfrac{L_2 \sin \Theta}{L_1 - L_2 \cos \Theta} \qquad 0 < \theta_1 < \pi \; ; \; \dfrac{\pi}{2} < \Theta < 2\pi$

———— ———— o ———— ————

$$\underset{\sim}{M} \; \underset{\sim}{X} = \underset{\sim}{P}$$

$$+$$

$$X_k = X^*$$

$$
\begin{bmatrix}
m_1^1 & \cdots & m_1^{k-1} & 0 & m_1^{k+1} & \cdots & m_1^N \\
\vdots & & \vdots & \vdots & \vdots & & \vdots \\
m_{k-1}^1 & \cdots & m_{k-1}^{k-1} & 0 & m_{k-1}^{k+1} & \cdots & m_{k-1}^N \\
0 & \cdots & 0 & 1 & 0 & \cdots & 0 \\
m_{k+1}^1 & \cdots & m_{k+1}^{k-1} & 0 & m_{k+1}^{k+1} & \cdots & m_{k+1}^N \\
\vdots & & \vdots & \vdots & \vdots & & \vdots \\
m_N^1 & \cdots & m_N^{k-1} & 0 & m_N^{k+1} & \cdots & m_N^N
\end{bmatrix}
\begin{bmatrix}
X_1 \\ \vdots \\ X_{k-1} \\ X_k \\ X_{k+1} \\ \vdots \\ X_N
\end{bmatrix}
=
\begin{bmatrix}
P_1 \\ \vdots \\ P_{k-1} \\ 0 \\ P_{k+1} \\ \vdots \\ P_N
\end{bmatrix}
-
\begin{bmatrix}
0 & \cdots & 0 & m_1^k & 0 & \cdots & 0 \\
\vdots & & \vdots & \vdots & \vdots & & \vdots \\
0 & \cdots & 0 & m_{k-1}^k & 0 & \cdots & 0 \\
0 & \cdots & 0 & 1 & 0 & \cdots & 0 \\
0 & \cdots & 0 & m_{k+1}^k & 0 & \cdots & 0 \\
\vdots & & \vdots & \vdots & \vdots & & \vdots \\
0 & \cdots & 0 & m_N^k & 0 & \cdots & 0
\end{bmatrix}
\begin{bmatrix}
0 \\ \vdots \\ 0 \\ X^* \\ 0 \\ \vdots \\ 0
\end{bmatrix}
$$

Figure 5-5. Treatment of prescribed variable.

For $\Theta < \dfrac{\pi}{2}$ both discharge components should be prescribed zero since the existence of a tangential flow is physically unreasonable

and also can introduce numerical difficulties.

A prescribed nodal value is simply treated by erasing the corresponding equation in (5.39). Computationally, this is done as sketched in Figure 5.5. If the k'th variable is prescribed, the k'th column in the coefficient matrix M is stored, then the k'th row and column in M are set to zero and the diagonal element set equal to one. Finally,
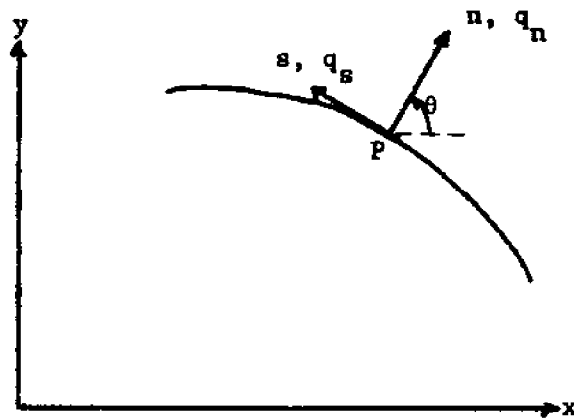
Figure 5-6. Prescribed normal discharge.

the stored column matrix is multiplied by the prescribed value x^* and subtracted from the right hand side. This procedure effectively replaces the k'th equation by the prescribed constraint and keeps the symmetry of M.

Finally, we show how a discharge in any arbitrary direction can be prescribed. If we for example want to specify the normal discharge q_n in a point P (Figure 5.6), where the normal (given by (5.44)) has an angle θ with the x-axis, then this is best achieved by transforming the discharges in P from the global x,y coordinate system to

a local n,s coordinate system. Simple geometry again gives

(5.45) $n = x \cos \theta + y \sin \theta$

             $s = x \sin \theta + y \cos \theta$

or

(5.46)
$$\begin{bmatrix} n \\ s \end{bmatrix} = \begin{bmatrix} \cos \theta & \sin \theta \\ -\sin \theta & \cos \theta \end{bmatrix} \begin{bmatrix} x \\ y \end{bmatrix}$$

$$= \underset{\sim}{T} \cdot \begin{bmatrix} x \\ y \end{bmatrix}$$

Since $\underset{\sim}{T}$ is an orthonormal matrix $T^T = T^{-1}$, the transpose is equal
to the inverse of $\underset{\sim}{T}$. Hence we have

(5.47)
$$\begin{bmatrix} Q_x \\ Q_y \end{bmatrix} = \underset{\sim}{T}^T \begin{bmatrix} Q_n \\ Q_s \end{bmatrix}$$

To demonstrate the procedure we simplify (5.34) to

(5.48) $\underset{\sim}{M}_2 \, \underset{\sim}{Q}_{,t} = \underset{\sim}{P}_Q$

and substitute (5.47) in (5.48), yielding

(5.49) $\underset{\sim}{M}_2 \, \underset{\sim}{T}_S^T \, \underset{\sim}{Q}_{1,t} = \underset{\sim}{P}_Q$

The system transformation matrix $\underset{\sim}{T}_S$ has the form

$$(5.50) \quad \underset{\sim}{T}_S = \begin{vmatrix} 1 & 0 & \cdot & \cdot & \cdot & \cdot & \cdot & \cdot & \cdot & \cdot & 0 \\ 0 & & & & & & & & & & \cdot \\ \cdot & & & & & & & & & & \cdot \\ \cdot & & & 1 & & & & & & & \cdot \\ \cdot & & & & \underset{\sim}{T} & & & & & & \cdot \\ \cdot & & & & & 1 & & & & & \cdot \\ \cdot & & & & & & & & & & \cdot \\ \cdot & & & & & & & & & & \cdot \\ \cdot & & & & & & & & & & 0 \\ 0 & \cdot & \cdot & \cdot & \cdot & \cdot & \cdot & \cdot & 0 & & 1 \end{vmatrix}$$

and $\underset{\sim}{Q}_1$ is the local discharge vector.

$$(5.51) \quad \underset{\sim}{Q}_1 = [\underbrace{Q_x \ Q_y}_{\text{node 1}} \cdots Q_x \ Q_y \cdots \underbrace{Q_n \ Q_s}_{\text{node k}} \cdots Q_x \ Q_y \cdots Q_x \ Q_y]$$

$$\text{node 1} \qquad \qquad \text{node k} \qquad \qquad \text{node NMNP}$$

The coefficient matrix is now $\underset{\sim}{M}_2 \ \underset{\sim}{T}_S^T$ which is unsymmetrical. Since it is desirable from a computational point of view to have a symmetric coefficient matrix, (5.49) is premultiplied by $\underset{\sim}{T}_S$

$$(5.52) \quad \underset{\sim}{T}_S \ \underset{\sim}{M}_2 \ \underset{\sim}{T}_S^T \ Q_{1,t} = \underset{\sim}{T}_S \ \underset{\sim}{P}_Q$$

which brings the structure of the system back to what we started with, viz. (5.48). The prescribed value of Q_n can now be handled exactly the same way as earlier discussed for a prescribed boundary value. Fortunately the transformation of $\underset{\sim}{M}_2$

$$(5.53) \quad \underset{\sim}{M}_2 \ \longrightarrow \ \underset{\sim}{T}_S \ \underset{\sim}{M}_2 \ \underset{\sim}{T}_S^T$$

only have to be done once for a problem.

Turning the attention towards an analysis of errors, we recall that convergence of the FE solution to the true solution of (4.18), (4.29) and (4.30) was shown by Mihklin [46]. The positive definiteness of the system coefficient matrix assures the existence and uniqueness of a solution. Our final concern is directed towards the accuracy of the approximate solution for a given discretization. As for the above properties, the theory only covers linear problems, a more complete treatment is left for the future.

If the order of the original differential equations is 2 m (or 2 m-1) in spatial derivatives, then convergence occurs if and only if the elements reproduce exactly any solution which is a polynomial of degree m; this is called the constant strain condition [68]. The measure of distance between the exact solution u of the weak form and the optimal trial function $u^{\Delta s}$ is

$$(5.54) \qquad a(u - u^{\Delta s}, u - u^{\Delta s}) \leq C^2 \, \Delta s^{2(k-m)} \, |u|^2_k$$

$$\simeq C^2 \, \Delta s^{2(k-m)} \, |f|^2$$

where $a(u-u^{\Delta s}, u-u^{\Delta s})$ now is the energy inner product; C is a constant depending on the construction of the element; Δs is a typical dimension of the element e.g. the largest height; k-1 is the order of the highest polynomial exactly representable by the element; and f_ρ is the data, i.e. prescribed forces. In order that any polynomial of degree k-1 can be described, the basis must be uniform as $\Delta s \rightarrow 0$. This is effectively a geometrical restriction which forbids arbitrarily small angles in triangular elements. A basis is a set of trial functions from

which any function in the solution space can be formed by linear combination.

Reiterating our problem with linear triangular elements, $k = 2$ and $m = 1$, thus the error measure is

$$(5.55) \qquad a(u - u^{\Delta s}, u - u^{\Delta s}) \leq C^2 \Delta s^2 |f_{\phi}|^2$$

and we see that the rate of convergence is proportional to Δs^2. The relation (5.54) holds for smooth f; but any data whose inner product with the test function is finite is admissible.

In the case where f_{ϕ} contains a δ-function, the error can be shown to be order of Δs and if a node is placed right at the discontinuity of f_{ϕ}, the error cannot be determined in general, however, convergence is still easy to prove [68]. We shall in an application with a point source see how these theories very nicely predict the solution behavior.

CHAPTER 6

TIME INTEGRATION

By using the finite element method, the original continuous problem is reduced to a system of ordinary differential equations in time. To complete the model, an effective technique must be developed to advance the solution in time from a given initial condition. The choice of scheme depends on required features of accuracy, stability, programmability and computational efficiency. These items have been studied fairly thoroughly for systems of equations derived by finite difference methods [60, 61], however, such studies have only recently been initiated for finite element equations [50].

For the set of first order ordinary differential equations resulting from our flow problem there is no real advantage of using the finite element over finite difference methods for time integration, especially since there are no complex topography or boundaries to fit. We therefore seek a scheme from the realm of time stepping or Runge-Kutta type methods.

Many sophisticated methods have been developed. However, we can quickly convince ourselves that not all these can be used. Our experience shows that to simulate the circulation properly in a coastal area like Massachusetts Bay,about 300 nodes are necessary when using the linear triangular element. Incidentally, the number of elements NMEL is approximately 1.5 times the number of nodes, NMNP. NMNP of course depends on the desired accuracy of the results and the magnitude of gradients in the area. Since there are three unknown variables in each node, H, q_x and q_y there is a total of 3 x NMNP $\sim$ 900 equations

107

and unknowns. To compute the circulation for a storm situation, a period of about 5 days must be accounted for. With a semidiurnal tide imposed we must compute the unknowns every half hour or preferably 20 times per tidal period to obtain real time accuracy. Therefore we must solve the system of equations at least 20·2·5 = 200 times. Often this number is increased by an order of magnitude when the stability requirements of the integration scheme limits the time step. Realistically, we must reckon on solving 900 equations up to 2000 times. Even using computers, only the simplest and fastest techniques can come into consideration.

The simplest scheme is the so-called Euler method. For lucidity we shall first demonstrate how each of the following methods that we shall discuss is applied to a single variable and equation of the form

$$(6.1) \qquad \frac{dy}{dt} + y = f_\phi(y,t)$$

These examples are also found in most books on numerical integration [47, 58, 60, 61]. We shall assume a given initial condition hence the problem is to propagate the solution from time $t_n = n \cdot \Delta t$ to $t_{n+1} = (n+1) \Delta t$, although this symbolism implicitly assumes the time step Δt is constant, it will appear as we proceed how variable Δt can be incorporated. Define

$$(6.2) \qquad y_n = y \quad \text{at} \quad t = t_n$$

and

$$(6.3) \qquad \dot{y}_n = \left(\frac{dy}{dt} \right)_{t=t_n}$$

then the Euler form of (1) is

$$(6.4) \qquad \frac{y_{n+1} - y_n}{\Delta t} + y_n = f(y_n, t_n)$$

This scheme is sometimes described as a replacement of the derivative by a forward difference. The discretization or truncation error TE committed in (6.4) is found by expanding y_{n+1} in a Taylor series, around y_n yielding a leading error:

$$(6.5) \qquad TE = \left| \dot{y}_n - \frac{y_{n+1} - y_n}{\Delta t} \right|$$

$$= \left| \dot{y}_n - \frac{1}{\Delta t} \left(y_n + \Delta t \, \dot{y}_n + \frac{1}{2!} \Delta t^2 \, \ddot{y}_n + 0(\Delta t^3) - y_n \right) \right|$$

$$= \frac{1}{2} \Delta t \left| \ddot{y}_n \right|$$

$$= 0 \, (\Delta t)$$

Because TE = 0 (Δt), this method is called a first order method.

Besides accuracy, we are interested in knowing the stability of a scheme. A stable scheme will not amplify a small introduced error as the integration progresses. To investigate this property for an arbitrary problem and scheme is mathematically untractable. So far we have only learned to deal in a systematic way with linear homogeneous initial value problems, i.e. disregarding boundary conditions.

To investigate the stability of the Euler method we use the method of von Neumann [60] and assume

(6.6) $y_{n+1} = \lambda y_n$

where both λ and y_n are complex quantities indicating a modulation
of amplitude and phase of the solution. Substituting (6.6) into (6.4)
neglecting the inhomogeneous term yields

(6.7) $\lambda y_n - y_n + \Delta t\, y_n = 0$

or solving for λ

(6.8) $\lambda = 1 - \Delta t$

The von Neumann necessary condition for stability when the true solu-
tion does not contain an exponentially growing function is

(6.9) $|\lambda| \leq 1$

In the example we would thus have to restrict the time increment to
the interval

(6.10) $0 < \Delta t \leq 2$

Due to the condition (6.10), the Euler method is called a conditionally
stable scheme.

Returning now to the circulation problem we introduce the de-
finition

(6.11) $\underset{\sim}{X} = \begin{bmatrix} \underset{\sim}{\eta} \\ \hline \underset{\sim}{Q} \end{bmatrix}$

which simplifies (5.34) and (5.30) to

$$(6.12) \qquad \underset{\sim}{M}_3 \underset{\sim}{\overset{\cdot\cdot}{X}} + \underset{\sim}{G}_3 \underset{\sim}{X} + \underset{\sim}{E}_3 \underset{\sim}{X} + \underset{\sim}{C}_3 \underset{\sim}{X} = \underset{\sim}{P}_3$$

The subscript 3 just indicates that the equations for each of the three variables have been assembled into one system, where

$$(6.13) \qquad \underset{\sim}{M}_3 = \begin{bmatrix} \underset{\sim}{M}_1 & 0 \\ 0 & \underset{\sim}{M}_2 \end{bmatrix}$$

$$(6.14) \qquad \underset{\sim}{G}_3 = \begin{bmatrix} 0 & G \\ G^T & 0 \end{bmatrix}$$

$$(6.15) \qquad \underset{\sim}{E}_3 = \begin{bmatrix} 0 & 0 \\ 0 & E \end{bmatrix}$$

$$(6.16) \qquad \underset{\sim}{C}_3 = \begin{bmatrix} 0 & 0 \\ 0 & C \end{bmatrix}$$

111

and

$$(6.17) \qquad \underset{\sim}{P}_3 = \left[\begin{array}{c} \underset{\sim}{P}_{!!} \\ \hline \underset{\sim}{P}_Q \end{array} \right]$$

Applying the Euler method to (6.12) results in

$$(6.18) \qquad \underset{\sim}{M}_3 \, (\underset{\sim}{X}_{n+1} - \underset{\sim}{X}_n) + \Delta t \, \{ \underset{\sim}{G}_3 + \underset{\sim}{E}_3 + \underset{\sim}{C}_3 \} \, \underset{\sim}{X}_m = \Delta t \, \underset{\sim}{P}_3$$

To investigate linear stability, we assume

$$(6.19) \qquad \underset{\sim}{X}_{n+1} = \lambda \underset{\sim}{X}_n$$

and substitute (6.19) into the homogeneous form of (6.18) leading to

$$(6.20) \qquad \lambda \, \underset{\sim}{M}_3 \, \underset{\sim}{X}_n - \underset{\sim}{M}_3 \, \underset{\sim}{X}_n + \Delta t \, \{ \underset{\sim}{G}_3 + \underset{\sim}{E}_3 + \underset{\sim}{C}_3 \} \, \underset{\sim}{X}_n = 0$$

or

$$(6.21) \qquad \lambda = \frac{\bar{X}_n^T \, [\underset{\sim}{M}_3 - \Delta t \, \{ \underset{\sim}{G}_3 + \underset{\sim}{E}_3 + \underset{\sim}{C}_3 \} \,] \, \underset{\sim}{X}_n}{\bar{X}_n^T \, \underset{\sim}{M}_3 \, \underset{\sim}{X}_n}$$

where $\bar{X}_n^T$ is the complex conjugate and transpose of $\underset{\sim}{X}_n$. Since $\underset{\sim}{M}_3$ is symmetric, positive real we have

$$(6.22) \qquad \bar{X}_n^T \, \underset{\sim}{M}_3 \, \underset{\sim}{X}_n = m_3 > 0 \qquad m_3 \varepsilon \, R^+$$

Similarly, we may write

$$(6.23) \qquad \bar{X}_n^T \, \underset{\sim}{G}_3 \, \underset{\sim}{X}_n = i \, g_3 \quad , \quad i = \sqrt{-1}, \quad g_3 \, \varepsilon \, R$$

112

$$(6.24) \qquad \underset{\sim n}{X}^T \underset{\sim 3}{E}_3 \underset{\sim n}{X} = e_3 \geq 0 \quad , \quad e_3 \in \{R \backslash R^-\}$$

$$(6.25) \qquad \underset{\sim n}{X}^T \underset{\sim 3}{C}_3 \underset{\sim n}{X} = ic_3 \quad , \quad c_3 \in R$$

To obtain these results, we have also used the fact that the inner product $(X, A X)$ is real when A is symmetric, and purely imaginary when A is purely skew-symmetric, i.e.

$$(6.26) \qquad \text{skew-symmetry} <\!\!\!=\!\!\!> \quad a_{ij} = - a_{ji} \quad \forall \ i,j$$

With these definitions, (6.21) is written

$$(6.27) \qquad \lambda = \frac{m_3 - \Delta t e_3 - \Delta t i (g_3 + c_3)}{m_3}$$

In spite of the simplicity of the Euler method, a closer discussion of Equation (6.27) is illustrative . First neglect eddy viscosity and coriolis, i.e. $e_3 = c_3 = 0$. The magnitude of the amplification factor λ is then

$$(6.28) \qquad |\lambda| = |1 - i\Delta t \frac{g_3}{m_3}| > 1$$

making the scheme unconditionally unstable! This result is somewhat surprising because the analogous approach for finite difference approximations of the hyperbolic wave equation, (the Lax-Wendroff method) [47], leads to conditional stability governed by the famous Courant-Friedrichs-Levy condition (2 spatial directions):

$$(6.29) \qquad \Delta t \leq \frac{\Delta s}{\sqrt{2gh}} = \Delta t_{cr}$$

Δs is the grid spacing, assumed equal in x and y; H is the

113

water depth, and Δt_{cr} is a critical time step often used as a reference.

A closer look at the Lax-Wendroff scheme reveals that the conditional stability is achieved by making the spatial differences of second order accuracy. With the first order accurate scheme exactly the same unconditional instability is found. This simple example serves as an illustration of the difference between FD and FE methods. With FD, the possibility of devising combinations of time and space differences to achieve better stability properties is very real. Although similar strategies for FE cannot be excluded, it is much more difficult to perceive. At least at the present stage, the spatial and temporal discretization are uncoupled.

Our experience confirms the instability predicted by Equation (6.28) which may be written

$$(6.30) \qquad |\lambda| = \begin{cases} 0 \ (\Delta t); \Delta t \ \text{"large"} \\ 1 + 0 \ (\Delta t \ ); \Delta t \ \text{"small"} \end{cases}$$

showing that the exponential growth, causing instability, indicated by $|\lambda| = 1 + 0 \ (\Delta t)$ [60] becomes very slow as Δt is made small. Thus we found the scheme (6.18) marginally stable for the problem of a wave propagating into a rectangular prismatic channel, when $\Delta t \leq \frac{1}{20} \Delta t_{cr}$. The unconditional instability of the Euler scheme applied to the finite element equations of the wave problem is a consequence of the special structure of these equations. The FEM as a rule leads to implicit solutions for transient problems, a cost paid for better spatial resolution and one of the main objections one

might have against this method.

If eddy viscosity is included, a stabilizing effect is observed as long as $\Delta t \ e_3 < 2 \ m_3$ and finally the effect of coriolis is unpredictable, but probably negligible because c_3 is proportional to the small coriolis parameter $f \ (\sim 10^{-4} \sec^{-1})$.

On account of its poor stability feature the Euler scheme is discarded. The next technique considered is the trapezoidal rule. Its application to our example (6.1) is first demonstrated:

$$(6.31) \qquad \int_{t_n}^{t_{n+1}} \frac{dy}{dt} \ dt + \int_{t_n}^{t_{n+1}} y \ dt = \int_{t_n}^{t_{n+1}} f_\bullet \ dt$$

Each term is integrated from time t_n to $t_{n+1} = t_n + \Delta t$ by replacing the integrand with its mean value in the interval:

$$(6.32) \qquad (y_{n+1} - y_n) + \Delta t \ \frac{1}{2} \ (y_{n+1} + y_n) = \frac{1}{2}\Delta t \ (f_{n+1} + f_n)$$

or

$$(6.33) \qquad (1 + \frac{1}{2} \Delta t) \ y_{n+1} - (1 - \frac{1}{2} \Delta t) \ y_n = \Delta t \ \frac{1}{2} \ (f_{n+1} + f_n)$$

The truncation error is

$$(6.34) \qquad TE = \left| \ \dot{y}_{n+\frac{1}{2}} - \frac{y_{n+1} - y_n}{\Delta t} + y_{n+\frac{1}{2}} - \frac{1}{2}(y_{n+1} + y_n) \ \right|$$

$$= 0 \ (\Delta t^2)$$

Note that (6.32) is a finite difference approximation to Equation (6.1) at time $t_{n+\frac{1}{2}}$; but we need not use the variables at this time. The scheme is unconditionally stable since the substitution of (6.6) into (6.33) leads to

$$(6.35) \qquad \lambda = \frac{1 - \frac{1}{2} \Delta t}{1 + \frac{1}{2} \Delta t}$$

which shows that $| \lambda | < 1$ for $\Delta t > 0$.

Using the trapezoidal rule on (6.12) yields

$$(6.36) \qquad \underset{\sim}{M}_3 (\underset{\sim}{X}_{n+1} - \underset{\sim}{X}_n) + \frac{1}{2} \Delta t (\underset{\sim}{G}_3 + \underset{\sim}{E}_3 + \underset{\sim}{C}_3)(\underset{\sim}{X}_{n+1} + \underset{\sim}{X}_n) =$$

$$\frac{1}{2} \Delta t (\underset{\sim}{P}_{3_{n+1}} + \underset{\sim}{P}_{3_n})$$

or

$$(6.37) \qquad (\underset{\sim}{M}_3 + \frac{1}{2} \Delta t (\underset{\sim}{G}_3 + \underset{\sim}{E}_3 + \underset{\sim}{C}_3)) \underset{\sim}{X}_{n+1} = (\underset{\sim}{M}_3 - \frac{1}{2} \Delta t (\underset{\sim}{G}_3 + \underset{\sim}{E}_3 + \underset{\sim}{C}_3)) \underset{\sim}{X}_n$$

$$+ \frac{1}{2} \Delta t (\underset{\sim}{P}_{3_{n+1}} + \underset{\sim}{P}_{3_n})$$

The linear stability analysis shows

$$(6.38) \qquad \lambda = \frac{m_3 - \frac{1}{2} \Delta t (ig_3 + e_3 + ic_3)}{m_3 + \frac{1}{2} \Delta t (ig_3 + e_3 + ic_3)}$$

$$= \frac{m_3 - \frac{1}{2} \Delta t \, e_3 - i \frac{1}{2} \Delta t (c_3 + g_3)}{m_3 + \frac{1}{2} \Delta t \, e_3 + i \frac{1}{2} \Delta t (c_3 + g_3)}$$

For $e_3 = c_3 = 0$:

$$(6.39) \qquad |\lambda|^2 = \lambda \cdot \overline{\lambda} = \frac{m_3 - i \frac{1}{2} \Delta t \, g_3}{m_3 + i \frac{1}{2} \Delta t \, g_3} \cdot \frac{m_3 + i \frac{1}{2} \Delta t \, g_3}{m - i \frac{1}{2} \Delta t \, g_3} = 1$$

and thus the scheme is said to be unconditionally stable. Adding any amount of eddy viscosity e_3 acts as damping, making $| \lambda | < 1$. The trapezoidal rule seems ideally suited for our problem, it is linearly

stable, sufficiently accurate,and simple to program. However, in the shown form the coefficient matrix, Equation (6.37), is unsymmetric and has the banded dimension 6 $\cdot$ NBAND x 3 (NMNP-1). NBAND is the size of the band of non-zero elements in $\underset{\sim}{M}$, over and including the diagonal. (Since $\underset{\sim}{M}_1$ is symmetric that is all we need to store for it.) The largeness of the matrix is due to the fact that all variables are solved for simultaneously and require a great deal of storage in the computer. Because of the large bandwidth it is also time consuming to solve. For larger problems NMNP > 100 , these requirements become

$$L_1^j = 0 \text{ for } j > i \qquad\qquad U_1^j = 0 \text{ for } j < i$$

Figure 6-1. Structure of lower and upper triangular matrices.

prohibitive and we therefore also discard this method; but note that it has been used successfully for the same problem by Partridge and Brebbia [56].

The major improvement has to come from a reduction in the number of unknowns solved simultaneously. To achieve this we recall equations (5.34) and (5.38)

$$(6.40) \qquad \underset{\sim}{M}_1 \underset{\sim}{\eta}_{,t} + \underset{\sim}{G} \underset{\sim}{Q} = \underset{\sim}{P}_H$$

$$(6.41) \quad M_2 \, Q_{,t} - G^T \, \eta + E \, Q + C \, Q = P_Q$$

Again using the trapezoidal rule we may formally write

$$(6.42) \quad M_1 \eta_{n+1} = M_1 \eta_n + \frac{\Delta t}{2} (P_{H_{n+1}} + P_{H_n}) - \frac{\Delta t}{2} G (Q_{n+1} + Q_n)$$

$$(6.43) \quad M_2 \, Q_{n+1} = M_2 \, Q_n + \frac{\Delta t}{2} (P_{Q_{n+1}} + P_{Q_n}) + \frac{\Delta t}{2} G^T (\eta_{n+1} + \eta_n)$$

$$- \frac{\Delta t}{2} (E + C) \cdot (Q_{n+1} + Q_n)$$

In order to solve (6.42) and (6.43) independently, we employ an iteration technique and write

$$(6.44) \quad M_1 \eta_{n+1}^{i+1} = M_1 \eta_n + \frac{\Delta t}{2} (P_{H_n} - G Q_n) + \frac{\Delta t}{2} (P_{H_{n+1}}^i - G \, Q_{n+1}^i)$$

$$(6.45) \quad M_2 \, Q_{n+1}^{i+1} = M_2 \, Q_n + \frac{\Delta t}{2} (P_{Q_n} + G^T \eta_n + (E+C) Q_n)$$

$$+ \frac{\Delta t}{2} (P_{C_{n+1}}^i + G^T \eta_{n+1}^{i+1} + (E+C) \, Q_{n+1}^i)$$

The strategy is to use a straight Euler integration :

η_{n+1}^o, Q_{n+1}^o, $P_{H_{n+1}}^o$ and $P_{Q_{n+1}}^o$ equal to η_n, Q_n, Q_n, P_{H_n} and P_{Q_n} to obtain η_{n+1}^1 and Q_{n+1}^1. These first estimates are used to improve the force terms on the right hand sides, the system is solved again and so on until the difference of successive iterates is less than a specified tolerance. In practice,(6.44) is solved first and then (6.45), using the updated η_{n+1} , then returning to (6.44), etc. By this approach we have achieved splitting the large matrix into two smaller cnes which furthermore are symmetric. The required storage is NBAND · NHNP + 2NBAND·2NMNP = 5NBAND·NMNP as opposed to the previous 18 NBAND·NMNP.

The solution of a system of the form

(6.46) $\quad \underset{\sim}{M} \underset{\sim}{X} = \underset{\sim}{Y}$

where $\underset{\sim}{M}$ is an arbitrary non-singular matrix, can be obtained by either inverting $\underset{\sim}{M}$ by an elimination technique or by an iteration method. When M is banded and constant while many solutions for different $\underset{\sim}{Y}$'s are desired, the most effective method is to factorize $\underset{\sim}{M}$ into a lower and upper triangular form [21].

(6.47) $\quad \underset{\sim}{M} = \underset{\sim}{L} \cdot \underset{\sim}{U}$

When $\underset{\sim}{M}$ is symmetric, (6.47) further simplifes to

(6.48) $\quad \underset{\sim}{M} = \underset{\sim}{U}^T \underset{\sim}{U}$

Figure 6.1 demonstrates the form of L and U. The unknown $\underset{\sim}{X}$ is then simply found by two successive substitutions:

(6.49) $\quad \underset{\sim}{L} \underset{\sim}{Z} = \underset{\sim}{Y}$

(6.50) $\quad \underset{\sim}{U} \underset{\sim}{X} = \underset{\sim}{Z}$

Banding is preserved in $\underset{\sim}{L}$ and $\underset{\sim}{U}$, so the solution proceeds very efficiently and accurately once $\underset{\sim}{M}$ is decomposed. As the number of operations (multiplications and divisions) is approximately two times the number of non-zero elements in $\underset{\sim}{L}$ or $\underset{\sim}{U}$, we can allow an average of 2-3 iterations before this scheme, (6.44)- (6.45), require the same amount of computation as (6.37). Besides the time integration

stability phenomenon which we have investigated, we must also ascertain that the iteration process converges. For simplicity we assume that (6.44) and (6.45) are iterated simultaneously so that we can use the symbolism of Equation (6.37). Neglecting forcing terms, the iteration is characterized by

$$(6.51) \qquad \underset{\sim}{M}_3 \, \underset{\sim}{X}_{n+1}^{i+1} \; = \; \frac{1}{2} \, \Delta t \, (\underset{\sim}{G}_3 + \underset{\sim}{E}_3 + \underset{\sim}{C}_3) \, \underset{\sim}{X}_{n+1}^{i}$$

Assuming a complex amplification factor, λ, we have

$$(6.52) \qquad \underset{\sim}{X}_{n+1}^{i+1} \; = \; \lambda \, \underset{\sim}{X}_{n+1}^{i}$$

and hence

$$(6.53) \qquad \underset{\sim}{M}_3 \, \lambda \underset{\sim}{X}_{n+1}^{i} \; = \; \frac{1}{2} \, \Delta t \, (\underset{\sim}{G}_3 + \underset{\sim}{E}_3 + \underset{\sim}{C}_3) \, \underset{\sim}{X}_{n+1}^{i}$$

or

$$(6.54) \qquad \lambda \; = \; \frac{1}{2} \, \Delta t \, \frac{e_3 + i(g_3 + c_3)}{m_3}$$

Since convergence requires $|\lambda| \leq 1$ and $\lambda = 0(\Delta t)$, the time step cannot be arbitrary. How large Δt may be is not known in general; but our experience indicates that the C-F-L Δt_{cr} cannot be exceeded.

At this stage, a more accurate, TE $= 0(\Delta t^3)$, iterative predictor-corrector method was developed in the search for a stabler scheme. The predictor is a simple parabolic extrapolation

$$(6.55) \qquad \underset{\sim}{X}_{n+1} \; = \; \underset{\sim}{X}_{n-2} - 3\underset{\sim}{X}_{n-1} + 3\underset{\sim}{X}_{n}$$

and as the corrector we used:

$$(6.56) \qquad \underset{\sim}{X}_{n+1} = \underset{\sim}{X}_n + \frac{\Delta t}{12} \left(5 \, \underset{\sim}{\dot{X}}_{n+1} + 8 \, \underset{\sim}{\dot{X}}_n - \underset{\sim}{\dot{X}}_{n-1} \right)$$

Again, it is necessary to iterate because $\underset{n+1}{\dot{X}}$ appears on the right hand side and, unfortunately, with the same poor results as before. Since (6.55) - (6.56) is a multilevel method, involving more than two time steps, it must be started with some other means.

Among the self-starting schemes, the Runge-Kutta methods are probably best known. We shall here discuss the fourth-order methods, since second-order methods are very similar to combinations of the already mentioned trapezoidal rule and Euler method. The R-K methods are known to be relatively accurate (often more accurate than same order predictor-correctors), however, for systems of equations, the algebra involved in an error analysis is untractable. This is a major disadvantage of these methods.

The procedure is best described on the basis of Equation (6.12), which we modify slightly:

$$(6.57) \qquad \underset{\sim}{M}_3 \, \underset{\sim}{\dot{X}} = \underset{\sim}{P}_3 - \underset{\sim}{G}_3 \, \underset{\sim}{X} - \underset{\sim}{E}_3 \, \underset{\sim}{X} - \underset{\sim}{C}_3 \, \underset{\sim}{X} = \underset{\sim}{P}_4$$

The 4th order R-K method with the smallest error bound [58] is then written:

$$(6.58) \qquad \underset{\sim}{X}_{n+1} = \underset{\sim}{X}_n + 0.17476028 \, \underset{\sim}{k}_1 - 0.55148053 \, \underset{\sim}{k}_2$$
$$+ 1.20553547 \, \underset{\sim}{k}_3 + 0.17118478 \, \underset{\sim}{k}_4$$

where

$$(6.59) \qquad \underset{\sim 3}{M_3} \, \underset{\sim 1}{k_1} = \Delta t \, \underset{\sim 4}{P_4} \, (t_n, \underset{\sim n}{X}_n)$$

$$(6.60) \qquad \underset{\sim 3}{M_3} \, \underset{\sim 2}{k_2} = \Delta t \, \underset{\sim 4}{P_4} \, (t_n + 0.4 \, \Delta t, \, \underset{\sim n}{X} + 0.4 \, \underset{\sim 1}{k_1})$$

$$(6.61) \qquad \underset{\sim 3}{M_3} \, \underset{\sim 3}{k_3} = \Delta t \, \underset{\sim 4}{P_4} \, (t_n + 0.45573726 \, \Delta t, \, \underset{\sim n}{X} + 0.29697760 \, \underset{\sim 1}{k_1}$$
$$+ \, 0.15875966 \, \underset{\sim 2}{k_2})$$

$$(6.62) \qquad \underset{\sim 3}{M_3} \, \underset{\sim 4}{k_4} = \Delta t \, \underset{\sim 4}{P_4} \, (t_n + \Delta t, \, \underset{\sim n}{X} + 0.21810038 \, \underset{\sim 1}{k_1} - 3.05096470 \, \underset{\sim 2}{k_2}$$
$$+ \, 3.83286432 \, \underset{\sim 3}{k_3})$$

Since only known information is used on the right hand sides of (6.59) – (6.62) we can solve for $\underset{\sim}{\eta}$ and $\underset{\sim}{Q}$ independently, saving storage and computation. The lack of error analysis makes it impossible to give an apriori convergence estimate on Δt. The R-K methods are characterized by being stable for sufficiently small Δt; but the admissible range must be established by trial and error. Our implementation of the 4'th order R-K-method (6.58)-(6.62) has been stable for Δt approximately equal to Δt_{cr} and it is by far the most accurate of all schemes tried. Although this method proved itself very useful in the initial stages of the circulation model development, there is a strong objection against using it for larger problems. The weak point is the need to solve the whole system of equations plus compute new right hand sides 4 times per advance in time, which makes the method rather slow and expensive.

Anticipating both large and long duration problems (especially looking forward to a two layer model), the search for a faster method went on until we finally came up with the SPLIT-TIME method. The idea

122

is not really new, but inspired by the time staggered finite difference methods mentioned in Chapter 2. It is however the first time such a method is applied to the finite element equations for hydrodynamic circulation.

Reviewing equations (6.40) and (6.41), we may isolate the inertial and gravitational terms as the more significant, i.e. we expect inertia and gravity to be the main forces. Doing this, we may formally write

$$(6.63) \qquad \underset{\sim}{M_1} \, \underset{\sim}{\eta}_{,t} + \underset{\sim}{G} \, \underset{\sim}{Q} = \underset{\sim}{P}_H$$

$$(6.64) \qquad \underset{\sim}{M_2} \, \underset{\sim}{Q}_{,t} - \underset{\sim}{G}^T \, \underset{\sim}{\eta} = \underset{\sim}{P}_Q - \underset{\sim}{E}_Q - \underset{\sim}{C} \, \underset{\sim}{Q}.$$

If we for a moment ignore the right hand sides, we observe that (6.63) and (6.64) lend themselves to central differencing in time (trapezoidal rule) if $\underset{\sim}{\eta}$ and $\underset{\sim}{Q}$ are staggered in time. To make this become clear, we define $\underset{\sim}{\eta}$ at times $t_{n-\frac{1}{2}}$, $t_{n+\frac{1}{2}}$ ... and $\underset{\sim}{Q}$ at times ... t_n, t_{n+1} ... and approximate (6.63) and (6.64) by

$$(6.65) \qquad \underset{\sim}{M_1} (\underset{\sim}{\eta}_{n+\frac{1}{2}} - \underset{\sim}{\eta}_{n-\frac{1}{2}}) + \Delta t \, \underset{\sim}{G} \, \underset{\sim}{Q}_n = \Delta t \underset{\sim}{P}_H \, (t_n, \underset{\sim}{\eta}_{n-\frac{1}{2}}, \underset{\sim}{Q}_n)$$

$$(6.66) \qquad \underset{\sim}{M_2} (\underset{\sim}{Q}_{n+1} - \underset{\sim}{Q}_n) - \Delta t \, \underset{\sim}{G}^T \, \underset{\sim}{\eta}_{n+\frac{1}{2}} = \Delta t \underset{\sim}{P}_Q \, (t_{n+\frac{1}{2}}, \underset{\sim}{\eta}_{n+\frac{1}{2}}, \underset{\sim}{Q}_n)$$

$$- \Delta t \, (\underset{\sim}{E} + \underset{\sim}{C}) \, \underset{\sim}{Q}_n$$

Assuming a given initial condition $\underset{\sim}{\eta}_{n-\frac{1}{2}}$, $\underset{\sim}{Q}_n$, the solution is executed by first solving (6.65) and then (6.66).

To study stability, we introduce

(6.67)

$$\underset{\sim}{X}_n = \left\{ \begin{array}{c} \underset{\sim}{\eta}_{n-\frac{1}{2}} \\ \underset{\sim}{Q}_n \end{array} \right\} \qquad \underset{\sim}{X}_{n+\frac{1}{2}} = \left\{ \begin{array}{c} \underset{\sim}{\eta}_{n+\frac{1}{2}} \\ \underset{\sim}{Q}_n \end{array} \right\} \qquad \underset{\sim}{X}_{n+1} = \left\{ \begin{array}{c} \underset{\sim}{\eta}_{n+\frac{1}{2}} \\ \underset{\sim}{Q}_{n+1} \end{array} \right\}$$

and

(6.68)

$$\underset{\sim}{G}_4 = \left[\begin{array}{c|cc} \underset{\sim}{0} & \underset{\sim}{G}_x & \underset{\sim}{G}_y \\ \hline \underset{\sim}{0} & & \underset{\sim}{0} \end{array} \right]$$

allowing us to write, (as usual ignoring $\underset{\sim}{P}_H$ and $\underset{\sim}{P}_Q$):

(6.69) $\qquad \underset{\sim}{M}_3 \, \underset{\sim}{X}_{n+\frac{1}{2}} = \underset{\sim}{M}_3 \, \underset{\sim}{X}_n - \Delta t \, \underset{\sim}{G}_4 \, \underset{\sim}{X}_n$

(6.70) $\qquad \underset{\sim}{M}_3 \, \underset{\sim}{X}_{n+1} = \underset{\sim}{M}_3 \, \underset{\sim}{X}_{n+\frac{1}{2}} + \Delta t \, \underset{\sim}{G}_4^T \, \underset{\sim}{X}_{n+\frac{1}{2}} - \Delta t \, (\underset{\sim}{E}_3 + \underset{\sim}{C}_3) \, \underset{\sim}{X}_{n+\frac{1}{2}}$

Since $\underset{\sim}{M}_3$ is regular, it has an inverse, so $\underset{\sim}{X}_{n+\frac{1}{2}}$ can be solved for:

(6.71) $\qquad \underset{\sim}{X}_{n+\frac{1}{2}} = (\underset{\sim}{I} - \Delta t \, \underset{\sim}{M}_3^{-1} \, \underset{\sim}{G}_4) \, \underset{\sim}{X}_n$

Substituting (6.71) in (6.70) yields

(6.72) $\qquad \underset{\sim}{M}_3 \, \underset{\sim}{X}_{n+1} = (\underset{\sim}{M}_3 + \Delta t \, \underset{\sim}{G}_\eta^T)(\underset{\sim}{I} - \Delta t \, \underset{\sim}{M}_3^{-1} \underset{\sim}{G}_4) \underset{\sim}{X}_n - \Delta t \, (\underset{\sim}{E}_3 + \underset{\sim}{C}_3) \cdot$

$\qquad\qquad\qquad (\underset{\sim}{I} - \Delta t \, \underset{\sim}{M}_3^{-1} \underset{\sim}{G}_4) \, \underset{\sim}{X}_n$

where $\underset{\sim}{I}$ is the unit matrix.

Multiplying by M_3^{-1} gives

$$(6.73) \quad \underset{\sim}{X}_{n+1} = (I + \Delta t \ M_3^{-1} G_4^T)(I - \Delta t \ M_3^{-1} G_4) \underset{\sim}{X}_n - \Delta t \ M_3^{-1} (E_3 + C_3) \cdot$$

$$(I - \Delta t \ M_3^{-1} G_4) \underset{\sim}{X}_n$$

Noting the special structure of G_4, Equation (6.68), and using the matrix rule

$$(6.74) \quad \begin{bmatrix} I & A \\ 0 & I \end{bmatrix}^{-1} = \begin{bmatrix} I & -A \\ 0 & I \end{bmatrix}$$

we may write

$$(6.75) \quad (I - \Delta t \ M_3^{-1} G_4^T) \underset{\sim}{X}_{n+1} = (I - \Delta t \ M_3^{-1} G_4) \underset{\sim}{X}_n - \Delta t (I - \Delta t \ M_3^{-1} G_4^T) M_3^{-1} \cdot$$

$$(E_3 + C_3)(I - \Delta t \ M_3^{-1} G_4) \underset{\sim}{X}_n$$

The last term can be reduced; thus

$$(6.76) \quad (E_3 + C_3) \cdot (I - \Delta t \ M_3^{-1} G_4) =$$

$$\begin{bmatrix} 0 & 0 \\ \hline 0 & E + C \end{bmatrix} \begin{bmatrix} I & -\Delta t \ M_1^{-1} G_4 \\ \hline 0 & I \end{bmatrix} =$$

125

$$\begin{bmatrix} \underset{\sim}{0} & \vdots & \underset{\sim}{0} \\ \text{------} & \vdots & \text{------} \\ \underset{\sim}{0} & \vdots & \underset{\sim}{E} + \underset{\sim}{C} \end{bmatrix} = (\underset{\sim}{E}_3 + \underset{\sim}{C}_3)$$

Finally, multiplying by $\underset{\sim}{M}_3$ results in

$$(6.77) \qquad (\underset{\sim}{M}_3 - \Delta t \; \underset{\sim}{G}_4^T) \underset{\sim}{X}_{n+1} = (\underset{\sim}{M}_3 - \Delta t \; \underset{\sim}{G}_4) \underset{\sim}{X}_n - \Delta t (\underset{\sim}{I} - \Delta t \; \underset{\sim}{G}_4^T \; \underset{\sim}{M}_3^{-1}) \cdot$$

$$(\underset{\sim}{E}_3 + \underset{\sim}{C}_3) \; \underset{\sim}{X}_n$$

To find the amplification factor, Equation (6.19) is substituted in (6.77) which is multiplied by $\bar{X}_n^T$ and reorganized to give

$$(6.78) \qquad \lambda = \frac{\bar{X}_n^T \underset{\sim}{M}_3 \underset{\sim}{X}_n - \Delta t \bar{X}_n^T \underset{\sim}{G}_4 \underset{\sim}{X}_n - \Delta t \bar{X}_n^T (\underset{\sim}{E}_3 + \underset{\sim}{C}_3) \underset{\sim}{X}_n + \Delta t^2 \bar{X}_n^T \underset{\sim}{G}_4^T \underset{\sim}{M}_3^{-1} (\underset{\sim}{E}_3 + \underset{\sim}{C}_3) \underset{\sim}{X}_n}{\bar{X}_n^T \underset{\sim}{M}_3 \underset{\sim}{X}_n - \Delta t \; \bar{X}_n^T \underset{\sim}{G}_4^T \underset{\sim}{X}_n}$$

$$= \frac{m_3 - \Delta t (g_4 + i g_5) - \Delta t \; e_3 - i \Delta t \; c_3}{m_3 - \Delta t (g_4 - i g_5)} + O (\Delta t^2)$$

We introduced the notation

$$(6.79) \qquad \bar{X}_n^T \; \underset{\sim}{G}_4 \; \underset{\sim}{X}_n = g_4 + i g_5 \qquad\qquad g_4, \; g_5 \epsilon \; R$$

and

$$(6.80) \qquad \bar{X}_n^T \; \underset{\sim}{G}_4^T \; \underset{\sim}{X}_n = (\overline{\bar{X}_n^T \; \bar{\underset{\sim}{G}}_4 \; \underset{\sim}{X}_n})^T = g_4 - i g_5$$

where g_4, g_5 are arbitrary real numbers. Neglecting e_3, c_3 for the moment yields

$$
(6.81) \qquad |\lambda|^2 = \left| \frac{m_3 - \Delta t g_4 - i\Delta t g_5}{m_3 - \Delta t g_4 + i\Delta t g_5} \right|^2 = \frac{\{(m_3 - \Delta t g_4) - i\Delta t g_5\}\{(m_3 - \Delta t g_4) + i\Delta t g_5\}}{\{(m_3 - \Delta t g_4) + i\Delta t g_5\}\{(m_3 - \Delta t g_4) - i\Delta t g_5\}}
$$

$$
= 1
$$

hence the split time scheme (6.65), (6.66) is linearly unconditionally stable as an initial value problem and without eddy viscosity or coriolis terms. (Isn't analysis beautiful?) Unfortunately, we can not show that adding eddy viscosity decreases $|\lambda|$ or what influence coriolis has, however, our experience with the split time scheme indicates that reasonable values of E_{ij} has a small stabilizing effect. On the other hand we have not found the split time scheme unconditionally stable in practice. In fact, the maximum time step we have achieved is approximately $1.5\ \Delta t_{cr}$. We have so far not resolved why instability sets in; but have nevertheless implemented the split-time scheme as the standard time integration scheme in our circulation. Of the methods discussed, this is the most efficient, comparing favorably to explicit finite difference methods, but still cannot match the time steps possible in implicit finite difference methods. More research could fruitfully be invested in developing an even better time integration method for the finite element equations, and we suggest such a project for future work.

CHAPTER 7

VERIFICATION

In this chapter, several simple problems are solved and compared to the exact analytical solution. The purposes of undertaking such a study are: 1. insure that the model is constructed correctly; 2. investigate the accuracy and stability of the model; and 3. evaluate the relative importance of various terms.

The first example is the problem of a standing wave in a rectangular prismatic channel shown in Figure 7-1. We consider only the linearized, one-dimensional problem governed by the wave equation

$$(7.1) \qquad \frac{\partial^2 u}{\partial t^2} = c^2 \frac{\partial^2 u}{\partial x^2}$$

$$(7.2) \qquad \frac{\partial^2 \eta}{\partial t^2} = c^2 \frac{\partial^2 \eta}{\partial x^2}$$

$$(7.3) \qquad c^2 = gh$$

The channel of length L is closed at one end $x = L$, and at the open end $x = 0$ the water level is forced up and down according to

$$(7.4) \qquad \eta_0 = a \sin \omega_f t$$

where a is the amplitude, and ω_f is the angular velocity of the forced oscillation with period T.

$$(7.5) \qquad \omega_f = \frac{2\pi}{T}$$
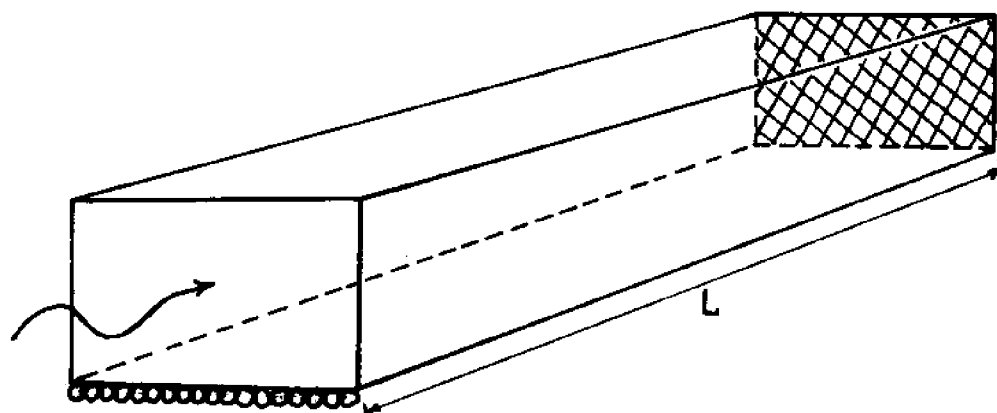
Channel perspective
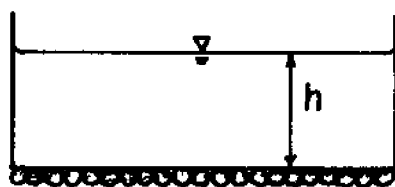
Channel cross section

Figure 7-1. Wave in prismatic channel.
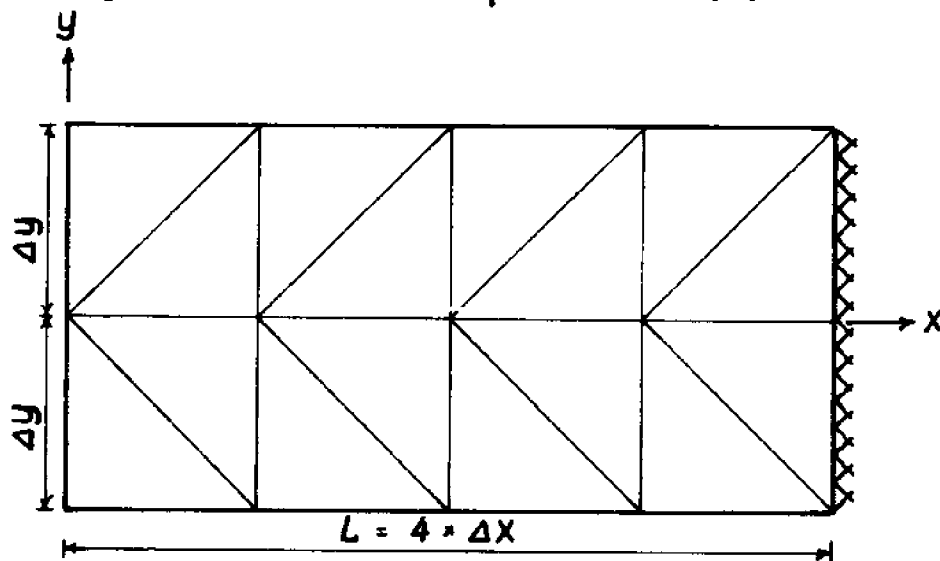
Figure 7-2. Plan of channel with FE grid.

The boundary condition at the solid boundary is

(7.6) $u = 0$ $x = L$

or equivalently

(7.7) $\eta_{,x} = 0$ $x = L$

The standing wave solution is easily found by separating the variables. The result is (see for example [   ]):

(7.8) $u = -\dfrac{a\sqrt{gh}}{h\cos\omega_f\dfrac{L}{\sqrt{gh}}}\sin\{\omega_f\dfrac{L}{\sqrt{gh}}(\dfrac{x}{L}-1)\}\cos\omega_f t$

(7.9) $\eta = \dfrac{a}{\cos\omega_f\dfrac{L}{\sqrt{gh}}}\cos\{\omega_f\dfrac{L}{\sqrt{gh}}(\dfrac{x}{L}-1)\}\sin\omega_f t$

For the test, the values of the parameters are listed in Table 7-1.

A finite element grid symmetric about the channel centerline is constructed as shown in Figure 7-2. The symmetry provides a first check on the results which, if correct, must also be symmetric.

The relatively small amplitude ($\dfrac{a}{h} = 0.025$) is chosen so that non-linear effects are negligible. At the 3 walls, the normal discharge is prescribed zero and in the 90° corners both discharge components are required to vanish. At the open end, the surface elevation is forced according to (7.4) while the discharge is left free. The problem was solved with the split time method, starting from an initial condition

L	200 m
h	4 m
T	200 sec.
ω_f	0.0314159 sec^{-1}
a	0.1 m
g	9.81 m/sec^2
c	6.26 m/sec
Δx	50 m
Δy	50 m
NMNP	15
NMEL	16
Δt	5 sec
Δt_{cr}	5.65 sec.

TABLE 7-1 Standing Wave in Channel

derived from (7.8) and (7.9) for $t = \frac{T}{4}$. The computed surface

elevations at $x = L$ are plotted together with the analytical solution

on Figure 7-3. A similar time history of the velocity at $x = 0$ is

shown in Figure 7-4. One whole tidal period was computed with $\Delta t=5$ sec.

showing the right tendencies, but not agreeing too well quantitatively

with the exact solution. To resolve whether the error was due to the

time integration, the time step was halved and the computations repeated.

As figures 7-3 and 7-4 show, the two solutions come out practically

identical. The error is therefore attributed to either the spatial dis-
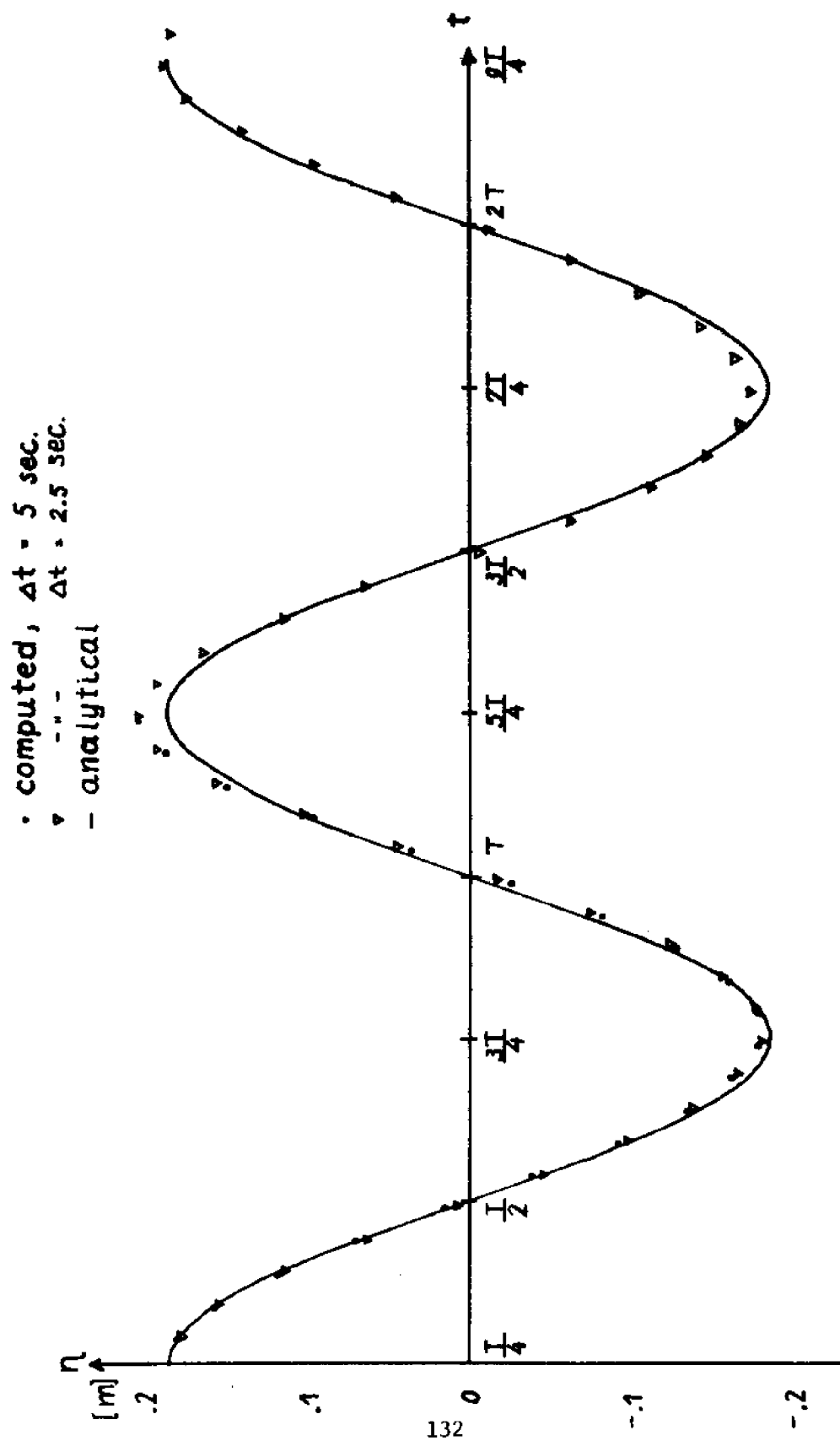
Figure 7-3. Surface elevation at x = L vs. time.
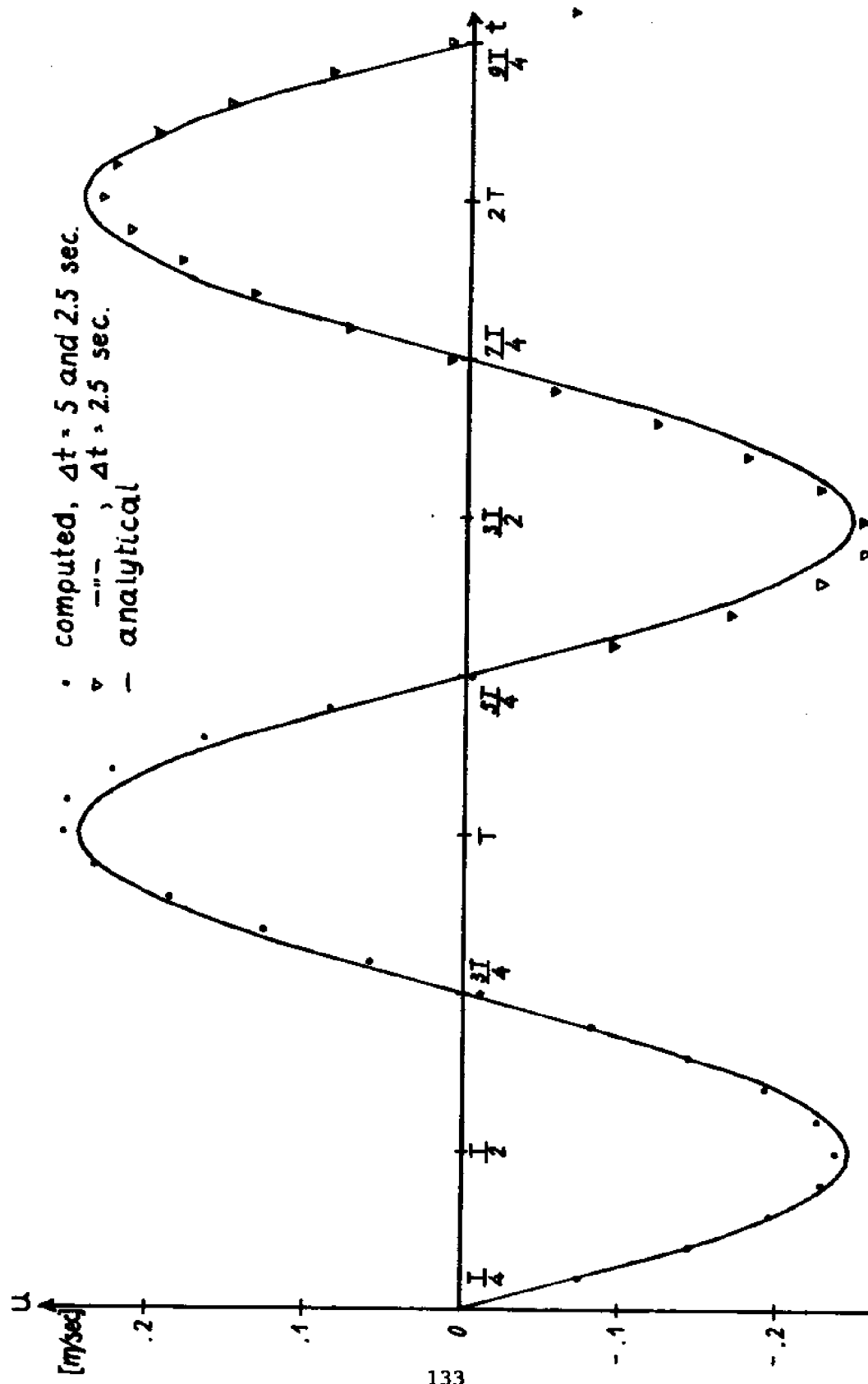
Figure 7-4 Velocity at x = 0 vs. time.

cretization or possibly excitation of one of the eigenmodes of the channel. Recalling the expression for the spatial error (5.54), this can be decreased by either making the grid smaller or the data f_o smoother. We choose the latter and increase the period of the forcing by a factor of 3, thus T = 600 sec. and the computations are repeated with Δt = 5 sec. As tables 7-2 and 7-3 show the ratio $\dfrac{\text{max error}}{\text{max value}}$ is now less than 1% over a period of more than 2T.

t x	$\dfrac{3T}{4}$	$\dfrac{5T}{4}$	$\dfrac{7T}{4}$	$\dfrac{9T}{4}$	$\dfrac{11T}{4}$	exact
0	-0.1	0.1	-0.1	0.1	-0.1	0.1
50	-0.1028	0.1025	-0.1027	0.1025	-0.1027	0.1026
100	-0.1047	0.1042	-0.1045	0.1042	-0.1046	0.1044
150	-0.1057	0.1053	-0.1055	0.1052	-0.1057	0.1055
200	-0.1063	0.1056	-0.1061	0.1056	-0.1062	0.1059

TABLE 7-2: Comparison of Computed Surface Elevation with the Exact Solution for T = 600 sec.

t x	$\dfrac{T}{2}$	T	$\dfrac{3T}{2}$	2 T	$\dfrac{5T}{2}$	exact
0	-0.05466	0.05446	-0.05431	0.05417	-0.05431	0.05440
50	-0.04125	0.04117	-0.04086	0.04096	-0.04087	0.04114
100	-0.02781	0.02772	-0.02751	0.02749	-0.02749	0.02759
150	-0.01388	0.01383	-0.01375	0.01370	-0.01381	0.01384
200	0.0	0.0	0.0	0.0	0.0	0.0

TABLE 7-3: Comparison of Computed Velocities with the Exact Solution for T = 600 sec.

In test runs of this problem using different integration techniques, the stability was preserved up to the Δt values given in Table 7-4.

Courant-Friedrichs-Lewy Δt_{cr}:	5.65 sec.
Euler:	~0.25 sec.
Predictor-Corrector:	4 sec
Runge-Kutta:	5 sec
Split-time:	7.5 sec.

TABLE 7-4: Critical Time Steps for Integration Methods
Applied to Simple Channel

Of all the schemes, the 4'th order Runge-Kutta method is the most accurate. The Euler method is useless for any longer term integration and the Predictor-Corrector method showed rather poor accuracy, presumably due to the iteration procedure. The split time scheme is as the example showed sufficiently accurate and efficient. Hence this method is chosen for further applications. Should an occasion arise where better accuracy is needed, the Runge-Kutta scheme is easily revived.

The second example consists of modeling the propagation of a wave into the channel shown in Figure 7-1 and 7-2, with the water initially at rest. Again only the linearized problem governed by Equation (7.2) is considered with the boundary conditions (7.7) and

(7.10) $\eta = a (1 - \cos(\omega t))$ at $x = 0$

however, now under the initial condition

(7.11) $u, \eta = 0$ for all x at $t = 0$

The exact solution to the problem is easily found since any solution to

the wave equation (7.2) can be written

(7.12) $\eta = f (x - ct) + g (x + ct)$

Condition (7.7) implies, ($\xi = (x-ct)$, $\zeta = (x+ct)$)

(7.13) $f_{,\xi} (L - ct) + g_{,\zeta} (L + ct) = 0$

which is integrated

(7.14) $\left| - \frac{1}{c} \int \frac{df}{d\xi} d\xi + \frac{1}{c} \int \frac{dg}{d\zeta} d\zeta \right|_{x=L} = $ constant

or

(7.15) $-f (L - ct) + g (L + ct) = $ constant

From the initial condition, the constant is determined to be zero,

leaving

(7.16) $f (L - ct) = g (L + ct)$

The complete solution is now written

(7.17) $f(x-ct) = \begin{cases} 0 & t < \frac{x}{c} \\ a \sin \omega (t - \frac{x}{c}) \; ; & t < \frac{2L+x}{c} \\ a \sin\{\omega(t - \frac{x}{c})\} - f(2L-x-ct) \; ; & t > \frac{2L+x}{c} \end{cases}$

$$(7.18) \quad g(x+ct) = \begin{cases} 0 & ;t < \dfrac{2L-x}{x} \\ f(2L - x - ct) & ;t > \dfrac{2L-x}{c} \end{cases}$$

combined with (7.11).

The computed and exact solutions at different times are again compared in Table 7-5. The split time scheme was used and Table 7-6 gives the values of the parameters. Some remarks are attached to the results shown in Table 7-5. Except for small times, only three significant digits are shown to avoid confusion by round off errors. The trend of the results agree well and the average error is less than 5% over a period of $2T = 1200$ sec. The $(1-\cos\omega t)$ forcing function was chosen to make the start-up as smooth as possible since the value of this function and its derivative vanishes at $t = 0$. The Runge-Kutta scheme was applied to the same problem with a $\Delta t = 2.5$ sec. yielding results with an average error of less than 1% showing that better accuracy can be obtained if desired.

All examples so far have been for horizontal bottom. To verify the variable depth feature of the model, the standing wave in a channel with sloping bottom was solved for. The longitudinal section of the channel is shown in Figure 7-5.

The depth is given by

$$(7.19) \qquad h = \alpha x$$

The governing equations for the linearized problems are

137
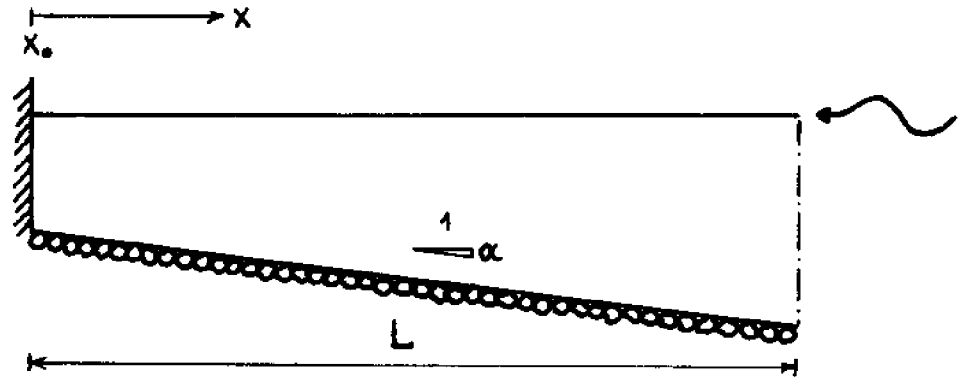
Figure 7-5. Channel with sloping bottom.
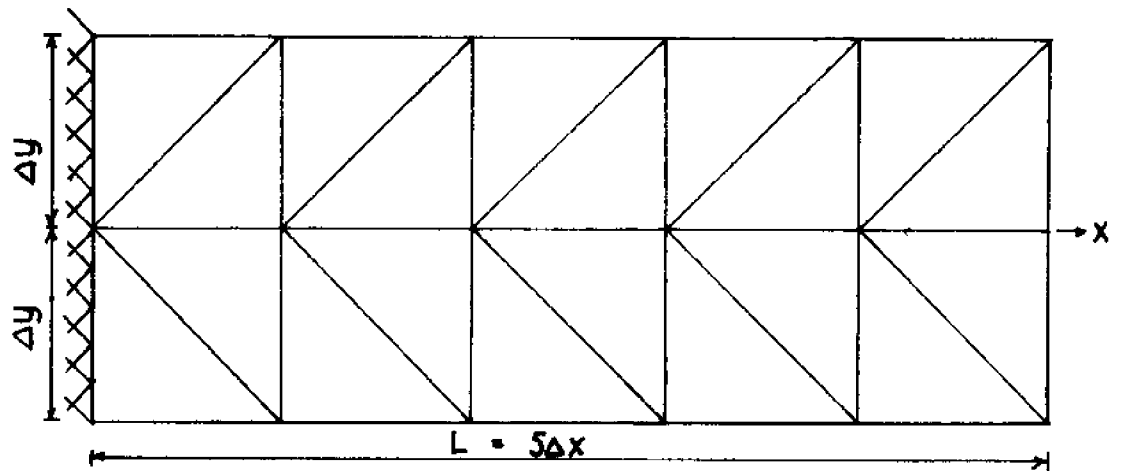
Figure 7-6. Plan of channel with FE grid.

(7.20)
$$\frac{\partial \eta}{\partial t} + \frac{\partial hu}{\partial x} = 0$$

(7.21)
$$\frac{\partial \eta}{\partial t} + g \frac{\partial \eta}{\partial x} = 0$$
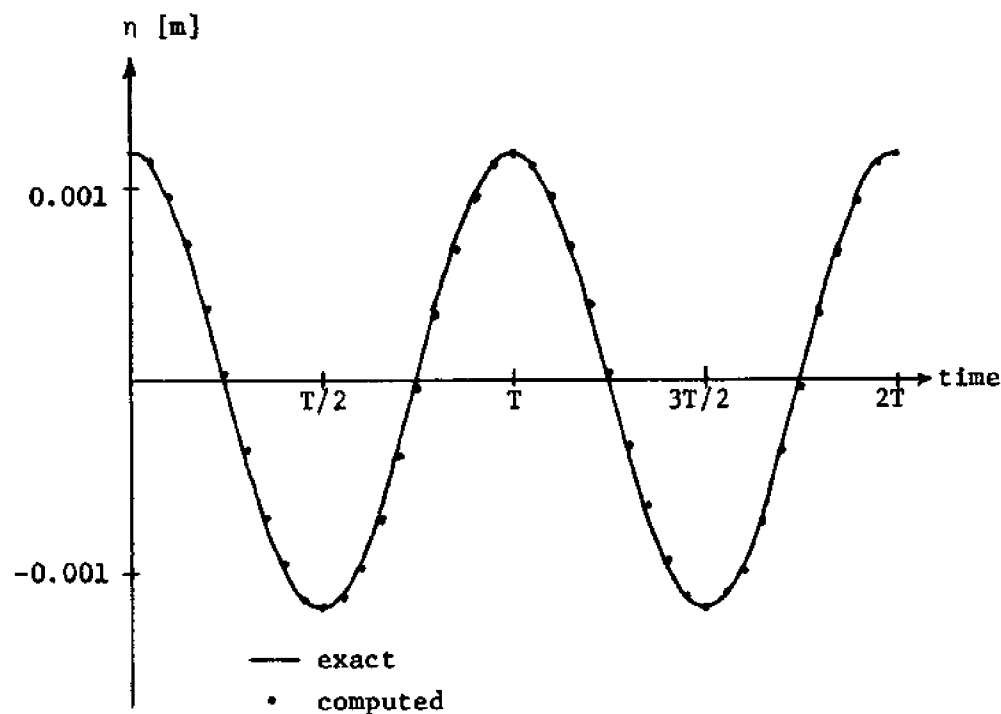
Figure 7-7. Surface elevation at $x = x_o + L$ for sloping channel.

The boundary conditions are again, as for the first example, given by

(7.22) $\eta = a \sin \omega_F t$ at $x = x_o + L$

(7.23) $\eta_{,x} = 0$ at $x = x_o$

The solution to this problem can be found in [36]. Assuming

(7.24) $\eta = \text{Im} \{\zeta(x) e^{i\omega_F t}\}$

139

TIME	computed (m)	exact [m]	X[m]	TIME	computed [m]	exact [m]
$\frac{T}{4}$	0.1 0.10088 0.10214 0.10286 0.10338	0.1 0.10089 0.10177 0.10257 0.10293	0 50 100 150 200	$\frac{5T}{4}$	0.1 0.102 0.104 0.105 0.105	0.1 0.101 0.103 0.104 0.104
$\frac{T}{2}$	0.2 0.2008 0.2010 0.2012 0.2015	0.2 0.201 0.202 0.2022 0.2022	0 50 100 150 200	$\frac{3T}{2}$	0.2 0.204 0.206 0.208 0.208	0.2 0.205 0.208 0.211 0.211
$\frac{3T}{4}$	0.1 0.0981 0.0965 0.0955 0.0952	0.1 0.097 0.0958 0.0947 0.0943	0 50 100 150 200	$\frac{7T}{4}$	0.1 0.0981 0.0968 0.0959 0.0959	0.1 0.1003 0.1007 0.1010 0.1012
T	0.0 -0.00291 -0.00441 -0.00533 -0.00677	0.0 -0.00311 -0.00556 -0.00726 -0.00793	0 50 100 150 200	2T	0.1 -0.00444 -0.00825 -0.0106 -0.0115	0.1 -0.00419 -0.00761 -0.00981 -0.0105

TABLE 7-5:   Comparison of Surface Elevations for a Propagation Wave

a   =   0.1 m

T   =   600 sec

ω =   0.01047 sec^{-1}

Δt =   7.5 sec.

TABLE 7-6:   Values of Parameters for Propagating Wave Example

140

and $\qquad \kappa = 2\,\omega_F\,\sqrt{\dfrac{x}{\alpha g}}$

we find the equation governing $\zeta(x)$:

$$(7.25) \qquad \kappa^2 \zeta_{,\kappa\kappa} + \kappa\,\zeta_{,\kappa} + \kappa^2 \zeta = 0$$

which is Bessels equation of zeroeth order. The solution for η is hence written:

$$(7.26) \qquad \eta = -\frac{a}{D}\,\{Y_1\,(2\omega_F\sqrt{\frac{x_0}{\alpha g}})\;\;J_0\,(2\omega_F\sqrt{\frac{x}{\alpha g}})\;\;J_1\,(2\omega_F\sqrt{\frac{x_0}{\alpha g}})\;\cdot$$

$$Y_0(2\omega_F\sqrt{\frac{x}{\alpha g}})\}\;\sin\,\omega_F t$$

where

$$(7.27) \qquad D = Y_0(2\omega_F\sqrt{\frac{x_0+L}{\alpha g}})\;J_1\,(2\omega_F\sqrt{\frac{x_0}{\alpha g}})\;-\;Y_1\,(2\omega_F\sqrt{\frac{x_0}{\alpha g}})\;J_0(2\omega_F\sqrt{\frac{x_0+L}{\alpha g}})$$

The velocity is easily found from Equation (7.21):
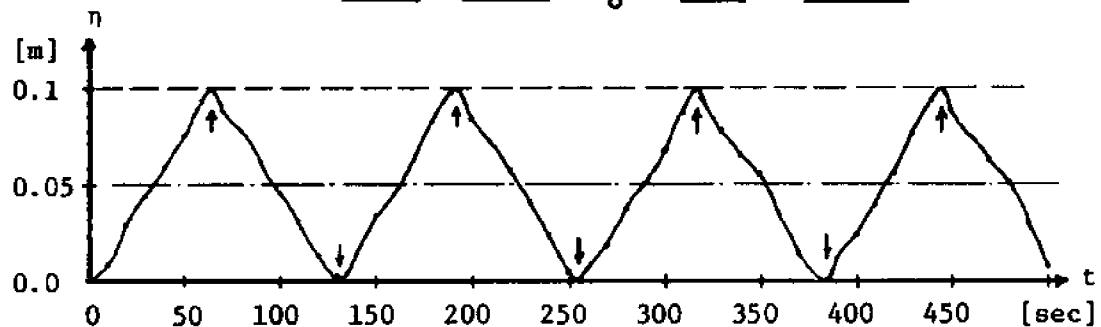
Figure 7-8. Surface elevation at x=L vs. time for wind example. The arrows indicate the exact times (eqs. (7.41) and (7.42)) of max and min occurences.

$$(7.28) \qquad u = \frac{a}{D}\,\sqrt{\frac{g}{x\alpha}}\,\{J_1(2\omega_F\sqrt{\frac{x_0}{\alpha g}})\;Y_1(2\omega_F\sqrt{\frac{x}{\alpha g}})-Y_1(2\omega_F\sqrt{\frac{x_0}{\alpha g}})J_1(2\omega_F\sqrt{\frac{x}{\alpha g}})\}\cdot$$

$$\cos\,\omega t$$

$$
\begin{array}{lll}
x_o & = & 500.0 \text{ m} \\[4pt]
L & = & 200.0 \text{ m} \\[4pt]
\alpha & = & 0.02 \\[4pt]
a & = & 0.001 \text{ m} \\[4pt]
T & = & 200 \text{ sec} \\[4pt]
\omega_F & = & 0.0314159 \text{ sec}^{-1} \\[4pt]
\Delta x & = & 50 \text{ m} \\[4pt]
\Delta y & = & 100 \text{ m} \\[4pt]
\Delta t & = & 2.0 \text{ sec.}
\end{array}
$$

TABLE 7-7 : Parameter Values for Sloping Channel

The finite element grid applied is shown in Figure 7-5. The split time scheme was used and the values of the test parameters are listed in Table 7-7. Figure 7-7 shows the excellent agreement of the computed with the exact surface elevations at $x = x_o + L$. Elevations and velocities at other x compare equally well although not shown here.

The channel examples were all repeated with only the direction of the x and y axis changed. This gives us reasonable assurance that both x and y components have been programmed correctly.

In the last one-dimensional test example, a constant uniform wind stress is applied to the channel in Figures 7-1 and 7-2. The governing equations are

$$
(7\text{-}29) \qquad \frac{\partial \eta}{\partial t} + h \frac{\partial u}{\partial x} = 0
$$

$$
(7\text{-}30) \qquad \frac{\partial u}{\partial t} + g \frac{\partial \eta}{\partial x} = \frac{\tau_x^s}{\rho h}
$$

with the boundary conditions

(7.31) $\eta = 0$ $x = 0$

(7.32) $u = 0$ $x = L$

and the initial condition

(7.33) $\eta, u = 0$ $\forall x$ at $t = 0$

To solve this system we introduce

(7.34) $\kappa = \eta - \dfrac{\tau_x^s}{\rho g h} x$

whereby Equation (7.29) and (7.30) change to

(7.35) $\dfrac{\partial \kappa}{\partial t} + h \dfrac{\partial u}{\partial x} = 0$

(7.36) $\dfrac{\partial u}{\partial t} + g \dfrac{\partial \kappa}{\partial x} = 0$

The boundary conditions remain the same for κ but the initial condition now becomes

(7.37) $\kappa = -\dfrac{\tau_x^s}{\rho g h} x$, $u = 0$, $0 \leq x \leq L$, $t = 0$

After some trivial computations, the complete solution may be written

(7.38) $u = \displaystyle\sum_{p=0}^{\infty} a_p \cos \{ (\tfrac{1}{2} + p) \tfrac{\pi x}{L} \} \sin\{ (\tfrac{1}{2} + p) \tfrac{\pi c}{L} t \}$

(7.39) $\eta = \dfrac{\tau_x^s}{\rho g h} - \dfrac{h}{c} \displaystyle\sum_{p=0}^{\infty} a_p \sin \{ (\tfrac{1}{2} + p)\tfrac{\pi x}{L} \} \cos\{ (\tfrac{1}{2} + p) \tfrac{\pi c}{L} t \}$

where

143

$$(7.40) \qquad a_p = (-1)^p \frac{\tau_x^s cL}{\rho g h^2 \pi^2} \frac{1}{(1+2p)^2}$$

The series are rather slowly convergent $(a_p = O(\frac{1}{p^2}))$, however, at x = L the maximum and minimum surface displacements are easily found together with their time of occurrence.

$$(7.41) \qquad \eta_{max} = 2 \frac{\tau_x^s L}{\rho g h} \qquad \text{at} \quad t = m \cdot (\frac{2L}{c}) \quad m = 1,3,5...$$

and

$$(7.42) \qquad \eta_{min} = 0 \qquad \text{at} \quad t = m (\frac{2L}{c}) \quad m = 0,2,4,...$$

The model was run with the split time integration scheme and the values of the test parameters are listed in Table 7-8.

τ_x^s/ρ =	0.0981 m^2/sec^2
L =	200 m
h =	4 m
c =	6.26 m/sec
η_{max} =	0.1 m
Δx =	50 m
Δy =	50 m
Δt =	5 sec

TABLE 7-8: Parameter Values for Wind on Channel

The computed results for η at x = L are plotted in Figure 7-8, where also the times of equations (7.41) and (7.42) have been indicated. Very good agreement between amplitudes and phases is found.

Finally, a two-dimensional test example was carried out. The detailed description of both numerical and analytical solution is contained in the report [12]. Figure 7-9 shows the geometry of the problem which is an approximation of the Massachusetts Bay. The bay is bounded by land on three sides, but has a wide opening on the east side towards the Atlantic Ocean. The analytical solution is governed by the wave equation, assumes a constant depth (h = 36.6 m) and a harmonic time dependence (standing wave). The amplitudes of surface elevations and velocities are shown in Figure 7-10. The finite element circulation model is adopted to the same problem. Thus non-linear terms are dropped from the formulation. On solid boundaries, the normal velocity is set to zero and at the opening, the surface is forced as a sinusoid

(7.43)   η = 1.31 (1-cosωt) $0 \leq x \leq 78000$,   y = 37000

where ω = 2π/T and T is 12.4 hours = 44640 sec. As initial condition, the water is assumed at rest and η = 0 everywhere for $t \leq 0$. The Runge-Kutta method was used for the time integration with Δt = 200 sec. The smallest grid size is approximately 5000 π and the grid consists of 71 elements with 48 nodes. It was found that after the first period of T/2 the surface elevations and flow velocities were practically periodic indicating convergence on the standing wave so-

lution. This rather fast convergence rate is due to the reasonable
initial condition and to the fact that the wave propagation velocity
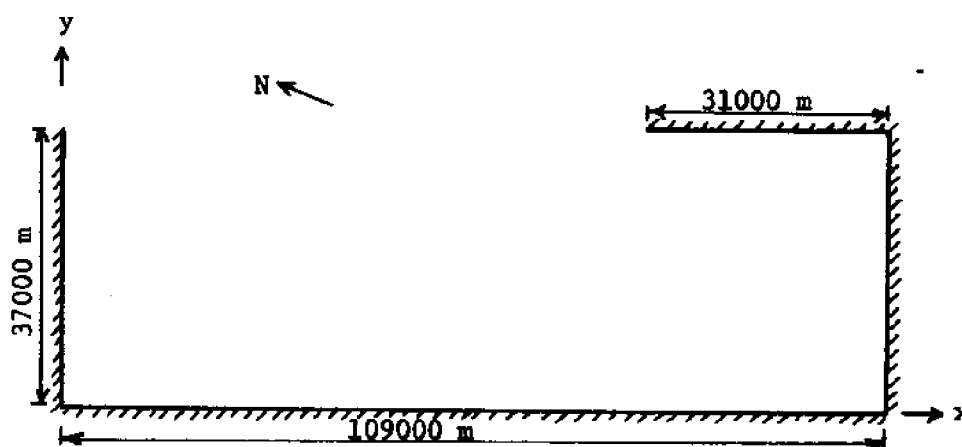
Figure 7-9. Rectangular approximation of Massachusetts
Bay. Sketch of geometry.

(7.44) $$c = \sqrt{gh} = 18.95 \text{ m/sec}$$

is relatively large in this case. Figures 7-11 and 7-12 show the
computed high tide and maximum ebb velocities. Comparing with Figure
7-10, good agreement is found between surface contours, tidal ranges,
velocity magnitudes and directions.

The discussed test examples provide reasonable assurance
that the model is constructed and programmed correctly. They also
constitute a basis on which modifications to this model or other
models can be compared.
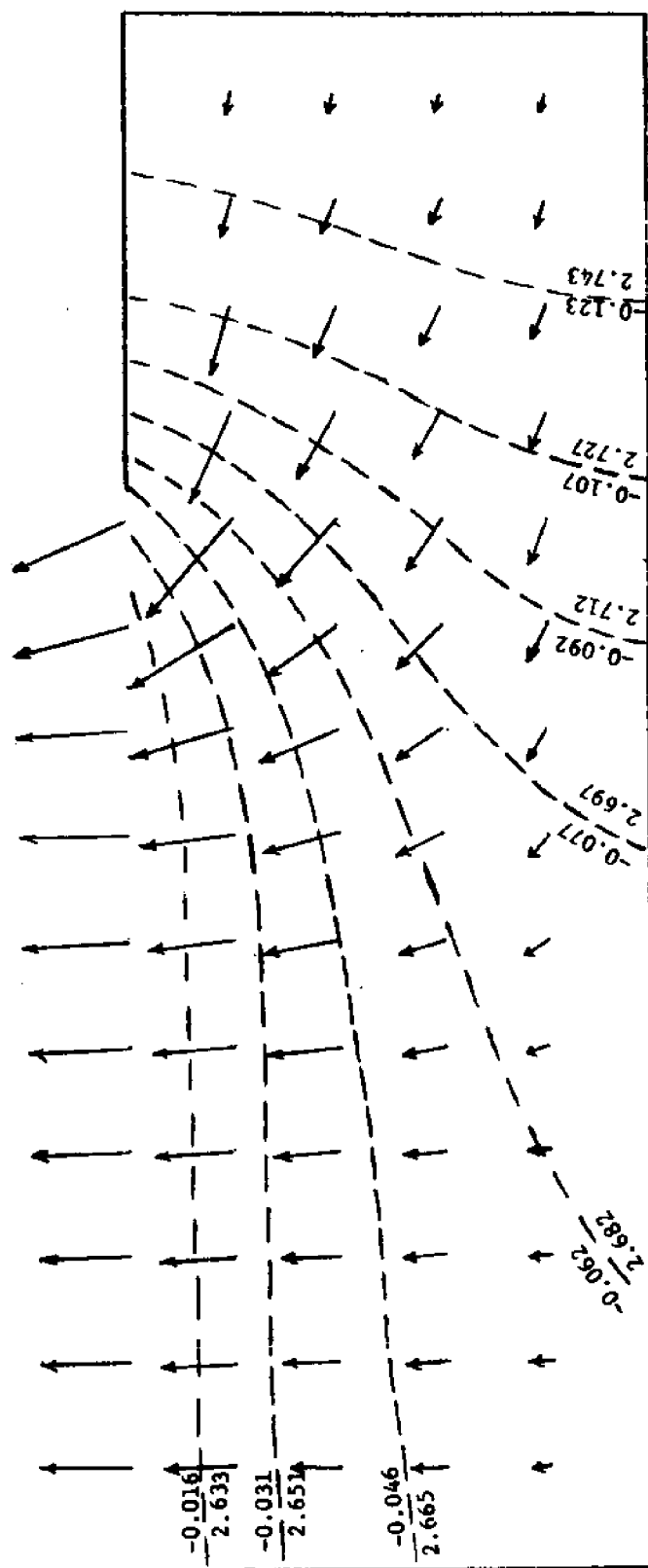
Figure 7-10. Rectangular model of Massachusetts Bay.
Analytical solution for surface elevations and currents.
On each contour line the tidal range in meters is indicated.

147

Figure 7-11.
Rectangular model of Massachusetts Bay.
Finite element solution. Runge-Kutta method, $\Delta t = 200$ sec.
Surface elevations at element centroids and surface contour
lines after 68000 sec, 1.5 tidal period. The computed approximate
tidal range in meters is given for each contour line.

Note: only the decimals
are given for cen-
troidal values.

148
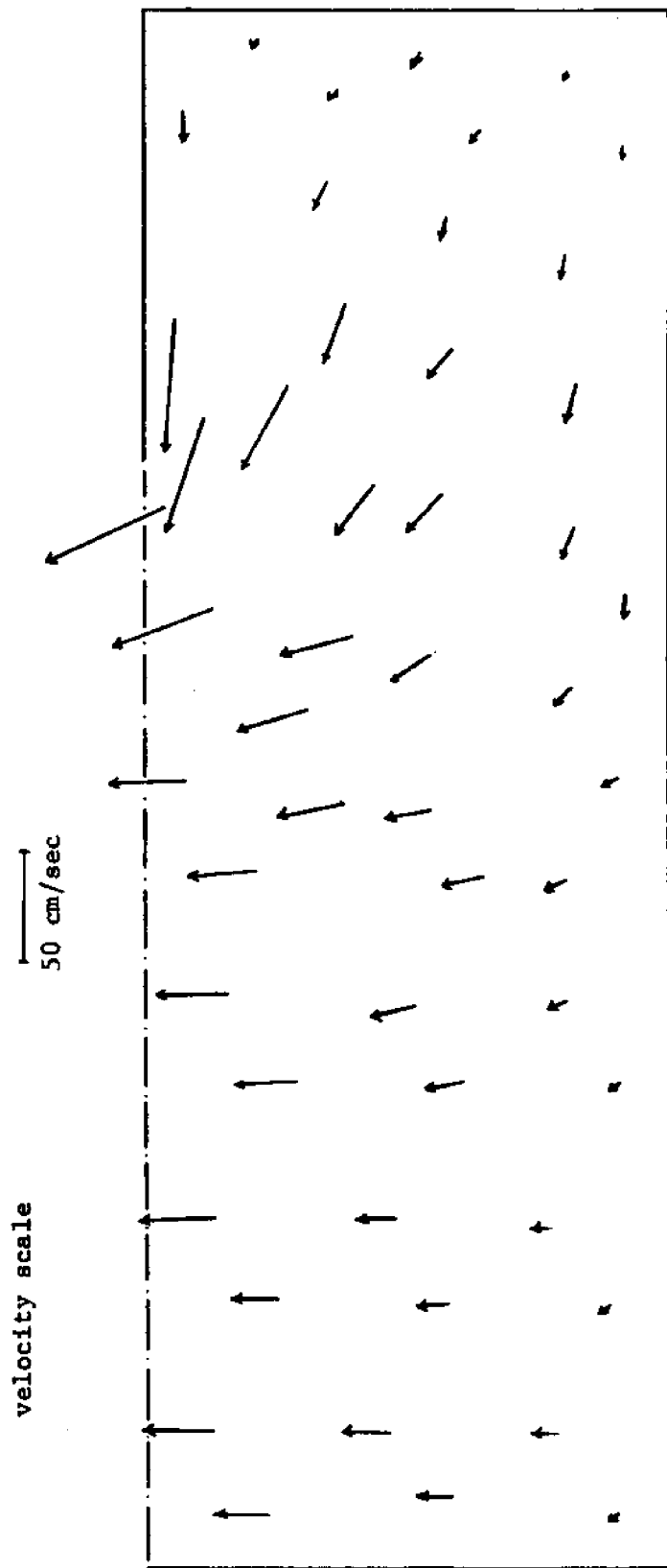
Figure 7-12. Computed ebb velocities for rectangular approximation of Mass Bay. Runge-Kutta method, Δt=200 sec.

velocity scale

50 cm/sec

8.1 APPLICATIONS

Several case studies are discussed in this chapter, with the emphasis placed on solution strategies rather than results. However, whenever possible, comparison of the computed flows against actual field data is attempted.

The first example is taken from Massachusetts Bay shown on Figure 8-1. The objective is to obtain an estimate of the circulation pattern. Laying out a good grid is essential for an efficient solution. This process requires skill on behalf of the solver, which can be gained only through experience. We shall give some guidelines which will make it easier for a beginner to tackle a new problem. The mistakes we have made and their corrections are also discussed.

8.2 THE FINITE ELEMENT GRID.

Before starting the subdivision of the domain into elements, the outer boundary must be established. It is wize to begin any new problem with the crudest approximation possible and then later make refinements as they become necessary.

Land boundaries do not cause many problems especially when too much detail is avoided initially. For ocean boundaries, the situation is quite different. The items that must come into consideration when choosing where to create this "artificial" boundary, which really is dictated by the limited size of computers, are:

    a. Where is data available for boundary conditions

Figure 8-1. Bathymetric map of Massachusetts Bay.

151

b. Since some inaccuracies are to be expected in the data, the boundary should be reasonably far away from any area of interest;

c. If wind is an essential factor and its effect on the boundary conditions are unknown, it is better to establish the boundary at greater depths.

Usually a compromise between a, b and c is unavoidable. The solution accuracy would thus benefit by moving the ocean boundary on Figure 8-2 further out to deeper water, but unfortunately no tidal data is available there.

After having determined the perimeter, the subdivision takes place. As a general rule, the best results are obtained if the grid is made to resemble a flow net. Good engineering judgement is important and the following factors must be considered.

d. Depth variations are modeled by placing nodes at the lowest and highest points of the bottom profile.

e. The grid must be finer where gradients are greater (flow net concept).

f. Grid dimensions should change gradually, and for accuracy the elements must not degenerate. For triangular elements, this means as previously mentioned that no apex angle should approach zero and preferably they should be almost equilateral.

g. Impossibilities should be avoided. This point will be demonstrated in examples.
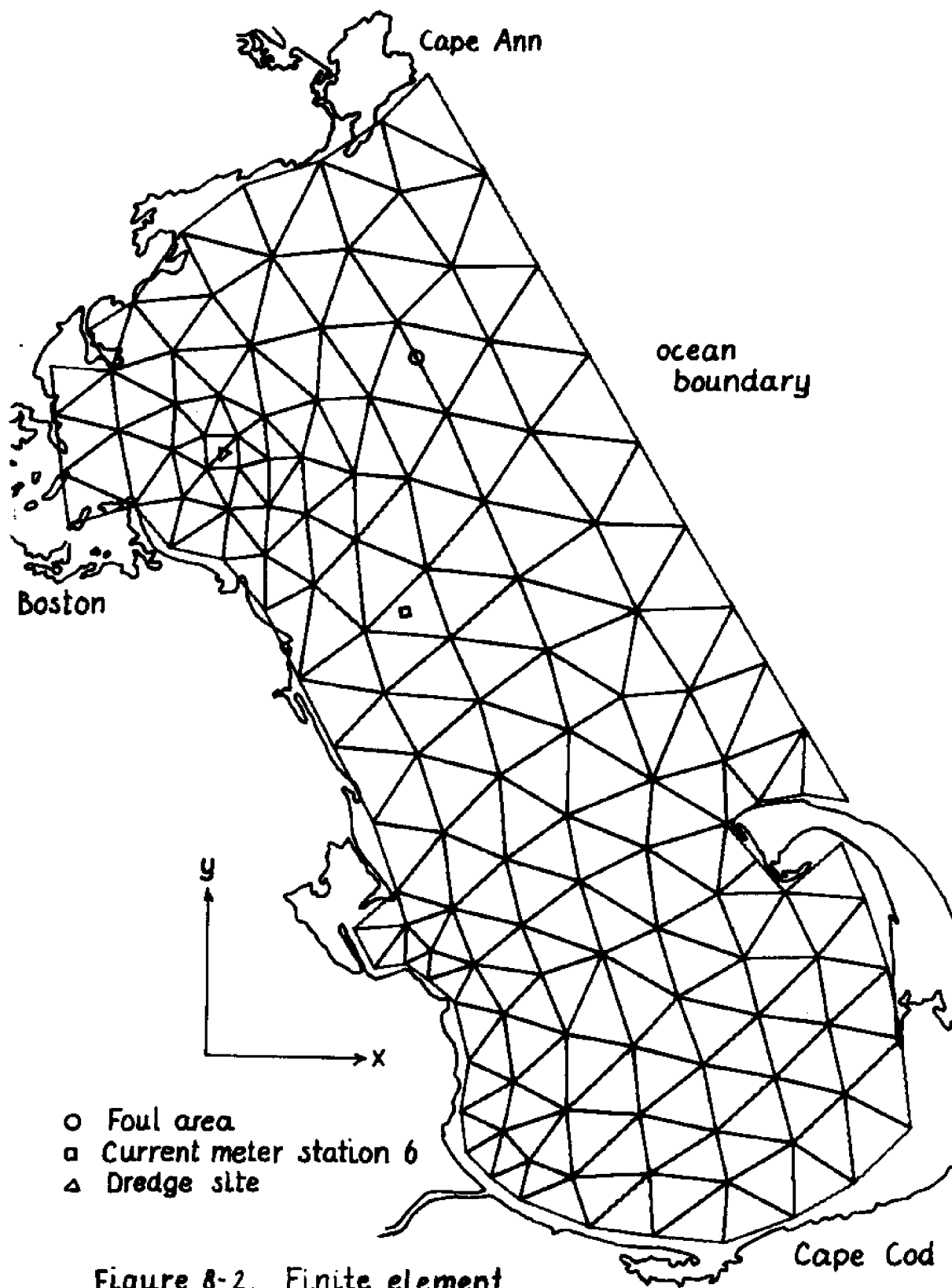
Figure 8-2. Finite element grid of Mass. Bay.

Cape Ann

ocean boundary

Boston

y
x

o Foul area
□ Current meter station 6
△ Dredge site

Cape Cod

153

Again a compromise must be found between accuracy and computational efficiency. In our grid of Mass Bay (Figure 8.2), we have thus not attempted excessive detail in describing the land boundaries. However, in three areas, a special interest is identified and the grid therefore made finer. These are: 1. a proposed (but now abandoned) sand and gravel dredge site approximately 13 km east of the entrance to Boston Harbor. 2. the coast around the Pilgrim nuclear power plant site at Rocky Point, and 3. the entrance of Cape Cod Canal into the bay.

The coastline and bottom topography are determined from the USCGS (U.S. Coast and Geodetic Survey) bathymetric chart of the area.

The only ocean boundary information available is the predicted tide from the tide tables [73]. The closest stations are Gloucester, Rockport, Race Point, and S.E. of Cape Cod Lighthouse. Unfortunately, the predictions for Race Point and Cape Cod are based on very old and limited data. Only mean tidal ranges and times of high and low tides are listed. Although the distance between the two stations is only about 19000 m, there is a reported difference in tidal range of 0.43 m (1.4 ft). Considering the many uncertainties it is decided to use an average tide as boundary condition and furthermore assume: 1. the semidiurnal (M_2) tide accounts for all the variation, 2. straight interpolation of tidal range between Race Point and Cape Cod Lighthouse, and between the southern and northern extremes of the boundary is valid, 3. mean low water is a horizontal surface at the ocean boundary, and finally 4. the tide is in phase all along the ocean boundary. These simplifying assumptions are made necessary by the lack of data. Their influence on the results can be investigated by doing

154

sensitivity studies with the model.

The model was applied to the grid shown in Figure 8-2 with the ocean boundary condition

$$(8.2.1) \qquad \eta = a (1 - \cos \omega t)$$

where

$$(8.2.2) \qquad \omega = \frac{2\pi}{T}$$

and $T = 45000$ sec. The amplitude varied linearly from 1.27 m at Cape Cod to 1.31 m at Cape Ann. Figure 8-3 and 8-4 show typical pictures of computed sea surface levels and velocities. Due to shoaling effects there is a significant change in tidal range and phase from point to point. A fine tuning of the model is possible by changing the bottom friction or eddy viscosity coefficients.

Increasing the bottom friction tends to magnify the phase lag in the direction of propagation. Tidal ranges are fairly insensitive to changes in C_f, however significant changes in the currents are noticeable. Eddy viscosity has little or no effect on tidal phases or ranges but affects currents. Short waves are damped and therefore small amounts of eddy viscosity E_{ij} help keep the numerically generated short wave noise down. The magnitude of E_{ij} can be estimated in the following way. Assume that the internal stress term is typically a fraction, a, of the linear pressure term:

$$(8.2.3) \qquad a \cdot g \frac{\partial \eta}{\partial x} \sim E_{xx} \cdot \frac{\partial u^2}{\partial x^2}$$

Introducing typical scales as before

155
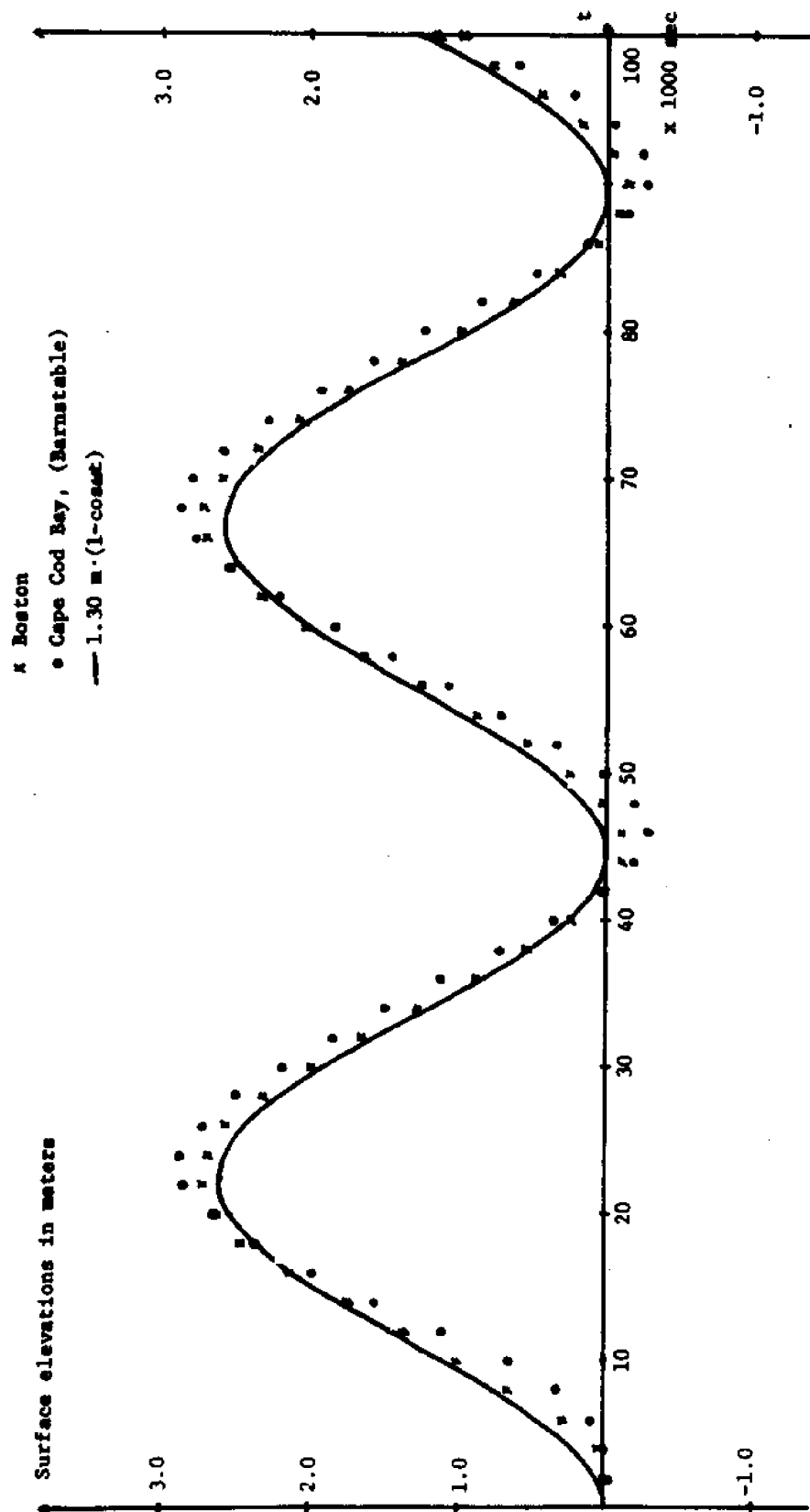
Figure 8-3. Time history of computed sea surface levels.

156
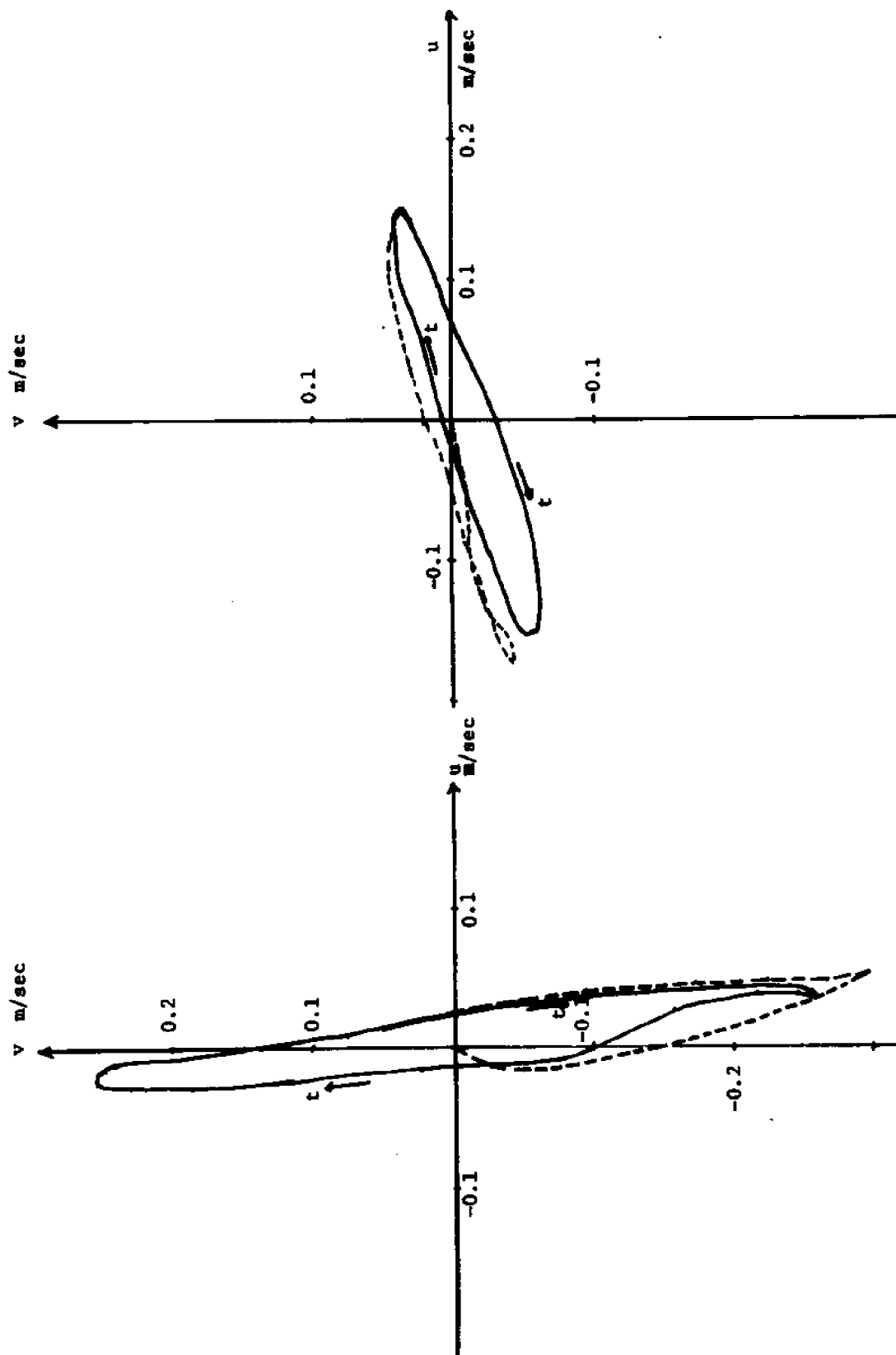
Figure 8-4. Time history of computed currents. a) Center of Cape Cod Bay. b) 15 km East of Boston.

$$(8.2.4) \qquad a \cdot g \frac{\hat{\eta}}{\hat{x}} \frac{\partial \eta}{\partial x} \sim E_{xx} \frac{\hat{u}^2}{\hat{x}^2} \frac{\partial^2 \eta}{\partial x^2}$$

where the derivatives now are order of 1 quantities, gives

$$(8.2.5) \qquad E_{xx} \sim ag \frac{\hat{\eta}}{\hat{u}} \cdot \hat{x}$$

Reasonable a's may range from 0.1 - 0.01. Let for example $\hat{\eta} = 2$ m; $\hat{u} = 0.2$ m/sec., $\hat{x} = 5000$ m and a = 0.02, then

$$(8.2.6) \qquad E_{xx} \sim 0.02 \cdot 10 \cdot \frac{2}{0.2} \cdot 5000 = 10000 \text{ m}^2/\text{sec.}$$

The validity of a crude estimate like (8.2.5) is supported by model
tests. When a is made significantly smaller than 0.01, the results
are insensitive to internal stresses. We have so far not had sufficient
data to attempt any adjusting of E_{ij}. Our use of internal stress terms
has been limited to controlling short wave noise, usually with a ≤ 0.02.
In the grid shown in Figure 8-2, the change in grid size around the
NOMES dredge site is thus too drastic causing entrapment of short wave
energy and consequent instability. By including some internal stress
in this local area, the problem was eliminated.

The computed tidal range at Boston Harbour is slightly larger
than the predicted mean tidal range of 2.77 m (9.1 ft). Since this
is a more dependable observation, the boundary conditions were scaled
down accordingly. Thus, the amplitude was prescribed as 1.25 m at
Cape Cod and 1.21 m at Cape Ann with a linear variation in between.

The bottom friction coefficient ranged from 0.01 - 0.02
according to the depth. The current fields at subsequent stages

of the tide are shown in Figures 8-5 to 8-10,and Figure 8-11 is a plot

of surface contours at high tide.

Model results have been compared with actual current meter

measurements,and sensitivity with respect to the ocean boundary condi-

tion was investigated by Christodoulou [8]. Figure 8-12 shows a com-

parison of model results with field current measurements at the foul

area location shown in Figure 8-2. The agreement is quite good,although

no attempts were made specifically to fit the data,and is largely due to

the fact that the current measurements were made during winter. In

this season, the water column is homogeneous and a vertically integrated

model is a good approximation.

Since the ocean boundary condition is rather uncertain, it

is useful to investigate the sensitivity of model results to reasonable

variations in prescribed values. Figure 8-13 shows the results of such

an analysis. Changing the tidal ranges along the ocean boundary has

a marked effect on the magnitude and direction of the currents and

the net drift. The figure also demonstrates how the model results can

be fitted to real data by adjusting the "tilt" at the boundary.

Changing the tidal phase or the reference level along the boundary has

similar effects.

To study the influence of wind, the Mass Bay model was exer-

cised again with a constant wind stress $\frac{\tau_y^s}{\rho_0}$ = -0.0000286 m^2/sec^2 applied

everywhere on the surface. This corresponds to a situation with north

wind at approximately 10 knots $\sim$ 5 m/sec. The real problem with

modeling wind is the open ocean boundary. It is usually not known how

wind effects the sea surface, however, such effects are decreased as the depth increases. This is the reasoning behind point c in the be= ginning of this chapter. Although we could not satisfy this everywhere, the assumption was made that the wind had no effect on the surface level at the ocean boundary, which therefore was forced according to (8.2.1) as before. Figure 8-14 shows a plot of the velocities after 120000 sec that may be compared with Figure 8-9. The wind caused little change, at most 2 cm/sec in the velocities. Sufficient field data for verification of wind driven circulation is not available. In general, good prediction of mass transport (discharge) is expected. However, because of the slow boundary layer development from the sur- face, the velocities may not be realistic. The vertically integrated formulation cannot describe wind driven circulation, other than dischar- ges, well.

For a detailed report on the application of the model to hurricane surges, reference is made to Pagenkopf and Pearce [53].

During the work on the Mass Bay grid, some ill behaved ele- ment arrangements were discovered. A typical example of an intrin- sically bad grid configuration is shown in Figure 8-15a. On a flooding tide, the filling of elements 1 and 4 must essentially be achieved by the tangential flow at point A; but this will always drain one element while filling the other, an "impossible" situation as referred to in guideline g. A better layout is shown in Figure 8-15b. However, to obtain accurate results it is necessary to increase the number of nodes and elements.

160

20　40 cm/sec
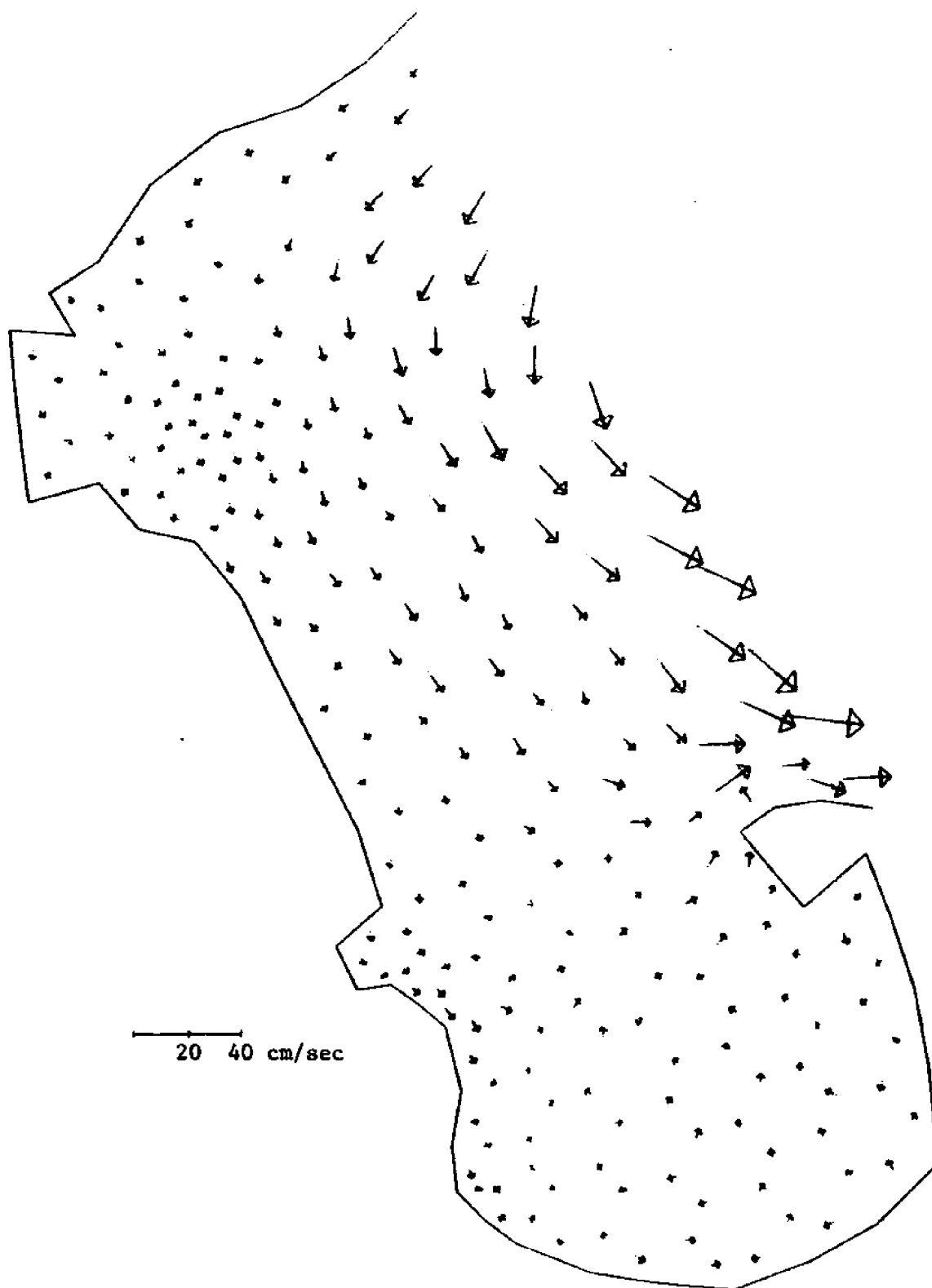
Figure 8-5. Computed tidal currents in Mass Bay. t=90000 sec=
low tide.

161
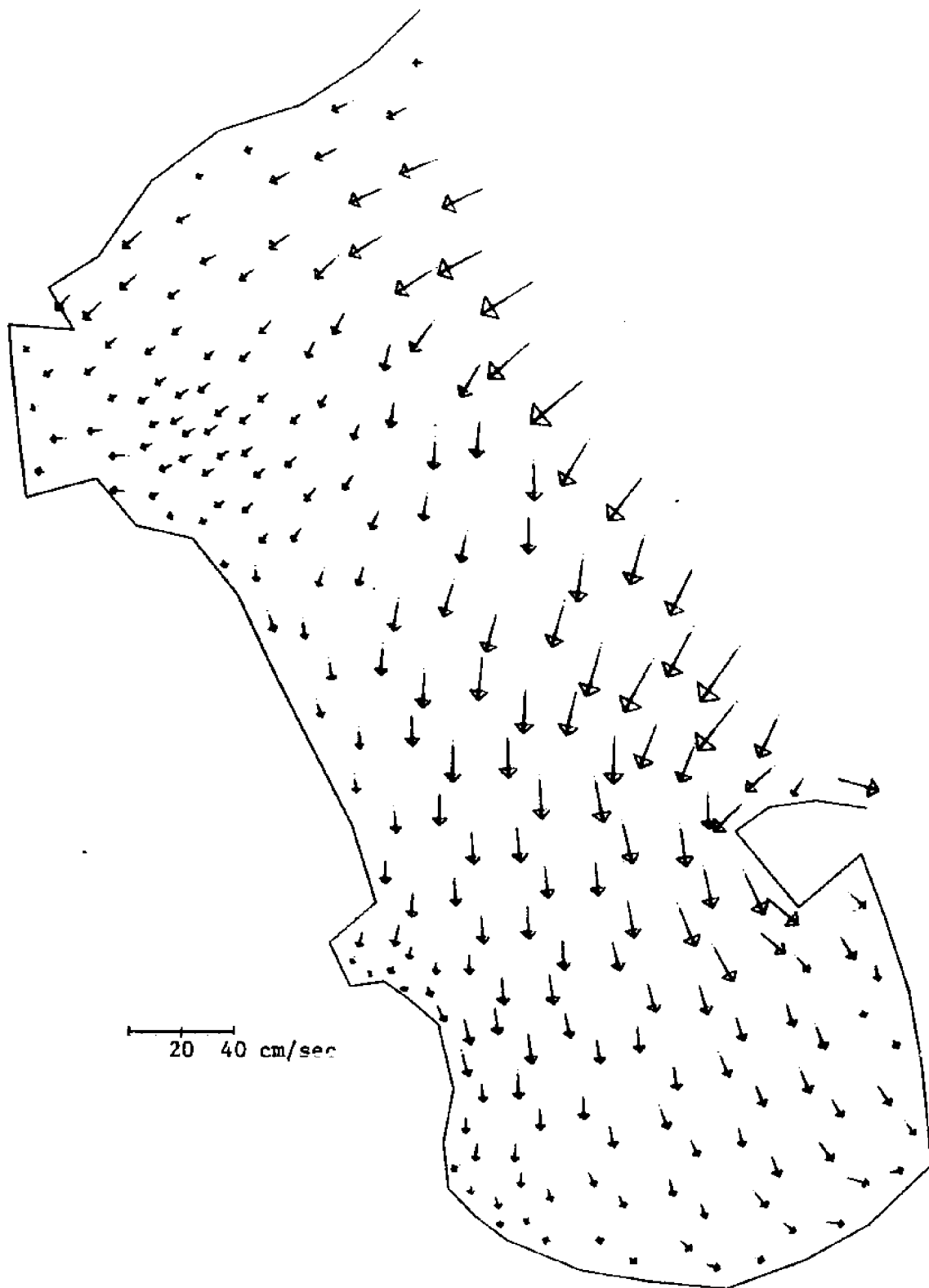
Figure 8-6. Computed tidal currents in Mass Bay. t=97500 sec=
T/6 after low tide.

162
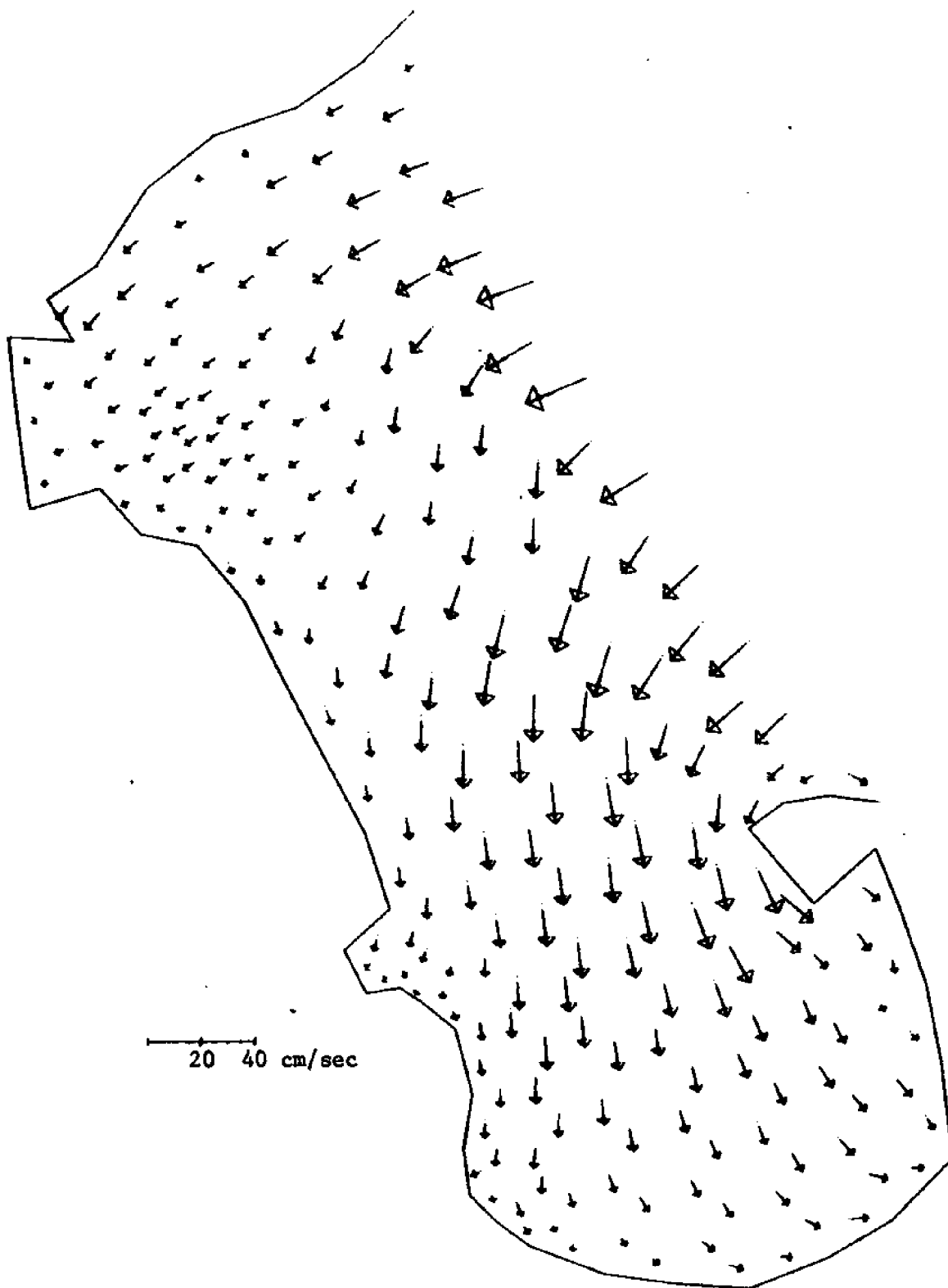
Figure 8-7. Computed tidal currents in Mass Bay. t=105000 sec=
T/3 after low tide.

163
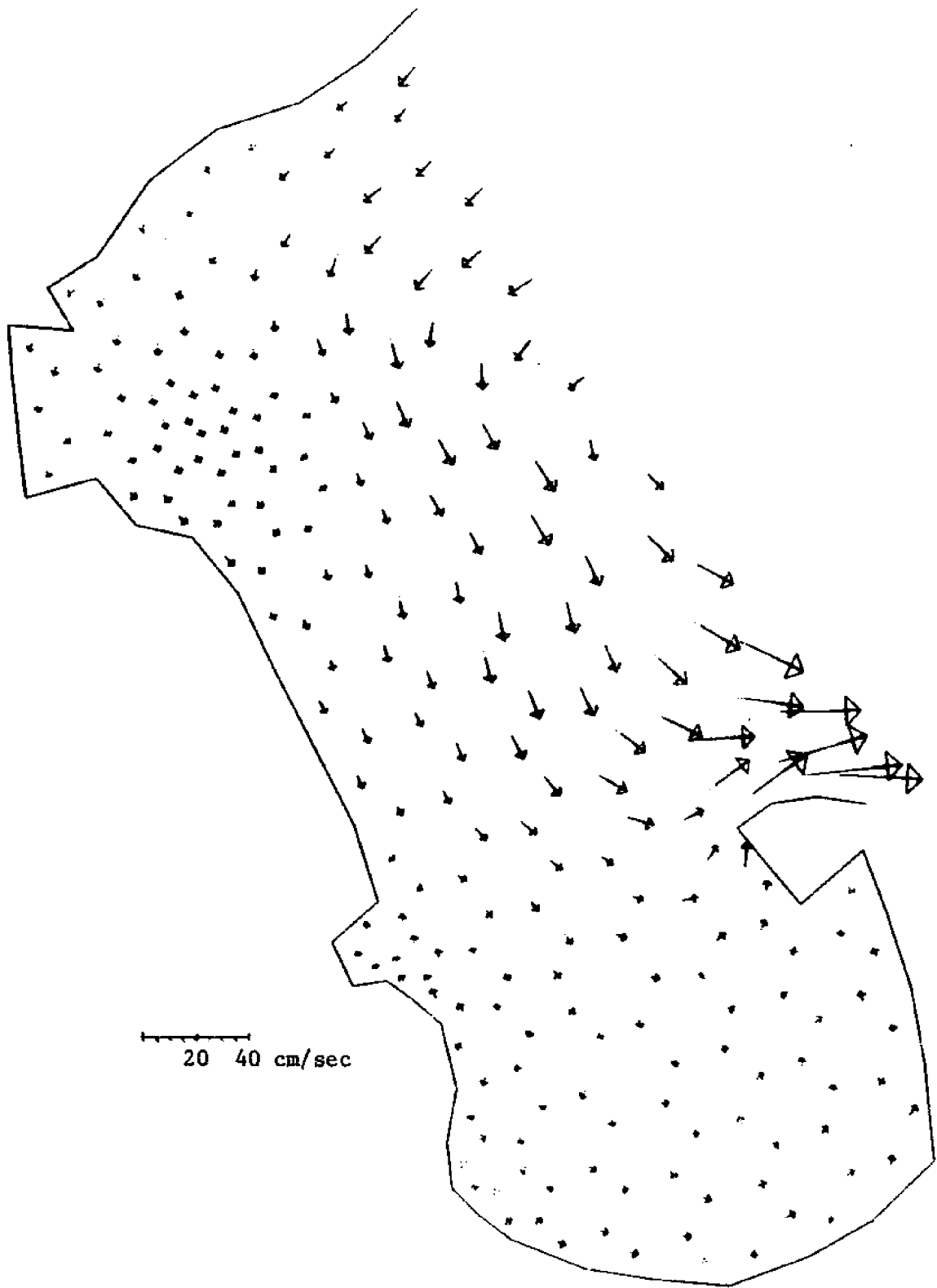
Figure 8-8. Computed tidal currents in Mass Bay. t=112500 sec=
T/2 after low tide=high tide.
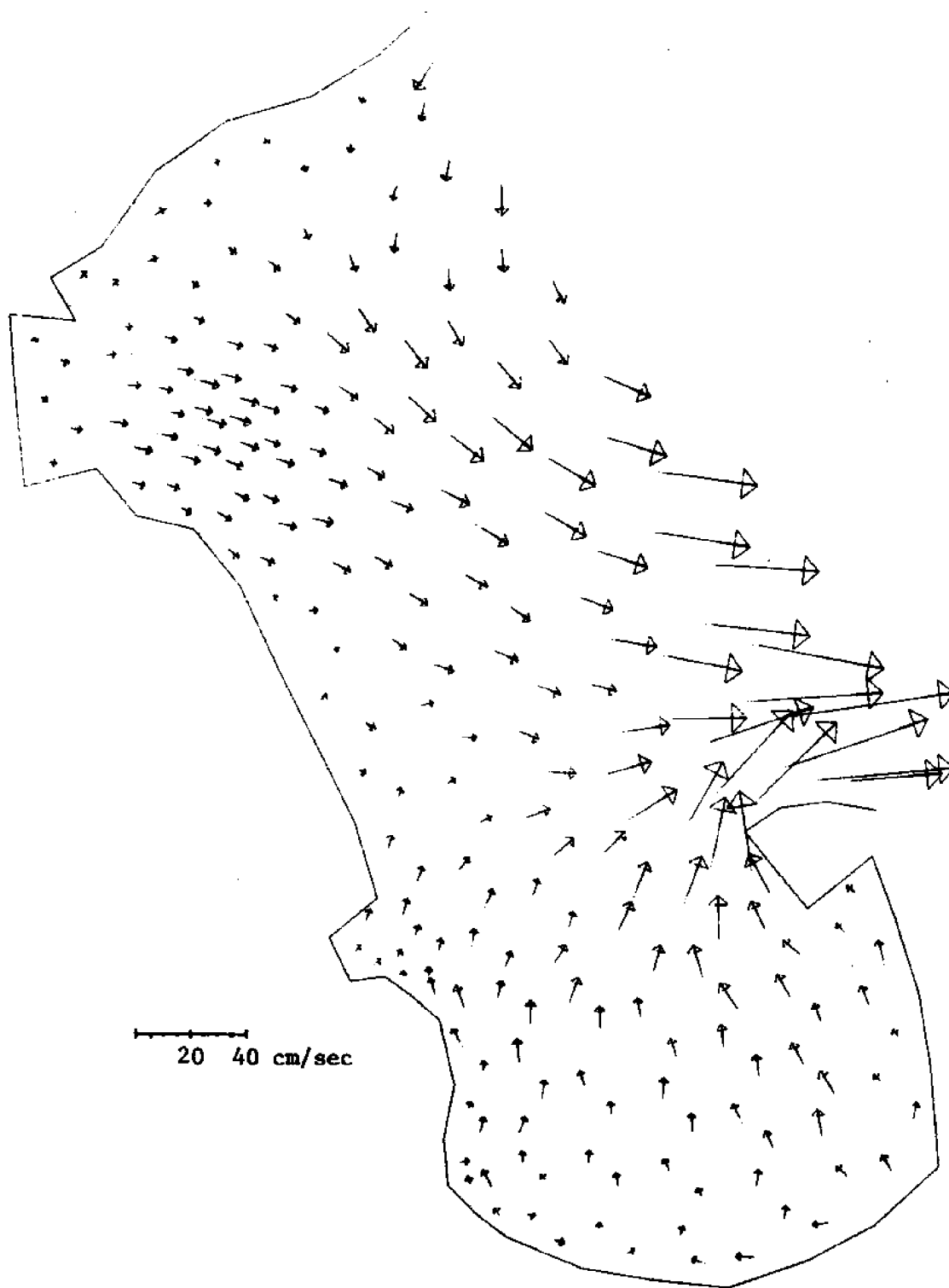
Figure 8-9. Computed tidal currents in Mass Bay. t=120000 sec=
T/6 after high tide.
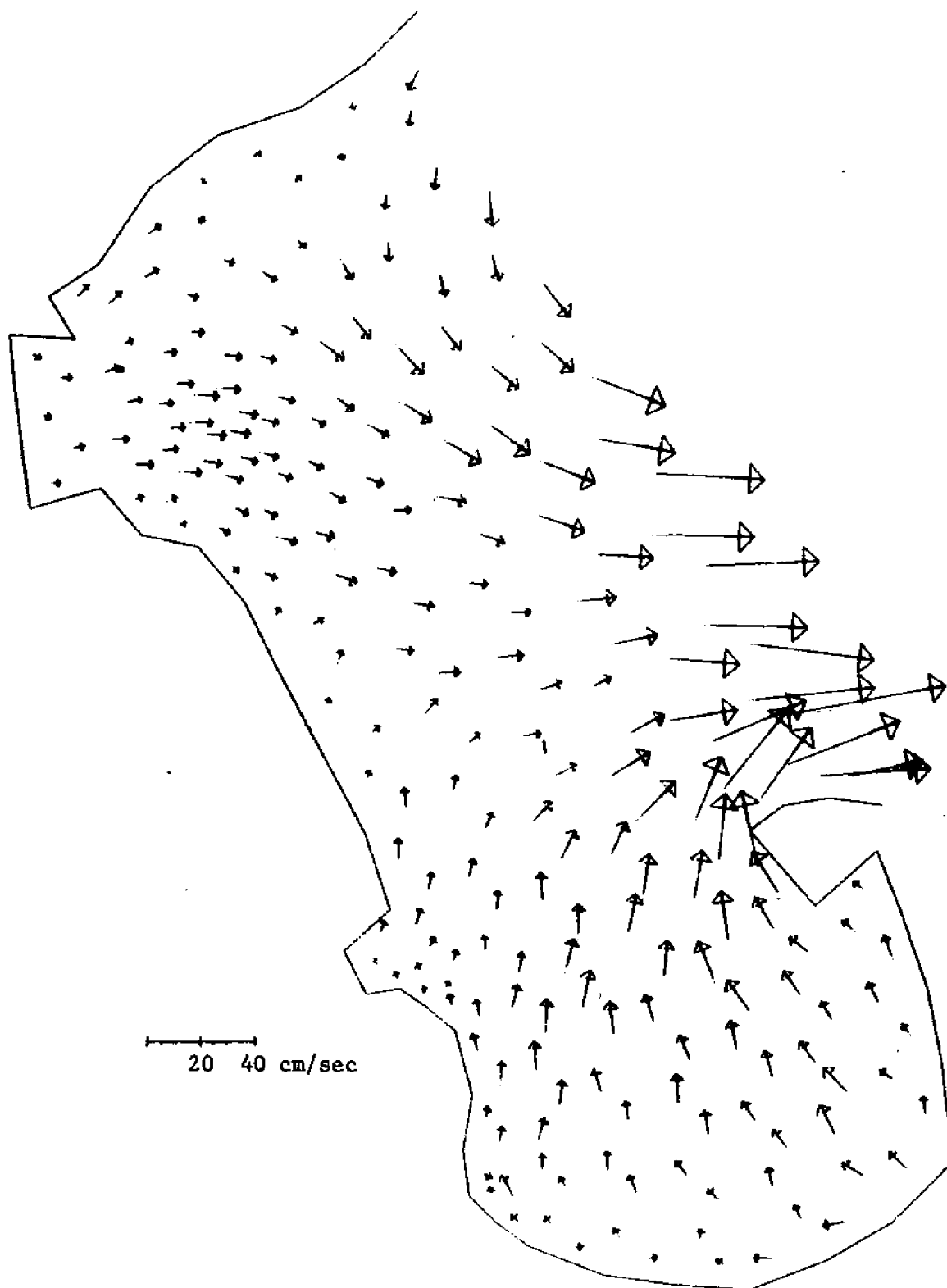
Figure 8-10. Computed tidal currents in Mass Bay. t=127500 sec=
T/6 before low tide.

166

numbers are in m.

Figure 8-11. Surface contours at high tide.
(112,500 sec. after cold start.)

167
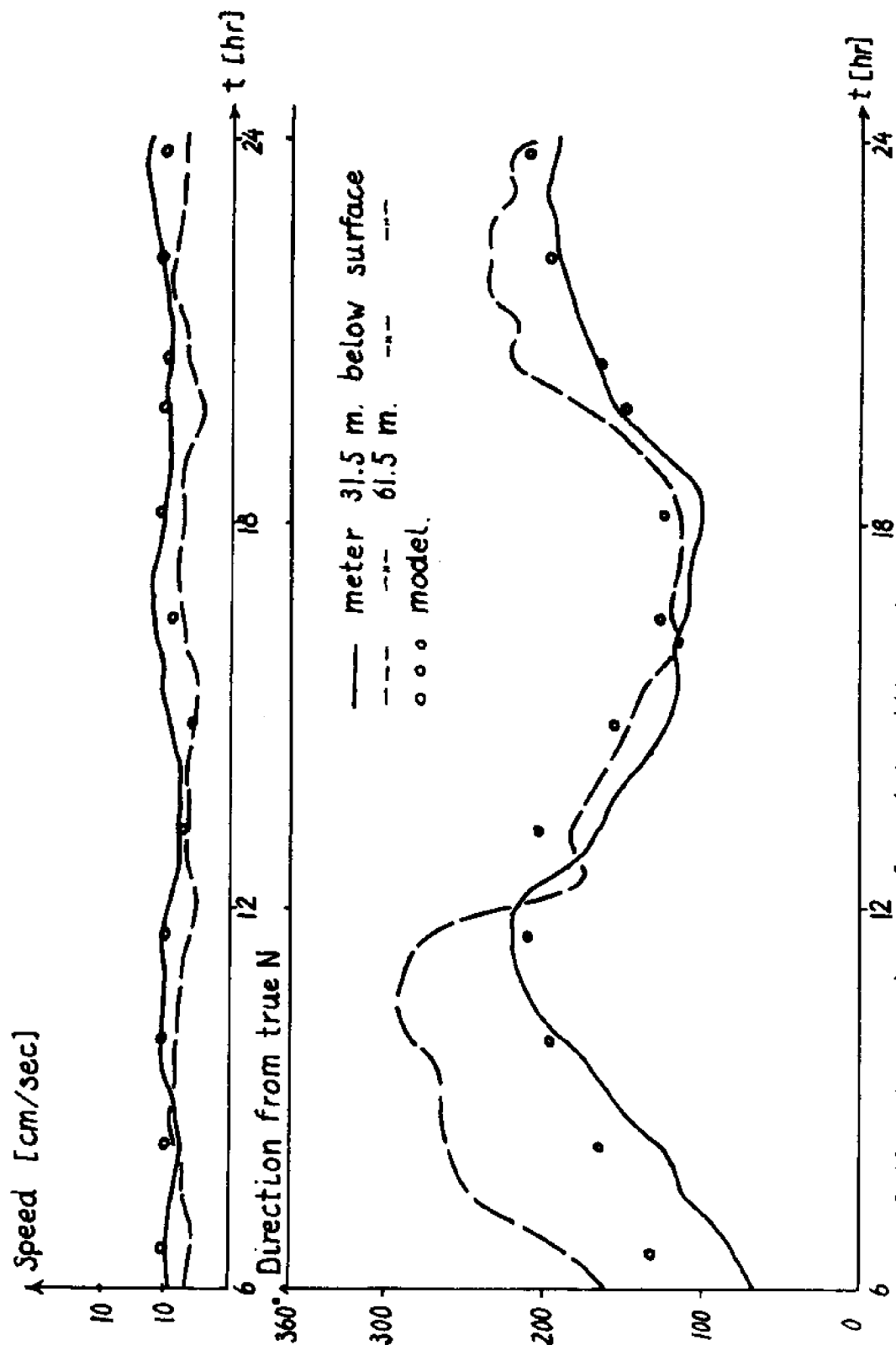
Figure 8-12. Comparison of model with foul area current meter station. Jan. 28, 1974
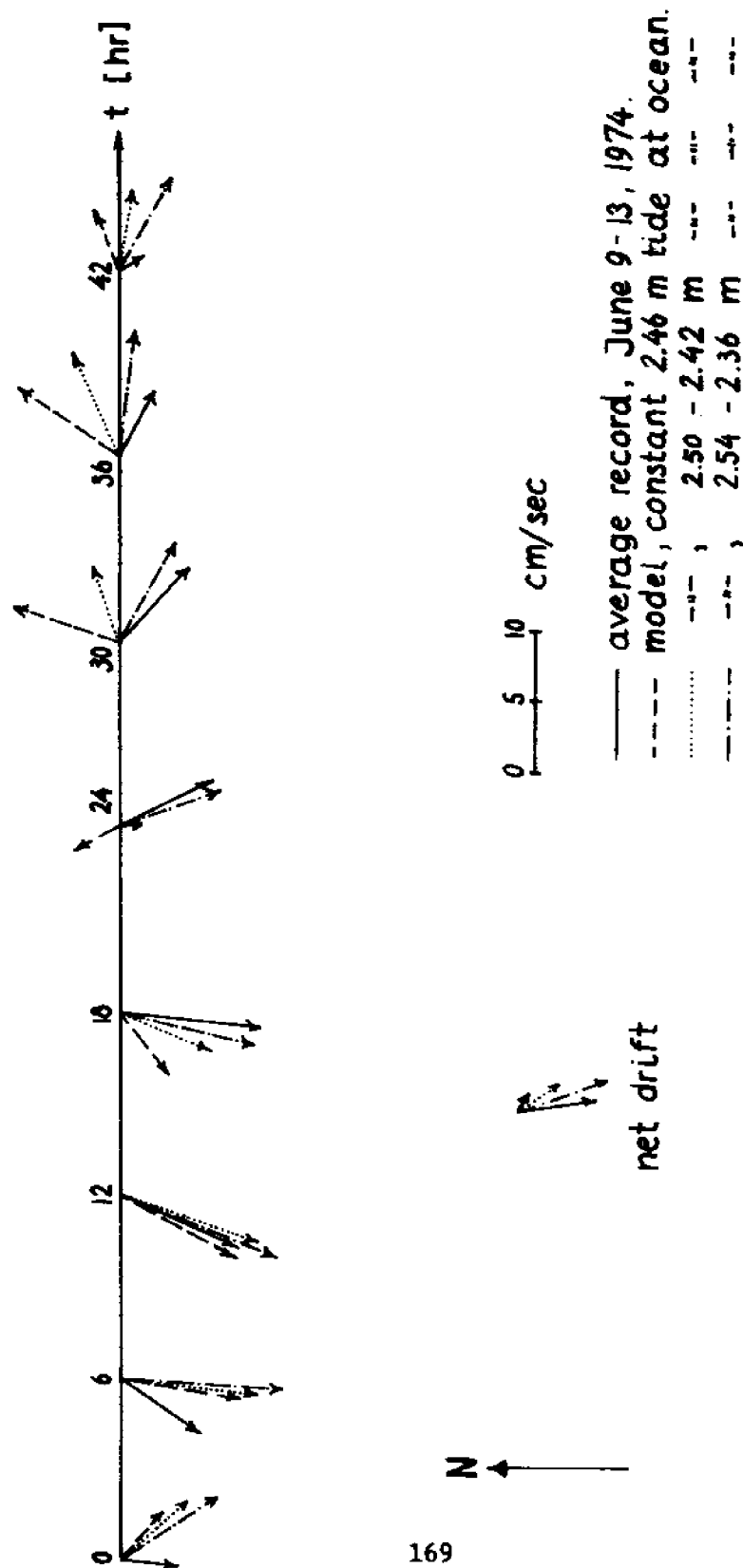
Figure 8-13. Comparison of velocity vectors and net drift at current
meter station 6.

Legend (as shown in figure):

t [hr]

cm/sec
0   5   10

—— average record, June 9-13, 1974.
---- model, constant 2.46 m tide at ocean.
⋯⋯ , 2.50 - 2.42 m
-·-·- , 2.54 - 2.36 m

net drift

N

169
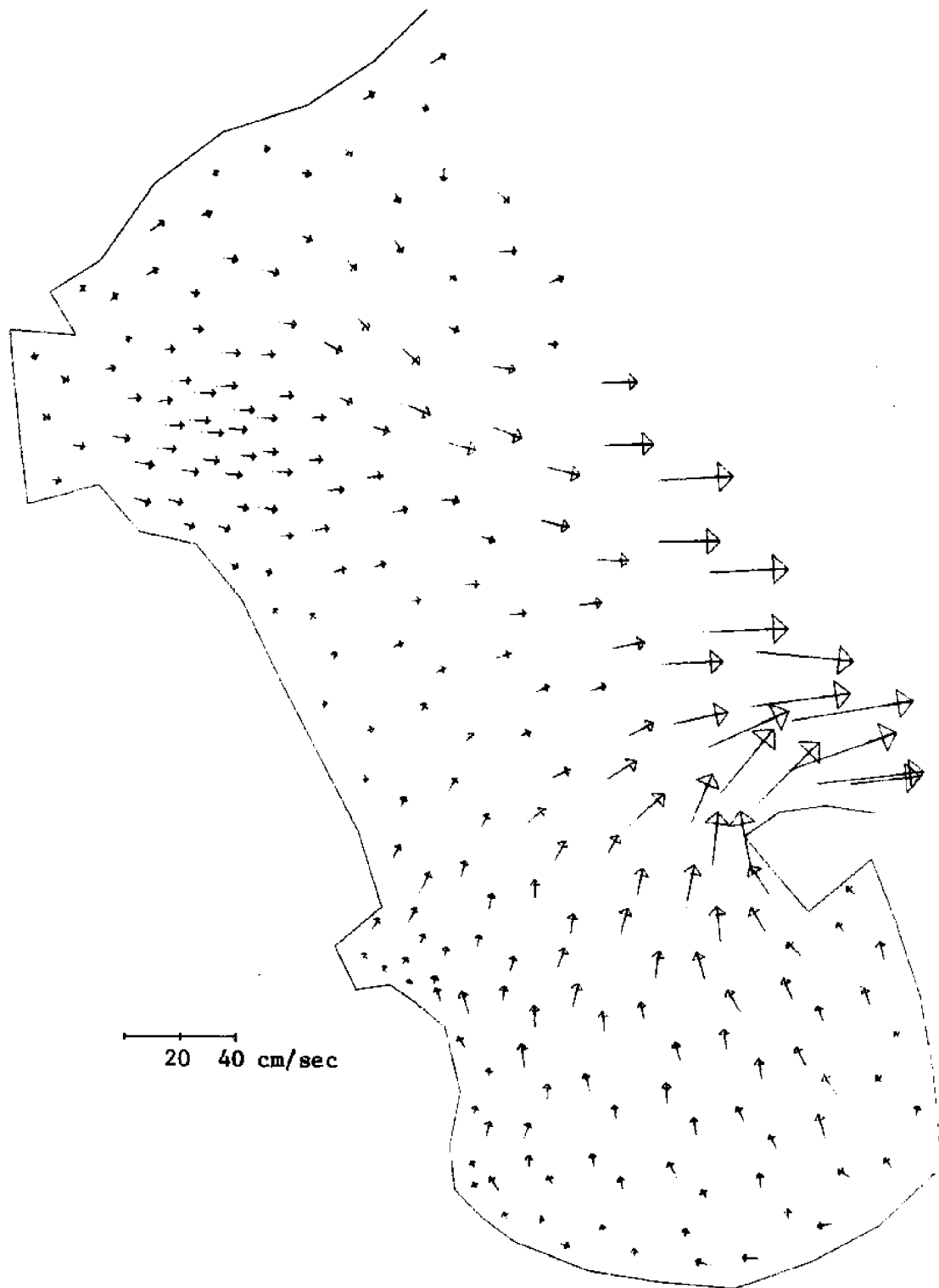
Figure 8-14. Computed tidal currents in Mass Bay, with an imposed
north wind of approximately 10 knots, $(\tau_y/\rho_o =$
$-0.0000286 \ m^2/sec^2)$. t=120000 sec=T/6 after high tide.

170
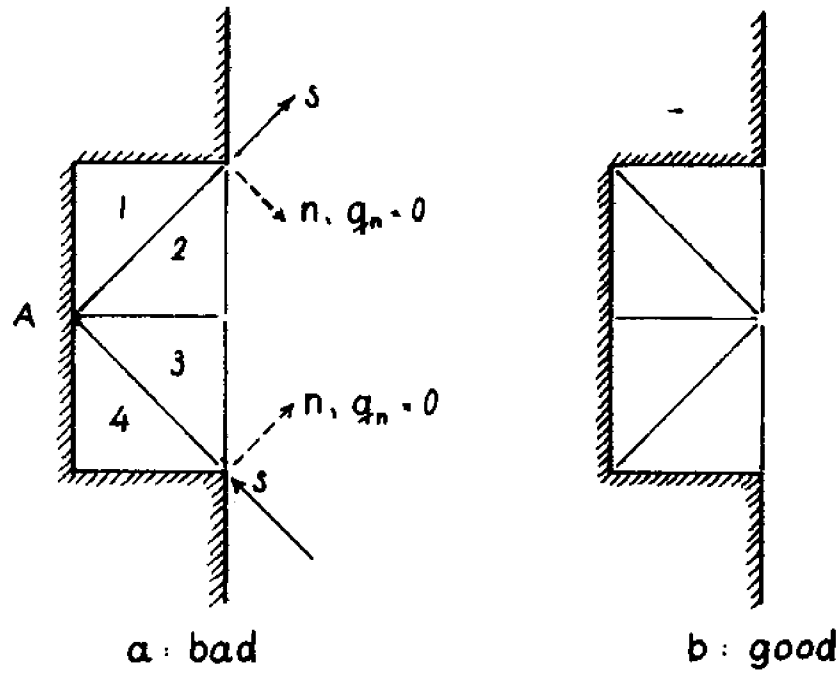
Figure 8-15. Grid layouts.
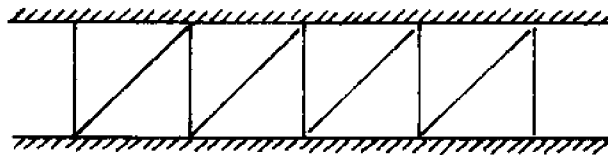
Figure 8-16. Example of invalid grid.

171

Another example is demonstrated in Figure 8-16. Although the channel shown is capable of transmitting flow in the longitudinal direction transversal flow is made impossible. Since the grid is unsymmetric, it will cause the water surface to slope transversally. This slope can grow in time since it is never equalized by transversal flow. The channel examples of Chapter 7 also had this fault, which was overcome by averaging over a cross section. To really avoid this problem, at least two rows of elements should always be used.

8.3 INTERNAL SOURCES

In the second case study, the tidal flow and the hypothetical circulation induced by a once through cooling water system in the West Passage of the Narragansett Bay is computed. The intent is to estimate the influence on existing flow patterns of the cooling water intake and discharge system of a hypothetical nuclear electric generating station located at Rome Point (see Figure 8-17).

To determine the undisturbed tidal flow, model boundaries were created north and south of the site and strip chart recording tide gauges of the bubbler type were installed to provide boundary conditions. Lack of time and funds were the reasons for using these rather crude gauges with inherent poor accuracy. After 6 weeks of field sampling, the data showed large daily variations in tidal ranges and relative phases. Considering all observations, an average lag time at Plum Beach referred to Quonset Point was found to be $+11 \rightarrow 12$ minutes. The data also show differences in mean wave heights between the gauge

172

Scale: 1:80000

| 0 | 1 | 2 | 3 | 4 | 5 | 6 | 7 | 8 | 9 | 10000 m |
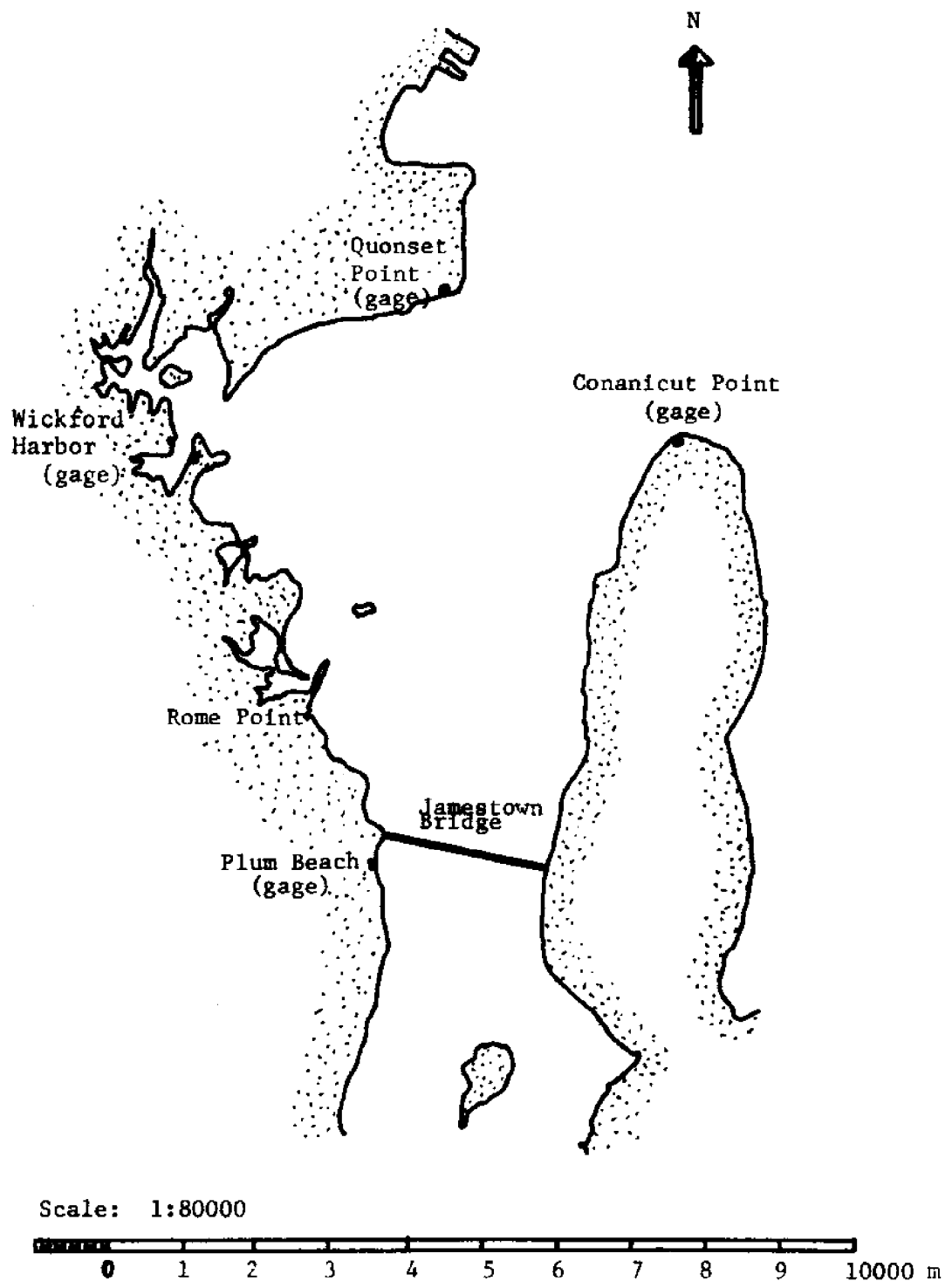
Figure 8-17. Rome Point study area.
West Passage, Narragansett Bay,
Rhode Island

locations. However, compared with the likely error of ±5 cm for the recorders, these differences are insignificant. Mean wave heights ranged between 104 cm and 111 cm over the area. The recorded maximum and minimum wave heights were 1.6 m and 0.55 m.

The two open boundaries were forced as sinusoids according to (8.2.1) with the southern boundary lagging 12 minutes behind the northern boundary. Figure 8-18 shows the grid and Table 8-1 lists the parameter values for tidal computations.

a	=	0.52 m
T	=	45000 sec.
latitude	=	41°55 N
C_f	=	0.0063
NMNP	=	103
NMEL	=	166
Δt	=	50 sec.

TABLE 8-1: Parameter Values for Rome Point Tidal Flow

As usual, the initial condition was taken to be no motion at t = 0, and the Runge-Kutta method was used. After less than half a tidal cycle, the influence of the initial condition had disappeared, as for Mass Bay. Figures 8-19 to 8-22 show the resulting flow fields at various stages of the tide. The magnitude of the currents agree well with current meter data taken by U.S. Coast and Geodetic Survey. It must however be emphasized that the results presented are typical

174
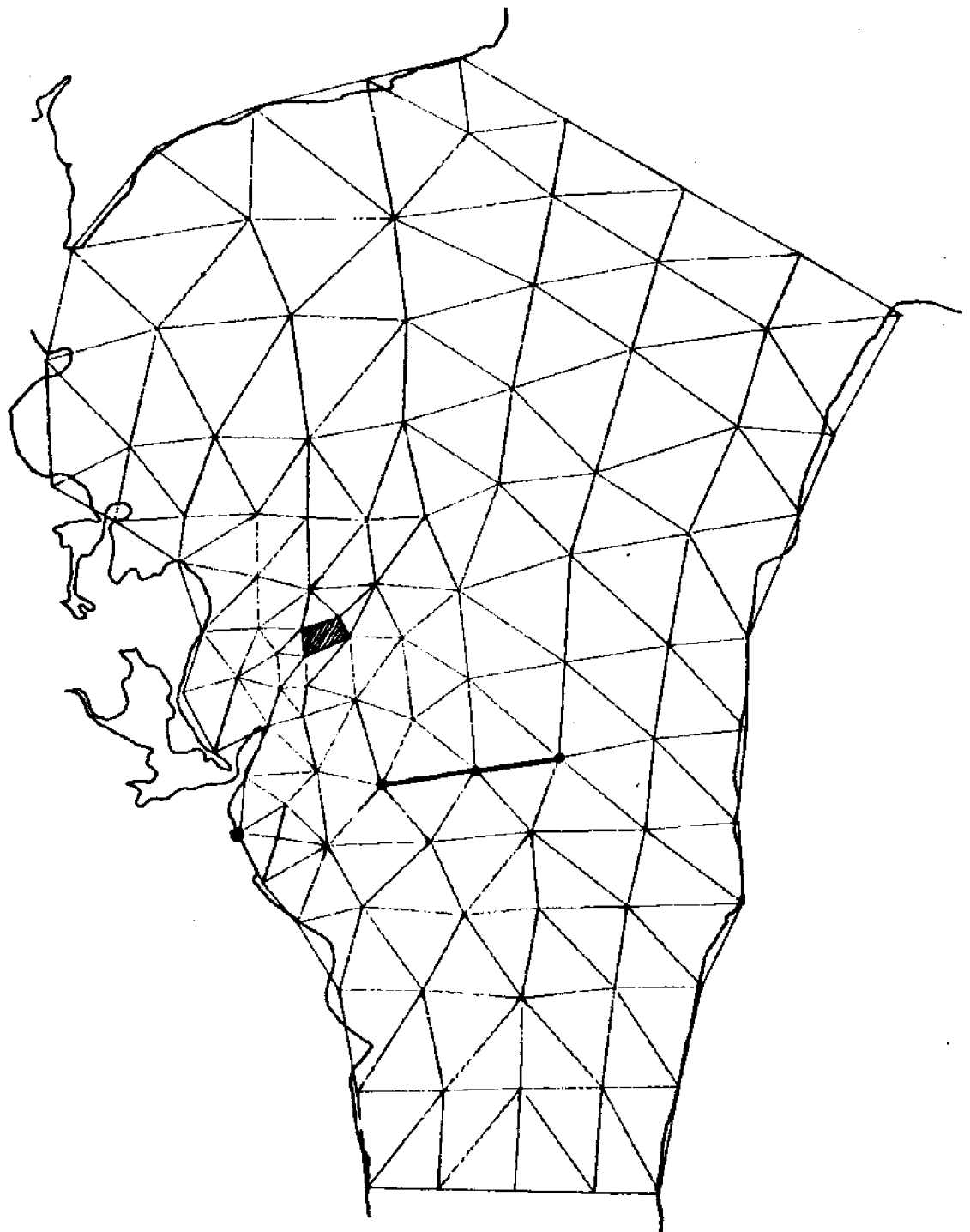
Figure 8-18. Finite Element Grid Layout. The Proposed Locations
of Intake Channel and Diffuser Pipe are Indicated

175
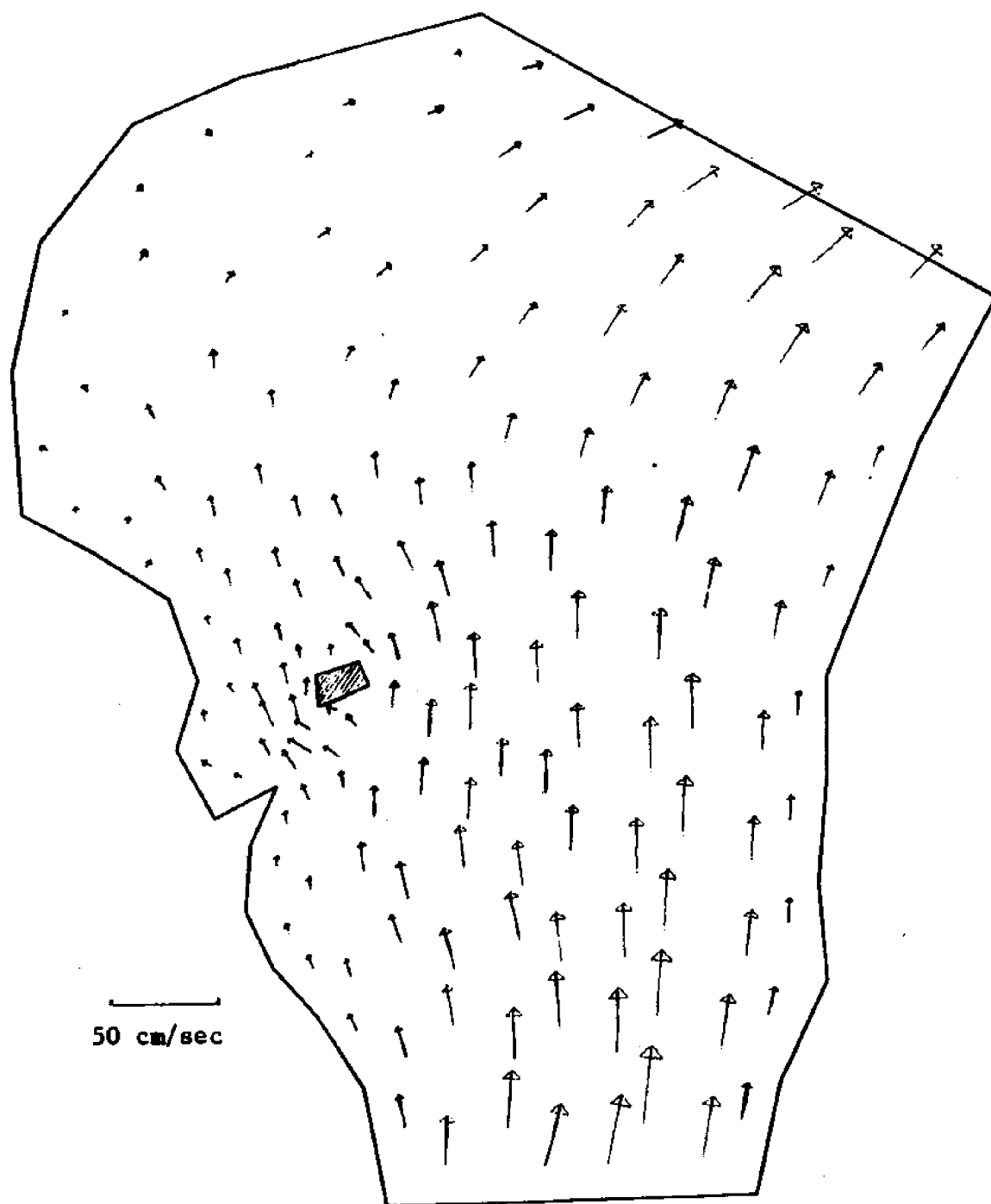
Figure 8-19. Computed tidal currents in West Passage.
Low Tide.

50 cm/sec
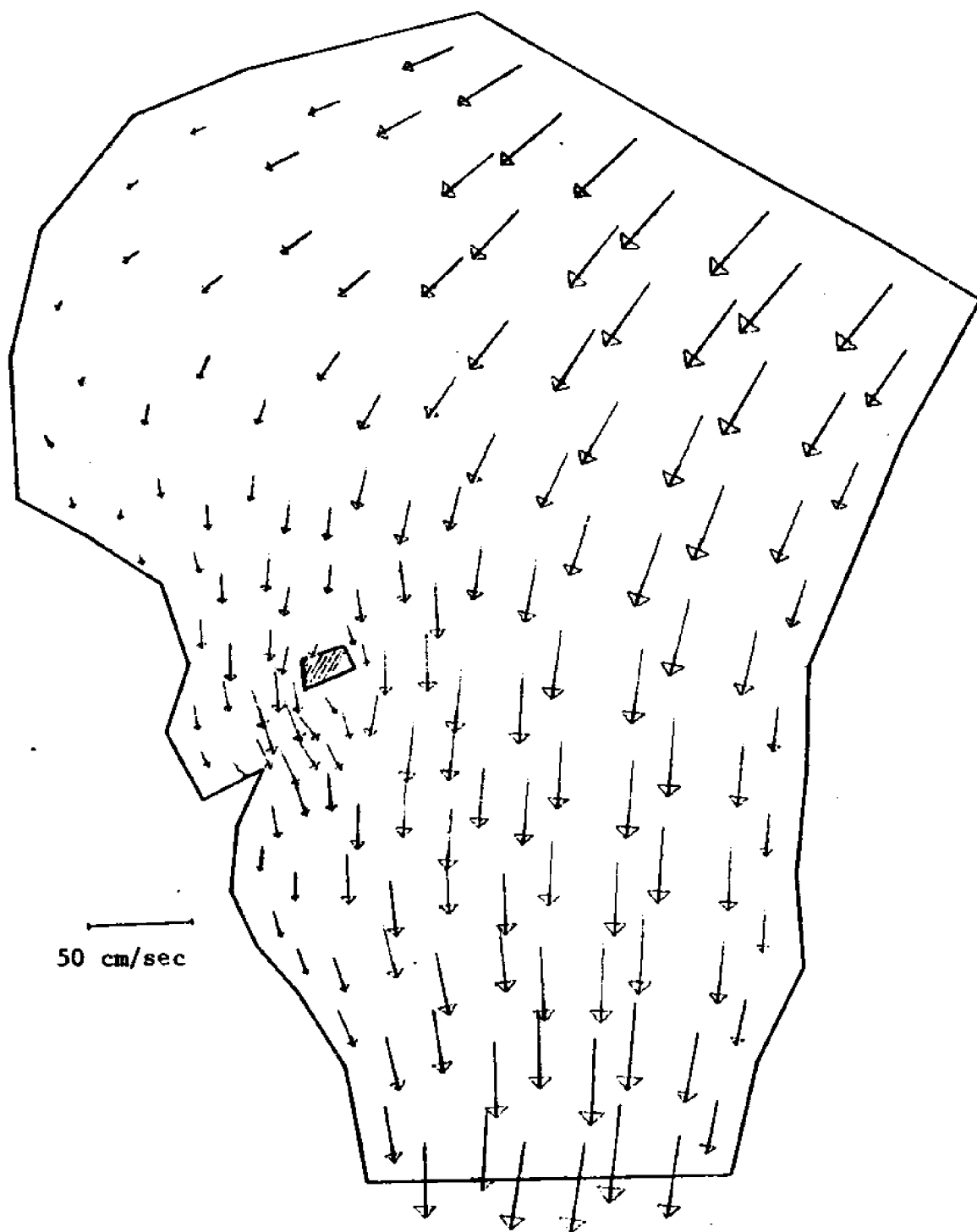
Figure 8-20. Computed tidal currents in West Passage.
T/4 after low tide.
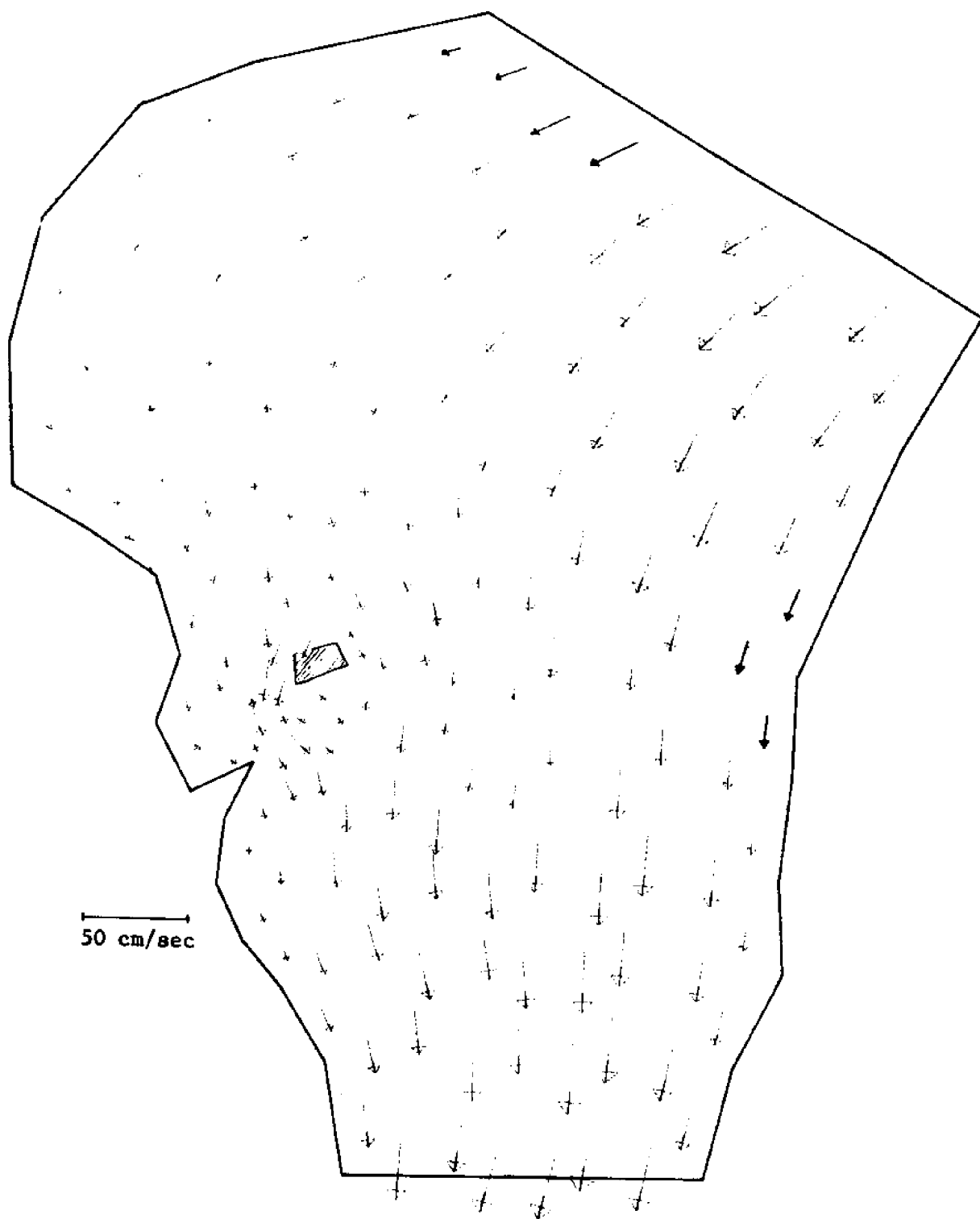
Figure 8-21. Computed tidal currents in West Passage.
High tide.
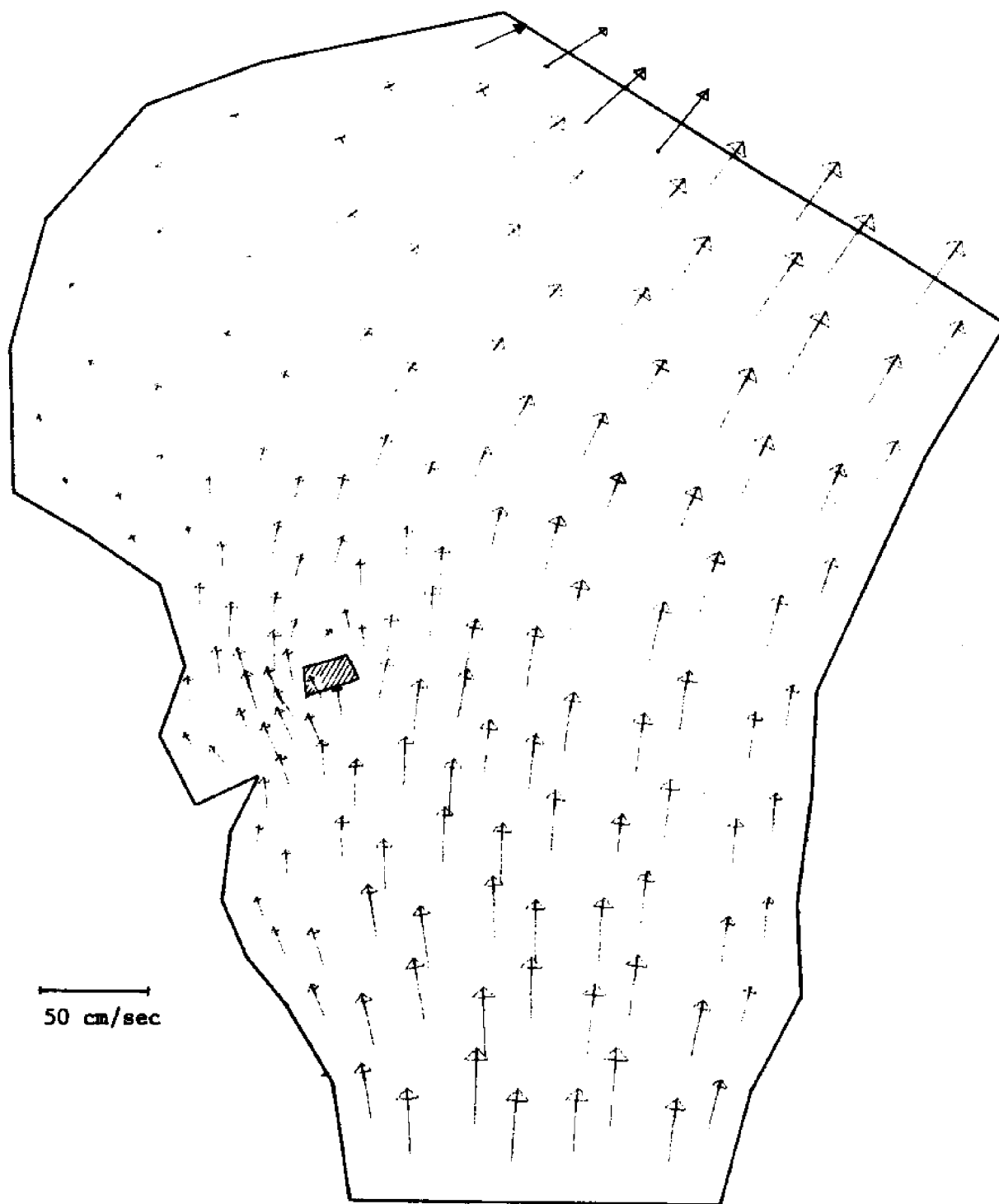
Figure 8-22. Computed tidal currents in West Passage.
T/4 after high tide.

179

average values for a 6 week period and that much daily and seasonal variation can be anticipated. Thus the current tide table [72] states that the currents in the area are too random to predict.

The proposed cooling system for the plant would have an intake channel and a diffuser discharge pipe located as shown in Figure 8-18. The estimated flow rate is 1350 cfs (38.23 m^3/sec) which we assumed was distributed evenly over the length of the diffuser,although the depth varies somewhat in that area.

At the time of this study, the possibility of prescribing a non-zero boundary discharge had not been developed. Consequently, we decided to model the intake as a sink, since a source feature would have to be implemented anyway to handle the diffuser pipes. To get a better idea of the plant generated flow, the two open boundaries were closed and the tidal forcing excluded. In the first run, the intake was modeled as a point sink and the diffuser as a line source. The resulting current field showed a marked net flow towards the intake and total mass was clearly not conserved. At the time, considerable effort was expended before the problem was resolved as the spatial truncation error described in Chapter 5. Referrring to Equation (5.54), the inconsistency is however easily explained. A point sink is a physical idealization which, in mathematical terms, is expressed as a delta function, $\delta(x,y)$. However, $\delta(x,y)$ does not belong to the admissible function space for which (5.54) was derived, assuming the data to be smooth, i.e. square integrable. From the knowledge that $|\delta(x,y)|^2$ is infinite, one can therefore not conclude that the error

is infinite. As a matter of fact, we have here exactly the case where a node and a discontinuity in the data coincide. The error is hence not predictable; but intuitively one would expect it to be very large. Conceptually, the use of δ-function loads is also a bad choice, since the L_2 norm is infinite, it is difficult to assure that the solution is convergent and unique.

In the first computations, the truncation error was obviously too large. Acting as false sources it completely obscured the results and also explains why mass was not conserved. To overcome this problem, the strategy was changed to spreading the loads over a small area and the grid was furthermore refined slightly at the intake. Figure 8-23 shows the equivalent distribution of point sinks used. To model the plant outflow it was assumed that the dilution of the diffuser flow was proportional to the local water depth. The rate of volume addition and its spatial distribution is shown in Figure 8-24. With this loading strategy, mass was conserved and the induced flow pattern is shown in Figure 8-25. On the basis of this result it was concluded that the plant generated flows were insignificant compared to the tidal flow and especially its daily variations (note the different velocity scales). No attempt was therefore made to run the model for the combined situation of tidal flow with operating plant.

The flexibility of the finite element grid was particularly useful in this case. The cooling water generated flow was modeled without considering buoyancy effects using the Runge-Kutta method at $\Delta t = 40$ sec. After approximately 600 sec. the solution had essentially reached its
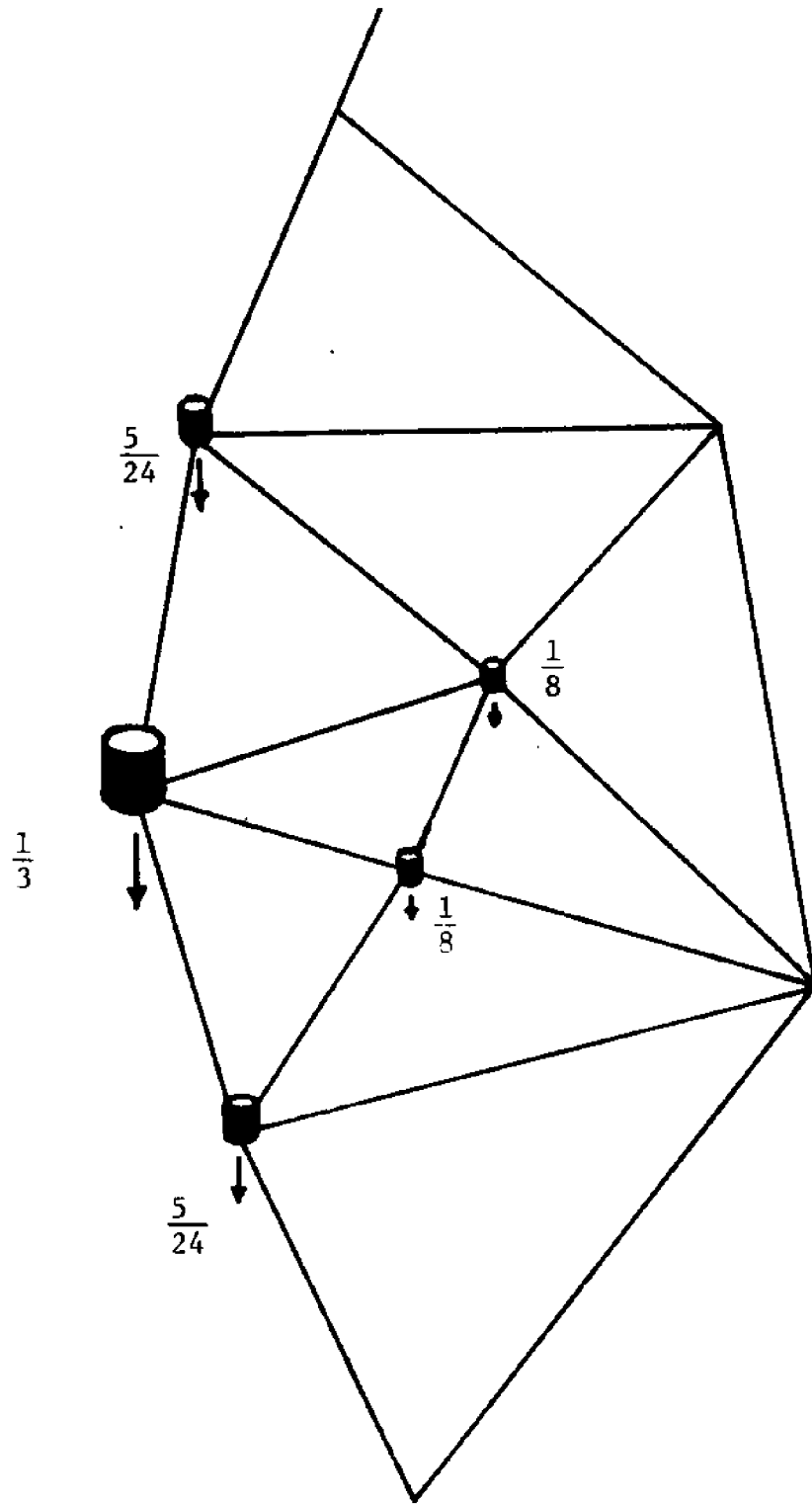
Figure 8-23. Intake Channel Modeled as 5 Discrete Sinks

182
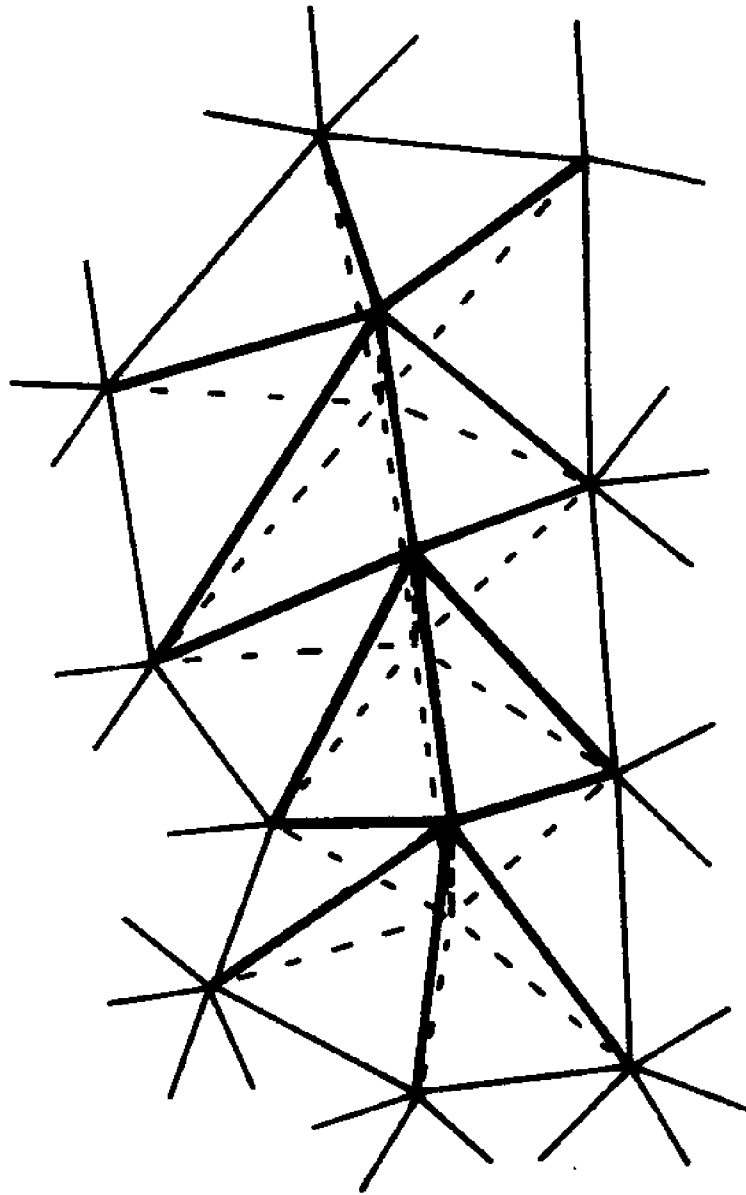
Figure 8-24.   Diffuser Flow Modeled as Distributed
Volume Source.   The Source Strength
is Represented by the Sketched "Roof-
structure".
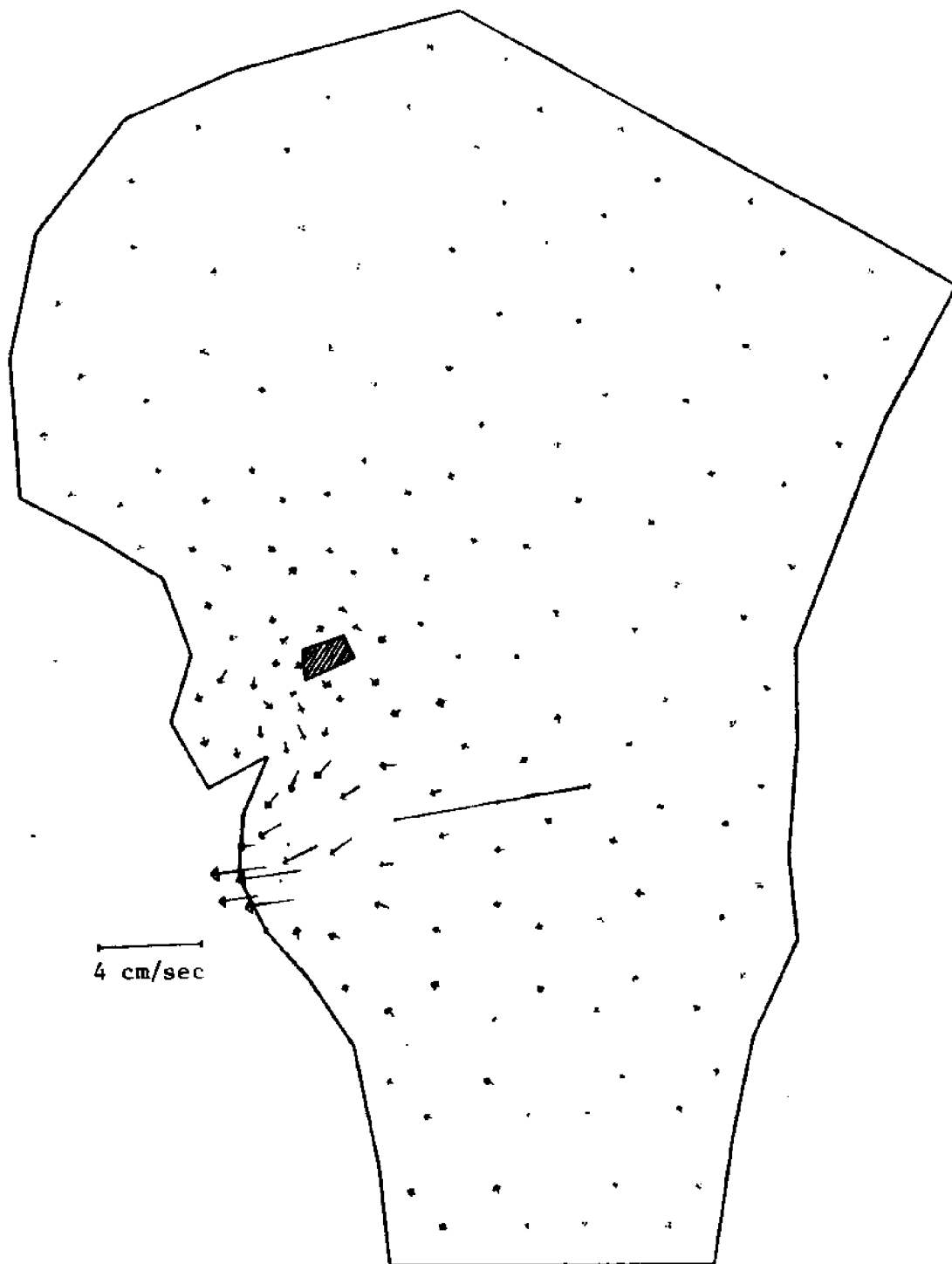
Figure 8-25. "Once Through" System.   Currents
680 sec. After Start-up

184

steady state everywhere, however some small oscillation around the mean value was noticeable.

8.4 PRESCRIBED DISCHARGES

The last important forcing situation we consider is the prescribed discharge boundary which could be a river but in this case is a tidal inlet. The concern is directed towards the proposed Atlantic Generating Station, AGS, located on the New Jersey Coast approximately 3 miles out from Beach Haven and Little Egg Inlets, see Figure 8-26. The tidal flow in the area and the influence of the plant must be determined. The two tidal inlets transmit significant flow and must be included. However, rather than modeling the inlets which extend far inland,   we have measurements of the velocities and discharges at the entrance of both inlets [44] which may be used for boundary conditions. At this time, work is still progressing on the project. Figures 8-27 and 8-28 show the grids in use. The coarse grid covering the larger area has the primary purpose of establishing boundary conditions for the finer grid which is used to study the circulation in more detail. The coarse grid have been used to solve the tidal flow with prescribed discharges at the inlets (Figure 8-29). The boundary at the continental shelf is forced as a sinusoid of amplitude 0.9 m. The two boundaries running from the shelf to land are assumed to be impermeable smooth walls. The lack of data make this crude approximation necessary. If the problem is well posed and the boundaries are far enough away from the area of interest, the results are hypothesized

185
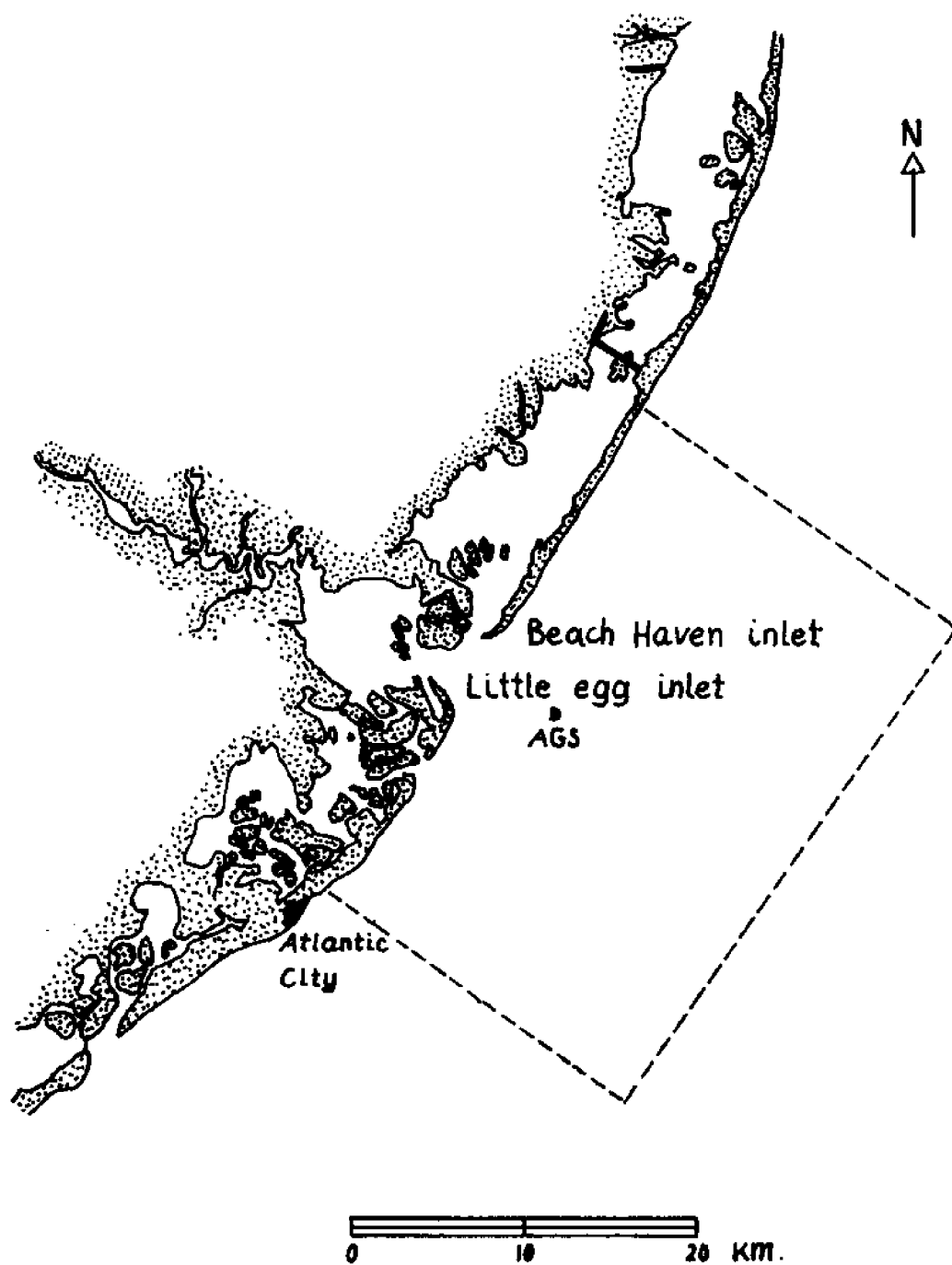
Figure 8-26. Atlantic generating station, AGS, site.
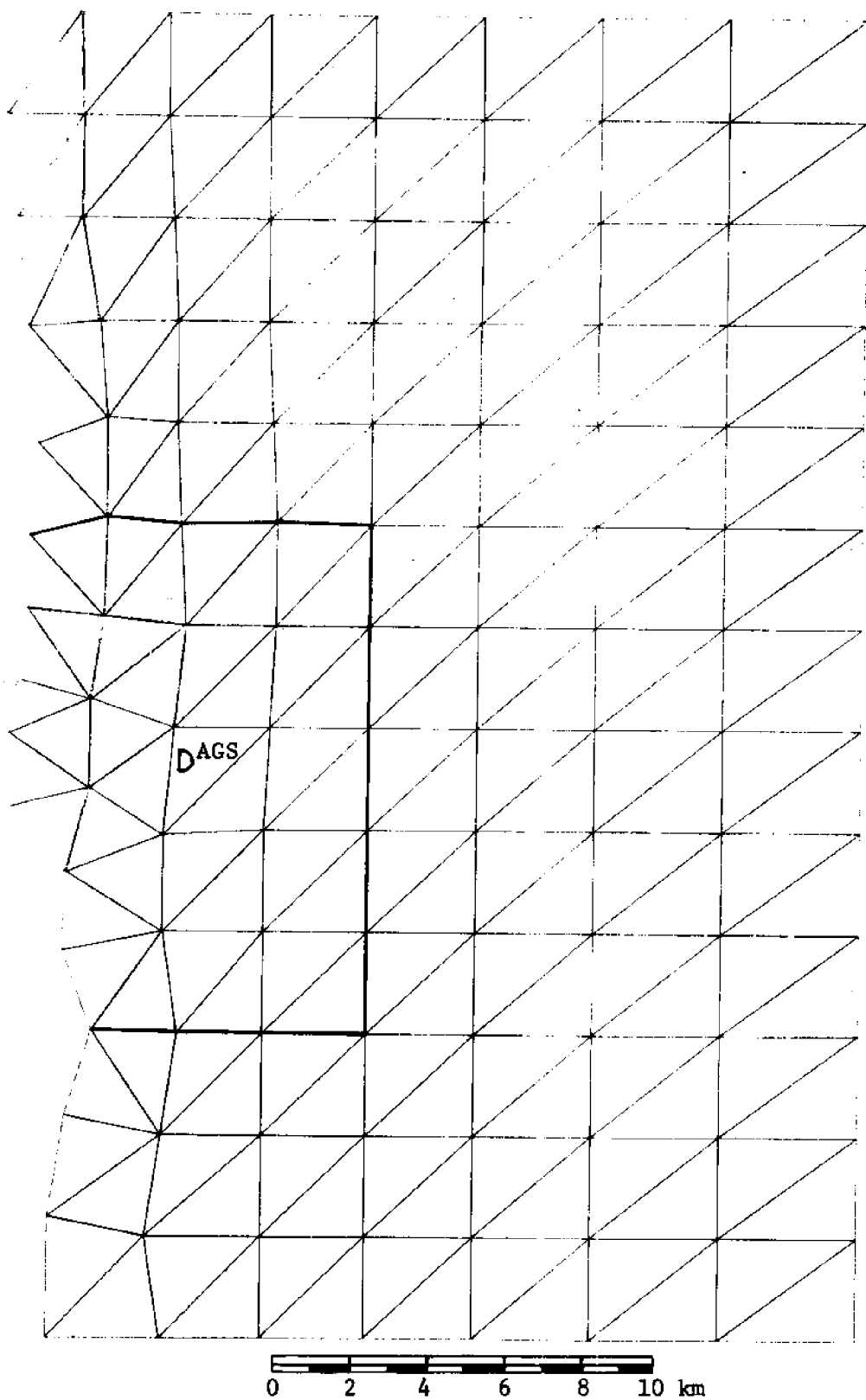
Figure 8-27. Coarse grid for circulation study at AGS. The
perimeter of the fine grid is indicated.   187
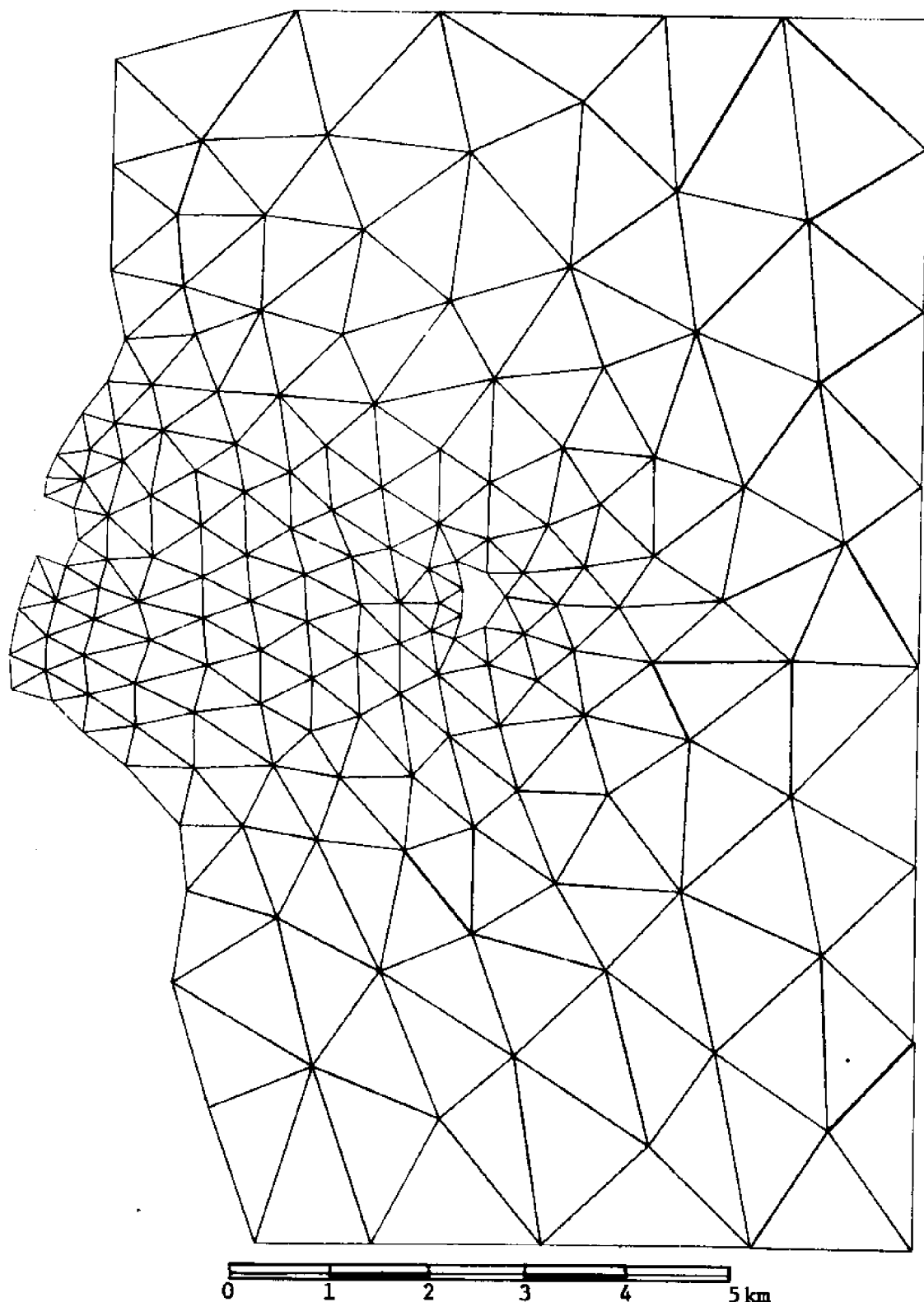
Figure 8-28. Fine grid for circulation study at AGS.
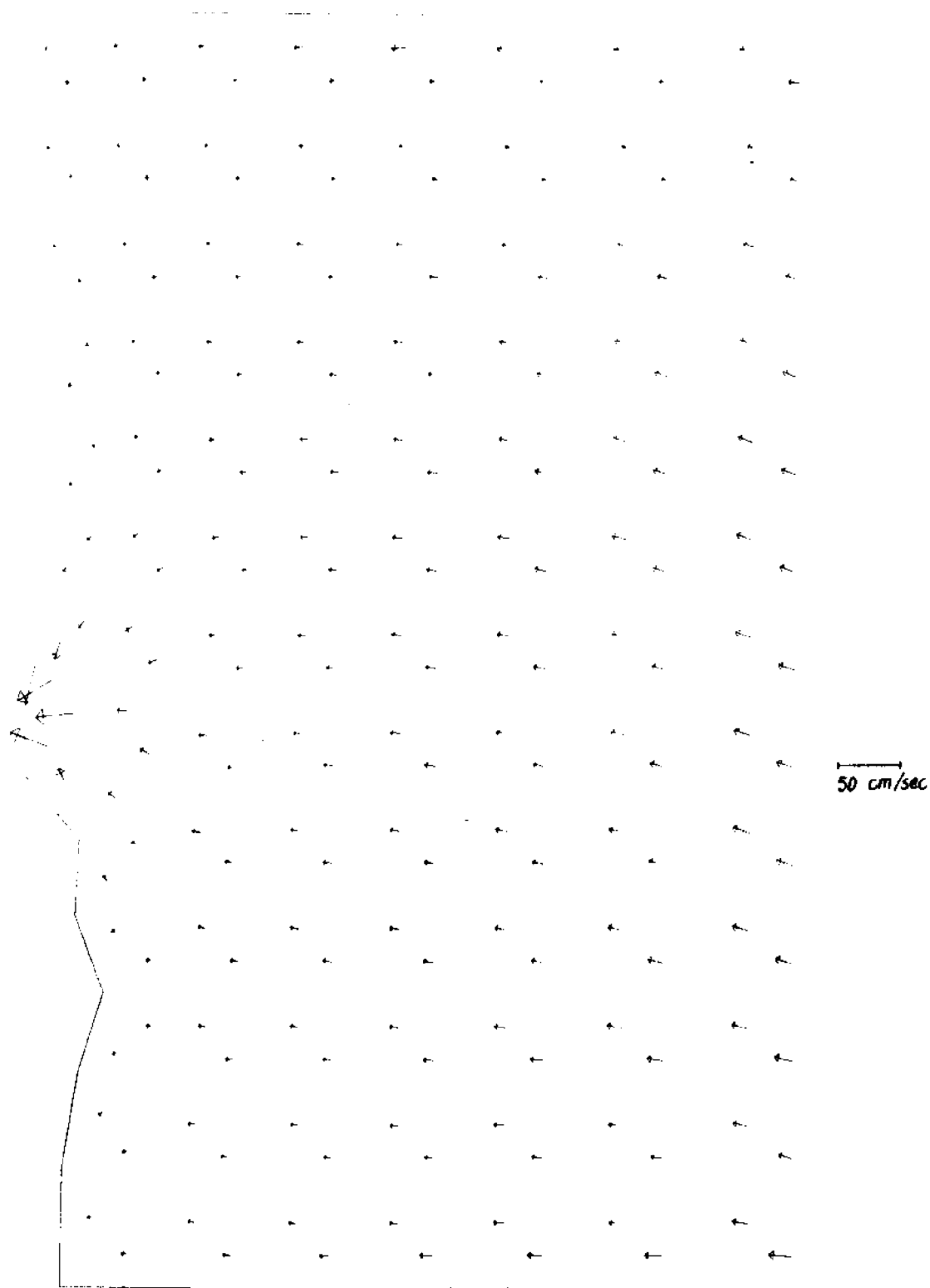
Figure 8-29. Large scale tidal circulation at AGS. Computed currents.

189

to be rather insensitive (guidelines b). At the land boundary, the normal discharge was prescribed zero except at the location of the inlets. Here a sinusoidally varying total discharge of approximately 3600 m^3/sec was prescribed such that high water slack occurred an hour after high tide at the shelf. The split time scheme with t = 100 sec. was used.

The fine grid has so far only been used to study flow induced by the actual discharges through the inlets. The sea surface at ocean boundaries was assumed fixed and the discharges through Little Egg and Beach Haven inlets were assumed to vary sinusoidally in time with maximum discharges of 2500 m^3/sec and 2000 m^3/sec. Figure 8-30 shows one resulting plot of velocities. The computational time step was $\Delta t = 30$ sec.

Field measurements will be used for boundary conditions and to verify the models. The coarse and fine grid models will be "patched" together to predict the complete tidal circulation in the neighborhood of the proposed generating site.

A point of warning is issued with respect to prescribed discharges. Referring to a hypothetical example shown in Figure 8-31 it is tempting to prescribe magnitude and direction of flow at nodes A, B and C. Although this seems reasonable it will, in most cases, lead to impossible situations where the sea surface has to be displaced large distances to satisfy equilibrium. The correct way is to prescribe only the normal discharge and allow the tangential free to adjust, at least at B and C.
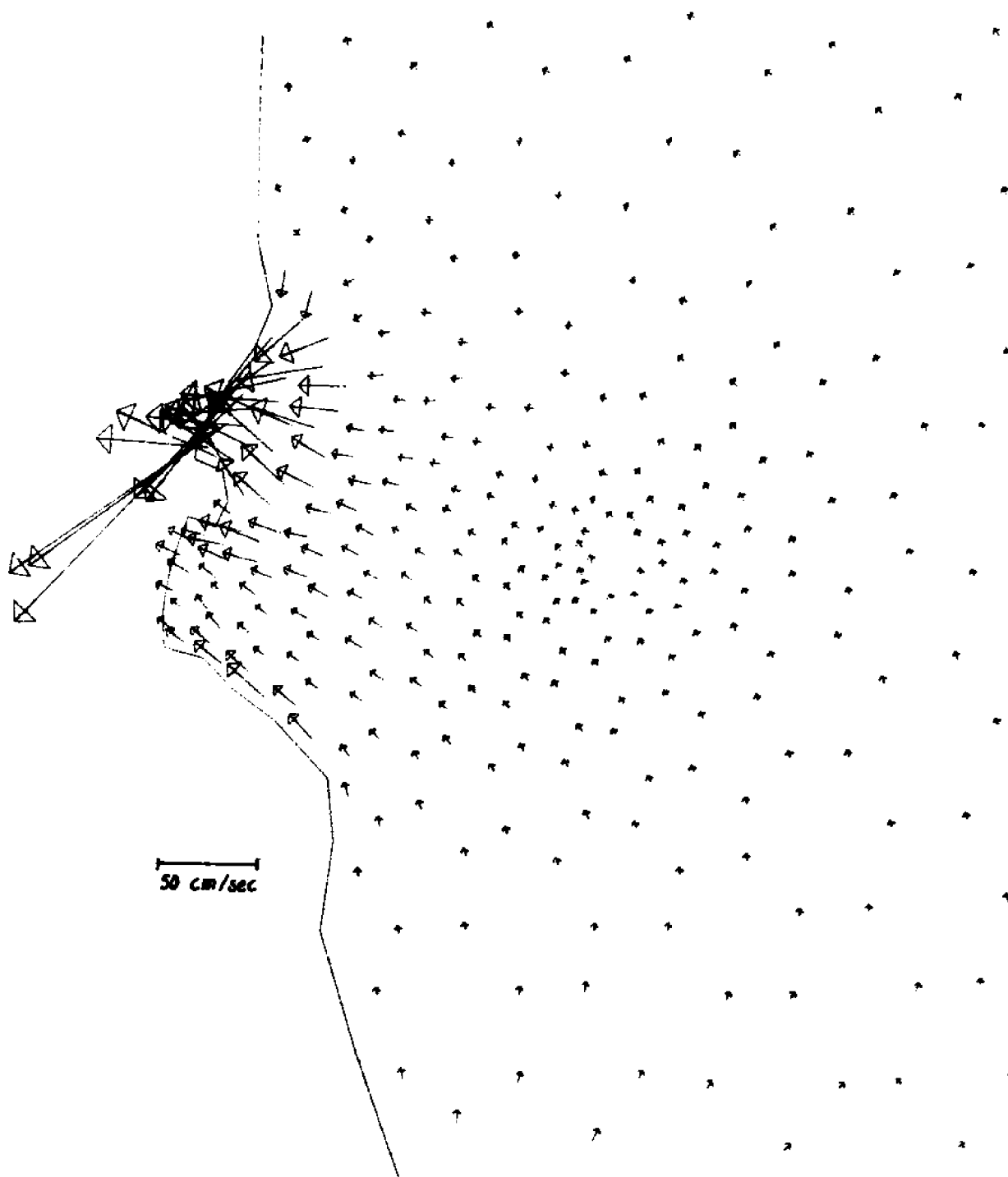
Figure 8-30. Small scale circulation at AGS. Prescribed inlet discharge only.
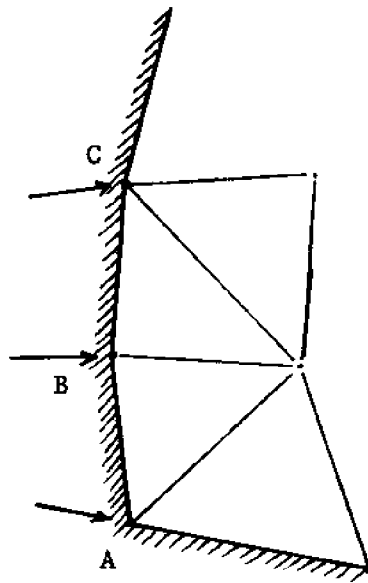
Figure 8-31. Specification of discharge.

As a final point, it is noted that for the triangular linear elements the best accuracy is obtained at the centroid of the triangle. This is due to the fact that in the interior of an element the trial functions are smooth, i.e. they have derivatives, which is not the case on element boundaries. When interpreting results, it is therefore better to use the element centroidal values, as we have done in the presented studies.

On an IBM 370/158 machine the solution of a problem with 225 elements, 150 nodes and 450 time steps takes approximately 112 sec CPU time and uses 180 K bytes of storage.

CHAPTER 9

REVIEW. MULTI-LAYERED MODELS

The basic difficulties in attempting a fully three-dimensional model are the parameterization of the constitutive equations and specification of the boundary conditions. By requiring better accuracy of the models, we must also be prepared to provide more accuracy in the applied loads, such as wind fields and tidal forces. It is even more obvious in this case that prescribing only the surface elevation at the ocean boundary is not sufficient. The actual velocities and their time variation must be known. Although none of the existing reports on three-dimensional models, or for that matter multilayered models, discusses these problems, it appears that these models at best are descriptive. The models must be calibrated before use by adjusting parameters such that actual field measurements are duplicated. Even though the usefulness of these models is somewhat reduced in this way, they can have significant impact on establishing trends and to help organize field monitoring programs.

The only attempt on modeling three-dimensional flow is outlined by Leonard and Melfi [40]. They propose a steady state finite element model for lake circulation without stratification. Their primary objective was to discuss the numerical framework on which a model could be based. Thus they present no results! Assumptions of incompressibility and hydrostatic pressure apparently led them to the equations

$$(9.1) \quad \frac{1}{\rho} (\tau_{xx,x} + \tau_{yx,y}) - f\,v + 0$$

$$(9.2) \quad \frac{1}{\rho} (\tau_{xy,x} + \tau_{yy,y}) + f\,u = 0$$

193

(9.3) $u_{,x} + v_{,y} + w_{,z} = 0$

with

(9.4) $\frac{1}{\rho} \tau_{ij} = -g(\eta-z) + \varepsilon(u_{i,j} + u_{j,i})$ $i,j = x,y$

and ε is a horizontal eddy viscosity coefficient. In the equations of motion, the convective inertia and the vertical momentum transfer terms are neglected. The latter assumption makes it impossible to handle a wind stress on the surface. Even if the stated problem can be solved by the proposed Newton-Raphson iteration technique, which yet has to be shown, the model utility is very limited.

We quickly turn towards more meaningful works on multilayer models. Simons prepared a report on lake circulation [65]. A multilayer formulation is derived using vertical integration over each layer which can be physical or imaginary. The density is assumed dependent on temperature only and the energy equation is used to find the temperature field.

The usual assumptions of hydrostatic pressure, incompressibility and small density variations are made. The layer interfaces are either assumed fixed (imaginary) in which case the vertical velocity is computed or movable material surfaces (physical) implying a computation of the displacement.

The governing equations are the vertically integrated conservation of mass and horizontal momentum equations for each layer. The problems of interfacial shear and mixing or boundary conditions are not discussed. In the case where the density stratification becomes unstable,

194

a strategy is suggested in which the water column is mixed instantaneously. The major parts of the report are devoted to discussions of a numerical solution technique. Finite differences are used with a leap frog (time centered) time integration scheme. Since the leap frog method leads to instability for dissipative terms, these are handled by simple forward differencing. A time averaging process may also be necessary to avoid the solution splitting characteristic of the three level leap frog method. Several schemes for the spatial differencing are tested as mentioned in Chapter 2. The accuracy of the results are found to be sensitive to the orientation of the grid in relation to the boundaries of the basin. For the model employing two space grids simultaneously, considerable grid dispersion is noticed starting at the boundaries where the two grids necessarily differ. No multilayer computations are presented; but work is apparently progressing in that direction along with extensive field measuring programs.

Along the same lines, Leendertse et al developed a three-dimensional model which really is a vertically integrated,layered model [39]. The water mass is assumed incompressible and the density is a function of salinity only. The equations of motion for layer k are:

$$(9.5) \quad (Hu)_{,t} + (Huu)_{,x} + (Hvu)_{,y} + (wu)_{k-\frac{1}{2}} - (wu)_{k+\frac{1}{2}}$$

$$- fHv + \frac{H}{\rho} p_{,x} + (\frac{1}{\rho} \tau_{xz})_{k-\frac{1}{2}} - (\frac{1}{\rho} \tau_{xz})_{k+\frac{1}{2}}$$

$$- \frac{1}{\rho} (HE_x u_{,x})_{,x} - \frac{1}{\rho} (HE_y u_{,y})_{,y} = 0$$

$$(9.6) \qquad (Hv)_{,t} + (Hvu)_{,x} + (Hv^2)_{,y} + (wv)_{k-\frac{1}{2}} - (wv)_{k+\frac{1}{2}}$$

$$+ fHu + \frac{h}{\rho} p_{,y} + (\frac{1}{\rho} \tau_{yz})_{k+\frac{1}{2}} - (\frac{1}{\rho} \tau_{yz})_{k-\frac{1}{2}}$$

$$- \frac{1}{\rho} (HE_x v_{,x})_{,x} - \frac{1}{\rho} (HE_y v_{,y})_{,y} = 0$$

where k is 1 at the surface and increases down through the layers
to b at the bottom. Subscripts $k \pm \frac{1}{2}$ refer to imaginary interfaces
at which the vertical velocities are computed from the continuity equation

$$(9.7) \qquad w_{k-\frac{1}{2}} = - \sum_{i=k}^{b} \{ Hu)_{,x} + (Hv)_{,y} \}$$

At the surface the elevation is computed instead of w

$$(9.8) \qquad \eta_{,t} = - \sum_{i=1}^{b} \{(Hu)_{,x} + (Hv)_{,y} \}$$

The salt concentration is governed by the dispersion
equation

$$(9.9) \qquad (Hs)_{,t} + (Hus)_{,x} + (Hvs)_{,y} + (ws)_{k-\frac{1}{2}} - (ws)_{k+\frac{1}{2}}$$

$$- (HD_x s_{,x})_{,x} - (HD_y s_{,y})_{,y} + (\kappa s_{,z})_{k+\frac{1}{2}} - (\kappa s_{,z})_{k-\frac{1}{2}} = 0$$

Aside from the fact that the structure of the eddy viscous
and dispersive terms is inconsistent ($\tau_{xy} \neq \tau_{yx}$ in their formulation
and dispersion definitely does not have principal axes along x- and y-

axes everywhere) these equations clearly point out the foremost problem

of three-dimensional models: there are many parameters that we presently

do not know how to determine. Predictive models can therefore be ruled

out for some time to come; but even descriptive models will need an

enormous amount of supporting field data. These issues are not discussed

or even mentioned in any of the reports on three-dimensional models.

Having indicated their mathematical formulation, equations

(9.5)-(9.9), Leendertse et al discuss the numerical finite difference

solution scheme in some detail. The explicit leap-frog method is used

in time to avoid the messy coupling of variables by implicit methods

such as the alternating direction implicit method (ADI). The spatial

grid structure is the same space staggered grid as Leendertse used in

his two-dimensional model, see Figures 2-3 and 9-1, except for the loca-

tion of the depth values. As many of these grids are placed on top of

each other as necessary to resolve the vertical variation, Figure 9-2.

For programming reasons, the bottom must be approximated in steps of the

layer thickness causing some numerical problems at the jumps. The model

was only capable of handling circulation in closed basins although work

is continuing on implementing an open boundary condition. Several test

examples are shown with and without density stratification in two or

three dimensions.

Two layer models are less ambitious than the three-dimensional

models discussed above, but can give very illuminating results because

there are fewer parameters to adjust.

Liggett and Lee [42] and Gedney et al [23] developed prac-

tically identical two layer models for steady state lake circulation based

Figure 9-1   ·The location of u (−), v (ı), and other parameters
(+) in the space-staggered grid [39]

Figure 9-2.   Relative position of the variables in the model [39]
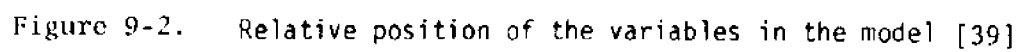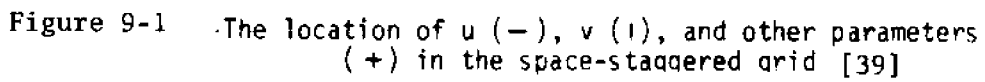
on earlier work by Welander. The equations solved for each layer of constant density are

(9.10) $\quad - fv = - \frac{1}{\rho} p_{,x} + E_z u_{,zz}$

(9.11) $\quad fu = - \frac{1}{\rho} p_{,y} + E_z v_{,zz}$

(9.12) $\quad g = - \frac{1}{\rho} p_{,z}$

(9.13) $\quad u_{,x} + v_{,y} + w_{,z} = 0$

The solution proceeds exactly as described in Chapter 2 for the rigid lid approximation. The explicit dependence of u, v on z is found from (9.10), (9.11) and boundary conditions. Equations (9.10) − (9.13) are integrated over each layer and then solved numerically for average u, v and p (or equivalently surface and interface levels) and finally w can be derived from (9.13). There are essentially only two parameters, E_z for each layer, in this formulation, although of course many others have been neglected through approximations. Both interface position and currents were found to be somewhat sensitive to variations in E_z.

As noted in reference [42] , the response time of a water body, homogeneous or stratified, may be of the order of days (we computed approximately one day for Mass Bay in Chapter 3). Steady state circulation may therefore rarely, if ever, be attained and such results can at best represent average long term conditions. This approach is hence less attractive for coastal areas.

Transient two layer, two-dimensional models are starting to

199

appear in the engineering literature. The situation of two distinct layers of different density is realistic for many natural water masses and can be reproduced in the laboratory. There is therefore a reasonable possibility of determining the parameters involved.

Abbott and Grubert [2] are extending previous work to layered flow, numerical algorithms, and representation of fronts on the interface.

A two layer model for thermal diffusion caused by outfall of cooling water is described by Wada [75]. The vertically integrated equations without the coriolis effect are used. Hydrostatic pressure and constant density in the bottom layer is assumed. Mixing or entrainment and heat exchange between layers have been omitted. Considerable efforts were expended to obtain reasonable dispersion coefficients. These were determined from current measurements using Taylor's theorem

$$(9.14) \qquad K_x = \overline{u'^2} \int_0^\infty R_u(\tau) \, d\tau$$

$$(9.15) \qquad K_y = \overline{v'^2} \int_0^\infty R_v(\tau) \, d\tau$$

where R_u and R_v are the Lagrangian autocorrelation functions of the u and v velocities. The density in the top layer is assumed to be a linear function of temperature. The usual quadratic interfacial and bottom shear laws are used although no data is given for the coefficients.

Finite difference approximations are used to obtain numerical solutions with the dependent variables staggered in space and time. Forward (explicit) time differences and centered space differences are em-

ployed. The accuracy and stability is not discussed for this scheme, which, in order to treat boundary conditions properly, has to introduce artificial nodes outside the boundary.

Some example computations for simplified geometries are presented, but detailed information about treatment of model boundaries is missing. Orthotropic dispersion is used, however with principal directions dictated by geometry rather than current patterns. No comparisons with known solutions or field verification are presented.

Perhaps the most in depth going report on two layer models is presented by Codell [9]. The mathematical formulation follows the works by Leendertse and Wada and the latter's vertically averaged equations are used with source terms included. They are:

$$(9.14) \qquad h_{1,t} + (h_1 u_1)_{,x} + (h_1 v_1)_{,y} + v_{ent} = 0$$

$$(9.15) \qquad u_{1,t} + u_1 u_{1,x} + v_1 u_{1,y} + g \ (h_{1,x} + h_{2,x}) +$$

$$\frac{1}{h_1} (\tau_x^{\ i} - \tau_x^{\ s}) - f \ v_1 + \frac{v_{ent} \ u_2}{h} = 0$$

$$(9.16) \qquad v_{1,t} + u_1 v_{1,x} + v_1 v_{1,x} + g \ (h_{1,y} + h_{2,y})$$

$$+ \frac{1}{h_1} (\tau_y^{\ i} - \tau_y^{\ s}) + f \ u_1 + \frac{v_{ent} \ v_2}{h_1} = 0$$

for the upper layer. For the lower layer:

$$(9.17) \qquad h_{2,t} + (h_2 u_2)_{,x} + (h_2 v_2)_{,y} - v_{ent} = 0$$

(9.18) $u_{2,t} + u_2 u_{2,x} + v_2 u_{2,y} + g\,(h_{1,x} + h_{2,x})$

$$+ \frac{g(\rho_2 - \rho_1)}{\rho}\, h_{2,x} - \frac{1}{h_2}\,(\tau_x^{\,i} - \tau_x^{\,b}) - f\,v_2 = 0$$

(9.19) $v_{2,t} + u_2 v_{2,x} + v_2 v_{2,y} + g(h_{1,y} + h_{2,y})$

$$+ g\,\frac{(\rho_2 - \rho_1)}{\rho}\, h_{2,y} - \frac{1}{h_2}\,(\tau_y^{\,i} - \tau_y^{\,b}) - fu_2 = 0$$

h_1 and h_2 are the layer thicknesses.

v_{ent} is the velocity of entrainment of water from lower layer to upper layer. The loss of momentum by entrainment in the lower layer is ignored. These equations of motion are coupled with a thermal energy equation for the upper layer only

(9.20) $(h_1 T_1)_{,t} + (h_1 u_1 T_1)_{,x} + (h_1 v_1 T_1)_{,y} + \{D_1 (h_1 T_1)_{,x}\}_{,x}$

$$+ \{D_1 (h_1 T_1)_{,y}\}_{,y} + s_1 T_1 + s_2 + v_{ent} \cdot T_2$$

where T_1 and T_2 (assumed constant) are the upper and lower layer temperatures, D_1 is a thermal diffusivity and s_1, s_2 are parameters in the heat source terms. Due to computer limitations only the one-dimensional version of the above equations were actually programmed as a model, and then only used to compare with a simplified stratified model.

The simplified model consists of a one layer analog of the two layer system. By assuming a rigid lid on the top layer, the lower layer to be of great constant depth, and neglecting its dynamics, the upper layer equations uncouple and reduce to, omitting subscript 1

$$(9.21) \qquad h_{,t} + (hu)_{,x} + (hv)_{,y} + v_{ent} = 0$$

$$(9.22) \qquad u_{,t} + uu_{,x} + vu_{,y} - fv + g' h_{,x} + \frac{1}{h} (\tau_x^1 - \tau_x^s + v_{ent} u_L) = 0$$

$$(9.23) \qquad v_{,t} + uv_{,x} + vv_{,y} + fu + g' h_{,y} + \frac{1}{h} (\tau_y^1 - \tau_y^s + v_{ent} v_L) = 0$$

where u_L, v_L are lower layer velocities which then presumably must be known, and g' is the reduced gravity.

$$(9.24) \qquad g' = g \cdot \frac{\rho_2 - \rho_1}{\rho_{average}}$$

The surface wave has been eliminated by this procedure and only the internal wave is resolved by the model. The advantage is a large reduction in the wave propagation velocity by a factor of $(\Delta \rho / \rho)$ with corresponding improved numerical stability. However, the applicability of such a model is clearly very limited.

Leendertse's space staggered grid is used with the leap frog time method to solve equations (9.21) - (9.23). The treatment of boundaries both physically and numerically is extremely poor and often overrestricts the problem. For a stream inflow, for example, prescription of both velocity and depth is suggested, which is necessary to specify a discharge, but is inadmissible. As noted before, this is one reason that we chose to use the more natural variables of depth and discharges. As an other example, both the normal velocity and the normal derivative of the surface elevation are required to be zero at land boundaries, which is inconsistent with the formulation. Although the models developed by Codell thus are very crude, the fundamentals of the

two layer formulation are listed in his report. He also paid some attention to the parametric expressions and tried to determine the parameters involved, which will be discussed in the next chapter.

We conclude this review by identifying what effort we feel is necessary in order to make three dimensional models a useful engineering tool. Our present understanding of the physical phenomena and the state of the art of field monitoring programs raises some serious questions as to the applicability of three dimensional models. The numerical techniques to solve the problem may be at hand, but there are so many unknown parameters in the formulation that probably any result could be produced by adjusting these properly. That is, however, a rather useless and expensive exercise. The multilayer idealization, specifically the two layer model, contains most promise of a predictive/descriptive tool in the near future. The possibility of using laboratory experiments which readily reproduce layered flow should not be underestimated. The full scope of a two layer model should therefore be investigated first. Its formulation is presented in the next chapter, followed by a finite element solution strategy, sample solutions and comparisons with analytical and experimental results.

CHAPTER 10

FORMULATION OF MULTI-LAYER CIRCULATION

Since there is no difference between formulations for two or more layers, we present here a general multilayer mathematical formulation. Predictably, relative density differences must have large influence on the final results and multilayered models should therefore ideally account for variations in the density field. In the review chapter attempts of including either a salt or heat balance equation were mentioned. To solve these additional equations numerically is, however, a very minor problem; the major difficulties lie in specifying source terms, spreading coefficients, boundary and initial conditions. We choose to concentrate our efforts on the pure circulation problem and consequently assume the density field is known. It is simple to build later, an extra structure into the model which will actually calculate the densities, salinity or transport of dissolved matter.

The vertically integrated layer equations are derived from the three dimensional equations of motion in the same manner as in the one layer case. Some of the repeated manipulations are therefore left out. On the sketch in figure 10-1 we define the variables for an arbitrary layer. To obtain the most general formulation the bottom is treated as any other interface. Assumptions of incompressibility and constant density over depth for each layer are made.

(10.1) $\qquad \rho_k = \rho_k(x,y,t)$

Conservation of mass, is expressed by

(10.2) $\qquad u_{,x} + v_{,y} + w_{,z} = e$
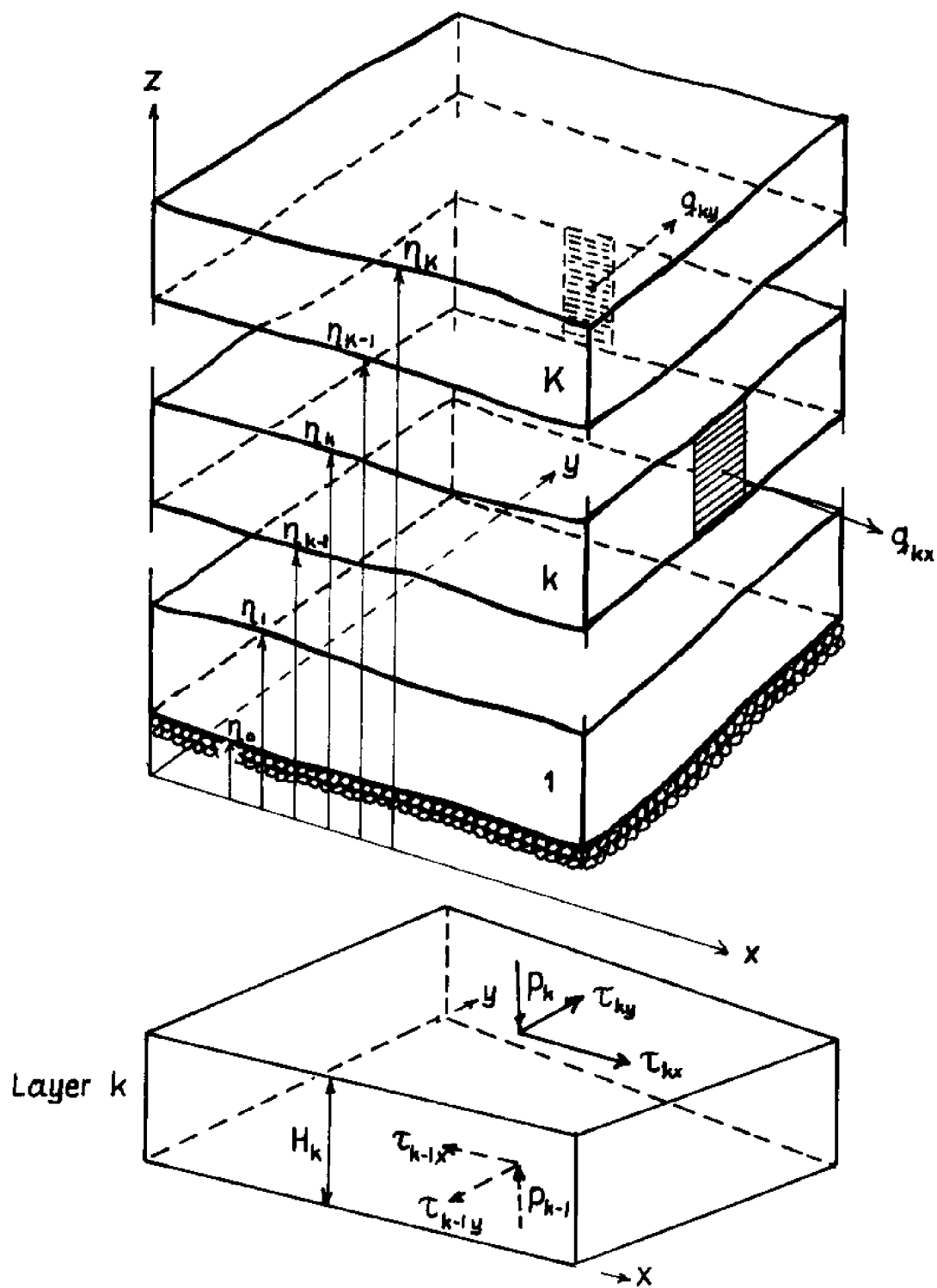
Figure 10-1. Sketch of multi layer system and forces on interfaces of layer k.

206

where e represents internal sources. Integrating equation (10.2) over layer k gives

$$(10.3) \qquad H_{k,t} + q_{kx,x} + q_{ky,y} = q_k - w_k + \frac{\rho_{k-1}}{\rho_k} w_{k-1}$$

where

$$(10.4) \qquad H_k = \eta_k - \eta_{k-1}$$

$$(10.5) \qquad q_{kx} = \int_{\eta_{k-1}}^{\eta_{k-1}} u_k dz$$

$$(10.6) \qquad q_{ky} = \int_{\eta_{k-1}}^{\eta} v_k dz$$

$$(10.7) \qquad q_k = \int_{\eta_{k-1}}^{\eta_k} e dz$$

and w_k, w_{k-1} are the relative normal velocities at interfaces k and k-1, that is, w_k is a net entrainment or mixing velocity between layers k and k+1.

After integrating over layer k we can write the momentum equations as

$$(10.8) \qquad q_{kx,t} + (\bar{u}_k q_{kx})_{,x} + (\bar{u} q_{ky})_{,y} = f q_{ky} - (F_{kp} - F_{kxx})_{,x}$$
$$+ F_{kyx,y} + \frac{1}{\rho_k}\{\tau_{kx} - \tau_{(k-1)x} + P_k \eta_{k,x} - P_{k-1}\eta_{k-1,x}\}$$
$$+ \bar{m}_{kx} - w_k \cdot \bar{u}_k + \frac{\rho_{k-1}}{\rho_k} w_{k-1}\bar{u}_{k-1}$$

$$(10.9) \qquad q_{ky,t} + (\bar{v}_k q_{kx})_{,x} + (\bar{v}_k q_{ky})_{,y} = - f q_{kx} + F_{kxy,x}$$
$$- (F_{kp} - F_{kyy})_{,y} + \frac{1}{\rho_k}\{\tau_{ky} - \tau_{(k-1)y} + P_k \eta_{k,y} - P_{k-1}\eta_{k-1,y}\}$$
$$+ \bar{m}_{ky} - w_k \bar{v}_k + \frac{\rho_{k-1}}{\rho_k} w_{k-1}\bar{v}_{k-1}$$

where only the significant coriolis terms are retained.

If vertical accelerations are negligible compared to gravity, which we reasonably can assume for tidal flow, the third momentum equation reduces, as usual, to the hydrostatic pressure relationship:

$$(10.10) \quad F_{kp} = \frac{1}{\rho_k} \int_{\eta_{k-1}}^{\eta_k} p\,dz = \frac{1}{\rho_k}\{p_k H_k + g\rho_k \eta_k H_k - \frac{1}{2}g\rho_k(\eta_k^2 - \eta_{k-1}^2)\}$$

$$= \frac{1}{\rho_k}\{p_k H_k + \frac{1}{2}\rho_{k0} g H_k^2 + \frac{1}{2}\Delta\rho_k g H_k^2\}$$

$$= \frac{1}{\rho_k}\{p_{k-1} H_k - \frac{1}{2}\rho_{k0} g H_k^2 - \frac{1}{2}\Delta\rho_k g H_k^2\}$$

where p_k is the pressure at interface k, and the density is assumed to consist of a constant average value ρ_{k0} and a small variable variation $\Delta\rho_k$

$$(10.11) \quad \rho_k(x,y,t) = \rho_{k0} + \Delta\rho_k(x,y,t)$$

Introducing Boussinesque's approximation, we obtain

$$(10.12) \quad F_{kp} \simeq \frac{1}{\rho_{k0}} p_k H_k + \frac{1}{2}g H_k^2 + \frac{1}{2}g\frac{\Delta\rho_k}{\rho_{k0}}g H_k^2$$

$$= \frac{1}{\rho_{k0}} p_{k-1} H_k - \frac{1}{2}g H_k^2 - \frac{1}{2}g\frac{\Delta\rho_k}{\rho_{k0}}g H_k^2$$

Additional relations are

$$(10.13) \quad p_{k-1} - p_k \simeq \rho_{k0} g H_k$$

and

$$(10.14) \quad F_{kp} = \frac{1}{2\rho_{k0}}(p_k + p_{k-1}) H_k$$

Equations (10.13), (10.8), (10.9) and (10.12) are the "fundamental" equations governing multilayer circulation, i.e. they are based

on physical laws. To solve the problem the mixing velocities w_k; the internal stresses F_{kxx}, F_{kxy}, F_{kyy}; and the interfacial shears τ_{kx}, τ_{ky} must be specified. To do this, with some confidence in the values employed, is not feasible at present except in very simplified situations.

Attention is called upon the fact that coastal areas seldom exhibit more than two layer stratification. The object of multilayer models is therefore to represent a three dimensional problem rather than to impose a layering on the system. Consistent with this, one visualizes the layers as having constant depths, with flow across the interfaces. In this case w_k becomes the actual normal velocity at the imaginary interface k, and equation (10.3) is rewritten

$$(10.15) \qquad w_k = \frac{\rho_{k-1}}{\rho_k} w_{k-1} - q_{kx,x} - q_{ky,y} + q_k$$

At the bottom w_o is zero and at the surface, which of course is allowed to move, we have

$$(10.16) \qquad \frac{\partial \eta_K}{\partial t} = \frac{\rho_{K-1}}{\rho_K} w_{K-1} - q_{Kx,x} - q_{Ky,y} + q_K$$

For small interfacial slopes w_k is approximately equal to the vertical velocity at the same point. Obviously, it is necessary to bookkeep the changes in density, which adds a further complexity to this kind of modeling. In view of these difficulties we restrict ourselves to two layers in the remainder of this report. This restriction simplifies the problem significantly; but is a sufficient extension of the one layer model to illustrate many new phenomena.

Writing out the specific equations for the two layer case, we

have for layer 1,

(10.17) $\quad H_{1,t} + q_{1x,x} + q_{1y,y} = q_1 - w_1$

(10.18) $\quad q_{1x,t} + (\bar{u}_1 q_{1x})_{,x} + (\bar{u}_1 q_{1y})_{,y} = fq_{1y} - (F_{1p} - F_{1xx})_{,x}$

$$+ F_{1yx,y} + \frac{1}{\rho_1}\{\tau_{1x} - \tau_{0x} + p_1 n_{1,x} - p_0 n_{0,x}\} + \bar{m}_{1x} - w_1 \bar{u}_1$$

(10.19) $\quad q_{1y,t} + (\bar{v}_1 q_{1x})_{,x} + (\bar{v}_1 q_{1y})_{,y} = -fq_{1x} + F_{1xy,x}$

$$- (F_{1p} - F_{1yy})_{,y} + \frac{1}{\rho_1}\{\tau_{1y} - \tau_{0y} + p_1 n_{1,y} - p_0 n_{0,y}\}$$

$$+ \bar{m}_{1y} - w_1 \bar{v}_1$$

and for layer 2, (top):

(10.20) $\quad H_{2,t} + q_{2x,x} + q_{2y,y} = q_2 + \frac{\rho_1}{\rho_2} w_1$

(10.21) $\quad q_{2x,t} + (\bar{u}_2 q_{2x})_{,x} + (\bar{u}_2 q_{2y})_{,y} = fq_{2y} - (F_{2p} - F_{2xx})_{,x}$

$$+ F_{2yx,y} + \frac{1}{\rho_2}\{\tau_{2x} - \tau_{1x} + p_2 n_{2,x} - p_1 n_{1,x}\}$$

$$+ \bar{m}_{2x} + \frac{\rho_1}{\rho_2} w_1 \bar{u}_1$$

(10.22) $\quad q_{2y,t} + (\bar{v}_2 q_{2x})_{,x} + (\bar{v}_2 q_{2y})_{,y} = -fq_{2x} + F_{2xy,x}$

$$- (F_{2p} - F_{2yy})_{,y} + \frac{1}{\rho_2}\{\tau_{2y} - \tau_{1y} + p_2 n_{2,y} - p_1 n_{1,y}\}$$

$$+ \bar{m}_{2y} + \frac{\rho_1}{\rho_2} w_1 \bar{v}_1$$

where p_2 is surface atmospheric pressure, and the specific pressure force measures are

(10.23) $\quad F_{1p} = \frac{1}{2}gH_1^2 + \frac{1}{2}g\frac{\Delta\rho_1}{\rho_{10}}H_1^2 + \frac{1}{\rho_{10}}p_1 H_1$

(10.24) $\quad F_{2p} = \frac{1}{2}gH_2^2 + \frac{1}{2}g\frac{\Delta\rho_2}{\rho_{20}}H_2^2 + \frac{1}{\rho_{20}}p_2 H_2$

The pressures at the interface and bottom are obtained from equation

(10.13):

(10.25) $\qquad p_1 = p_2 + \rho_{20}gH_2$

(10.26) $\qquad p_0 = p_2 + \rho_{20}gH_2 + \rho_{10}gH_1$

Bottom shear stress is handled in the same manner as in chapter 3.

(10.27) $\qquad \dfrac{\tau_{0x}}{\rho_{10}} = C_f(q_{1x}^2 + q_{1y}^2)^{1/2}\dfrac{q_{1x}}{H_1^2}$

(10.28) $\qquad \dfrac{\tau_{0y}}{\rho_{10}} = C_f(q_{1x}^2 + q_{1y}^2)^{1/2}\dfrac{q_{1y}}{H_1^2}$

where the friction coefficient C_f is determined from table 3-1 using H_1 as the depth.

Similarly, surface wind stress τ_2 is determined with the same relationship used for τ^s in chapter 3, equations (3.3.23) and (3.3.28).

The essential difficulties are encountered in the treatment of the interface. A two layer idealization cannot represent explicitly the mass and momentum exchanges taking place in the transition region between layers. We include a shear stress τ_1 and a velocity of entrainment w_1 at the interface to simulate these processes. However, their functional dependence on the mean flow variables must be specified. In most cases the effect of τ_1 predominates.

The standard approach relates τ_1 to the square of the velocity differences of the two layers, namely

(10.29) $\qquad \dfrac{\tau_{1x}}{\rho_{10}} = C_1\{(\bar{u}_1 - \bar{u}_2)^2 + (\bar{v}_1 - \bar{v}_2)^2\}^{1/2}(\bar{u}_2 - \bar{u}_1)$

and

$$(10.30) \qquad \frac{\tau_{1y}}{\tau_{10}} = C_1 \left[(\bar{u}_1 - \bar{u}_2)^2 + (\bar{v}_1 - \bar{v}_2)^2 \right]^{1/2} (\bar{v}_2 - \bar{v}_1)$$

where C_1 is an interfacial shear stress coefficient; $\bar{u}_1$, $\bar{u}_2$, $\bar{v}_1$, $\bar{v}_2$ are the average layer velocity components; and τ_{1x}, τ_{1y} act in the positive x, y directions on the bottom layer, figure 10-1. Experiments have shown that (10.29) and (10.30) are reasonable approximations for the interfacial shear. However, since the flow regimes in the two layers are highly variable it is sometimes found that C_1 is dependent on the Reynolds and densimetric Froude numbers. Unlike the one layer case where flow conditions are usually rough, turbulent, it is possible to have all combinations of smooth - rough and laminar - turbulent situations at the interface for two layer flow.

Unfortunately most data on C_1 are obtained for cases where one layer is stagnant. A very comprehensive report on published data and methodologies for treating momentum and mass transfer in stratified flows has recently been published [33]. When the available data is compared, no apparent relationship between C_1 and Reynolds or Froude numbers are evident. These dimensionless numbers are defined by

$$(10.31) \qquad \mathbb{R} = \frac{\hat{u} \cdot \hat{L}}{\nu}$$

$$(10.32) \qquad \mathbb{F}_\Delta = \frac{\hat{u}}{\sqrt{g \frac{\Delta \rho}{\rho} \hat{L}}}$$

$\mathbb{R}$ is a ratio of inertial to viscous forces, whereas $\mathbb{F}_\Delta$ is a ratio of inertial to gravitational forces; $\hat{u}$ and $\hat{L}$ are velocity and length scales; ν is the kinematic viscosity; ρ and $\Delta\rho$ are density and density difference and g is the gravitational acceleration. For stratified

flows a Richardson number is used instead of $\mathbb{F}_\Delta$

$$(10.33) \qquad Ri = \frac{1}{\mathbb{F}_\Delta^2}$$

For laminar flow an inverse proportionality between C_1 and $\mathbb{R}$ is implied from inspectional analysis:

$$(10.34) \qquad C_1 \sim \frac{1}{\mathbb{R}} \qquad \text{for } \mathbb{R} \leq 2000$$

For turbulent flow, on the other hand, it is expected that C_1 is a function of $\mathbb{F}_\Delta$. While (10.34) has been verified qualitatively, the scatter of data points is too large to determine an explicit functionality between C_1 and $\mathbb{F}_\Delta$. In [33] average values for C_1 are found for:

$$(10.35) \qquad \text{stagnant bottom layer} \qquad C_1 = 4 \cdot 10^{-4}$$

$$(10.36) \qquad \text{stagnant top layer} \qquad C_1 = 15 \cdot 10^{-4}$$

$$(10.37) \qquad \text{counterflow} \qquad C_1 = 7 \cdot 10^{-4}$$

Based on Blasius' empirical friction law for turbulent boundary layer flow over a smooth plate [62], Codell [9] suggest the following relation for C_1

$$(10.38) \qquad C_1 = 0.0099 \, \mathbb{R}^{-1/4}$$

where

$$(10.39) \qquad \mathbb{R} = \frac{4 \cdot H \cdot \Delta u}{\nu}$$

H is the depth of the fastest moving layer and Δu is the absolute velocity difference. For $\mathbb{R} = 10^4$ equation (10.38) gives $C_1 = 10 \cdot 10^{-4}$ in good agreement with (10.37).

The uncertainty in C_1 is obviously large. Experience with computations of salt water and hot water wedges shows that interface location is quite sensitive to the value of C_1. For any particular problem

we suggest that extreme values [(10.35) - (10.36)] be used to bracket the solution or that fitting to actual field data is used to determine reasonable C_1. Equations (10.38) and (10.39) seem to give reasonable values for C_1, but may not be valid for large $\mathbb{R}$.

Interfacial mixing or mass transfer between layers is of less importance to us in this work which assumes the densities to be given functions. Entrainment from a slowly moving layer into a faster moving layer is of interest. We shall assume that the flow is subcritical such that $\mathbb{F}_\Delta < 1$ and $Ri > 1$. Under this condition, in fact for $Ri > 0.5$ all experiments exhibit the qualitative relation between the entrainment rate and Ri:

$$(10.40) \qquad E = E_0 Ri^{-1}$$

where

$$(10.41) \qquad E = \frac{w_1}{2\Delta u}$$

and

$$(10.42) \qquad Ri = \frac{g\frac{\Delta\rho}{\rho}H_1}{(2\Delta u)^2}$$

where Δu is the velocity difference and H_1 is the upper layer thickness. Although the inverse proportionality (10.40) is reflected by all experiments there is a large spread in the coefficient E_0. The order of magnitude of E_0 seems to be 1 when the shear velocity $u_s = (\tau/\rho)^{1/2}$ is used instead of Δu. Considering future developments, it is also desirable to be able to determine the turbulent interfacial mixing in order to compute mass and heat transfers. Some theoretical thoughts on this are also presented in [33].

Codell [9] derived an expression from a graph presented by Lean

214

and Whillock [37], finding the coefficient to be 0.00208 using (10.40) - (10.42).

Finally we resort again to the eddy viscosity concept to express the internal stresses F_{xx}, F_{xy}, F_{yy}. The experience with these in stratified flow is very limited. Recent developments in modeling of turbulence have found more success in a different approach. The Reynolds stresses, mass fluxes and density fluctuations are all treated as transport quantities leading to 10 equations and unknowns. The triple correlations which cannot be directly related to flow parameters are quantified in terms of turbulent energy and dissipation. Even for a vertically integrated formulation there would be 6 flow parameters to determine per layer, which is a doubling of our 3 equations and un- knowns. At this time we feel that more is gained by using the "cruder" eddy viscosity approach for coastal circulation, especially because of the uncertainty in boundary conditions. Analogous to the one layer case we define:

$$(10.43) \qquad F_{kxx} = E_{kxx} \cdot 2q_{kx,x}$$

$$(10.44) \qquad F_{kxy} = F_{kyx} = E_{kxy}(q_{kx,y} + q_{ky,x}) \qquad \Big\} \quad k = 1,2$$

$$(10.45) \qquad F_{kyy} = E_{kyy} \cdot 2q_{ky,y}$$

As noted in [33] it is interesting that due to the assumptions in the derivation of the turbulent transport equations it is found as a first approximation that F_{xx} is related to $u_{,z}$ and not $q_{x,x}$ as we have assumed, when flow in the vertical plane (2-dimensional) is con- sidered. The internal stresses in our case also contain contributions from the vertical velocity profile in addition to the turbulent

215

stresses, and there is therefore not necessarily a contradiction between the two approaches. When turbulence is the dominating phenomenon, it is possible that (10.43) - (10.45) represent the actual process rather poorly.

The values of the eddy viscosity coefficients can be estimated in the same manner as indicated in chapter 3. The importance of internal stress terms is not known in general, but expected to be small.

All parameters for a first approximation have now been expressed in terms of the mean flow. Specification of model boundary conditions remains.

Exactly as was the case for one layer circulation, information about the discharges or forces is needed at boundaries. At discharge boundaries S_{1q} and S_{2q} the normal and tangential discharges are pre-scribed.

$$(10.46) \qquad q_{kn} = q_{kn}^*$$
$$(10.47) \qquad q_{ks} = q_{ks}^* \qquad \qquad \text{on } S_{kq} \quad \text{for } k = 1.2$$

At land boundaries, the prescribed values q_{kn}^* and q_{ks}^* are usually zero. For a stream connecting to the area q_{kn}^* is in general a time dependent function.

Ocean boundaries should, as discussed before, preferably have prescribed discharges also. In many cases the effect of internal stresses must however be neglected in order that pressure be used as specified condition. Pressure is easily translated to layer depths, whence we obtain

$$(10.48) \qquad F_{kp} = F_{kp}^* \quad \text{or} \quad H_k = H_k^* \quad \text{on } S_{kF}, \ k = 1,2$$

An often overlooked but important item in the problem formulation is the initial condition. A two layer system obviously has more degrees of freedom than the one layer system and specification of reasonable initial conditions therefore become more critical. Both discharges and layer depths must be known at some initial time, $t = 0$:

$$(10.49) \qquad q_{kx}, \; q_{ky} = q_{kx0}, \; q_{ky0}$$

at $t=0$ for all x,y in Ω and $k = 1,2$

$$(10.50) \qquad H_k = H_{k0}$$

Because it generally requires more time to get rid of the effects of imposed initial conditions it is advantageous to choose these carefully.

Summarising this chapter, the two layer formulation uses the vertically integrated variables: layer depths and discharges, governed by the equations (10.17) - (10.22). Pressure forces are given by (10.23) - (10.24). Bottom friction is derived from (10.27) - (10.28) with table 3-1. Surface wind stress is approached as in chapter 3. Interfacial shear and mixing can as first approximations be determined from equations (10.29) - (10.30), (10.35) - (10.37) and (10.40), (10.42) with a coefficient of 0.0021. Finally, the boundary and initial conditions must be specified according to (10.46) - (10.48) and (10.44) - (10.50).

WEAK FORM AND SOLUTION SCHEME

11.1 WEAK FORM OF TWO LAYER FLOW EQUATIONS

The transformation of the two layer equations into their weak form proceeds in exactly the same way as described in Chapter 4, and therefore we just write down the result here.

Layer 1. (Bottom)

(11.1.1)
$$\int_\Omega \{ H_{1,t} + q_{1x,x} + q_{1y,y} - q_1 + w_1 \} \, \Delta H_1 \, dA = 0$$

(11.1.2)
$$\int_\Omega [\{ q_{1x,t} + (\bar{u}_1 q_{1x})_{,x} + (\bar{u}_1 q_{1y})_{,y} - f q_{1y}$$

$$- \frac{1}{\rho_1} (\tau_{1x} - \tau_{ox} + p_1 \eta_{1,x} - p_o \eta_{o,x}) - \bar{m}_{1x} + w_1 \bar{u}_1 \} \, \Delta q_{1x}$$

$$- (F_{1p} - F_{1xx}) \, \Delta q_{1x,x} + F_{1yx} \cdot \Delta q_{1x,y}] \, dA +$$

$$\int_{S_{1F}} \alpha_{nx} F_{1p}^{*} \, \Delta q_{1x} \, ds \ -$$

$$\int_{S_{1q}} [\{ \alpha_{nx}(F_{1xx} - F_{1p}) + \alpha_{ny} F_{yx} \} + \{ \alpha_{nx} q_{1n} - \alpha_{ny} q_{1s} - q_{1x}^{*} \}] \cdot$$

$$\Delta q_{1x} \, ds = 0$$

(11.1.3)
$$\int_\Omega [\{ q_{1y,t} + (\bar{v}_1 q_{1x})_{,x} + (\bar{v}_1 q_{1y})_{,y} + f q_{1x}$$

$$- \frac{1}{\rho_1} (\tau_{1y} - \tau_{oy} + p_1 \eta_{1,y} - p_o \eta_{o,y}) - \bar{m}_{1y} + w_1 \bar{v}_1 \} \, \Delta q_{1y}$$

$$+ F_{1xy} \, \Delta q_{1y,x} - (F_{1p} - F_{1yy}) \, \Delta q_{1y,y}] \, dA \ +$$

$$\int_{S_{1F}} \alpha_{ny} F_{1p}^* \Delta q_{1y} \, ds \, -$$

$$\int_{S_{1q}} [\{\alpha_{nx} F_{xy} + \alpha_{ny}(F_{1yy} - F_{1p})\} \div \{\alpha_{ny} q_{1n} + \alpha_{nx} q_{1s} - q_{1y}^*\}] \cdot$$

$$\Delta q_{1y} \, ds = 0$$

Layer 2. (Top)

$$(11.1.4) \qquad \int_\Omega \{H_{2,t} + q_{2x,x} + q_{2y,y} - q_2 + \frac{\rho_1}{\rho_2} w_1\} \, \Delta H_2 \, dA = 0$$

$$(11.1.5) \qquad \int_\Omega [\{q_{2x,t} + (\bar{u}_2 q_{2x})_{,x} + (\bar{u}_2 q_{2y})_{,y} - f q_{2y} -$$

$$\frac{1}{\rho_2}(\tau_{2x} - \tau_{1x} + P_2 \eta_{2,x} - P_1 \eta_{1,x}) - \bar{m}_{2x} - w_1 \bar{u}_1\} \, \Delta q_{2x} \, -$$

$$(F_{2p} - F_{2xx}) \, \Delta q_{2x,x} + F_{2yx} \, \Delta q_{2x,y} \,] \, dA \, +$$

$$\int_{S_{2F}} \alpha_{nx} F_{2p}^* \Delta q_{2x} \, ds \, -$$

$$\int_{S_{2q}} [\{\alpha_{nx}(F_{2xx} - F_{2p}) + \alpha_{ny} F_{2yx}\} + \{\alpha_{nx} q_{2n} - \alpha_{ny} q_{2s} - q_{2x}^*\}] \cdot$$

$$\Delta q_{2x} \, ds = 0$$

$$(11.1.6) \qquad \int_\Omega [\{q_{2y,t} + (\bar{v}_2 q_{2x})_{,x} + (\bar{v}_2 q_{2y})_{,y} + f q_{2x} -$$

$$\frac{1}{\rho_2}(\tau_{2y} - \tau_{1y} + P_2 \eta_{2,y} - P_1 \eta_{1,y}) - \bar{m}_{2y} - w_1 \bar{v}_1\} \, \Delta q_{2y} \, +$$

$$+ F_{2xy} \Delta q_{2y,x} - (F_{2p} - F_{2yy}) \Delta q_{2y,y}]\ dA +$$

$$\int_{S_{2F}} \alpha_{ny}\ F_{2p}^{*}\ \Delta q_{2y}\ ds\ -$$

$$\int_{S_{2q}} [\{\alpha_{nx}\ F_{2xy} + \alpha_{ny}\ (F_{2yy} - F_{2p})\} + \{\alpha_{ny}\ q_{2n} + \alpha_{nx} q_{2s} - q_{2y}\}]\cdot$$

$$\Delta q_{2y}\ ds\ =\ 0$$

The integrals over S_{kq} should theoretically vanish. However, when the finite element method is applied with a fairly coarse grid, a discrepancy between segmental and nodal normals exists with linear triangles. The correct definition of the nodal normal direction was discussed in Chapter 5, and the S_{kq} boundary integrals contain corrections which vanish, in the limit, as the grid is refined.

The functional requirements are as before that H_k, q_{kx}, q_{ky}, Δq_{kx} and Δq_{ky} belong to W_2^1 whereas only ΔH_k can be chosen from the extended space W_2^0 .

11.2 FINITE ELEMENT EQUATIONS

The application of the finite element method is again merely a repetition of the procedure described in Chapter 5. Linear triangles are the simplest elements satisfying the continuity condition imposed on trial and test functions. Substituting these expansions into the weak equations and carrying out the area integration results in

$$(11.2.1) \qquad \underset{\sim}{M} \cdot \underset{\sim}{H}_{1,t} = \underset{\sim}{P}_{H1}$$

$$(11.2.2) \qquad \underset{\sim}{M_2} \, \underset{\sim}{Q}_{1,t} = \underset{\sim}{P}_{Q1}$$

and

$$(11.2.3) \qquad \underset{\sim}{M} \, \underset{\sim}{H}_{2,t} = \underset{\sim}{P}_{H2}$$

$$(11.2.4) \qquad \underset{\sim}{M_2} \, \underset{\sim}{Q}_{2,t} = \underset{\sim}{P}_{Q2}$$

The $\underset{\sim}{M}$ and $\underset{\sim}{M_2}$ coefficient matrices are the same as defined in Chapter 5. $\underset{\sim}{H}_1$ and $\underset{\sim}{H}_2$ are the nodal values of layer depths H_1 and H_2. As before, we define a combined nodal discharge vector (Equation (5.32)) for each layer $\underset{\sim}{Q}_1$, $\underset{\sim}{Q}_2$ in order to treat boundary conditions properly. The load vectors $\underset{\sim}{P}_{H1}$, $\underset{\sim}{P}_{Q1}$, $\underset{\sim}{P}_{H2}$ and $\underset{\sim}{P}_{Q2}$ are functions of $\underset{\sim}{H}_1$, $\underset{\sim}{H}_2$, $\underset{\sim}{Q}_1$, $\underset{\sim}{Q}_2$ and external forcings.

It is convenient to use the same FE grid for upper and lower layers. Different grids could be used but would necessitate an interpolation of variables between the grids.

11.3 TIME INTEGRATION.

The split time method is applied to the FE equations with the layer depths defined at times... $t - \frac{1}{2} \Delta t$, $t + \frac{1}{2} \Delta t$ ... and discharges at times ... t, $t + \Delta t$ .... . Then we may write

$$(11.3.1) \qquad \underset{\sim}{M} \, \underset{\sim}{H}_{1(n+\frac{1}{2})} = \underset{\sim}{M} \, \underset{\sim}{H}_{1(n-\frac{1}{2})} + \Delta t \, \underset{\sim}{P}_{H1}$$

$$(11.3.2) \qquad \underset{\sim}{M} \; \underset{\sim}{H}_{2(n+\frac{1}{2})} = \underset{\sim}{M} \; \underset{\sim}{H}_{2(n-\frac{1}{2})} + \Delta t \; \underset{\sim}{P}_{H2}$$

and

$$(11.3.3) \qquad \underset{\sim}{M}_2 \; \underset{\sim}{Q}_{1(n+1)} = \underset{\sim}{M}_2 \; \underset{\sim}{Q}_{1n} + \Delta t \; \underset{\sim}{P}_{Q1}$$

$$(11.3.4) \qquad \underset{\sim}{M}_2 \; \underset{\sim}{Q}_{2(n+1)} = \underset{\sim}{M}_2 \; \underset{\sim}{Q}_{2n} + \Delta t \; \underset{\sim}{P}_{Q2}$$

Assuming the values of $\underset{\sim}{H}_{1(n-\frac{1}{2})}$, $\underset{\sim}{H}_{2(n-\frac{1}{2})}$, $\underset{\sim}{Q}_{1n}$ and $\underset{\sim}{Q}_{2n}$ are given the solution is propagated by first solving (11.3.1) and (11.3.2) with the load vectors determined at time equal to t_n, except that $\underset{\sim}{H}_{kn}$ are replaced by $\underset{\sim}{H}_{k(n-\frac{1}{2})}$ and $\underset{\sim}{H}_{kn}^{*}$. Next, Equations (11.3.3) and (11.3.4) are solved, evaluating $\underset{\sim}{P}_{Q1}$ and $\underset{\sim}{P}_{Q2}$ at time $t_{n+\frac{1}{2}}$ with the exception that $\underset{\sim}{Q}_{k(n+\frac{1}{2})}$ is replaced by $\underset{\sim}{Q}_{kn}$ and $\underset{\sim}{Q}_{kn}^{*}$. The split time scheme is therefore equivalent to a centered time differencing of local acceleration, principal gravitational and all external load terms, whereas a simple forward differencing is used for non-linear, coriolis and internal stress terms. The accuracy is hence essentially of order Δt^2, but could deteriorate to $0 \, (\Delta t)$ if the forward differenced terms become dominant. A theoretical stability analysis is made difficult by the coupling between layers and is therefore not attempted. Experience with this scheme has shown it to be reasonably stable and accurate. Thus time increments in the neighborhood of Δt_{cr} for the external wave can be used. Note that, as a first approximation for long waves, the external wave velocity is given by:

$$(11.3.5) \qquad c_e^2 = g \, (H_1 + H_2)$$

222

and the internal wave velocity is similarly:

$$(11.3.6) \qquad c_i^{\ 2} = \frac{g(\rho_1-\rho_2)H_1H_2}{\rho_1(H_1+H_2)}$$

The external wave propagates with the same velocity as if the medium was homogeneous and the internal wave moves slower by an approximate factor of $\sqrt{\frac{\rho_1-\rho_2}{\rho_1}}$. For numerical stability, c_e is the decisive factor whereas c_i determines the time interval where the specified initial condition still plays a role. Due to c_i it is generally necessary to integrate over much longer periods in order that the results become independent of initial conditions than in the one layer case.

Figure 11-1 shows a flow chart for the two-layer model.

```
┌─────────────────────────────────────────────────┐
│ INPUT:   GRID INFORMATION                        │
│          SYSTEM PROPERTIES                       │
│          INTEGRATION PARAMETERS                  │
└─────────────────────────────────────────────────┘
                        │
                        ▼
┌─────────────────────────────────────────────────┐
│ COMPUTE: SYSTEM MATRICES                         │
│          ACCOUNT FOR PRESCRIBED VAL.             │
│          DECOMPOSE                               │
└─────────────────────────────────────────────────┘
                        │
                        ▼
           ┌────────────────────────┐
           │ INITIATE   PROBLEM     │
           └────────────────────────┘
                        │
                        ▼
┌─────────────────────────────────────────────────┐
│ t + Δt/2 :  COMPUTE H1 , H2                      │
│          USING :  H1 , H2  AT  t - Δt/2          │
│                   Q1 , Q2  AT  t                 │
└─────────────────────────────────────────────────┘
                        │
                        ▼
┌─────────────────────────────────────────────────┐
│ t + Δt :  COMPUTE Q1 , Q2                        │
│          USING :  H1 , H2  AT  t + Δt/2          │
│                   Q1 , Q2  AT  t                 │
└─────────────────────────────────────────────────┘
                        │
                        ▼
              ┌──────────────────┐
              │    OUTPUT        │
              └──────────────────┘
```
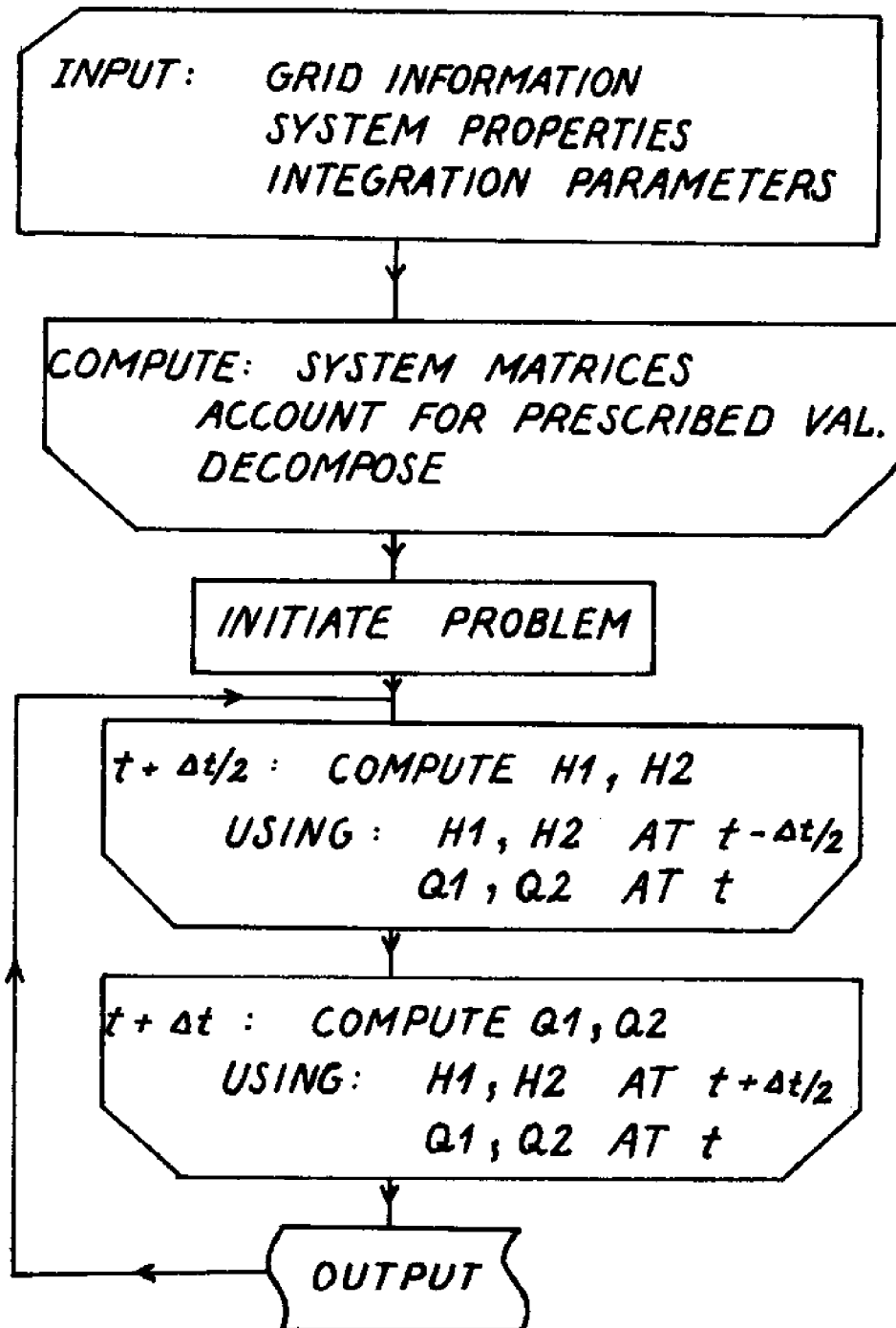
Figure 11-1 :   Flow Chart for Two-Layer Model

224

CHAPTER 12

VERIFICATIONS AND APPLICATIONS

The relatively short time the two layer model has been opera-
tional limits our experience with it as a predictive tool. Some compari-
sons with known analytical solutions and also a verification against ex-
perimental data are presented here. An application of the model to a
rectangular idealization of Massachusetts Bay is included to illustrate
its potential.

12.1 Analytical Study - One Dimensional Channel

The first example consists of the system shown in Figure 12-1,
a rectangular channel of length L having two layers of water with depths
h_1, h_2 and densities ρ_1, ρ_2. The channel is closed with a vertical
wall at x=0 and the surface and interface are forced according to

$$(12.1.1) \qquad \eta_1 = \eta_{10} + b \cos \omega t \qquad x = -L$$

$$(12.1.2) \qquad \eta_2 = \eta_{20} + a \cos \omega t \qquad x = -L$$

where η_{10} and η_{20} are the mean positions.

Neglecting friction, coriolis and external forces, the governing
differential equations, are (Layer 1):

$$(12.1.3) \qquad q_{1,t} + gH_1 \left\{ \frac{\Delta\rho}{\rho_1} \eta_{1,x} + \frac{\rho_2}{\rho_1} \eta_{2,x} \right\} = 0$$

$$(12.1.4) \qquad H_{1,t} + q_{1,x} = 0$$
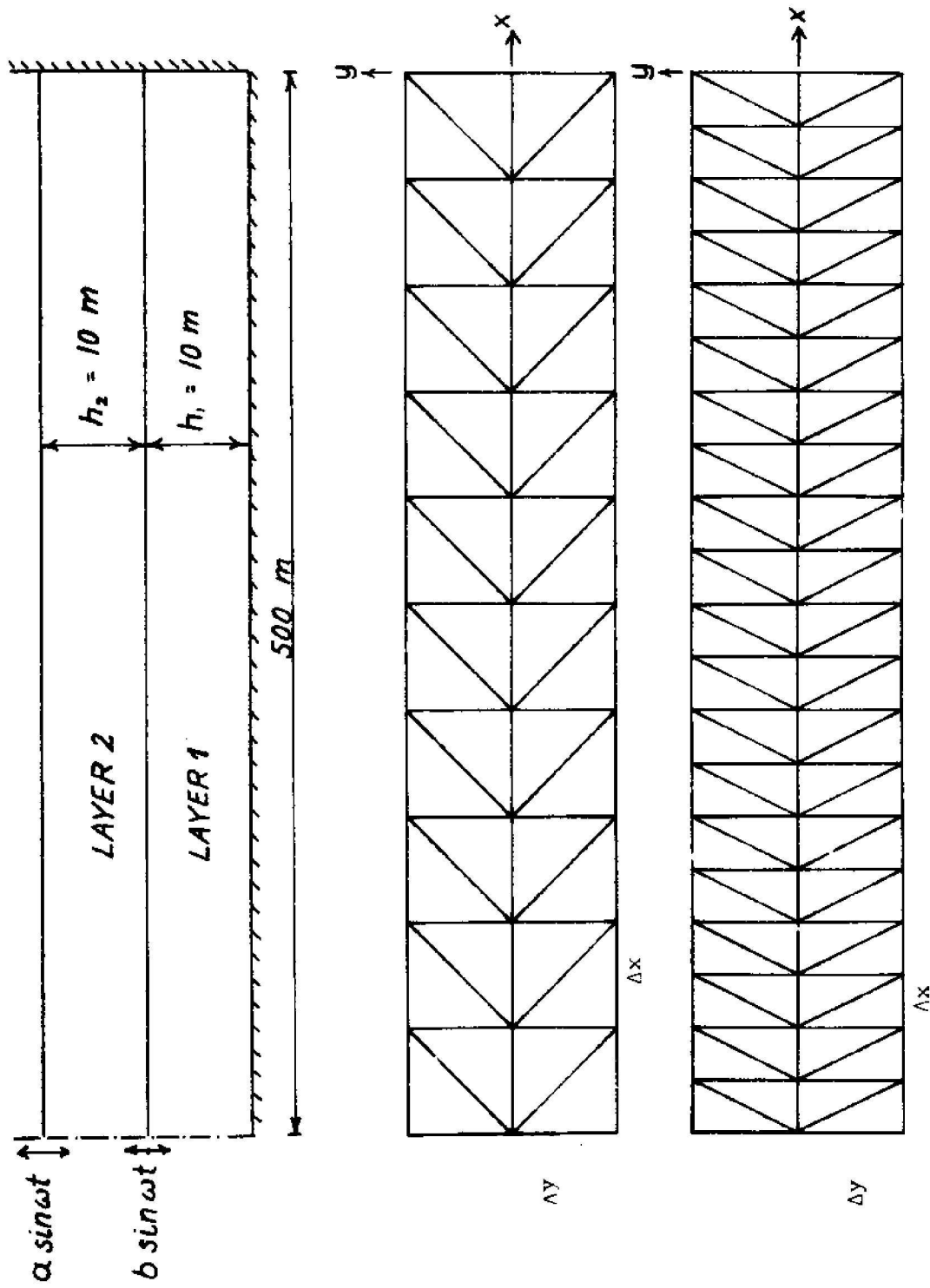
Figure 12-1. Two layer channel. Vertical section and finite element grids.

where $(\Delta\rho = \rho_1 - \rho_2)$

Layer 2 :

(12.1.5) $\quad q_{2,t} + gH_2 \, \eta_{2,x} = 0$

(12.1.6) $\quad H_{2,t} + q_{2,x} = 0$

This set of equations is further simplified by linearizing and assuming the bottom to be horizontal. Let

(12.1.7) $\quad H_1 = \eta_1 - \eta_0 \approx \eta_{10} - \eta_0 = h_1$

(12.1.8) $\quad H_2 = \eta_2 - \eta_1 \approx \eta_{20} - \eta_{10} = h_2$

One obtains after some calculations

(12.1.9) $\quad \eta_{1,tt} - gh_1 \left\{ \dfrac{\Delta\rho}{\rho} \, \eta_{1,xx} + \dfrac{\rho_2}{\rho_1} \, \eta_{2,xx} \right\} = 0$

(12.1.10) $\quad \eta_{2,tt} - \eta_{1,tt} - gh_2 \, \eta_{2,xx} = 0$

The boundary conditions are given by (12.1.1), (12.1.2) and

(12.1.11) $\quad \eta_{1,x} = 0 \quad\quad x = 0$

(12.1.12) $\quad \eta_{2,x} = 0 \quad\quad x = 0$

The two latter conditions are derived from (12.3) and (12.5) by requiring the discharges to vanish at $x = 0$ for $t \geq 0$. We look for a harmonic solution and assume

$$(12.1.13) \qquad \eta_j = \text{Real } \{\zeta_j \, k^{i\omega t}\}$$

Equations (12.1.10) and (12.1.9) then given

$$(12.1.14) \qquad \zeta_1 = \zeta_2 + \frac{gh_2}{\omega^2} \, \zeta_{2,xx}$$

$$(12.1.15) \qquad \zeta_2 + g \frac{(h_1+h_2)}{\omega^2} \, \zeta_{2,xx} + \frac{\Delta\rho}{\rho_1} \frac{gh_1 \, gh_2}{\omega^4} \, \zeta_{2,xxxx} = 0$$

The problem is now reduced to finding ζ_2 and we assume a cosine series solution

$$(12.1.16) \qquad \eta_2 = \text{Real } \{\sum_n^\infty A_n \cos k_n \, x \, e^{i\omega t}\}$$

which satisfies (12.1.12). Inserting in (12.1.15) gives

$$(12.1.17) \qquad k_n^4 - \frac{\rho_1}{\Delta\rho} \frac{(h_1+h_2)}{gh_1 h_2} \omega^2 k_n^2 + \frac{\rho_1}{\Delta\rho} \frac{\omega^4}{gh_1 \, gh_2} = 0$$

$$(12.1.18) \qquad k_n^2 = \frac{1}{2} \frac{\rho_1}{\Delta\rho} \frac{(h_1+h_2)}{gh_1 \, h_2} \omega^2 \pm \omega^2 \sqrt{\left(\frac{1}{2} \frac{\rho_1}{\Delta\rho} \frac{(h_1+h_2)}{gh_1 \, h_2}\right)^2 - \frac{\rho_1}{\Delta\rho} \frac{1}{gh_1 \, gh_2}}$$

It is easily verified that the argument of the square root is always positive and therefore there are only two wave numbers.

$$(12.1.19) \qquad k_2^2 = \frac{1}{2} \frac{\rho_1}{\Delta\rho} \frac{(h_1+h_2)}{gh_1 \, h_2} \omega^2 + \omega^2 \sqrt{\left(\frac{1}{2} \frac{\rho_1}{\Delta\rho} \frac{(h_1+h_2)}{gh_1 \, h_2}\right)^2 - \frac{\rho_1}{\Delta\rho} \frac{1}{gh_1 gh_2}}$$

$$\approx \frac{\rho_1}{\Delta\rho} \frac{(h_1+h_2)}{gh_1 h_2} \omega^2$$

228

$$(12.1.20) \qquad k^2_2 = \frac{1}{2} \frac{\rho_1}{\Delta\rho} \frac{(h_1+h_2)}{gh_1 \, h_2} \omega^2 - \omega^2 \sqrt{\left(\frac{1}{2} \frac{\rho_1}{\Delta\rho} \frac{(h_1+h_2)}{gh_1 \, h_2}\right)^2 - \frac{\rho_1}{\Delta\rho} \frac{1}{gh_1 gh_2}}$$

$$\approx \frac{\omega^2}{g(h_1+h_2)}$$

Noting the relation

$$(12.1.21) \qquad c^2 = \frac{\omega^2}{k^2}$$

the wave velocities given in Equations (11.3.5) and (11.3.6) are easily derived.

The final solution is

$$(12.1.22) \qquad \eta_2 = \{A \cos k_1 x + B \cos k_2 x\} \cos \omega t$$

$$(12.1.23) \qquad \eta_1 = \{A\left(1 - \frac{gh_2}{\omega^2} k_1^2\right) \cos k_1 x + B\left(1 - \frac{gh_2}{\omega^2} k_2^2\right) \cos k_2 x\}$$
$$\cos \omega t$$

where

$$(12.1.24) \qquad A = \frac{a\left(1 - \frac{gh_2}{\omega^2} k_2^2\right) - b}{(k_1^2 - k_2^2) \frac{gh_2}{\omega^2} \cos k_1 L}$$

$$(12.1.25) \qquad B = \frac{a\left(\frac{gh_2}{\omega^2} k_1^2 - 1\right) - b}{(k_1^2 - k_2^2) \frac{gh_2}{\omega^2} \cos k_2 L}$$

In the first test the density difference was assumed zero and the channel was forced as a homogeneous medium. Table 12-1 lists

229

the parameters used. For an interval of more than 3 T, the computed

solution agreed with the analytical result presented in Chapter 8.

The velocities in both layers were equal at all times and the inter-

face displacement was exactly half of the surface displacement. The

split time method was used and the surface and interface position was

prescribed as initial condition at $t = 0$ with all velocities zero.

a	=	0.2 m
b	=	0.1 m
h_1	=	10 m
h_2	=	10 m
L	=	500 m
T	=	2500 sec.
ρ_1 = ρ_2	=	1000 kg/m^3
Δx	=	50 m
Δy	=	50 m
Δt	=	2.5 sec.

Table 12-1. STANDING WAVE IN HOMOGENEOUS
TWO LAYER CHANNEL

For the second test, the densities were assigned different

values. The interface was assumed fixed at $x = -L$ and the period of

the forcing was adjusted so that approximately 2 full interfacial waves

were contained in the length of the channel. Table 12-2 contains the

values of the parameters and Figure 12-2 shows the exact position of

both surface and interface with the error of the computed interface po-

sition (error $= (\eta_1)_{exact} - (\eta_1)_{FE}$) plotted underneath. The computed solution was started

a	=	0.2 m
b	=	0 m
h_1	=	10 m
h_2	=	10 m
L	=	500 m
T	=	500 sec.
ρ_1	=	1005 kg/m^3
ρ_2	=	1000 kg/m^3
Δx	=	50 m
Δy	=	50 m
Δt	=	2.5 sec.

Table 12-2:   STANDING WAVE IN TWO LAYER
CHANNEL COURSE GRID

at time 0 with the correct initial condition and the results shown
are for time t = T. Since the results are rather inaccurate, the
FE discretization was improved by halving the grid spacing in the
x direction. Computed errors for this grid at t = T and t = 2T
are also shown in Figure 12-2; the time step used was Δt = 1.25 sec.
Finally, to settle whether the errors are caused by grid dispersion
(spatial truncation error), the forcing period was doubled leaving
only one internal wave in the channel. The parameters for the numerical

231
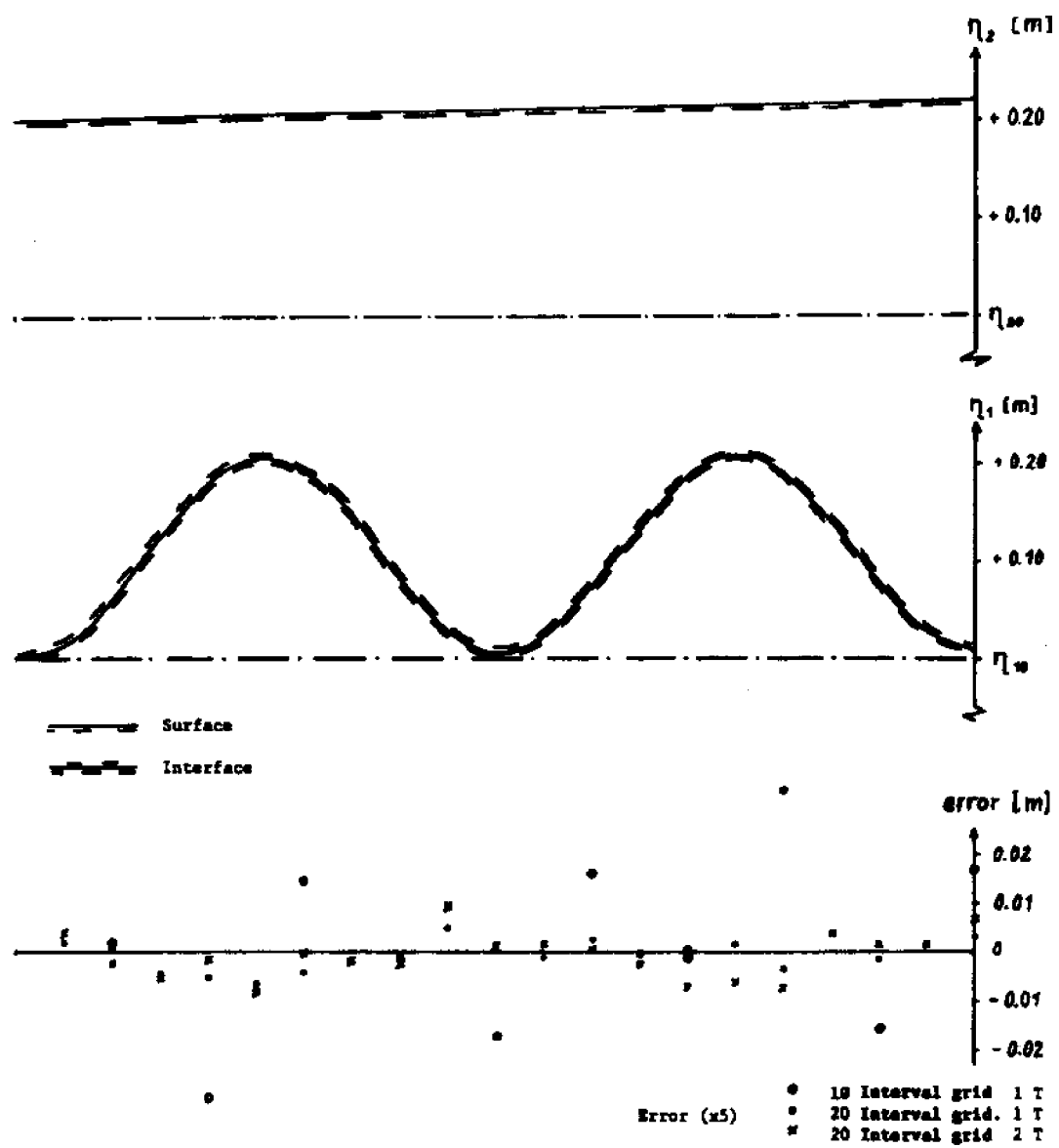
Figure 12-2. Standing wave in two layer channel. Comparison
between analytical and FE solutions. T = 500 sec.
Error is difference between exact and computed
solutions for the indicated grids and times.

computation are listed in Table 12-3 and the comparison between exact and FE solution is again shown in terms of the error in Figure 12-3. Close agreement is found and we conclude that to accurately describe a full wave, approximately 20 points/wavelength are necessary for linear triangles. For higher order elements, such as quadratic triangles, fewer points are needed which is the main advantage of such elements.

$$
\begin{array}{lcl}
a & = & 0.2 \text{ m} \\
b & = & 0 \text{ m} \\
h_1 & = & 10 \text{ m} \\
h_2 & = & 10 \text{ m} \\
L & = & 500 \text{ m} \\
T & = & 1000 \text{ sec} \\
\rho_1 & = & 1005 \text{ kg/m}^3 \\
\rho_2 & = & 1000 \text{ kg/m}^3 \\
\Delta x & = & 25 \text{ m} \\
\Delta y & = & 50 \text{ m} \\
\Delta t & = & 1.25 \text{ sec.}
\end{array}
$$

Table 12-3: PARAMETER VALUES FOR TWO LAYER
CHANNEL. FINE GRID.

The fact that forced interfacial waves are shorter than surface waves often necessitates the use of a finer grid for stratified flow than for homogeneous flow and failure to recognize this can produce spurious results.

233
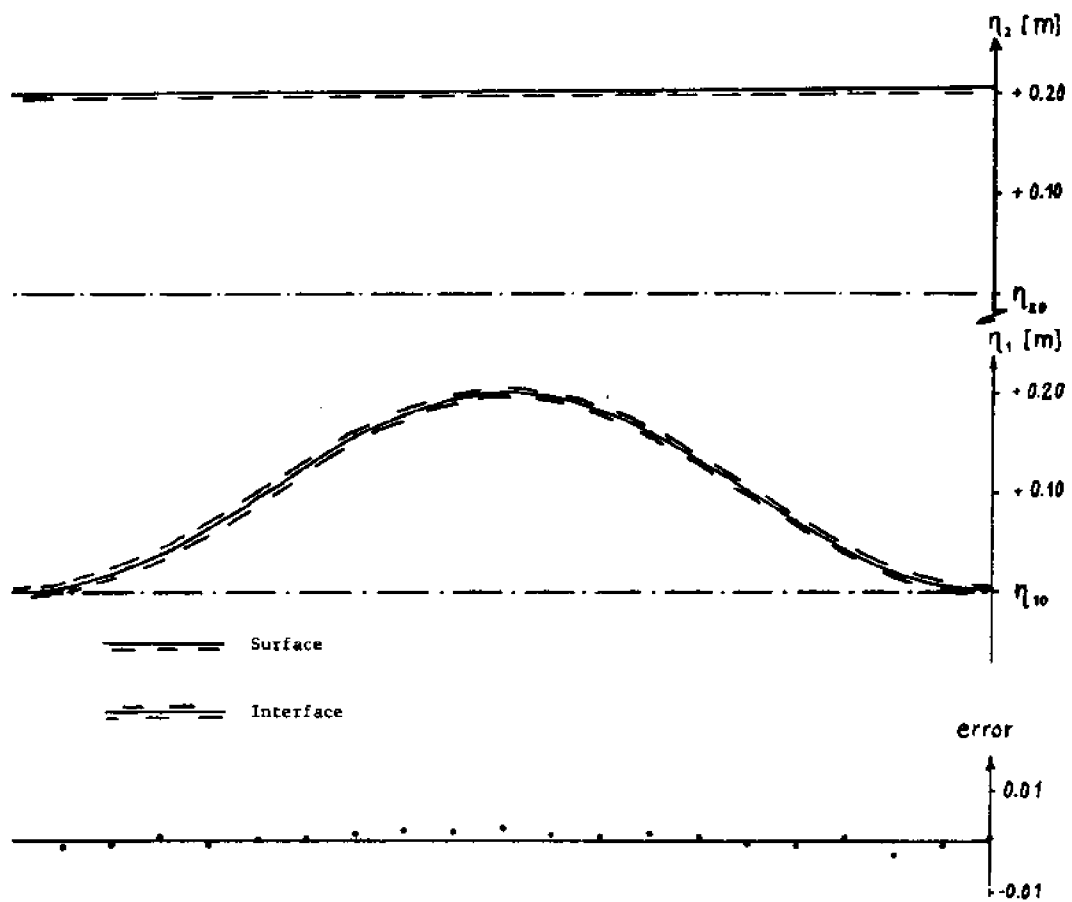
Error (x5) • 20 Interval grid, 2 T

Figure 12-3. Standing wave in two layer channel. Comparison
between analytical and FE solution for 20 inter-
val grid at t=2T, where T = 1000 sec.

12.2 Comparison with Experimental Study

The problem of wave propagation in a two layered channel was approached experimentally and theoretically by Hyden [30, 31]. His analytical model assumed one-dimensional flow and employed the method of characteristics for numerical solution. We take his experimental results for run 1 as a basis for comparison with our FE model. Figures 12-4 and 12-5 show the experimental set-up, and dimensions and initial conditions are listed in Table 12-4 . Equation (12.2.1) is

Length	16.72 m	
width	0.60 m	
bottom layer depth	0.493 m	
top layer depth	0.506 m	
bottom layer density		1007.36 kg/m^3
top layer density		998.75 kg/m^3
period of piston rotation, T	235 sec	
log time at start t_{lag}	0.641 rad.	

Table 12-4: INITIAL DATA FOR HYDEN'S RUN NO. 1

an expression for the discharge from the top into the bottom layer.

$$(12.2.1) \quad q = \frac{0.01471}{0.6} \cdot \frac{2\pi}{T} \cos\left(\frac{2\pi}{T} \cdot t + t_{lag}\right) \ [m^3/msec]$$

The top layer thickness was measured at both ends of the channel and the maximum velocity in the bottom layer was also observed.
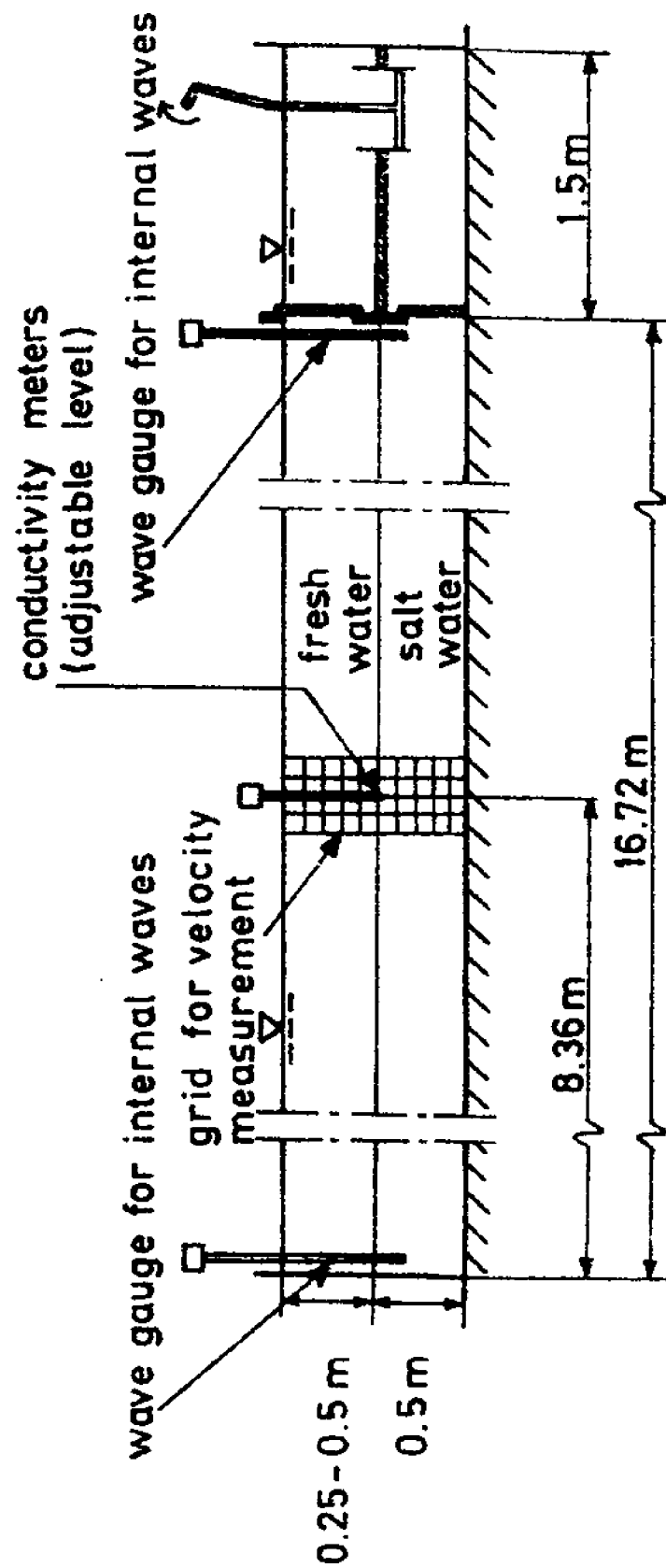
Figure 12-4. Sketch of channel used for two layer experiments by Hydén [30].

conductivity meters
(adjustable level)

wave gauge for internal waves

wave gauge for internal waves

grid for velocity measurement

fresh water

salt water

1.5 m

16.72 m

8.36 m

0.25 - 0.5 m

0.5 m
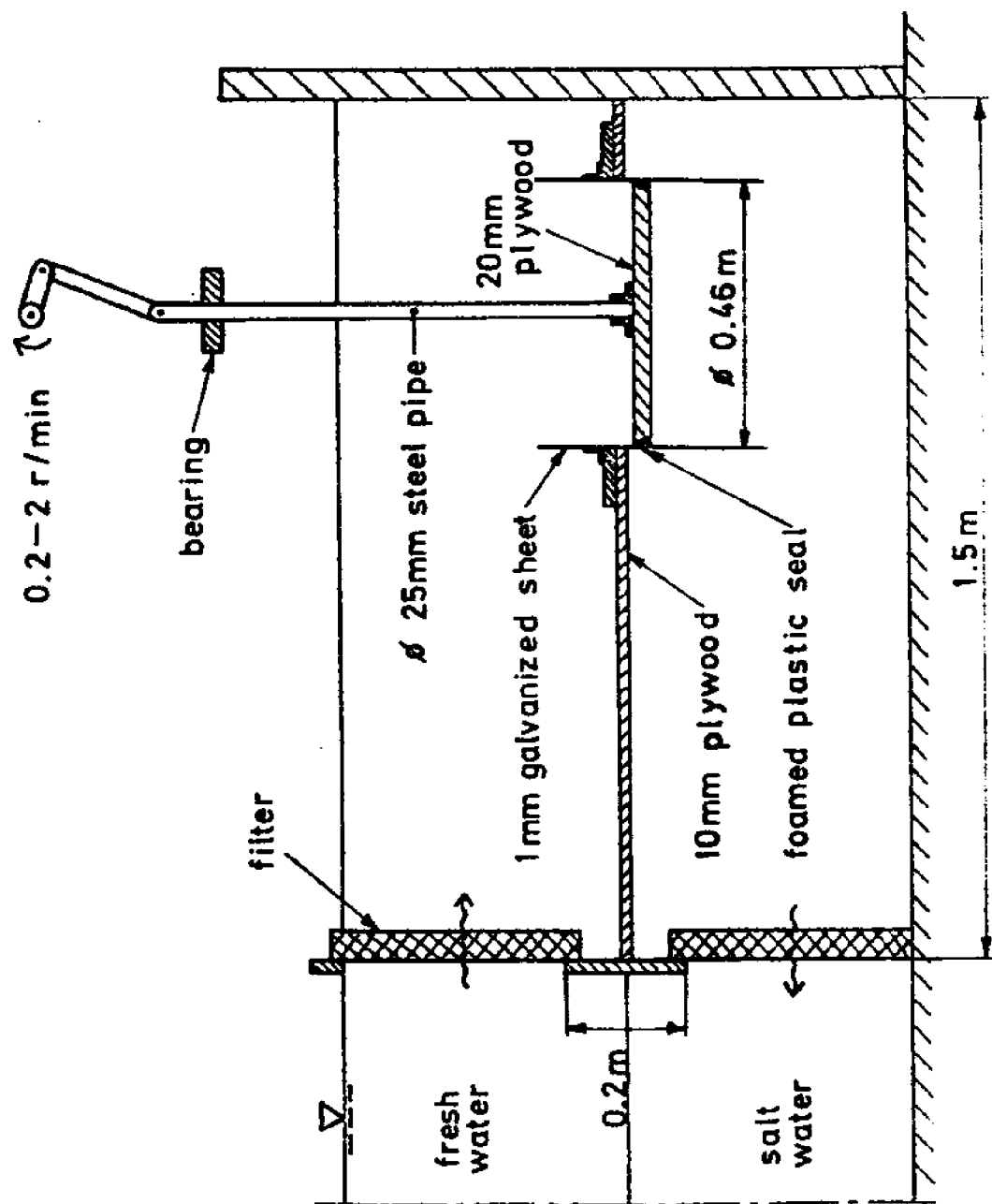
Figure 12-5. Sketch of flow generator, Hydén [30].

A FE grid similar to the one shown in Figure 12-1 was employed. Grid dimensions and other parameters are listed in Table 12-5. The problem was solved using the split time integration scheme with a Δt of 0.4 sec. Although this Δt is somewhat larger than Δt_{cr}, no instabilities were experienced, indicating the same advantage over explicit schemes as found for the one layer case. Figure 12-6 shows the measured and computed top layer thicknesses vs. time at the closed end of the channel.

$$\Delta x = 16.72/12 = 1.3935 \text{ m}$$

$$\Delta y = 50 \text{ m}$$

$$c_e = \sqrt{g(H_1+H_2)} \approx 3.13 \text{ m/sec}$$

$$\Delta t_{cr} = \frac{\Delta x}{\sqrt{2} \, c_e} = 0.3148 \text{ sec}$$

$$\Delta t = 0.4 \text{ sec}$$

$$C_f = C_1 = 0$$

Table 12.5 PARAMETERS FOR FE SOLUTION

Both bottom and interfacial friction were neglected in the computations and the computed results therefore peak slightly before the actual measured peak. The amplitudes are also somewhat greater than the measured values. It is reasonable to expect that by including some friction, the measurements could be fitted closer as shown by Hyden [30]. The measured maximum velocity in the bottom layer was $u_{1max} = 0.021$ m/sec, whereas the FE model gave 0.015 m/sec after 1420 sec. If the computations were carried through to a harmonic steady state,
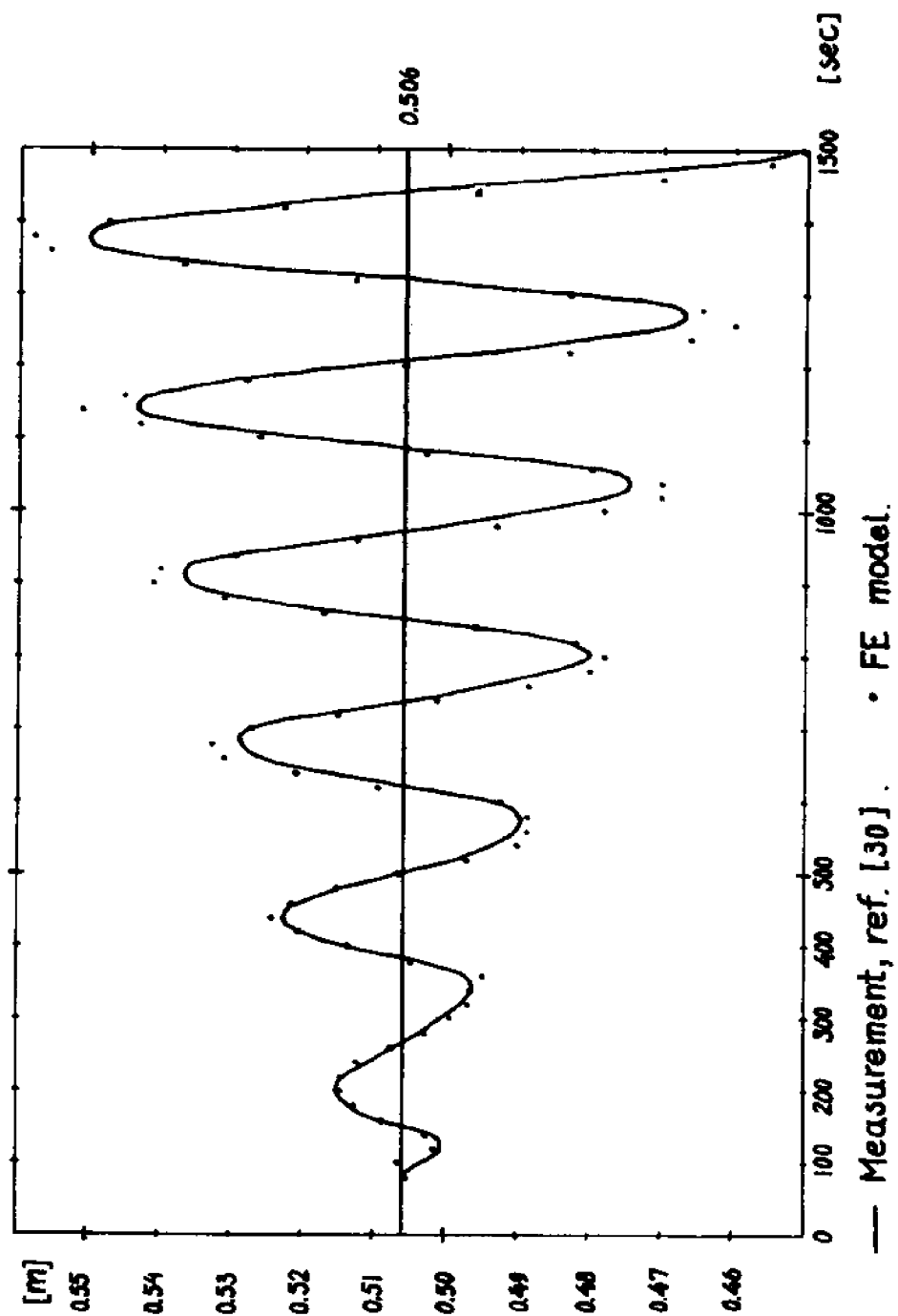
Figure 12-6. Measured and computed top layer thicknesses at closed end.

— Measurement, ref. [30].   • FE model.

which was not reached after 1500 sec, much better agreement would be found.

12.3 Rectangular Model - Massachusetts Bay

The two layer model was applied to the rectangular approxima-
tion of Massachusetts Bay which was also considered in Chapter 8. The
rectangular simplification allows us to compare the results qualita-
tively with an analytical solution by Briggs and Madsen [12]. Since
the FE model requires both layers to exist over the entire domain, it
would not be reasonable to model the Bay geometry correctly,but at the
same time make gross assumptions about the bathymetry. Also, we avoid
problems concerning the specification of boundary and initial con-
ditions by restricting the analysis to the simplified case.

Figure 12-7 shows the FE grid, which has a considerably smaller
mesh size than the one used for the one layer case in anticipation of
shorter interfacial waves. The split time scheme was applied for
the integration and the parameters are shown in Table 12-6. Since prac-
tically no information is available about the movement of the lower
layer, it was decided to fix the interface elevation at its initial
position along the ocean boundary. The surface was then forced as
before according to

$$(12.3.1) \qquad \eta_2 = \eta_{20} + \eta_{2b} \cdot (1 - \cos \omega t)$$

Wind, coriolis and friction are neglected and the computations were
carried out until a harmonic steady state was reached after approxi-
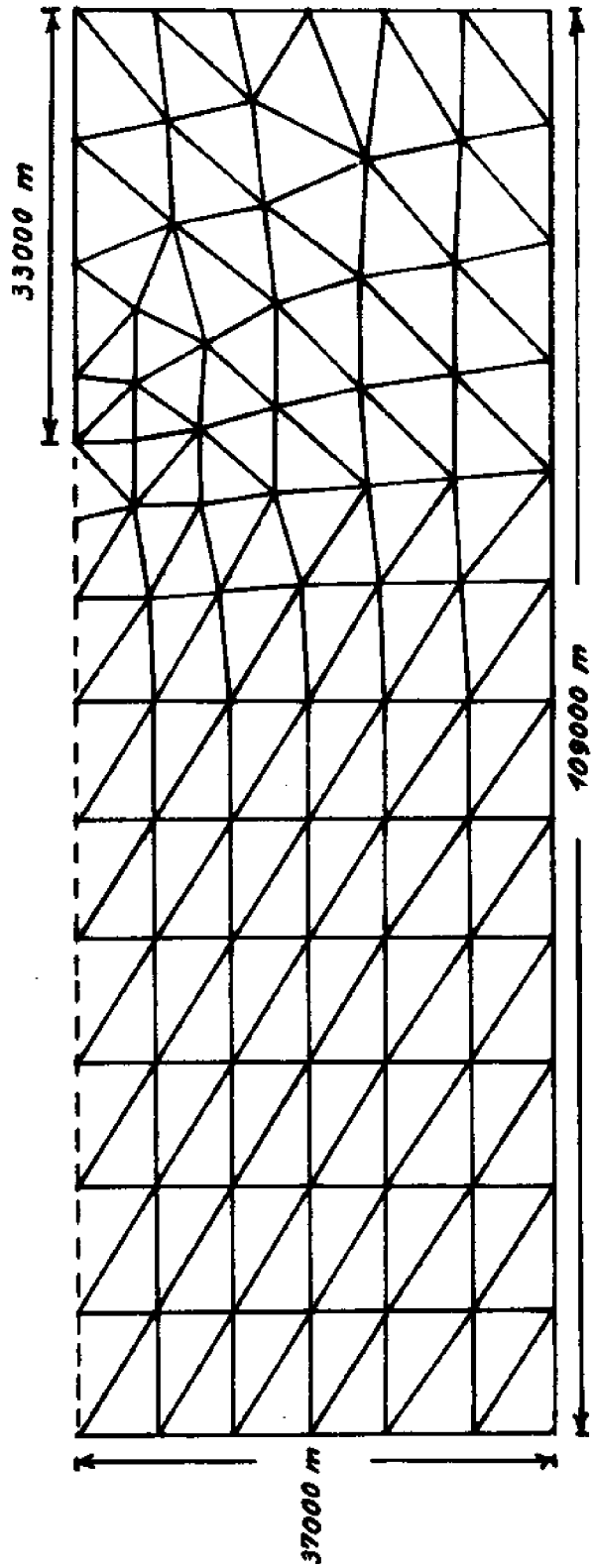
Figure 12-7.

RECTANGULAR APPROXIMATION OF MASSACHUSETTS
BAY. 94 NODES, 149 ELEMENTS.
$h_1 = 24.4\,m,\; h_2 = 12.2\,m,\; \varrho_1 = 1005\; Kg/m^3\; ;\; \varrho_2 = 1000\; Kg/m^3$
$\Delta t = 250\; sec.$

mately 200000 sec.

$$NMNP = 94$$

$$NMEL = 149$$

total initial depth $= 36.6$ m

$$\eta_{10} = 24.4 \text{ m}$$

$$\eta_{20} = 12.2 \text{ m}$$

$$\rho_1 = 1005.0 \text{ kg/m}^3$$

$$\rho_2 = 1000.0 \text{ kg/m}^3$$

$$\eta_{2b} = 1.30 \text{ m}$$

$$\eta_{1b} = 0.0 \text{ m}$$

$$T = 45000 \text{ sec}$$

$$\omega = \frac{2\pi}{T} \quad 0.001396 \text{ sec}^{-1}$$

$$\Delta t_{cr} \simeq 200 \text{ sec}$$

$$\Delta t = 250 \text{ sec.}$$

Table 12-6:   PARAMETERS FOR TWO LAYER
APPROXIMATION OF MASS. BAY

Figures 12-8 to 12-10 show the interface displacements at
different times. The symmetry in interface position between Figures
12-9 and 12-10 indicates that the standing wave has been obtained.
Figure 12-11 shows the surface displacement which is quite smooth in
x, y, as expected. Snapshot pictures of the currents in the two
layers are shown in the figures 12-12 to 12-20. The effect of strati-
fication is quite evident in the current fields which often display a
counterflow behavior and demonstrate the importance of two or multi-

242

layer models. Although the boundary conditions in our example are different from those used by Briggs and Madsen in their analytical solution, there are several resemblances both in current fields and the wave lengths of the internal waves.

The descriptive capability of the two layer model for stratified flow is obviously much improved over one layer models. Our experience with the model is still limited and more applications are necessary to determine the model's sensitivity to the various parameters. In applications, the specification of boundary and initial conditions and field verification are certainly the major problems.

The computational effort expended for a two layer solution is approximately twice that of the one layer model.
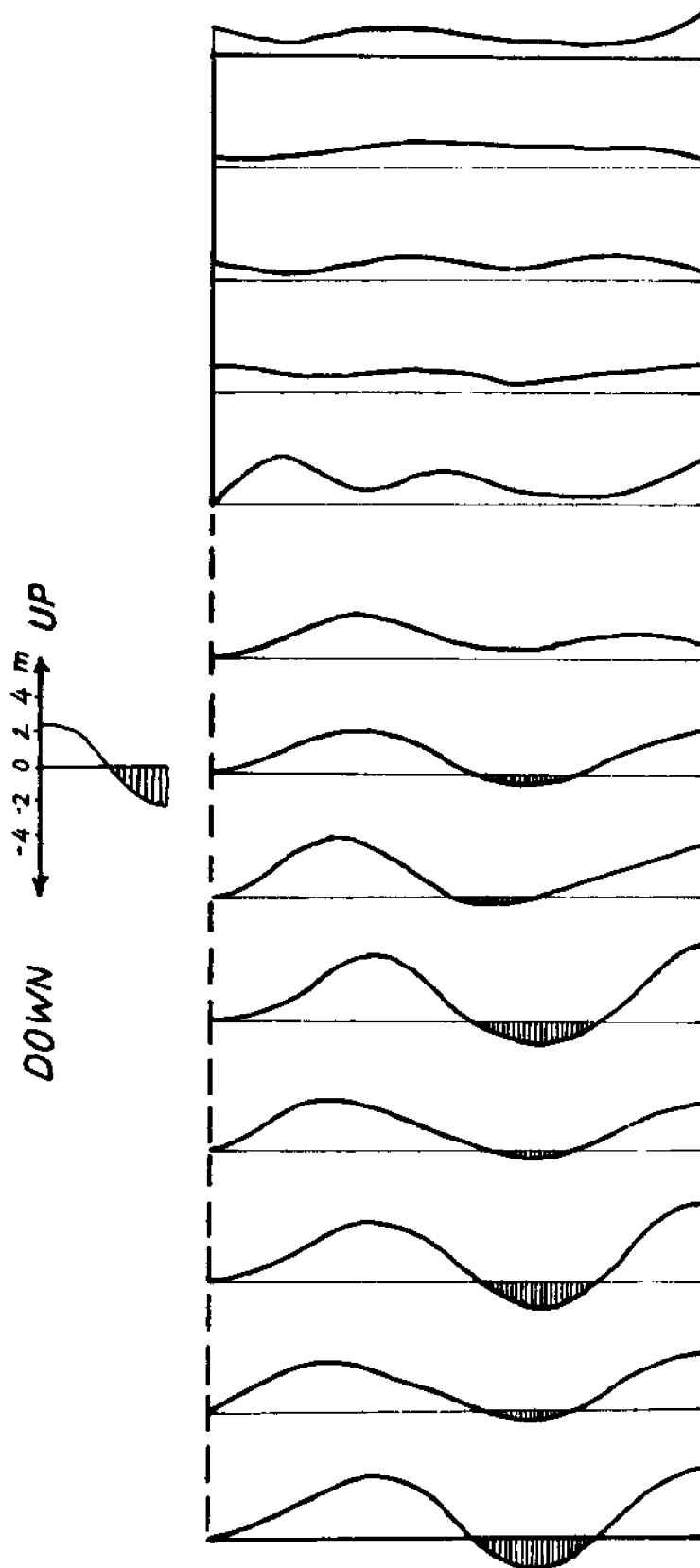
Figure 12-8.
Rectangular approximation of Massachusetts Bay.
94 Node Grid. Interface displacement, 3.2 T (145000Sec.) after startup.
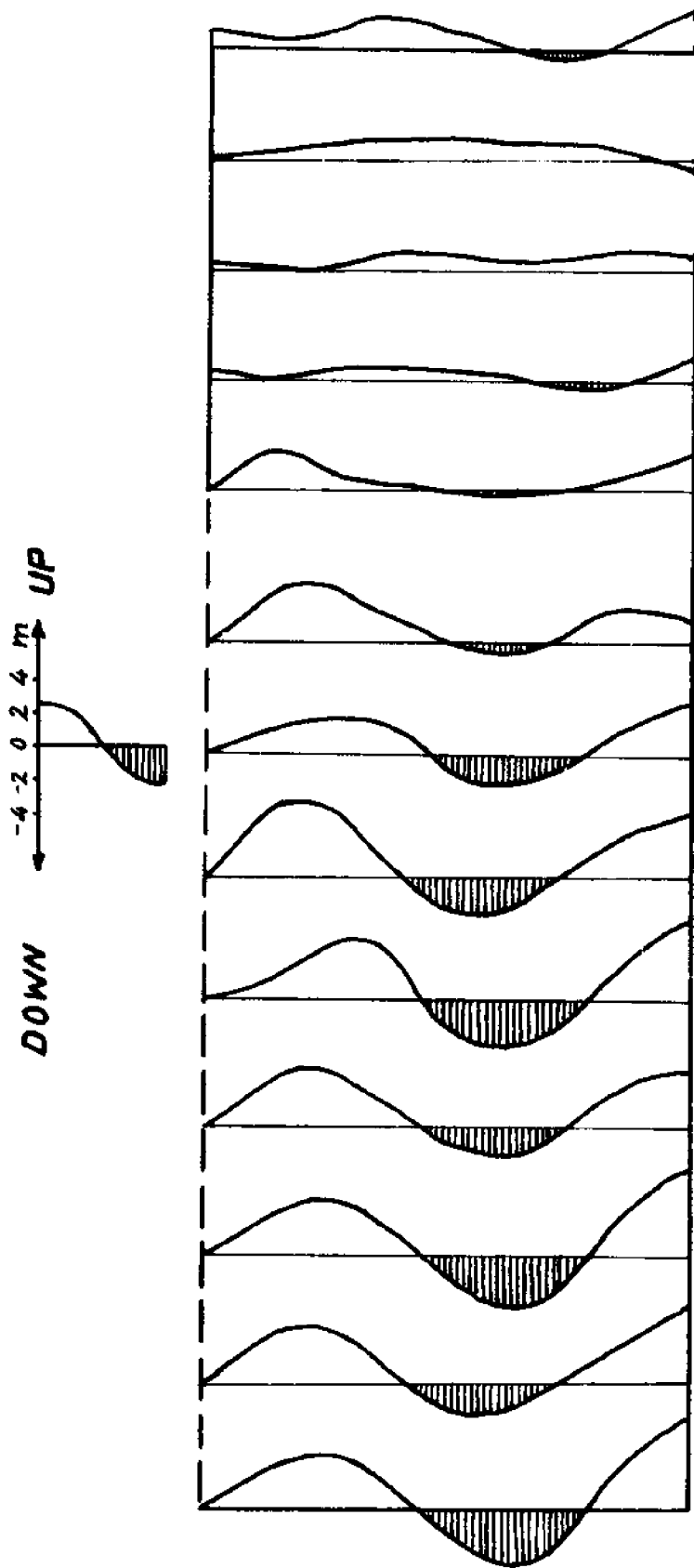
Figure 12-9.
Rectangular approximation of Massachusetts Bay.
94 Node grid. Interface displacement, 4.2 T (187500 sec.) after startup.
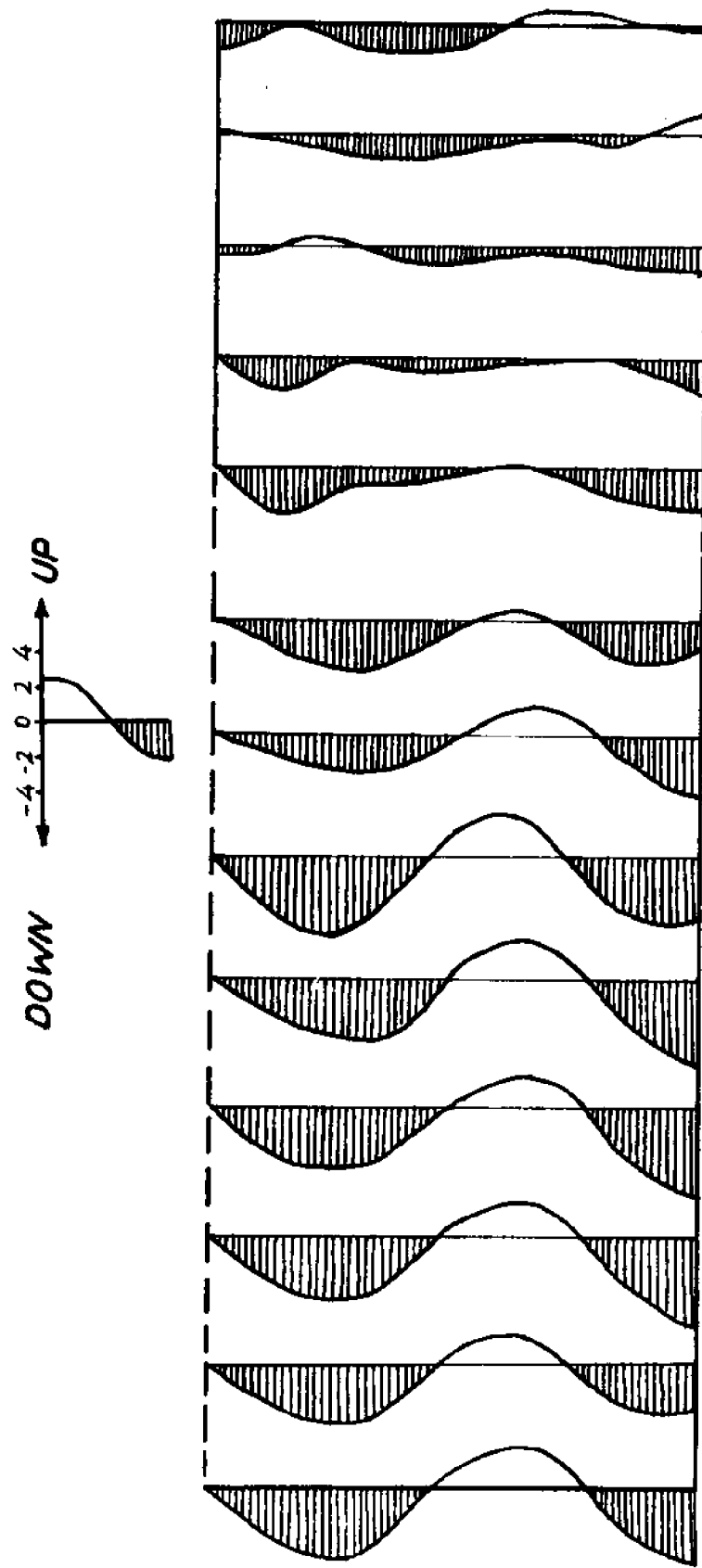
Figure 12-10.

Rectangular approximation of Massachusetts Bay.
94 Node Grid. Interface displacement, 4.8 T (212500 Sec.) after startup.
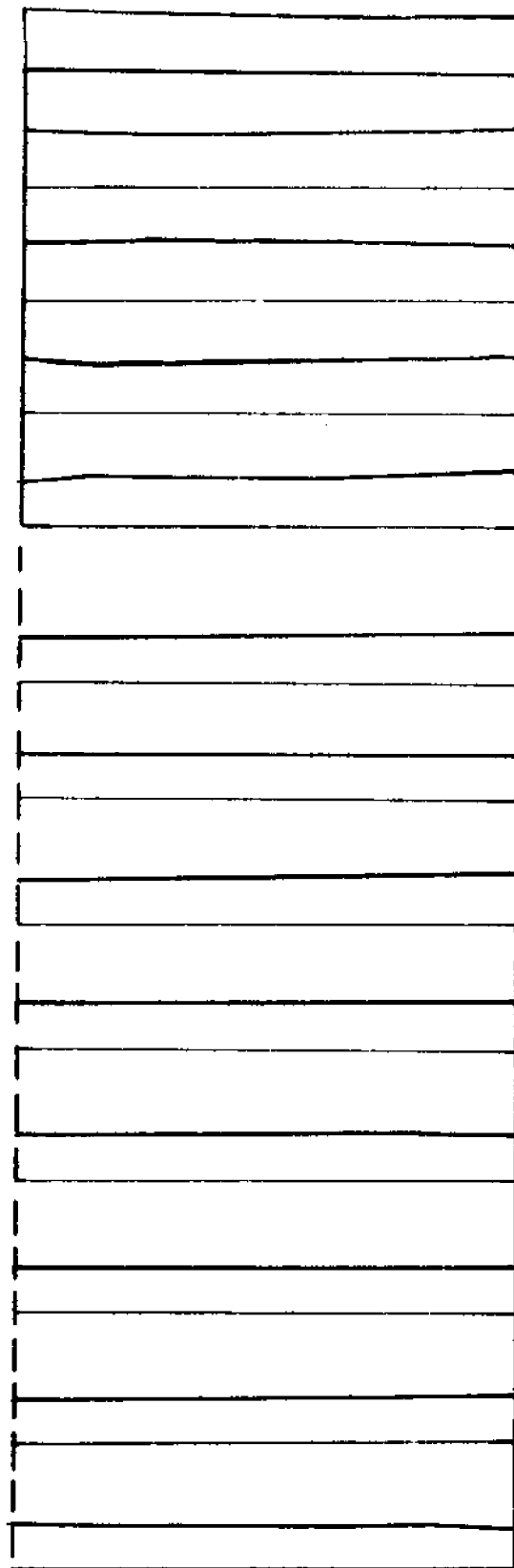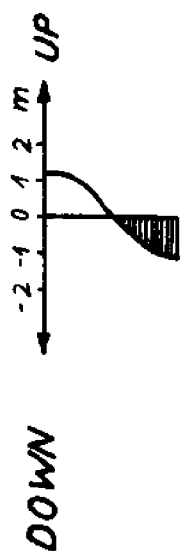
Figure 12-11.

Rectangular approximation of Massachusetts Bay.
94 Node grid. Surface displacement, 4.3 T (192500 sec) after startup.
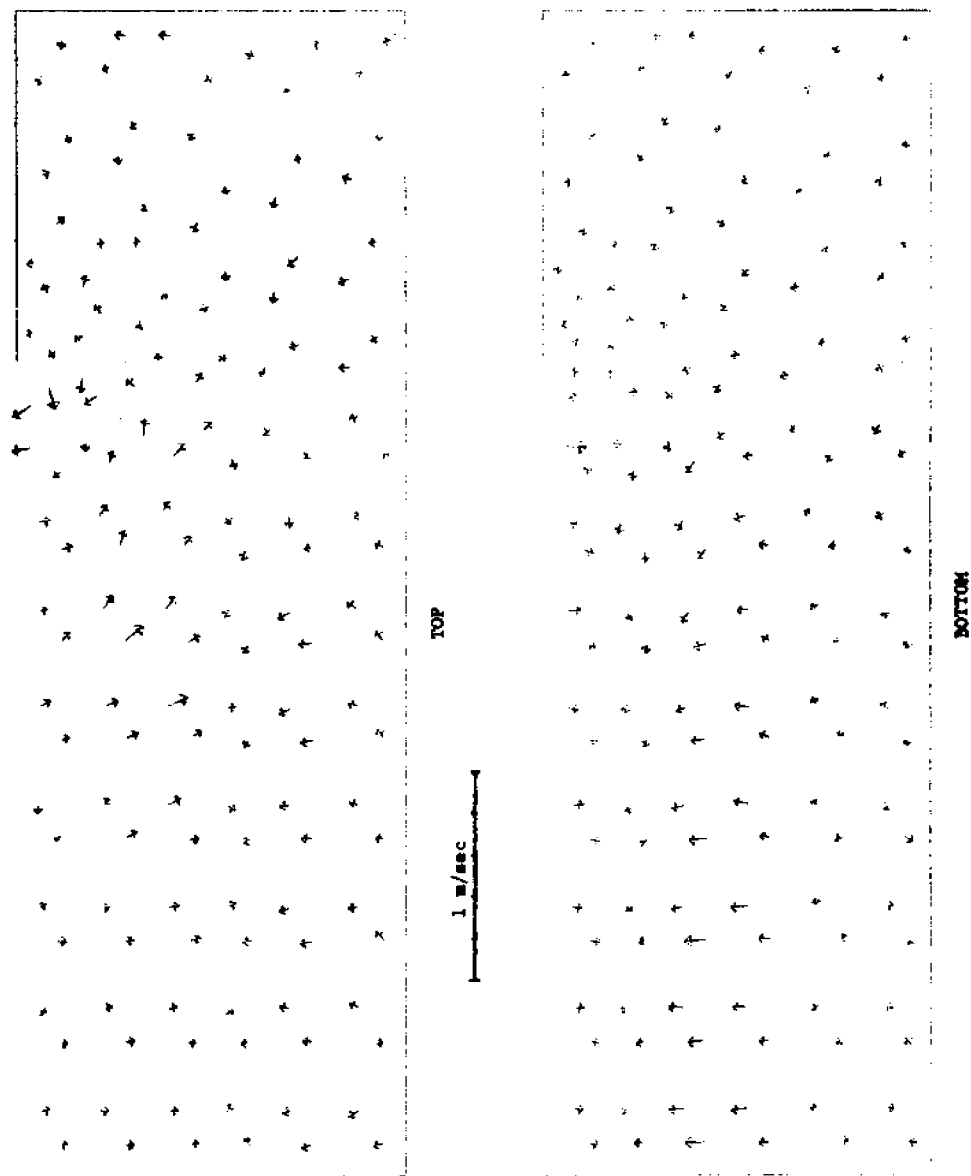
Figure 12-12. Currents in two layer approximation of Mass Bay. 182500 sec = 4.06 T after startup.

TOP

BOTTOM

1 m/sec

top

bottom
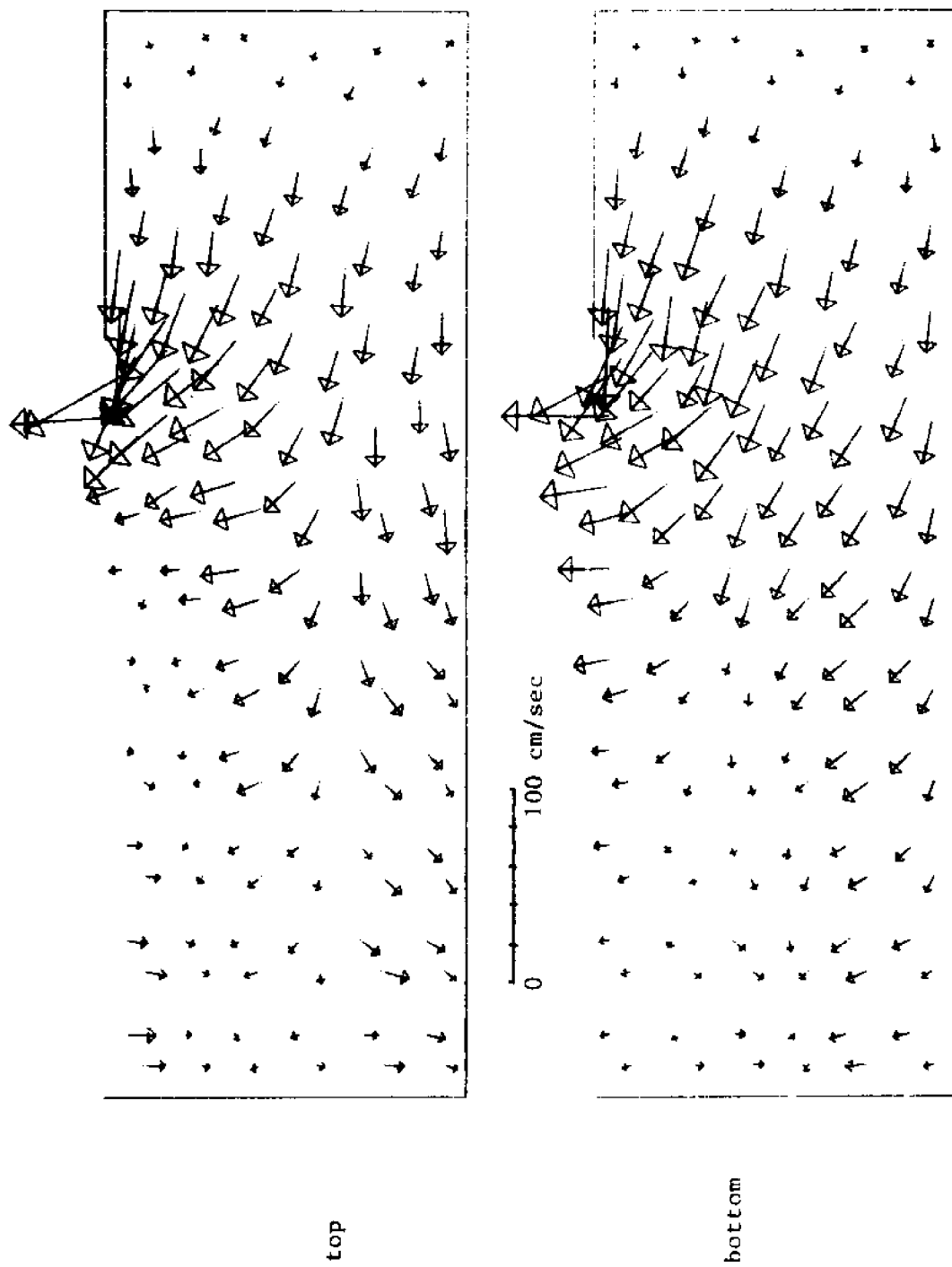
Figure 12-13. Currents in two layer approximation of Mass. Bay. 192500 sec = 4.28 T after startup.

100 cm/sec

0

249
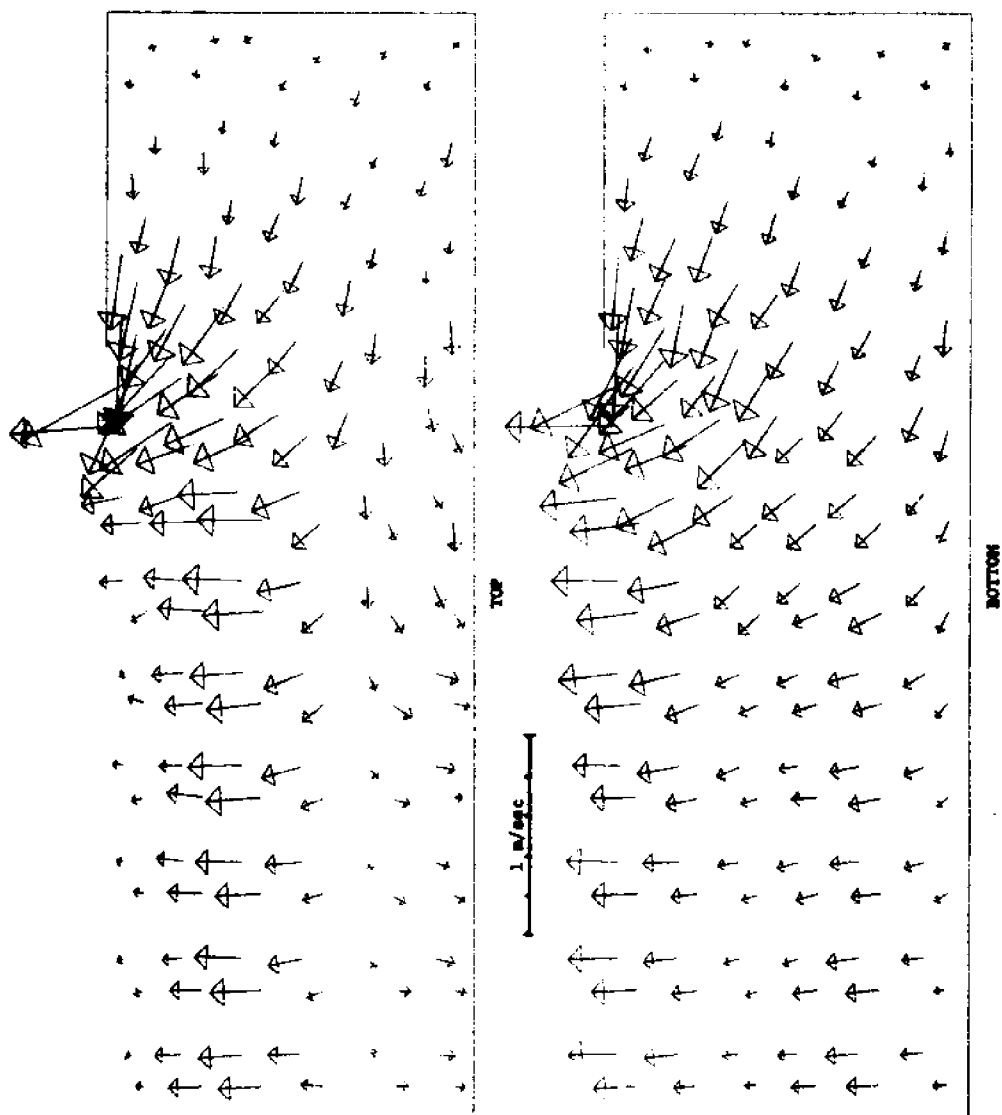
Figure 12-14. Currents in two layer approximation of Mass. Bay. 195000 sec = 4.33 T after startup.

250
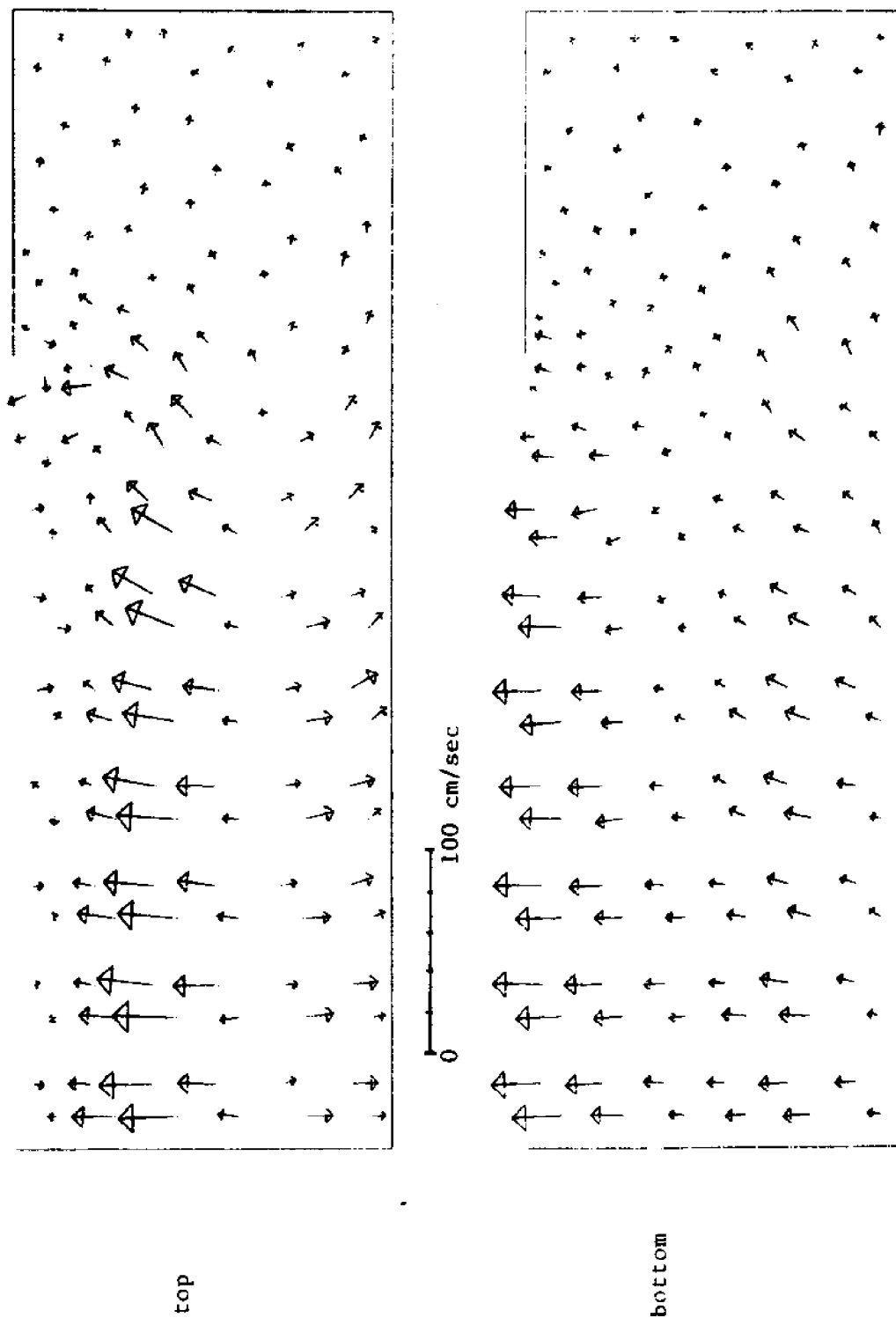
Figure 12-15. Currents in two layer approximation of Mass. Bay. 197500 sec = 4.38 T after startup.

top

bottom

100 cm/sec

top

bottom

100 cm/sec

0
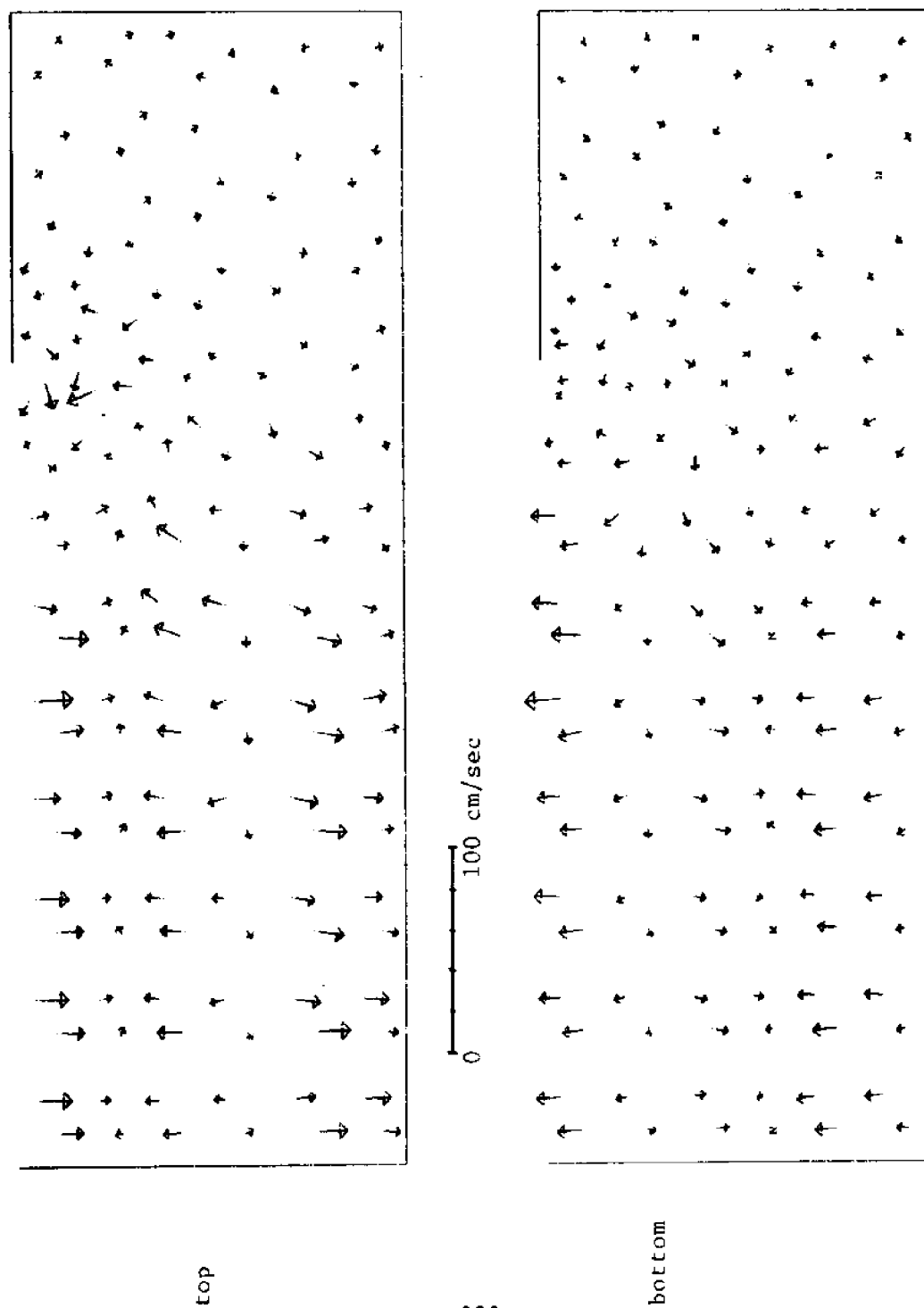
Figure 12-16. Currents in two layer approximation of Mass. Bay. 200000 sec = 4.44 T after startup.

252

top

bottom

100 cm/sec
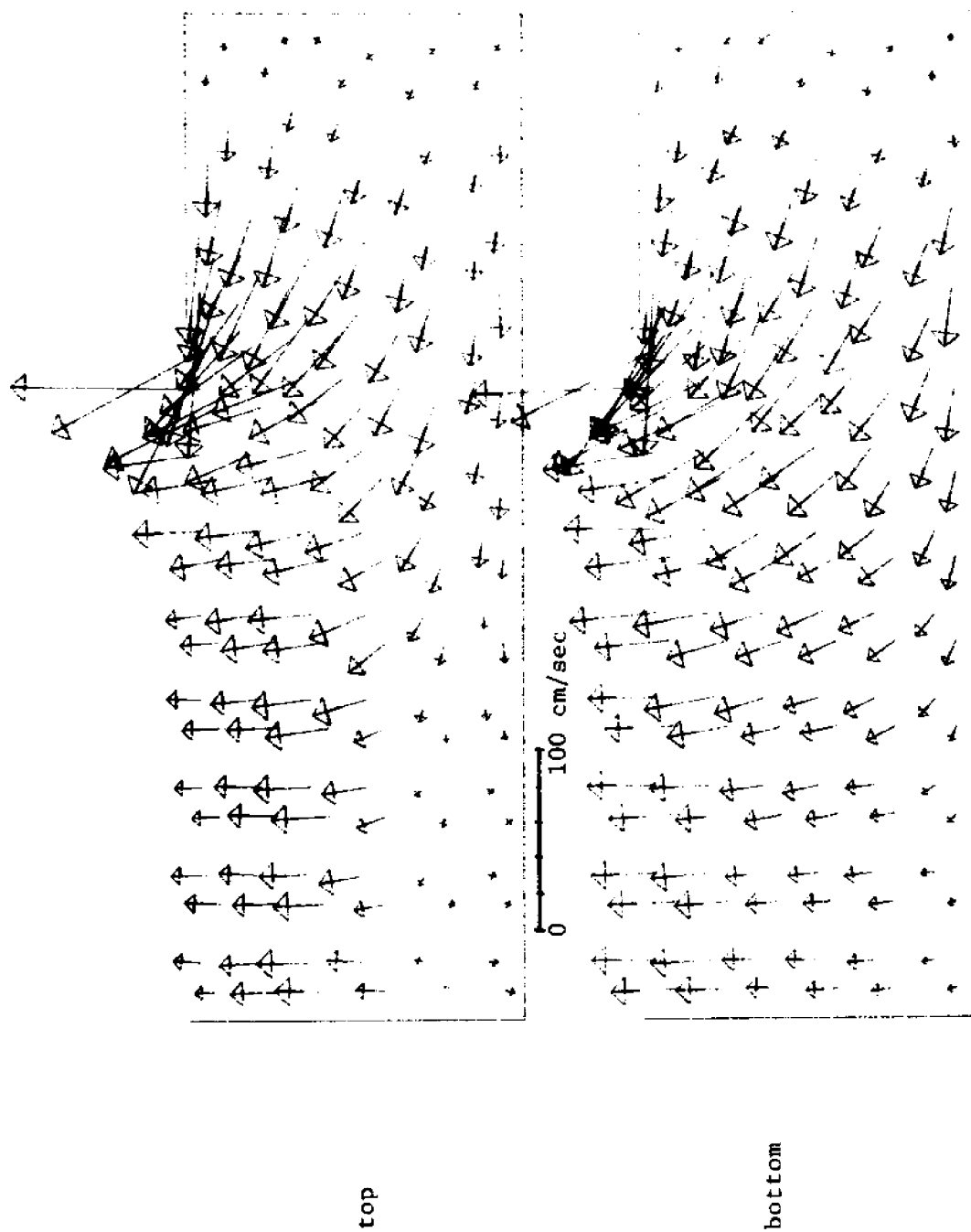
Figure 12-17. Currents in two layer approximation of Mass. Bay. 205000 sec = 4.55 T after startup.

253

top

bottom

0 — 100 cm/sec
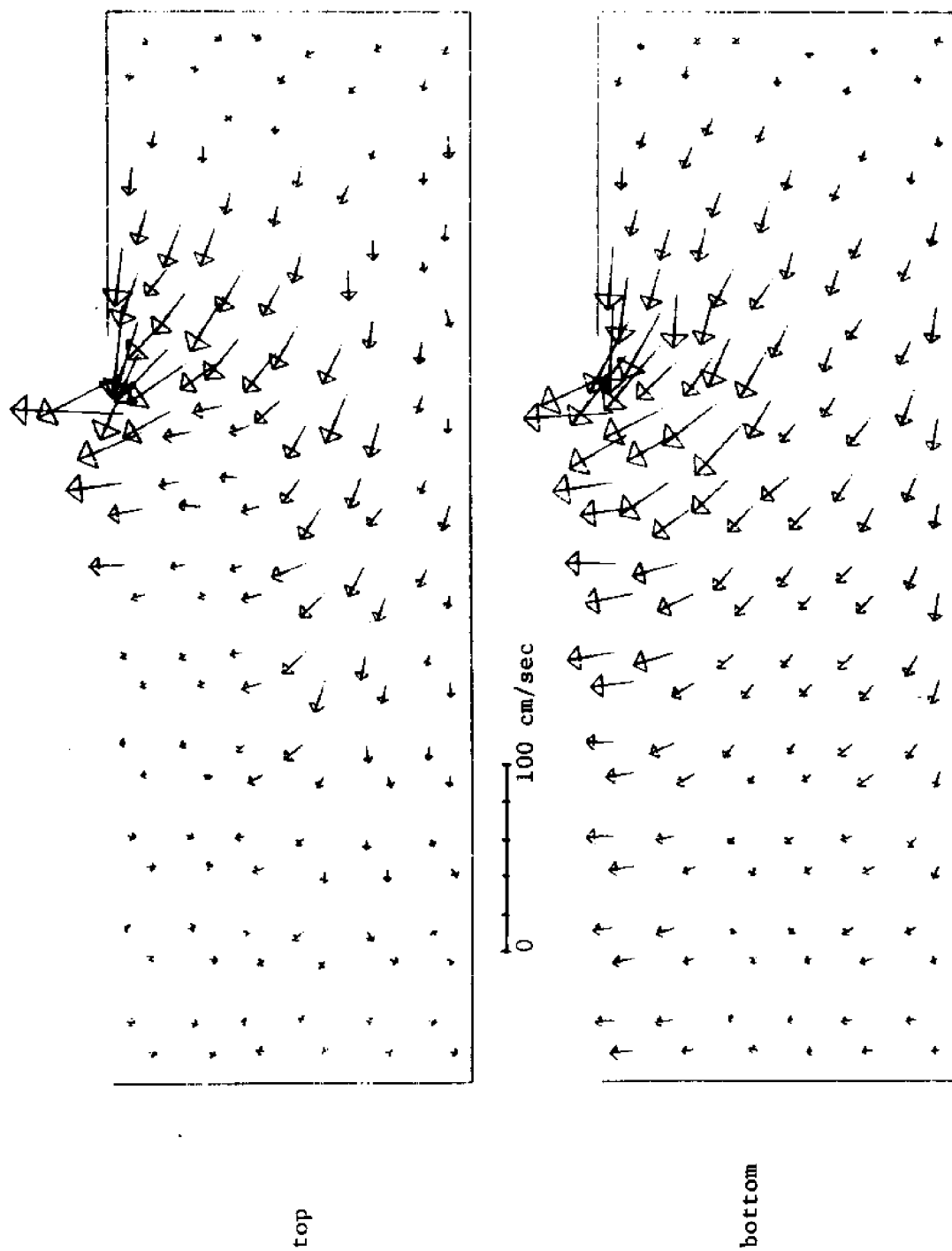
Figure 12-18. Currents in two layer approximation of Mass. Bay. 207500 sec = 4.61 T after startup.

TOP

BOTTOM

1 m/sec
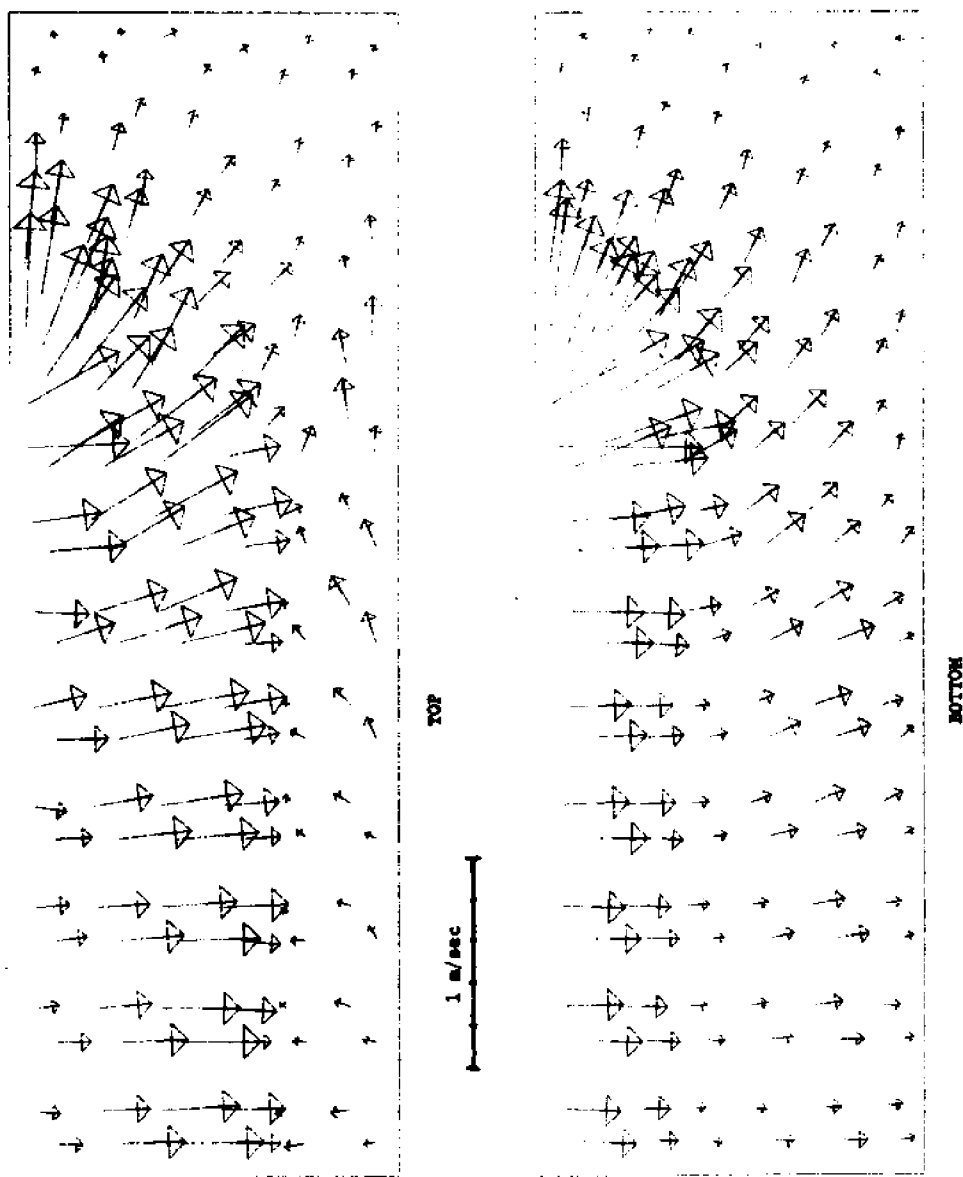
Figure 12-19. Currents in two layer approximation of Mass. Bay. 220000 sec = 4.89 T after startup.

255

TOP

BOTTOM

1 m/sec
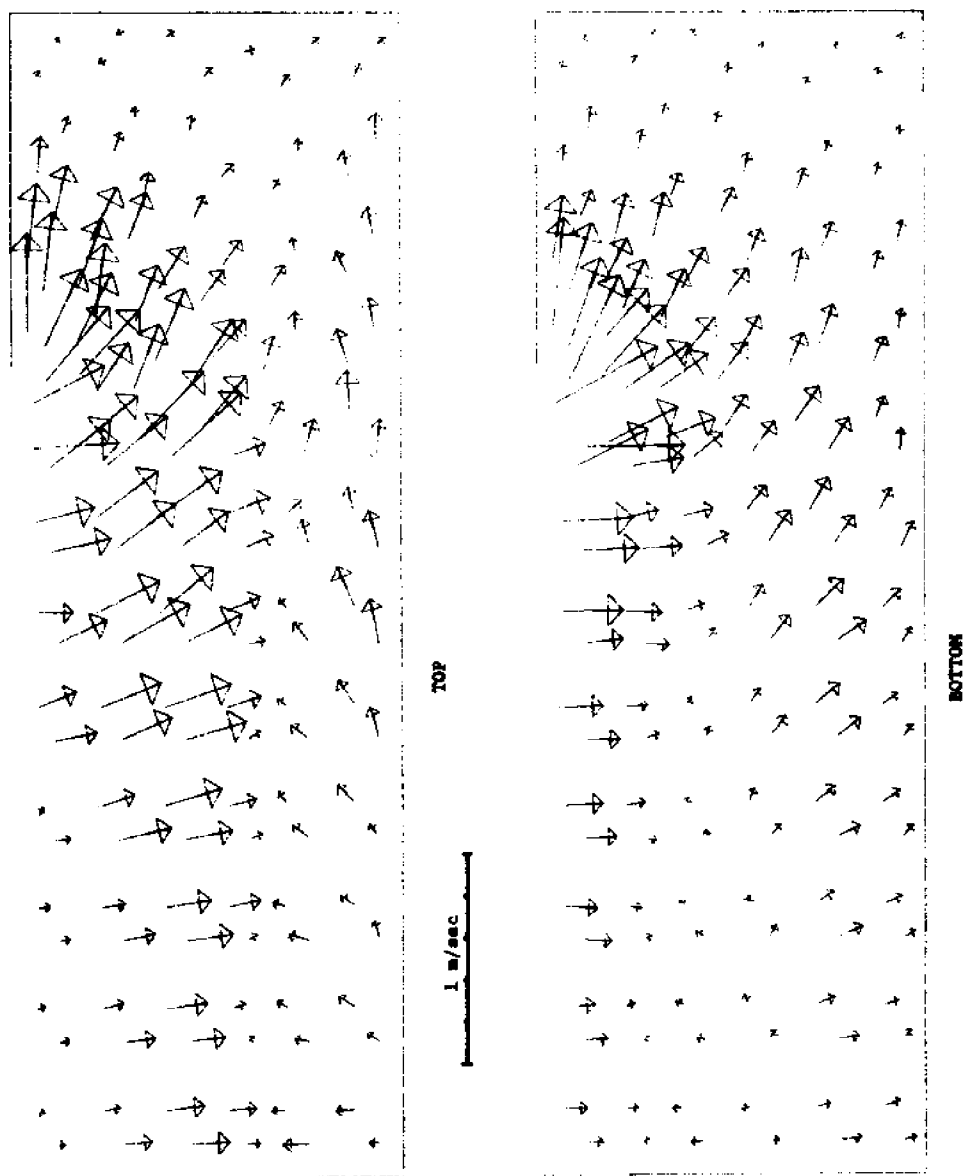
Figure 12-20. Currents in two layer approximation of Mass. Bay. 225000 sec = 5 T after startup.

CHAPTER 13

CONCLUSION

Much experience has been gained through applications of the one layer model. It is a powerful and efficient computer based tool for predicting circulation when applied to situations for which it is intended. These are predominantly long wave propagation and streamflow simulations in vertically homogeneous shallow (<200m) water bodies. Long period wind driven circulation is also handled well by the model. However, due to the relatively slow growth of a boundary layer from the surface, only total mass transport is predicted for short period wind events. As a first approximation the model can also be used to predict the far field circulation of an intake outfall system, such as employed for cooling by large electric generating plants.

A well defined simulation problem necessarily requires specified boundary conditions. In terms of the natural dependent variables, total depth and specific discharges per unit width, the correct boundary conditions consist of either prescribed normal and tangential force measures or normal and tangential discharges. Existing field monitoring programs presently do not satisfy these minimal requirements, partly because of inadequate technology. However, to improve modeling accuracy, it is important that consistent measurements in the field are obtained.

The finite element spatial discretization is found to be superior to other approaches for general purpose model systems. The flexibility of the grid layout is an enormous advantage. More accurate models (i.e. with higher order truncation errors) are easily constructed. Several applications have shown that reasonable solutions are found

even with quite coarse grids.

For temporal discretization we employ finite difference schemes. Since there are no topographical problems in the time domain it is easier to construct an efficient finite difference scheme. Stability analysis of FE generated systems of differential equations is still in an embryonic stage. The difficulty in establishing stability criteria, and not having the possibility of "playing" with combinations of space and time discretizations, are presently the main objections to the FEM. For the one layer model we proved stability in a linear initial value problem sense. However, we have been able to exceed the critical time step for explicit FDM, only by approximately 50%. More research is needed in this area.

Analysis and many verification studies have established the accuracy of computed solutions to the formulated problem.

To improve predictions in transient wind and stratified situations a two layer idealized model has been developed. Although multi layer models can be and have been constructed to better describe the flow patterns, it is felt that in most cases the uncertainty and inaccuracy of measurements in the field cannot justify the use of more than two layers.

An attempt to determine the interfacial mass and momentum transfers from published studies is not conclusive. The strategy in using the two layer model is therefore to try to bracket a solution by performing sensitivity studies on the various parameters. Open ocean boundary conditions present a major problem inherent in all types of models. This necessitates extensive field monitoring programs, a point which

perhaps cannot be over emphasized.

Future model development work could try to approach the problems of having a moving land boundary for the lower layer and in flooding situations also of the top layer. With implementation of a mass balance equation to predict the changes in density, one also has to address the problem of instability in the density structure. Lastly, the ultimate objective of circulation studies should not be forgotten, namely prediction of transport and spreading of dissolved or suspended matter.

REFERENCES

1. Abbott, M.B., et al., "System 21, Jupiter", Journal of Hydraulic Research, Vol. 11, No. 1, 1973.

2. Abbott, M.B., Grubert, J.P., "Towards a Design System for Stratified Flows", Int. Symp. on Stratified Flows, IAHR, Novosibirsk, 1972.

3. Aranha , J., "Private Communication", 1974.

4. Batchelor, G.K., "An Introduction to Fluid Dynamics", Cambridge University Press, 1967.

5. Bengtsson, L., "Wind Stress on Small Lakes", Tekniska Högskolan, Lund, 1973.

6. Chan, S.T.K., et al., "Free-Surface Ideal Fluid Flows by Finite Elements", Journal Hydraulics Division, ASCE, Hy 6, June 1973.

7. Christodoulou, G.C., et al., "A Mathematical Model for the Dispersion of Suspended Sediments in Coastal Waters", TR 179, R.M. Parsons Laboratory for Water Resources and Hydrodynamics, M.I.T., January 1974.

8. Christodoulou, G.C., "Private Communication", R.M. Parsons Laboratory for Water Resources and Hydrodynamics, M.I.T., 1975.

9. Codell, R.B., "Digital Computer Simulation of Thermal Effluent Dispersion in Rivers, Lakes and Estuaries", TR-73-16, U.S. Army Missile Command, Redstone Arsenal, Alabama.

10. Connor, J.J., "A Survey of Finite Element Methods in Continuum Mechanics", Variational Methods in Engineering,Proceedings, Southampton, September, 1972.

11. Connor, J.J., "Fundamentals of Finite Element Techniques", Butterworth, London, 1973.

12. Connor, J.J., et al., "Mathematical Models of the Massachusetts Bay, Part 1 and Part 2", TR 172, R.M. Parsons Laboratory for Water Resources and Hydrodynamics, M.I.T., October, 1973.

13. Crickmore, M.J., "Tracer Tests of Eddy Diffusion in Field and Model", Journal of Hydraulics Division, Hy 10, October, 1972, ASCE.

14. Csanady, G.T., "Turbulent Diffusion in Lake Huron", Journal of Fluid Mechanics, V17, 1963.

15. Daily, J.W., Harleman, D.R.F., "Fluid Dynamics", Addison-Wesley, 1966.

16. Denman, K.L., Miyake, M., "Behavior of the Mean Wind, The Drag Coefficient, and the Wave Field in the Open Ocean", Journal of Geophysical Research, Vol. 78, No. 12, April 20, 1973.

17. Dorman, C.E., "The Relationship Between Microscales and Wind Wave Spectral Development", Ph.D. Thesis, M.I.T., November, 1971.

18. Dronkers, J.J., "Tidal Computations for Rivers, Coastal Areas, and Seas", Journal Hydraulics Division, ASCE, HY 1, January, 1969.

19. Eraslan, A.H., "A Transient, Two-Dimensional Discrete-Element Model for Far-Field Analysis of Thermal Discharges in Coastal Regions", Proceedings Conference on Thermal Pollution Analysis, Virginia Polytechnic Institute and State University, May, 1974.

20. Finlayson, G.A., Scriven, L.E., "The Method of Weighted Residuals and Its Relation to Certain Variational Principles for the Analysis of Transport Processes", Chemical Engineering Science, Vol. 20, 1965.

21. Fröberg, G.E., "Lärobok Numerisk Analys", Svenska Bokförlaget Bonniers, 1962.

22. Gallagher, R.H., et al., "Finite Element Shallow Lake Circulation Analysis", Journal Hydraulics Division, ASCE Hy 7, July 1973.

23. Gedney, R.T., et al., "Effect of Eddy Diffusivity on Wind-Driven Currents in a Two-Layer Stratified Lake", T.N. E-6776, Lewis Research Center, NASA, Cleveland, Ohio, June 1972.

24. Gedney, R.T., Lick, W., "Wind-Driven Currents in Lake Erie", Journal of Geophysical Research, Vol. 77, No. 15, May 20, 1972.

25. Groscup, W.D., "Observations of the Mean Wind Profile Over the Open Ocean", M.S. Thesis, M.I.T., November, 1971.

26. Grotkop, G., "Finite Element Analysis of Long-Period Water Waves", Computer Methods in Applied Mechanics and Engineering, Vol. 2, No. 2, May, 1973.

27. Hansen, W., "Theorie zur Errechnung des Wasserstandes und der Strömungen in Randmeeren Nebst Anwendungen", Tellus, Vol. 8, No. 3, August, 1956.

28. Heaps, N.S., "A Two-Dimensional Numerical Sea Model", Royal Society of London, Philosophical Transactions, Ser. A, Vol. 265, No. 1160, October, 1969.

29. Hildebrand, F.B., "Advanced Calculus for Engineers", Prentice-Hall, 1962.

30. Hydén, H., "Språngskiktsrörelser och Turbulens i Densitetsskiktade Vatten", Kungl. Tekniska Högskolan, Inst. för Vattenbygnad, Stockholm, 1974.

31. Hydén, H., "Water Exchange in Two-Layer Stratified Waters", Journal Hydraulics Division, ASCE, HY 3, March 1974.

32. Ippen,A.T., (ed), "Estuary and Coastline Hydrodynamics", McGraw-Hill 1966.

33. Karelse, M. et al., "Momentum and Mass Transfer in Stratified Flows", R880, Delft Hydraulics Laboratory, December 1974.

34. Ladyzhenskaya, O.A., "The Mathematical Theory of Viscous Incompressible Flow", Gordon and Breach, 1969.

35. Laevastu, T. et al., "A Vertically Integrated Hydrodynamical-Numerical Model", (Part 1 of four reports), Environmental Prediction Research Facility, Naval Postgraduate School, Technical Note No 1-74, January 1974.

36. Lamb, H., "Hydrodynamics", Dover, 1945.

37. Lean, G.H., Whillock, A.F., "The Behavior of a Warm Water Layer Flowing Over Still Water", Proc. IAHR, 11th Congress, Lenningrad, 1965.

38. Leendertse, J.J., "Aspects of a Computational Model for Long-Period Water-Wave Propagation", Memorandum, RM-5294-PR, Rand Corporation, May 1967.

39. Leendertse, J.J., et al., "A Three-Dimensional Model for Estuaries and Coastal Seas", R-1417-OWRR, Rand, Santa Monica, California, December 1973.

40. Leonard, J.W., Melfi, D., "3-D Finite Element Model for Lake Circulation", Proc. 3rd Conference on Matrix Methods in Structural Mechanics, Dayton, Ohio 1971.

41. Liggett, J.A., "Unsteady Circulation in Shallow, Homogeneous Lakes", Journal Hydraulics Division, ASCE, HY 4, July 1969.

42. Liggett, J.A., Lee, K.K., "Properties of Circulation in Stratified Lakes", Journal Hydraulics Division, ASCE, HY 1, January 1971.

43. Liggett, J.A., Woolhiser, D.A., "Difference Solutions of the Shallow-Water Equation", Journal Engineering Mechanics Division, ASCE, EM 2, April 1967.

44. McCarey, K., Cooper, J.W., "Winter Inlet Current Study, Atlantic Generating Site", TR 3, EG&G, Waltham, Mass.

45. McNider, R.T., O'Brien, J.J., "A Multi-Layer Transient Model of Coastal Upwelling", Journal of Physical Oceanography, Vol. 3, No. 3, July 1973.

46. Mikhlin, S.G., "Variational Methods in Mathematical Physics", Pergamon, 1964.

47. Mitchell, A.R., "Computational Methods in Partial Differential Equations", J. Wiley & Sons, 1969.

48. Noble, B., "Applied Linear Algebra", Prentice-Hall, 1969.

49. Norton, W.R., et al., "A Finite Element Model for Lower Granite Reservoir", Water Resources Engineers, Inc., Walnut Creek, California, March 1973.

50. Oden, J.T., et al. (eds.), "Finite Element Methods in Flow Problems", UAH Press, University of Alabama, Huntsville, Alabama, 1974.

51. Oden, J.T., Wellford, L.E, Jr., "Analysis of Flow of Viscous Fluids By the Finite Element Method", AIAA, Vol. 10, No. 12, December 1972.

52. Okubo, A., Pritchard, "Summary of Our Present Knowledge of the Physical Processes of Mixing in the Ocean and Coastal Waters", Chesapeake Bay Institute, Johns Hopkins, Ref. 69-1. September 1969.

53. Pagenkopf, J.R., Pearce, B.R., "Evaluation of Techniques for Numerical Calculation of Storm Surges", TR 199, R.M. Parsons Laboratory for Water Resources and Hydrodynamics, M.I.T., February 1975.

54. Palmer, M.D., Izatt, J.B., "Dispersion Prediction from Current Meters", Journal of Hydraulic Division, ASCE, HY 8, August 1970.

55. Parker, B.B., Pearce, B.R., "The Response of Massachusetts Bay to Wind Stress", TR 198, R.M. Parsons Laboratory for Water Resources and Hydrodynamics, M.I.T., February 1975.

56. Partridge, P., Brebbia, C., "Suitability of Higher Order Finite Element Models for Shallow Water Problems", Dept. of Civil Engineering, University of Southampton, November 1974.

57. Phillips, O.M., "The Dynamics of the Upper Ocean", Cambridge University Press, 1966.

58. Ralston, A., "A First Course in Numerical Analysis", McGraw-Hill, 1965.

59. Reid, R.O., Bodine, B.R., "Numerical Model for Storm Surges in Galveston Bay", Journal Waterways and Harbours Division, ASCE, WW1, February 1968.

60. Richtmeyer, R.D., Morton, K.W., "Difference Methods for Initial-Value Problems", Interscience, 1967.

61. Roache, P.J., "Computational Fluid Dynamics", Hermosa, 1972.

62. Schlichting, H., "Boundary-Layer Theory", McGraw-Hill, 1968.

63. Siman-Tov, M., "A Time Dependent, Two-Dimensional Mathematical Model for Simulating the Hydraulic, Thermal and Water Quality Characteristics in Shallow Water Bodies", ORNL-TM-4626, Oak Ridge National Laboratory, Oak Ridge, Tennessee, August 1974.

64. Simons, T.J., "Development of Numerical Models of Lake Ontario", Proceedings 14th Conference Great Lakes Research, 1971.

→65. Simons, T.J., "Development of Three-Dimensional Numerical Models of the Great Lakes", Proceedings 15th Conference on Great Lakes Research, 1972.

66. Sobey, R.J., "Finite-Difference Schemes Compared for Wave-Deformation Characteristics in Mathematical Modeling of Two-Dimensional Long-Wave Propagation", T.M. 32, U.S. Army Corps of Engineers, CERC, October 1970.

67. Starr, V.P., "Physics of Negative Viscosity", McGraw-Hill, 1968.

68. Strang, G., Fix, G.J., "An Analysis of the Finite Element Method", Prentice-Hall, 1973.

69. Taylor, C., Davis, J., "Tidal and Long Wave Propagation – A Finite Element Approach", Department of Civil Engineering, University College of Swansea, C/R/189/72.

70. Tracor, "Estuarine Modeling: An Assessment", Report Prepared for EPA, February 1971.

71. Tsai, Y.J., Chang, Y.C., "Two Dimensional Transient Hydro-Thermal Mathematical Model", 1st World Congress on Water Resources, Chicago, September 1973.

72. U.S. Department of Commerce, NOAA, Nos, "Tidal Current Tables", 1974.

73. U.S. Department of Commerce, NOAA, Nos, "Tide Tables", 1975.

74. Van Dorn, W., "Wind Stress on an Artificial Pond", Journal of Marine Research, Vol. 12, No. 3, 1953.

75. Wada, A., "Study of Thermal Diffusion in a Two-Layer Sea Caused by Outfall of Cooling Water", International Symposium on Stratified Flows, IAHR, Novosibirsk, 1972.

76. Welander, P., "Wind Action on a Shallow Sea: Some Generalizations of Ekman's Theory", Tellus, Vol. 9, No. 1, January 1957.

77. Whitaker, R.E., et al., "Drag Coefficients at Hurricane Wind Speeds as Deduced from the Numerical Simulation of Dynamical Water Level Changes in Lake Okeechobee", Ref. 73-13-5, Texas A&M, August 1973.

78. Wiegel, R.L., Johnson, J.W., "Ocean Currents, Measurement of Currents and Analysis of Data", Journal Water Pollution Control Federation, Vol. 38, No. 7, July 1966.

79. Wu, J., "Wind Stress and Surface Roughness at Air-Sea Interface", Journal of Geophysical Research, Vol. 74, No. 2, January 1969.

80. Zienkewicz, O.C., Cheung, Y.K., "The Finite Element Method in Structural and Continuum Mechanics", McGraw-Hill, 1967.

81. Zienkewicz, O.C., "The Finite Element Method in Engineering Sciences", McGraw-Hill, 1971.

BIOGRAPHY

John D. Wang was born in Copenhagen, Denmark in 1948. After graduating from the Technical University of Denmark with a M.Sc. degree in Civil Engineering in June 1971, he continued as a graduate student and full time research assistant at M.I.T. He was married to Josephine in December 1974 and finished his Ph.D. degree in Civil Engineering in April 1975.

Publications:

"Interaction between waves and currents", Proc., Twelfth Coastal Engineering Conf., September 1970, Washington, D.C. (Published with I.G. Jonsson, C. Skougaard).

"Finite element modeling of hydrodynamic circulation", International Conf. on Numerical Methods in Fluid Dynamics, September 1973, University of Southampton, England (With J.J. Connor).

"Finite element model of two layer coastal circulation", Proc., Fourteenth Coastal Engineering Conf., June 1974, Copenhagen, Denmark (With J.J. Connor).

APPENDIX A

DERIVATION OF FINITE ELEMENT ANALOGUE FOR THE

EQUATIONS OF MOTION

Following the same approach as in Chapter 5, the equation for an arbitrary element is first developed. Thereafter, the system equations are easily obtained by summing the contributions from all the elements. Where nothing else is mentioned, a variable is assumed expanded according to (5.13).

Starting with Equation (4.29), we find term by term

$$(A.1) \qquad \int_{A_1} q_{x,t} \, \Delta q_x \, dA \;=\; \Delta q_x^T \int_{A_1} \phi^T \, \phi \, dA \, Q_{x,t} \;=\; \Delta q_x^T \, M \, Q_{x,t}$$

Defining

$$(A.2) \qquad c_{ij} \;=\; \frac{q_i q_j}{H} \qquad i,j \;=\; x,y$$

the convective terms are written

$$(A.3) \qquad \int_{A_1} (\bar{u} q_x)_{,x} \, \Delta q_x \, dA \;\simeq\; \Delta q_x^T \int_{A_1} \phi^T \, \phi_{,x} \, dA \, c_{xx}$$

$$(A.4) \qquad \int_{A_1} (\bar{u} q_y)_{,y} \, \Delta q_x \, dA \;\simeq\; \Delta q_x^T \int_{A_1} \phi^T \, \phi_{,y} \, dA \, c_{xy}$$

$$(A.5) \qquad \int_{A_1} - f q_y \, \Delta q_x \, dA \;=\; -f \Delta q_x^T \int_{A_1} \phi^T \, \phi \, dA \, Q_y \;=\; -\Delta q_x^T \, f \, M \, Q_y$$

Letting $\dfrac{\tau_x^s}{\rho_0} \;=\; \phi^T_x{}^s$

$$(A.6) \quad \int_{A_1} \frac{1}{\rho_0} \tau_x^s \, \Delta q_x \, dA = \Delta q_x^T \int_{A_1} \phi^T \phi \, dA \, T_x^s = \Delta q_x^T \, M \, T_x^s$$

Assuming

$$(A.7) \quad (q_x^2 + q_y^2)^{1/2} \frac{q_x}{H^2} = \phi \, T_x^b$$

leads to

$$(A.8) \quad -\int_{A_1} \frac{1}{\rho_0} \tau_x^b \, \Delta q_x \, dA = -\Delta q_x^T \int_{A_1} C_f \, \phi^T \phi \, dA \, T_x^b = -\Delta q_x^T \, C_f \, M \, T_x^b$$

$$(A.9) \quad -\int_{A_1} \overline{m}_x \, \Delta q_x \, dA = -\Delta q_x^T \int_{A_1} \phi^T \phi \, dA \, M_x = -\Delta q_x^T \, M \, M_x$$

$$(A.10) \quad -\frac{1}{\rho_0} \int_{A_1} p^s \, H_{,x} \Delta q_x \, dA = -\Delta q_x^T \frac{1}{\rho_0} \int_{A_1} \phi^T \phi \, P^s \, \phi_{,x} \, dA \, H =$$

$$-\Delta q_x^T \frac{1}{\rho_0} \, M \, P^s \, \frac{1}{2A_1} (a_1 \, H_1 + a_2 H_2 + a_3 \, H_3)$$

$$(A.11) \quad -\frac{g}{\rho_0} \int_{A_1} \Delta \rho H \, h_{,x} \, \Delta q_x \, dA = \Delta q_x^T \frac{g}{\rho_0} \int_{A_1} \phi^T \phi \, \Delta \rho \, \phi \, H \, \phi_{,x} \, h \, dA$$

$$(A.12) \quad -g \int_{A_1} \eta \, h_{,x} \Delta q_x \, dA = -\Delta q_x^T \, g \int_{A_1} \phi^T \phi \, \eta \, \phi_{,x} \, h \, dA$$

$$(A.13) \quad -\int_{A_1} F_p \, \Delta q_{x,x} \, dA = -\int_{A_1} \{ g h \eta + \frac{1}{2} \, g \eta^2 + \frac{1}{2} \frac{\Delta \rho}{\rho_0} \, g H^2 +$$

$$\frac{p^s}{\rho_0} \, H \} \, \Delta q_{x,x} \, dA = -\Delta q_x^T \int_{A_1} \phi_{,x}^T \{ g \, \phi \, h \, \phi \, \eta +$$

$$\frac{1}{2} \, g \, \phi \, \eta \, \phi \, \eta + \frac{g}{2\rho_0} \phi \, \Delta \rho \, \phi H \, \phi \, H + \frac{1}{\rho_0} \phi \, P^s \, \phi \, H \} \, dA$$

$$(A.14) \quad \int_{A_1} F_{xx} \, \Delta q_{x,x} \, dA = \Delta q_x^T \int_{A_1} \phi_{,x}^T \, E_{xx} \, \phi_{,x} \, Q_x \, dA$$

$$\text{(A.15)} \qquad \int_{A_i} F_{yx} \, \Delta q_{x,y} \, dA = \Delta q_x^T \int_{A_i} \phi_{,y}^T \, E_{yx} \, (\phi_{,x} \, Q_y + \phi_{,y} \, Q_x) \, dA$$

$$\text{(A.16)} \qquad - \int_{S_q} \alpha_{nx} \, F_{xx} \, \Delta q_x \, ds = -\Delta q_x^T \int_{S_q} \alpha_{nx} \, \phi^T \, E_{xx} \, \phi_{,x} \, Q_x \, ds$$

$$\text{(A.17)} \qquad \int_{S_q} \alpha_{nx} \, F_p \, \Delta q_x \, ds = \Delta q_x^T \int_{S_q} \alpha_{nx} \, \phi^T \, \{ g \, \phi \, h \, \phi \, \eta + \tfrac{1}{2} \, g \, \phi \, \eta \, \phi \, \eta$$

$$+ \frac{g}{2\rho_0} \, \phi \, \Delta\rho \, \phi \, H \, \phi \, H + \frac{1}{\rho_0} \, \phi \, P^s \, \phi \, H \, \} \, ds$$

$$\text{(A.18)} \qquad - \int_{S_q} \alpha_{ny} \, F_{yx} \, \Delta q_x \, ds = - \Delta q_x^T \int_{S_q} \alpha_{ny} \, E_{yx} \, \phi^T (\phi_{,y} \, Q_x + \phi_{,x} \, Q_y) \, ds$$

$$\text{(A.19)} \qquad \int_{S_F} \alpha_{nx} \, F_p^* \, \Delta q_x \, ds = \Delta q_x^T \int_{S_F} \alpha_{nx} \, \phi^T \, \{ g \phi h \phi \eta^* + \tfrac{1}{2} \, g \phi \eta^* \, \phi \, \eta^*$$

$$+ \frac{g}{2\rho_0} \, \phi \, \Delta\rho \, \phi \, H^* \, \phi \, H^* + \frac{1}{\rho_0} \phi \, P^s \, \phi \, H^* \} \, ds$$

The last integral over S_q always vanishes. If we, for the moment neglect all external loads and ignore the non-linear terms, we are left with

$$\text{(A.20)} \qquad (\Delta q_x^{e_i})^T \int_{A_i} \{ \phi^T \, \phi \, Q_{x,t}^{e_i} - f \, \phi^T \, \phi \, Q_y^{e_i} - g \, \phi^T \, \phi \, \eta^{e_i} \, \phi_{,x} \, h^{e_i}$$

$$+ E_{xx}^i \, \phi_{,x}^T \, \phi_{,x} \, Q_x^{e_i} + E_{yx}^i \, \phi_{,y}^T \, (\phi_{,x} \, Q^{e_i} + \phi_{,y} \, Q_x^{e_i}) \} \, dA = 0$$

The boundary integrals have also been ignored since we are considering the interior. For slowly varying depth, i.e. $g\eta \cdot h_{,x} \ll g \, h \, \frac{\partial \eta}{\partial x}$, the third term in the integrand may also be dropped. The expression (A.20) is then written

$$(\text{A.21}) \qquad (\Delta q_{\underset{\sim}{x}}^{e_i})^T \{ \underset{\sim}{M}^i \underset{\sim}{Q}_{x,t}^{e_i} - f \underset{\sim}{M}^i \underset{\sim}{Q}_y^{e_i} - (\underset{\sim}{G}_x^i)^T \underset{\sim}{\eta}^{e_i} + \underset{\sim}{E}_{xx}^i \underset{\sim}{Q}_x^{e_i} + \underset{\sim}{E}_{yx}^i \underset{\sim}{Q}_y^{e_i} \} = 0$$

where we have used (5.21) and

$$(\text{A.22}) \qquad \underset{\sim}{E}_{xx}^k = \int_{A_k} \{ E_{xx}^k \underset{\sim}{\phi}_{,x}^T \underset{\sim}{\phi}_{,x} + E_{yx} \underset{\sim}{\phi}_{,y}^T \underset{\sim}{\phi}_{,y} \} \, dA$$

$$(\text{A.23}) \qquad \underset{\sim}{E}_{yx}^k = (\underset{\sim}{E}_{xy}^k)^T = \int_{A_k} E_{yx}^k \underset{\sim}{\phi}_{,y}^T \underset{\sim}{\phi}_{,x} \, dA$$

Exactly the same way we obtain for the y-direction

$$(\text{A.24}) \qquad (\Delta q_{\underset{\sim}{y}}^{e_i})^T \{ \underset{\sim}{M}^i \underset{\sim}{Q}_{y,t}^{e_i} + f \underset{\sim}{M}^i \underset{\sim}{Q}_x^{e_i} - (\underset{\sim}{G}_y^i)^T \underset{\sim}{\eta}^{e_i} + \underset{\sim}{E}_{xy}^i \underset{\sim}{Q}_x^{e_i} + \underset{\sim}{E}_{yy}^i \underset{\sim}{Q}_y^{e_i} \} = 0$$

where

$$(\text{A.25}) \qquad \underset{\sim}{E}_{yy}^k = \int_{A_k} \{ E_{yy}^k \underset{\sim}{\phi}_{,y}^T \underset{\sim}{\phi}_{,y} + E_{xy}^k \underset{\sim}{\phi}_{,x}^T \underset{\sim}{\phi}_{,x} \} \, dA$$

Returning now to the original form of the equations, all the ignored terms are lumped into a load vector. Thus

$$(\text{A.26}) \qquad - \underset{\sim}{P}_x^{e_i} = (\Delta q_{\underset{\sim}{x}}^{e_i})^T \int_{A_i} \{ \underset{\sim}{\phi}^T \underset{\sim}{\phi}_{,x} \underset{\sim}{c}_{xx}^{e_i} + \underset{\sim}{\phi}^T \underset{\sim}{\phi}_{,y} \underset{\sim}{c}_{yx}^{e_i} + \underset{\sim}{\phi}^T \underset{\sim}{\phi} \underset{\sim}{T}_x^s$$

$$- c_f^i \underset{\sim}{\phi}^T \underset{\sim}{\phi} \underset{\sim}{T}_x^b - \underset{\sim}{\phi}^T \underset{\sim}{\phi} \underset{\sim}{M}_x^{e_i} - \frac{1}{\rho_0} \underset{\sim}{\phi}^T \underset{\sim}{\phi} \underset{\sim}{P}^s \underset{\sim}{\phi}_{,x}^{e_i} \underset{\sim}{H}^{e_i}$$

$$- \frac{g}{\rho_0} \underset{\sim}{\phi}^T \underset{\sim}{\phi} \Delta \rho^{\bar{e}_i} \underset{\sim}{\phi} \underset{\sim}{H}^{e_i} \underset{\sim}{\phi}_{,x} \underset{\sim}{h}^{e_i} - g \underset{\sim}{\phi}^T \underset{\sim}{\phi} \underset{\sim}{\eta}^{e_i} \underset{\sim}{\phi}_{,x} \underset{\sim}{h}^{e_i} - \frac{1}{2} g \underset{\sim}{\phi}_{,x}^T \underset{\sim}{\phi} \underset{\sim}{\eta}^{e_i} \underset{\sim}{\phi} \underset{\sim}{\eta}^{e_i}$$

$$- \frac{1}{2} \frac{g}{\rho_0} \underset{\sim}{\phi}_{,x}^T \underset{\sim}{\phi} \Delta \rho^{e_i} \underset{\sim}{\phi} \underset{\sim}{H}^{e_i} \underset{\sim}{\phi} \underset{\sim}{H}^{e_i} - \frac{1}{\rho_0} \underset{\sim}{\phi}_{,x}^T \underset{\sim}{\phi} \underset{\sim}{P}^s \underset{\sim}{\phi} \underset{\sim}{H}^{e_i} \} \, dA$$

$$-(\Delta q_{\sim x}^{e_i})^T \int_{S_{q_1}} \{ \alpha_{nx} \phi_{\sim}^T E_{xx}^i \phi_{\sim,x} Q_{\sim x}^{e_i} - \alpha_{nx} \phi_{\sim}^T (g \phi_{\sim} h_{\sim}^{e_i} \phi_{\sim} \eta_{\sim}^{e_i}$$

$$- \frac{1}{2} g \phi_{\sim} \eta_{\sim}^{e_i} \phi_{\sim} \eta_{\sim}^{e_i} - \frac{g}{2\rho_0} \phi_{\sim} \Delta\rho^{e_i} \phi_{\sim} H_{\sim}^{e_i} \phi_{\sim} H_{\sim}^{e_i} - \frac{1}{\rho_0} \phi_{\sim} P^{s e_i} \phi_{\sim} H_{\sim}^{e_i})$$

$$+ \alpha_{ny} E_{yx}^i \phi_{\sim}^T (\phi_{\sim,y} Q_{\sim x}^{e_i} + \phi_{\sim,y} Q_{\sim y}^{e_i}) \} \, ds$$

$$+ (\Delta q_{\sim x}^{e_i})^T \int_{S_{F_1}} \alpha_{nx} \phi_{\sim}^T \{ g \phi_{\sim} h^{e_i} \phi_{\sim} \eta^{*e_i} + \frac{1}{2} g \phi_{\sim} \eta^{*e_i} \phi_{\sim} \eta^{*e_i}$$

$$+ \frac{g}{2\rho_0} \phi_{\sim} \Delta\rho^{e_i} \phi_{\sim} H^{*e_i} \phi_{\sim} H^{*e_i} + \frac{1}{\rho_0} \phi_{\sim} P^{s e_i} \phi_{\sim} H^{*e_i} \} \, ds$$

Again letting

$$(A.27) \qquad \frac{T_y^s}{\rho_0} \simeq \phi_{\sim} T_y^s$$

$$(A.28) \qquad (q_x^2 + q_y^2)^{1/2} \frac{q_y}{H^2} \simeq \phi_{\sim} T_y^b$$

we may write for the load in y-direction:

$$(A.29) \qquad - P_{\sim y}^{e_i} = (\Delta q_{\sim y}^{e_i})^T \int_{A_1} \{ \phi_{\sim}^T \phi_{\sim,x} c_{\sim xy}^{e_i} + \phi_{\sim}^T \phi_{\sim,y} c_{\sim yy}^{e_i} + \phi_{\sim}^T \phi_{\sim} T_{\sim y}^s$$

$$- c_f^i \phi_{\sim}^T \phi_{\sim} T_{\sim y}^b - \phi_{\sim}^T \phi_{\sim} M_{\sim y}^{e_i} - \frac{1}{\rho_0} \phi_{\sim}^T \phi_{\sim} P^{s e_i} \phi_{\sim,y} H_{\sim}^{e_i} -$$

$$- \frac{g}{\rho_0} \phi_{\sim}^T \phi_{\sim} \Delta\rho^{e_i} \phi_{\sim} H_{\sim}^{e_i} \phi_{\sim,y} h_{\sim}^{e_i} - g \phi_{\sim}^T \phi_{\sim} \eta_{\sim}^{e_i} \phi_{\sim,y} h_{\sim}^{e_i}$$

$$- \frac{1}{2} g \phi_{\sim,y}^T \phi_{\sim} \eta_{\sim}^{e_i} \phi_{\sim} \eta_{\sim}^{e_i} - \frac{1}{2} \frac{g}{\rho_0} \phi_{\sim,y}^T \phi_{\sim} \Delta\rho^{e_i} \phi_{\sim} H_{\sim}^{e_i} \phi_{\sim} H_{\sim}^{e_i}$$

$$- \frac{1}{\rho_0} \phi_{\sim,y}^T P^{s e_i} \phi_{\sim} H_{\sim}^{e_i} \} \, dA$$

271

$$- (\Delta q_{\sim y}^{e_i})^T \int_{S_{q_i}} \{ \alpha_{ny} \underset{\sim}{\phi}^T E_{yy}^i \underset{\sim}{\phi}_{,y} Q_{\sim y}^{e_i} - \alpha_{ny} \underset{\sim}{\phi}^T (g \underset{\sim}{\phi} h^{e_i} \underset{\sim}{\phi} \eta^{e_i}$$

$$- \frac{1}{2} g \underset{\sim}{\phi} \eta^{e_i} \underset{\sim}{\phi} \eta^{e_i} - \frac{g}{2\rho_0} \underset{\sim}{\phi} \Delta\rho^{e_i} \underset{\sim}{\phi} H^{e_i} \underset{\sim}{\phi} H^{e_i} - \frac{1}{\rho_0} \underset{\sim}{\phi} P^{s\,e_i} \underset{\sim}{\phi} H^{e_i})$$

$$+ \alpha_{nx} E_{xy}^i \underset{\sim}{\phi}^T (\underset{\sim}{\phi}_{,x} Q_{\sim y}^{e_i} + \underset{\sim}{\phi}_{,y} Q_{\sim x}^{e_i}) \} ds$$

$$+ (\Delta q_{\sim x}^{e_i})^T \int_{S_{F_i}} \alpha_{ny} \underset{\sim}{\phi}^T \{ g \underset{\sim}{\phi} h^{e_i} \underset{\sim}{\phi} \eta^{*e_i} + \frac{1}{2} g \underset{\sim}{\phi} \eta^{*e_i} \underset{\sim}{\phi} \eta^{*e_i}$$

$$+ \frac{g}{2\rho_0} \underset{\sim}{\phi} \Delta\rho^{e_i} \underset{\sim}{\phi} H^{*e_i} \underset{\sim}{\phi} H^{*e_i} + \frac{1}{\rho_0} \underset{\sim}{\phi} P^{s\,e_i} \underset{\sim}{\phi} H^{*e_i} \} ds$$

Finally, assembling the system equations by summing over all elements, become:

$$(A.30) \qquad \underset{\sim}{M} Q_{\sim x,t} - G_{\sim x}^T \underset{\sim}{\eta} + E_{\sim xx} Q_{\sim x} + E_{\sim yx} Q_{\sim y} - fMQ_{\sim\sim y} = P_{\sim x}$$

$$(A.31) \qquad \underset{\sim}{M} Q_{\sim y,t} - G_{\sim y}^T \underset{\sim}{\eta} + E_{\sim xy} Q_{\sim x} + E_{\sim yy} Q_{\sim y} + fMQ_{\sim\sim x} = P_{\sim y}$$